

# Numerical and Analytical Investigation of a Phase Field Model for Fracture

vom Fachbereich Maschinenbau und Verfahrenstechnik  
der Technischen Universität Kaiserslautern  
zur Verleihung des akademischen Grades  
Doktor-Ingenieur (Dr.-Ing.)  
genehmigte Dissertation

von  
Dipl.-Math. Charlotte Kuhn  
aus Mainz

Hauptreferent: Prof. Dr.-Ing. Ralf Müller  
Korreferenten: Prof. Dr.-Ing. Thomas Seelig  
Prof. Tarek I. Zohdi  
Vorsitzender: Prof. Dr.-Ing. Jan C. Aurich  
Dekan: Prof. Dr.-Ing. Bernd Sauer

Tag der Einreichung: 07.10.2012  
Tag der mündlichen Prüfung: 21.01.2013

Kaiserslautern, 2013

D 386

## **Herausgeber**

Lehrstuhl für Technische Mechanik  
Technische Universität Kaiserslautern  
Gottlieb-Daimler-Straße  
Postfach 3049  
67653 Kaiserslautern

© Charlotte Kuhn

Ich danke der „Prof. Dr. Hans Georg und Liselotte Hahn Stiftung“ für die finanzielle Unterstützung bei der Drucklegung.

## **Druck**

Technische Universität Kaiserslautern  
ZTB – Abteilung Foto-Repro-Druck

Alle Rechte vorbehalten, auch das des auszugsweisen Nachdrucks, der auszugsweisen oder vollständigen Wiedergabe (Photographie, Mikroskopie), der Speicherung in Datenverarbeitungsanlagen und das der Übersetzung.

ISBN 978-3-942695-06-0

# Vorwort

Die vorliegende Arbeit entstand während meiner Tätigkeit als wissenschaftliche Mitarbeiterin am Lehrstuhl für Technische Mechanik der Technischen Universität Kaiserslautern und am Fachgebiet für Festkörpermechanik der Technischen Universität Darmstadt. Um es mit Goethes Worten auszudrücken:

So eine Arbeit wird eigentlich nie fertig, man muß sie für fertig erklären, wenn man nach Zeit und Umständen das mögliche getan hat.

In diesem Sinne gilt mein besonderer Dank Herrn Prof. Dr.-Ing. Ralf Müller nicht nur für die in jeder Hinsicht hervorragende Betreuung und Unterstützung meiner wissenschaftlichen Arbeit, sondern auch für seine Geduld bei der Fertigstellung der Dissertation. Ebenso danke ich Herrn Prof. Dr.-Ing. Thomas Seelig und Herrn Prof. Tarek Zohdi für die freundliche Bereitschaft zur Übernahme der Korreferate und das damit verbundene Interesse an meiner Arbeit. Weiterhin danke ich Herrn Prof. Dr.-Ing. Jan C. Aurich für die Übernahme des Vorsitzes.

Herzlich bedanken möchte ich mich auch bei allen ehemaligen und aktuellen Kollegen an der TU Darmstadt und der TU Kaiserslautern. Die konstruktive und kollegiale Arbeitsatmosphäre sowie diverse außeruniversitäre Aktivitäten haben dazu beigetragen, dass ich meine Promotionszeit in guter Erinnerung behalten werde.

Zu guter Letzt möchte ich meinen Eltern und meiner Großmutter für den familiären Rückhalt und ihre fortwährende Unterstützung nicht nur während der Promotion danken.

Kaiserslautern, Mai 2013

Charlotte Kuhn



# Kurzfassung

Die Bruchmechanik befasst sich mit der Entstehung und Ausbreitung von Rissen in unterschiedlichen Materialien. Da Risswachstum das Versagen ganzer Strukturen verursachen kann, spielen bruchmechanische Untersuchungen eine wichtige Rolle bei der Auslegung von technischen Bauteilen. Während der eigentliche Bruchvorgang auf elementare Versagensprozesse auf der Mikroebene zurückzuführen ist, beschränkt sich die klassische Bruchmechanik auf die Bewertung von Rissen aus makroskopischer Sicht. Die Bruchkriterien basieren dabei meist auf der Untersuchung kontinuumsmechanischer Feldgrößen wie zum Beispiel Spannungen und Verzerrungen in der Nähe von Rissen. In der linearen Bruchmechanik wird davon ausgegangen, dass sich das Material im gesamten Gebiet bis zum Versagen linear elastisch verhält. Dabei handelt es sich um eine Vereinfachung, da es in unmittelbarer Nähe der Risspitze immer zu inelastischem Materialverhalten kommt und auch die elementaren Versagensprozesse auf der Mikroebene nicht durch die lineare Elastizitätstheorie erfasst werden können. Die Methoden der linearen Bruchmechanik können nur zweckmäßig angewendet werden, wenn die Zone, in der diese inelastischen Vorgänge stattfinden, aus makroskopischer Sicht vernachlässigbar klein ist. Dies ist insbesondere bei spröden Materialien häufig gegeben. Ein bedeutendes Kriterium der linearen Bruchmechanik geht auf A. A. Griffith (1893-1963) zurück. Sein energetisches Kriterium basiert auf der Annahme, dass die Rissausbreitung aus einem Konkurrenzkampf zwischen der im Körper gespeicherten elastischen Energie und der zur Trennung des Materials benötigten sogenannten Oberflächenenergie resultiert. Demnach kommt es zur Rissausbreitung wann immer dies energetisch günstiger ist. Die vorliegende Arbeit befasst sich mit einem Phasenfeldmodell zur Beschreibung von Bruchvorgängen, welches auf denselben Energieprinzipien beruht.

Risse werden dabei mit Hilfe eines skalaren Ordnungsparameters dargestellt, der mit den Materialeigenschaften gekoppelt ist, um den Steifigkeitsverlust von gebrochenem gegenüber intaktem Material zu modellieren. An Stellen, an denen intaktes Material vorliegt, hat der Ordnungsparameter den Wert eins, und das Material besitzt die volle Steifigkeit. Gebrochenes Material wird durch den Wert null charakterisiert und die Steifigkeit reduziert sich entsprechend. Risse werden in der Formulierung also nicht als Materialgrenzen behandelt, sondern sind Linien bzw. Flächen im Material, entlang derer das Rissfeld den Wert null annimmt und die Steifigkeit deutlich herabgesetzt ist. Für die numerische Umsetzung mit der Methode der Finiten Elemente ist dies sehr vorteilhaft. Zwischen gebrochenem und

intaktem Material findet ein glatter Übergang des Ordnungsparameters zwischen den Werten null und eins statt. Die Breite dieser Übergangszone, von der die Risse umgeben sind, wird durch einen Regularisierungsparameter festgelegt. Für das in dieser Arbeit betrachtete Phasenfeldmodell lässt sich zeigen, dass die der Formulierung zugrunde liegenden Energieausdrücke gegen die elastische und die Oberflächenenergie im Griffithschen Modell konvergieren, wenn der Regularisierungsparameter gegen null geht. Insofern kann das Modell als Regularisierung des Griffithschen Bruchkriteriums aufgefasst werden.

Um numerische Simulationen durchzuführen, wurde das Phasenfeldmodell in das Finite Elemente Programm *FEAP (Finite Element Analysis Program)* implementiert. Das Rissfeld wurde dabei als zusätzlicher Knotenfreiheitsgrad neben dem Verschiebungsvektor behandelt. Die numerischen Untersuchungen in dieser Arbeit beschränken sich auf ebene Probleme. In einem ersten Schritt wurden ebene Vierknotenelemente mit linearen Ansatzfunktionen für die Diskretisierung gewählt. Da beim verwendeten Phasenfeldansatz auch an Rissen keine unstetigen Verschiebungsfelder auftreten, ist die Implementierung des Modells vergleichsweise unkompliziert, und auch eine Erweiterung auf den dreidimensionalen Fall stellt keine besondere Schwierigkeit dar. Ein weiterer Vorteil ist, dass sich die Implementierung komplett auf die Elementebene beschränkt. So kann das Modell auch problemlos in andere FE-Programme eingebunden werden. Die zeitliche Entwicklung des Rissfelds wird durch eine thermodynamisch motivierte Evolutionsgleichung vom Ginzburg-Landau-Typ beschrieben. Deren numerische Integration wird mit dem impliziten Euler-Verfahren durchgeführt, um eine robuste Implementierung zu erzielen. Die diskrete Form des nichtlinearen gekoppelten globalen Gleichungssystems aus den mechanischen Feldgleichungen und der Evolutionsgleichung des Rissfelds wird mit einem Newton-Raphson-Algorithmus gelöst.

In numerischen Simulationen zeigt sich, dass das Phasenfeldmodell über die Grenzen der klassischen Griffith-Theorie hinaus in der Lage ist, viele bei der Rissausbreitung auftretenden Phänomene abzubilden. So kann beispielsweise eine Richtungsänderung des Rissfortschritts oder die Entstehung neuer Risse simuliert werden, ohne dass dafür zusätzliche Kriterien formuliert und neue Parameter eingeführt werden müssten. Diese Einfachheit und Universalität vereint mit einer einem Kontinuumsmodell angemessenen Qualität der Ergebnisse macht die Methode attraktiv für praktische Anwendungen. Um die erhaltenen Ergebnisse richtig interpretieren zu können, ist ein tieferes Verständnis der physikalischen Eigenschaften des Modells notwendig. Die Antriebsmechanismen der Rissausbreitung im Phasenfeldmodell sind jedoch nicht direkt ersichtlich, da die komplette Rissausbreitung implizit aus der Lösung des gekoppelten Gleichungssystems aus den elastomechanischen Feldgleichungen und der Evolutionsgleichung für das Rissfeld folgt.

Zur Veranschaulichung und zum besseren Verständnis der risstreibenden Mechanismen im Phasenfeldmodell, werden in dieser Arbeit verallgemeinerte Konfigurationskräfte für das Phasenfeldmodell hergeleitet und deren Zusammenhang mit dem Rissfortschritt untersucht. In gewisser Weise kann dieser Zugang auch als Brückenschlag zwischen dem Phasenfeldmodell und der Griffithschen Theorie aufgefasst werden, welche ebenfalls mit Hilfe von Konfigurationskräften formuliert werden kann.

Ein weiterer Aspekt, der genauer betrachtet wird, ist die Entstehung neuer Risse in ursprünglich ungeschädigtem Material. Da das Modell keinen Parameter beinhaltet, der in direktem Zusammenhang mit der Bruchfestigkeit des Materials steht, ist es nicht offensichtlich, bei welcher Last es im Phasenfeldmodell zur Rissentstehung kommt. Der Zusammenhang zwischen den Parametern des Phasenfeldmodells und der kritischen Last, bei der es zur Entstehung neuer Risse kommt wird zunächst im eindimensionalen Fall am Beispiel eines homogenen Stabes untersucht. Dazu werden bei vorgegebener Belastung zwei qualitativ unterschiedliche Lösungen der gekoppelten Phasenfeldgleichungen betrachtet und miteinander verglichen. Es handelt sich dabei einerseits um eine rissfreie Lösung mit räumlich konstantem Rissfeld und andererseits um eine Lösung mit einem räumlich lokalisiertem Rissfeld, die einem gebrochenen Stab entspricht. Beim Übergang von der rissfreien homogenen Lösung zur gebrochenen Konfiguration handelt es sich um ein Verzweigungsproblem. Die Rissentstehung ist auf einen Stabilitätsverlust der rissfreien Lösung zurückzuführen. Die am Stabilitätspunkt der homogenen Lösung erreichte maximale Spannung kann als Bruchfestigkeit des Materials interpretiert werden. Sie lässt sich aus der Steifigkeit und Bruchzähigkeit des Materials und dem Regularisierungsparameter des Phasenfeldmodells berechnen. Dies hat eine neue Interpretation des Regularisierungsparameters zur Konsequenz. Er ist in diesem Zusammenhang nicht mehr lediglich eine beliebige numerische Hilfsgröße, sondern ist durch die Bruchfestigkeit im Zusammenspiel mit den anderen Materialkenngrößen festgelegt und somit selbst als eine Art Materialparameter anzusehen. Die im eindimensionalen Fall gewonnenen Erkenntnisse lassen sich nicht ohne weiteres auf den mehrdimensionalen Fall verallgemeinern, da hier in der Regel inhomogene Belastungszustände vorliegen, für die eine analytische Stabilitätsuntersuchung nicht möglich ist. Aus der Betrachtung homogener Lastfälle lassen sich jedoch Abschätzungen für die Bruchfestigkeit im zweidimensionalen Fall herleiten, die sich in numerischen Simulationen als gute Näherung herausstellen.

Hinsichtlich der numerischen Umsetzung des Phasenfeldmodells liegt ein weiterer Schwerpunkt dieser Arbeit auf der Formulierung spezieller Ansatzfunktionen für das Rissfeld. Bei der Diskretisierung des Modells mit herkömmlichen linearen Ansatzfunktionen ist darauf zu achten, dass das FE-Netz fein genug ist, um den Übergangsbereich zwischen gebrochenem und intaktem Material hinreichend genau abzubilden. Dies erfordert insbesondere wenn der Regularisierungsparameter sehr klein

ist eine sehr feine Diskretisierung, was den Rechenaufwand erheblich erhöht. Um eine Steigerung der Effizienz der Methode zu erreichen, wurden deswegen spezielle Ansatzfunktionen für das Rissfeld entwickelt, deren Gestalt sich aus der analytischen Lösung des eindimensionalen stationären Problems ableitet. Bei der Verwendung dieser sogenannten exponentiellen Ansatzfunktionen zeigt sich, dass sie das Rissfeld in der Tat besser approximieren als lineare Ansatzfunktionen. Somit kann ohne Abstriche bezüglich der Genauigkeit der Ergebnisse eine gröbere Diskretisierung verwendet werden.



# Abstract

Fracture mechanics deals with the nucleation and propagation of cracks in different kinds of materials. Since crack extension can lead to total failure of a technical component, fracture mechanics plays an important role in the design process of structural components. While crack propagation actually results from failure processes on the micro scale, such as the breaking of atomic bonds, cracks are treated from a macroscopic point of view in classical fracture mechanics. Fracture criteria are based on the evaluation of continuum mechanical quantities like stresses and strains in the vicinity of cracks. In linear elastic fracture mechanics, it is assumed that the material response is linear elastic up to the point of failure. This is a simplification, because crack propagation is always preceded by inelastic processes in the fracture zone. Since these processes cannot be described by the means of linear elastic theory, linear elastic fracture mechanics is only appropriate if the zone where the material response is inelastic is negligibly small compared to the macroscopic dimensions of the sample. This is particularly the case for brittle materials. An important failure criterion of linear elastic fracture mechanics was established by A. A. Griffith (1893-1963). In his energetic criterion, fracture is interpreted as the result of a competition between the elastic stored energy in the bulk and the so called surface energy which is needed to create new fracture surfaces. A crack is assumed to propagate, whenever this is energetically favorable. The work at hand deals with a phase field model for fracture, which bases on the same energetic principles.

In the phase field model, fracture is indicated by a scalar order parameter, which is coupled to the material properties in order to model the change in stiffness between broken and undamaged material. Where the material is undamaged, the order parameter has the value one and the material properties remain unaltered. Broken material is characterized by the value zero and the stiffness of the material is reduced accordingly. Thus, in the phase field model, cracks are represented through lines or areas in the material, where the order parameter has the value zero and the stiffness is significantly reduced. Consequently, a crack does not need to be treated as a material boundary, which is especially advantageous for the finite element implementation of the fracture model. At interfaces between broken and undamaged material, the order parameter interpolates smoothly between the values assigned to the different material phases. The width of this transition zone, which surrounds the phase field cracks, is controlled by a regularization parameter. For the considered phase field fracture model, it can be shown that

the underlying energy expressions converge to the elastic and surface energy of Griffith's formulation in the limit of a vanishing regularization length. In this respect, the phase field fracture model may be interpreted as a regularization of Griffith's fracture criterion.

In order to perform numerical simulations, the phase field model has been implemented into the finite element code *FEAP* (*Finite Element Analysis Program*). In addition to the displacement vector, the phase field order parameter is treated as a supplementary nodal degree of freedom. Since the phase field formulation avoids the occurrence of discontinuities in the displacement and crack fields, the implementation is not very complex and usual linear shape functions can be used for the interpolation of the nodal values within the elements. The implementation is described in detail for the two dimensional case, where four noded elements are used for the discretization of plane structures. An adaption of the implementation to the three dimensional setting is very straightforward and does not require special consideration. The entire implementation of the phase field fracture model is restricted to the element level. This is another advantage of the proposed method, since it facilitates a smooth integration of the implementation into different finite element codes. The evolution of the crack field with respect to time is described by a thermodynamically motivated Ginzburg-Landau type evolution equation. In order to obtain a robust implementation, an implicit time integration scheme is employed for the temporal discretization of the transient evolution equation. In every time step, the nonlinear coupled system of equations formed by the discretized elastomechanical field equations and the evolution equation is solved using a Newton-Raphson algorithm.

Numerical simulations show, that beyond the scope of classical Griffith theory, the phase field fracture model is able to reproduce many phenomena which can be observed during fracture processes without any further extension of the model. This includes the deflection or branching of pre-existing cracks as well as the nucleation of new cracks in originally undamaged material. The simplicity and generality of the phase field approach, together with a reasonable quality of the results in the sense of a continuum fracture model, makes the method attractive for practical applications. However, a correct interpretation of the obtained results requires a profound understanding of the crack driving mechanisms in the phase field model. Yet these mechanisms are not very obvious, since the crack evolution in the phase field model follows implicitly from the solution of the coupled system of equations formed by the elastomechanical field equations and the evolution equation.

In order to visualize the crack driving mechanisms in the phase field model and to gain a deeper understanding thereof, the concept of configurational forces is generalized to the phase field model in this work. The derived relations between the generalized configurational forces and the crack evolution additionally highlight

the connection between the phase field fracture model and Griffith's energetic fracture criterion, which alternatively can be formulated in terms of configurational forces.

Another aspect that is addressed, is the phenomenon of crack nucleation in originally undamaged material. Since the phase field model does not feature a material parameter which is directly connected to the strength of the material, the critical load level for the nucleation of new cracks is not obvious. In a first step, the connection between the parameters of the phase field model and the critical load for crack nucleation is analyzed in the one dimensional setting. Therefore, two qualitatively different solutions of the coupled phase field equations are compared to each other. On the one hand this is a crack-free homogeneous solution, with spatially constant crack field, and on the other hand a solution with localized crack field which corresponds to a fractured structure. A stability analysis reveals that the transition of the crack-free homogeneous solution to the fractured configuration is caused by the loss of stability of the crack-free solution. The maximal stress response of the homogeneous solution indicates the stability point of the crack-free solution. Therefore, this maximal stress may be interpreted as the strength of the material. The value of the fracture stress is obtained from the stiffness and cracking resistance of the material in conjunction with the regularization parameter of the phase field formulation. Consequently, in this context, the regularization parameter is not only an auxiliary numerical quantity, but should be regarded as a material parameter.

In general, analytical solutions for nonhomogeneous two dimensional problems are not available, and thus, a rigorous mathematical stability analysis cannot be carried out. However, on the basis of the results in the one dimensional case, strength estimates can be deduced for the two dimensional setting. Numerical simulations show that these strength estimates are a good approximation of the actual fracture stress in the two dimensional phase field model.

Concerning the numerical implementation of the phase field model, another focus of this work is on the construction of special shape functions for the crack field. If standard linear shape functions are used for the discretization, the finite element mesh must be refined enough in order to properly resolve the transition zone between broken and undamaged material. Thus, especially if the regularization parameter is comparably small, a high level of mesh refinement is required, which is numerically demanding concerning computation time and required memory. In order to increase the efficiency of the simulations, special shape functions that qualitatively capture the shape of the one dimensional fractured crack field have been constructed. Simulations show, that through the improved approximation of the crack field, the exponential shape functions actually allow for a coarser discretization without compromise on the accuracy of the results.



# Contents

<b>1</b>	<b>Introduction</b>	<b>1</b>
1.1	Motivation and Background . . . . .	1
1.2	Objectives and Overview . . . . .	4
<b>2</b>	<b>Continuum Mechanics</b>	<b>9</b>
2.1	Kinematics . . . . .	9
2.2	Strain Measures . . . . .	11
2.3	Stress Measures . . . . .	13
2.4	Balance Laws . . . . .	14
2.4.1	Conservation of Mass . . . . .	14
2.4.2	Conservation of Linear and Angular Momentum . . . . .	15
2.4.3	Conservation of Energy . . . . .	16
2.4.4	Entropy . . . . .	17
2.5	Linear Theory . . . . .	19
2.5.1	Small Deformations . . . . .	19
2.5.2	Linear Elasticity . . . . .	20
<b>3</b>	<b>Linear Elastic Fracture Mechanics</b>	<b>23</b>
3.1	General Remarks . . . . .	23
3.2	Model Assumptions in LEFM . . . . .	24
3.3	Stress Intensity Factors and the $K$ -Concept . . . . .	24
3.4	The Griffith Criterion . . . . .	26
3.5	Configurational Forces in LEFM . . . . .	29
3.6	A Variational Formulation of Brittle Fracture . . . . .	32
<b>4</b>	<b>A Phase Field Model for Fracture</b>	<b>37</b>
4.1	Approximation of the Variational Formulation of Brittle Fracture . . . . .	37
4.2	Evolution Equation . . . . .	41
4.2.1	Thermodynamical Background . . . . .	41
4.2.2	Irreversibility of Cracking . . . . .	44
4.3	Dimensional Analysis . . . . .	46
4.4	Analytical Solutions of the 1d Quasi Static Problem . . . . .	48
4.4.1	The Unloaded Crack . . . . .	49
4.4.2	Tensile Loading . . . . .	50
4.4.3	Conclusion . . . . .	63
4.5	Modifications and Extensions . . . . .	64

## Contents

4.5.1	Compression . . . . .	64
4.5.2	Thermal Fracture . . . . .	65
4.5.3	Finite Deformations . . . . .	67
<b>5</b>	<b>Finite Element Implementation</b>	<b>69</b>
5.1	Weak Forms and Spatial Discretization . . . . .	69
5.2	Time Discretization and Iterative Solution . . . . .	72
5.3	Isoparametric Representation and Numerical Quadrature . . . . .	75
5.4	Irreversibility . . . . .	77
5.5	Examples . . . . .	79
5.5.1	Simulation of Cyclic Loading of a CT Specimen . . . . .	79
5.5.2	Crack Interaction . . . . .	84
5.6	Exponential Shape Functions . . . . .	86
5.6.1	1d Exponential Shape Functions . . . . .	88
5.6.2	Extension to 2d . . . . .	90
5.6.3	Numerical Examples . . . . .	93
5.6.4	Summary and Outlook . . . . .	99
<b>6</b>	<b>Configurational Forces in the Context of Phase Field Models</b>	<b>103</b>
6.1	Generalized Configurational Force Balance . . . . .	104
6.2	Relations to Crack Propagation . . . . .	105
6.2.1	Elastic Forces and the $\mathcal{J}$ -Integral . . . . .	106
6.2.2	Cohesive Forces . . . . .	107
6.2.3	Dissipative Forces . . . . .	108
6.2.4	Implementation into FEM . . . . .	109
6.3	Simulations . . . . .	112
6.3.1	Unloaded Crack . . . . .	112
6.3.2	Crack Growth under Mode I Loading . . . . .	113
<b>7</b>	<b>Crack Nucleation</b>	<b>117</b>
7.1	Simulation of Crack Nucleation . . . . .	117
7.2	Strength Estimates . . . . .	121
7.3	Tensile Specimen with Different Hole Sizes . . . . .	127
<b>8</b>	<b>Conclusion and Outlook</b>	<b>131</b>
	<b>Bibliography</b>	<b>133</b>

# 1 Introduction

## 1.1 Motivation and Background

Fracture is generally understood as the complete or incomplete separation of an initially undamaged body or structure due to the application of excessive loads. The prevention of failure induced by fracture is a major constraint in the design of an engineering structure. The integrity of different components of a structure can be investigated by means of experimental testing or numerical computer aided simulations. As experimental tests are expensive and time consuming, they cannot be carried out at all stages of a design process in an efficient and economic way. Thus, conclusions drawn from numerical simulations often play a crucial role in design decisions. As a consequence, lots of research effort is put into the development of reliable fracture models and the numerical implementation thereof. The key objective of these fracture models is the prediction of the fracture evolution in a given loading situation. On the one hand, this requires criteria for the onset of crack extension of pre-existing cracks and for the nucleation of new cracks in originally undamaged material. On the other hand, the geometry of the crack path, including possible kinking of a crack or bifurcation into several crack branches, needs to be predicted. In dynamic fracture mechanics, also the velocity of crack propagation is an issue.

The theoretical foundations of the contemporary theory of brittle fracture were laid in the works of Griffith [1921] and Irwin [1957]. Griffith was the first to link the energy necessary for the breaking of atomic bonds to an energy density of crack surfaces. As a consequence, he formulated an energetic fracture criterion, where crack propagation results from the competition of elastic energy stored in the solid and surface energy needed to create new fracture surfaces. The actual breakthrough of this new concept was achieved through the works of Irwin. Besides a refinement of the surface energy density proposed by Griffith, he characterized the loading of a crack in terms of singular stresses at the crack tip, and proved the equivalence of his method and Griffith's energetic approach. This link allows to evaluate cracks using the tools of classical continuum mechanics and opened the door to practical applications of the new concepts and to further research in the field of theoretical fracture mechanics.

The failure criteria mentioned above are only able to predict the onset of crack propagation along an a priori known crack path. In order to predict also the crack path in a mixed mode loading situation, additional criteria are necessary. For brittle crack extension in a 2d isotropic setting, there are numerous, partially

## 1 Introduction

contradictory, deflection criteria available in the literature. The most popular among them are probably the maximum hoop stress criterion from Erdogan and Sih [1963], the principle of local symmetry according to Goldstein and Salganik [1974] and the criterion of maximum energy release by Nuismer [1975]. However, no final consensus about which of these theories is the most appropriate has been reached so far, and for the 3d case, the task of crack path prediction becomes even more intricate due to the more complex possible crack geometries.

Further issues which are not finally solved in fracture mechanics are the nucleation of new cracks in the absence of macroscopically detectable initial cracks, and the transition from crack nucleation to macroscopic crack extension.

In an effort to establish a self-contained continuum theory, which does not require additional tools in order to determine the crack path and crack nucleations, Francfort and Marigo [1998] propose a variational formulation of brittle fracture, which bases on the well accepted energetic ideas of Griffith and the postulation of global minimality of the total energy. Despite the scarcity of the ingredients, this theory is able to predict the entire crack evolution, including the crack path. However, the precise mathematical framework in which the variational theory of brittle fracture is formulated is a complicated topic by itself.

Besides the development of physically sound and appropriate models of crack propagation, numerical instruments are needed to describe the elastic deformations of complex structures, which generally cannot be obtained analytically. To this end, particularly the finite element method (FEM) is widely used in industrial applications. The essential characteristic of this method is the discretization of a continuous structure into a set of sub-domains referred to as elements with a certain number of element nodes. The partial differential equations for the unknown field variables are then recast into a finite dimensional set of equations for the discrete nodal values. In between the element nodes, the unknown field variables are usually approximated by means of continuous shape functions. Consequently, finite elements do not cope well with field discontinuities. This challenges their application in the context of fracture mechanics, because at a crack the displacement field may suffer jump discontinuities. Most commonly, remeshing strategies, where the mesh is updated after every crack progression in order to match the new geometry of the discontinuity set, are employed for the simulation of fracture processes. As an alternative, the so called extended finite element method (X-FEM) has been introduced by Moës et al. [1999]. Through an enrichment of the displacement shape functions with discontinuities, based on the partition of unity method of Babuska and Melenk [1996], this method allows to simulate crack growth without remeshing. However, in the case of complex crack patterns, the application of this technique becomes very difficult especially in a 3d setting.

In this regard, a conceptually different modeling approach to fracture has gained importance in recent years. The so called phase field method bases on concepts



elaborated by Ginzburg and Landau [1959] and was originally introduced by Collins and Levine [1985] and Caginalp and Fife [1986] in order to model solidification processes. The general idea of this modeling approach is the incorporation of an additional continuous field variable – the phase field order parameter – whose value describes the condition of the system. At interfaces between different material phases, the order parameter interpolates smoothly between the values assigned to the different phases, avoiding discontinuous jumps. The width of the diffuse transition zone between different material phases is controlled by a model inherent length scale. If this length scale becomes infinitesimal small, the underlying sharp interface model is recovered. In a phase field model, the motion of the interfaces is given implicitly by the solution of a partial differential equation for the order parameter. This so called evolution equation is coupled to the elastic field equations in order to model the mutual interaction between the phase state and the elastic properties of the material. This coupling also has the effect that the boundary conditions at phase interfaces are automatically satisfied, thus avoiding an explicit treatment thereof. This property is also very advantageous concerning numerical simulations and significantly facilitates the study of structures with more complex interface geometries. Thus, the phase field method is a very powerful numerical tool to solve moving boundary problems.

The general approach of phase field modeling can be applied to a broad variety of different free boundary problems, see for example Karma and Rappel [1998] for the modeling of dendritic growth, Echebarria et al. [2004] for modeling the solidification of binary alloys, Kobayashi and Warren [2005] for a 3d model for the formation of polychristals, or Schrader et al. [2007] and Müller et al. [2007] for applications to ferroelectric phase transitions.

Applications of the phase field concept to fracture mechanics have been introduced and discussed e.g. in Aranson et al. [2000], Karma et al. [2001], Eastgate et al. [2002], Karma and Lobkovsky [2004], Henry and Levine [2004], Hakim and Karma [2005] or Corson et al. [2009], where additionally thermal effects are considered. In this particular case, the phase field order parameter is referred to as the crack field. The value 1 is assigned to undamaged material, and 0 indicates cracks. Thus, fracture is addressed as a phase transition of the order parameter from phase 1 (undamaged) to phase 0 (broken). The change in stiffness between broken and undamaged material is modeled by means of a degradation function which also establishes the coupling between the elastic field equations and the evolution equation of the order parameter. The entire crack evolution implicitly follows from the solution of the coupled system of equations. As no jump discontinuities need to be considered, phase field fracture models can be implemented into standard finite element software, using standard shape functions. Remeshing is not necessarily required in order to simulate crack growth. Thus, the phase field approach allows to study even problems with difficult topological changes, such as multiple branching or the merging of cracks, which is anticipated to be an especially challenging task

## 1 Introduction

for many sharp crack models. The phase field model discussed in this thesis as well as the model proposed in Miehe et al. [2010b] or Borden et al. [2012] base upon a regularized approximation of the variational formulation of brittle fracture, which was introduced by Bourdin et al. [2000]. Based on the theory of  $\Gamma$ -convergence, it is assured that this particular type of phase field fracture model converges to an energetically motivated fracture criterion with a Griffith type surface energy in the sharp interface limit.

From the standpoint of material modeling, phase field fracture models are conceptually very similar to models of continuum damage mechanics, where a scalar field describes the damage state of the material, see e.g. the books Kachanov [1986] or Murakami [2012] for an extensive overview on the topic. In order to overcome problematic issues like strain localization and mesh dependency that local damage models are plagued by, so called gradient damage models have been introduced e.g. by Triantafyllidis and Aifantis [1986]; see also de Borst et al. [1995] for a review of gradient enhanced damage and plasticity models. In these models, the damage rate additionally depends on the gradient of the damage variable. The resulting coupled system of equations has a structure that is equivalent to the structure of the field equations of a phase field fracture model. Thus, the improved behavior concerning strain localization and mesh dependency also applies to the phase field fracture models. The main difference between gradient damage and phase field fracture lies in the interpretation of the damage or crack field and the intrinsic length scales. In damage models, the damage field describes the development of micro cracks and voids in a homogenized macroscopic sense. The characteristic length scale of a gradient damage model is anticipated to be connected with the maximum size of material inhomogeneities. In contrast, the crack field and the regularization length of a phase field fracture model are generally regarded as purely auxiliary quantities, which approximate the sharp crack setting.

### 1.2 Objectives and Overview

A phase field fracture model based on Bourdin's regularization of the variational fracture criterion by Francfort and Marigo is the subject of this thesis. The energy density functional of the regularized model provides a solid ground for the formulation of a phase field fracture model, because convergence results are available which attest that the surface energy of the diffuse crack field converges to the surface energy of a sharp Griffith crack in the limit of a vanishing regularization length. As for earlier phase field models based on different formulations of the energy density, no rigorous mathematical analysis of the convergence behavior is available.

The high potential of phase field modeling in computational fracture mechanics lies in its simplicity and generality combined with a reasonable validity of the results in the sense of a continuum fracture model. Numerical experiments have shown

that phase field fracture models can capture even complex crack behavior, such as crack nucleation and branching, or the coalescence of different cracks, without introducing any additional ad hoc criteria and without the need of employing remeshing strategies. However, despite the simplicity of the numerical application of phase field fracture models, a detailed understanding of the model's physical properties is crucial for a correct interpretation of the obtained results. Hence, the focus of this work is on a thorough investigation of the proposed phase field fracture model in order to gain deeper insight into the fundamental characteristics of the formulation.

The analysis includes a discussion of different approaches of modeling the irreversibility of fracture processes in the phase field model. In this respect, the original phase field approach requires a modification when applied to fracture mechanics, as the original formulation allows for phase transitions in either direction, i.e. cracks could heal. The impact of the different proposed strategies on the crack field evolution is compared in numerical simulations.

Another aspect which is highlighted is the close connection between the present phase field fracture model and the classical energy criterion of Griffith. In this regard, the concept of configurational forces provides an illustrative visualization of the energetic driving mechanisms of crack propagation in the phase field model. Additionally configurational forces enable the evaluation of the criticality of a stationary phase field crack. Thus, providing information which is not immediately obtained by the phase field model. Numerical simulations demonstrate the anticipated benefit of the configurational forces.

A further issue that is addressed, is the phenomenon of crack nucleation in originally crack-free structures. This is of particular interest, because the phase field model is able to reproduce crack nucleations on the one hand, but it does not feature a material parameter which is obviously connected to the strength of the material on the other hand. Thus, the critical load at which cracks can nucleate is not a priori clear. At this point, a stability analysis of the 1d phase field model yields the conclusion, that crack nucleation in the phase field model is triggered by the loss of stability of the crack-free solution. Furthermore, the results encourage the definition of a critical fracture stress, which consequently means a reinterpretation of the phase field regularization length as a material parameter.

On the numerical side, the thesis contributes a robust implementation of the phase field fracture model into a finite element code with implicit time integration. The implementation is given for a 2d plane strain setting. However, an extension to 3d is straightforward and does not require special consideration. Besides the implementation with standard finite element shape functions, a new discretization technique using special shape functions is introduced. These shape functions are constructed in such a way that they qualitatively capture the shape of the crack field. Compared to standard linear finite element shape functions, they allow a coarser discretization without compromise on the accuracy of the results.

## 1 Introduction

This thesis is composed of eight chapters. To set the stage, the fundamental kinematics and balance equations of continuum mechanics, which are relevant to the work at hand, are briefly summarized in the next chapter.

Chapter 3 gives a brief overview over the classical concepts of linear elastic fracture mechanics. The focus is laid on the energetically motivated Griffith criterion, which is the basis of the variational formulation of brittle fracture outlined at the end of the chapter.

Chapter 4 begins with the introduction of Bourdin's regularization of the variational formulation of brittle fracture. The regularized model already resembles a phase field model. However, just as in the variational formulation, the crack evolution is governed by the postulation of global minimality, rather than by an evolution equation in the sense of a phase field model. For the phase field formulation, a thermodynamically consistent Ginzburg-Landau type evolution equation is derived in the second section of the chapter. Different strategies of addressing the irreversibility of fracture processes are discussed. An analysis of the 1d model on the one hand motivates the special discretization technique discussed in section 5.6, and provides insight into the mechanisms of crack nucleation in the phase field model on the other hand. Some refinements and extensions of the phase field fracture model are discussed in the end of the chapter.

The implementation of the 2d phase field fracture model into a finite element framework with implicit time integration of the evolution equation is outlined in chapter 5. Illustrative examples point out the capabilities of the phase field approach in the field of fracture simulation. A special focus of this chapter is on a new discretization technique which allows a coarser discretization and therefore increases the efficiency of the simulations.

In chapter 6, the concept of configurational forces of linear elastic fracture mechanics is generalized to the phase field fracture model. Relations between the generalized configurational forces and the crack evolution in the phase field model are derived for mode I loading scenarios. This chapter also comprises an implementation of the generalized configurational forces into the finite element code. The technique which is used is an efficient tool for the computation of discrete configurational forces, as it merely requires a post-processing of already computed data. It is pointed out, that the computation of configurational forces is not necessary in order to determine the crack evolution in the phase field model, which immediately follows from the solution of the coupled field equations. Nevertheless, the discrete configurational forces are a valuable tool for the visualization of the energetic driving mechanisms of crack propagation in the phase field model.

Chapter 7 is concerned with the simulation of crack nucleation in originally crack-free structures. From an application point of view, these simulations do not require special consideration, even though the nucleation of a new crack means a drastic

topological change, and the transition from brutal crack nucleation to stable crack growth needs to be mastered. The simulation results suggest that, as well as in the 1d case, the nucleation of new cracks is connected with a stability problem. As a general stability analysis of the 2d problem is not available, parts of the analytic results for the 1d model are translated into the 2d setting in order to obtain estimates for the fracture stress in 2d. The validity of these estimates is tested in different simulations. Furthermore, the capability of the phase field model to reproduce size effects is studied in a failure simulation of tension strips with different hole sizes. The simulation results are compared with experimental data and results obtained with Leguillon's failure criterion.

Chapter 8 gives a short conclusion and an outlook on future work.

## *1 Introduction*

# 2 Continuum Mechanics

In order to fix the notation and to provide some basic relations for later reference, this chapter gives a brief introduction into the subject of classical continuum mechanics. The outline is based on comprehensive textbooks on the subject, such as Holzapfel [2000] or Gurtin [1981].

## 2.1 Kinematics

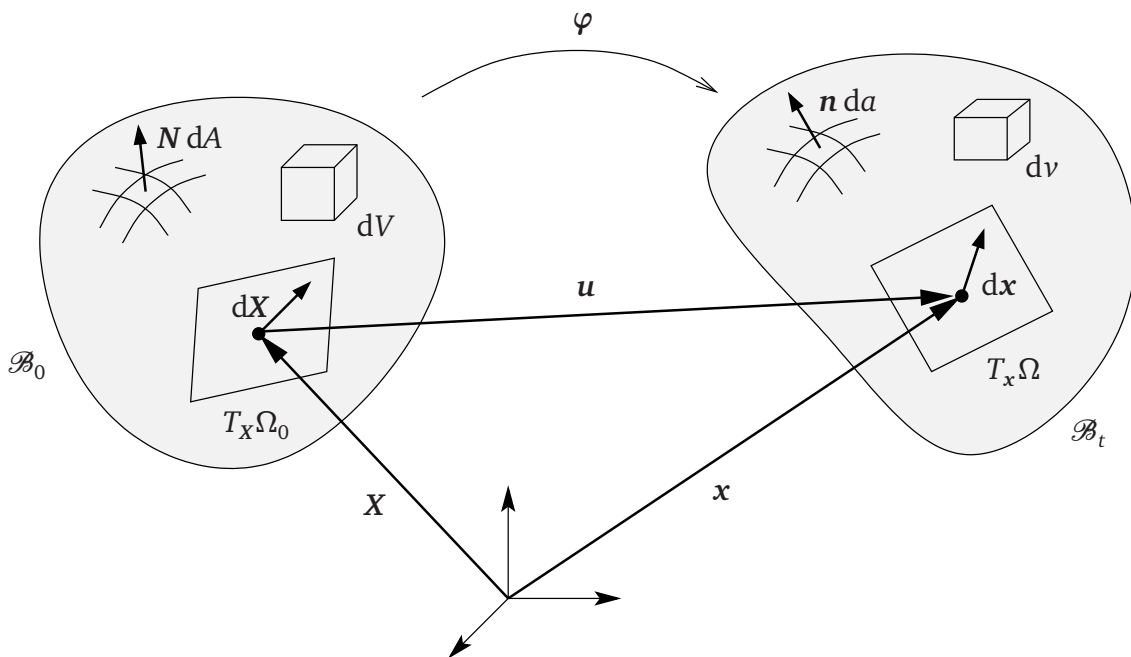


Figure 2.1: Reference and actual configuration.

In continuum mechanics, a material body is usually identified with the spatial position  $X$  of its material points in a so called *reference configuration*  $\mathcal{B}_0$ . The motion of the material points to their current position  $x$  in the *current or actual configuration*  $\mathcal{B}_t$  is given by the generally non-linear deformation mapping

$$\mathbf{x} = \varphi(\mathbf{X}, t), \quad (2.1)$$

where the scalar  $t$  denotes time. As illustrated in Fig. 2.1, the *displacement vector*  $\mathbf{u}$

## 2 Continuum Mechanics

is defined by the difference

$$\mathbf{u} = \mathbf{x} - \mathbf{X} = \varphi(\mathbf{X}, t) - \mathbf{X}. \quad (2.2)$$

The Jacobian of the deformation mapping  $\varphi$

$$\mathbf{F} = \frac{\partial \varphi(\mathbf{X}, t)}{\partial \mathbf{X}} = \frac{\partial \mathbf{x}}{\partial \mathbf{X}} = \text{Grad } \mathbf{x} \quad (2.3)$$

is called the *deformation gradient*. The index notation is given by

$$F_{ij} = \frac{\partial x_i}{\partial X_j}. \quad (2.4)$$

It is closely related to the *displacement gradient*

$$\mathbf{H} = \frac{\partial \mathbf{u}}{\partial \mathbf{X}} = \frac{\partial \mathbf{x}}{\partial \mathbf{X}} - \frac{\partial \mathbf{X}}{\partial \mathbf{X}} = \mathbf{F} - \mathbf{1}, \quad (2.5)$$

with  $\mathbf{1}$  denoting the second order identity tensor with the components  $\delta_{ij}$  (the Kronecker symbol). Besides the tacit assumption of smoothness with respect to  $\mathbf{X}$  and  $t$ , the deformation mapping  $\varphi$  is assumed to be invertible and orientation preserving for any fixed time  $t$ . Thus, the condition

$$J = \det \left( \frac{\partial \varphi(\mathbf{X}, t)}{\partial \mathbf{X}} \right) = \det(\mathbf{F}) > 0 \quad (2.6)$$

for the Jacobian determinant  $J$  holds at any time  $t$ . The deformation gradient  $\mathbf{F}$  maps line elements  $d\mathbf{X}$  from the tangent space  $T_{\mathbf{X}}\mathcal{B}_0$  of the reference configuration to line elements  $d\mathbf{x}$  in the tangent space  $T_{\mathbf{x}}\mathcal{B}_t$  of the current configuration, i.e.

$$d\mathbf{x} = \mathbf{F}d\mathbf{X} \quad \Leftrightarrow \quad dx_i = F_{ij}dX_j, \quad (2.7)$$

where Einstein's summation convention applies for the index notation. A surface element  $dA$  with normal vector  $\mathbf{N}$  in the cotangent space  $T_{\mathbf{X}}^*\mathcal{B}_0$  of the reference configuration transforms into a surface element  $da$  with normal vector  $\mathbf{n}$  in the cotangent space  $T_{\mathbf{x}}^*\mathcal{B}_t$  of the actual configuration according to Nanson's relation

$$\mathbf{n} da = J\mathbf{F}^{-T}\mathbf{N} dA, \quad (2.8)$$

with  $\mathbf{F}^{-T}$  being the inverse of the transpose of the deformation gradient, i.e.  $\mathbf{F}^{-T} = (\mathbf{F}^T)^{-1}$ . Volume elements  $dV$  and  $d\nu$  of the reference and actual configuration, respectively, are transformed by

$$d\nu = J dV. \quad (2.9)$$

The *velocity* of a material point in the current configuration is given by the material



time derivative (denoted by a superposed dot) of the actual position  $\mathbf{x}$

$$\mathbf{v} = \frac{d\mathbf{x}}{dt} = \dot{\mathbf{x}}. \quad (2.10)$$

Accordingly, the acceleration of a material point is

$$\mathbf{a} = \frac{d\mathbf{v}}{dt} = \dot{\mathbf{v}} = \ddot{\mathbf{x}}. \quad (2.11)$$

The computation of the material time derivative of the deformation gradient  $\dot{\mathbf{F}}$  yields the relation

$$\mathbf{l} = \frac{\partial \mathbf{v}}{\partial \mathbf{x}} = \text{grad } \mathbf{v} = \dot{\mathbf{F}}\mathbf{F}^{-1} \quad (2.12)$$

for the *spatial velocity gradient*  $\mathbf{l}$ .

## 2.2 Strain Measures

It can be shown, that there is a unique multiplicative decomposition of the deformation gradient  $\mathbf{F}$  into a proper orthogonal rotation  $\mathbf{R}$  and a symmetric, positive definite right stretch tensor  $\mathbf{U}$  or left stretch tensor  $\mathbf{V}$ , so that

$$\mathbf{F} = \mathbf{R}\mathbf{U} = \mathbf{V}\mathbf{R}. \quad (2.13)$$

The *right* and *left Cauchy-Green tensors*  $\mathbf{C}$  and  $\mathbf{b}$  defined by

$$\mathbf{C} = \mathbf{F}^T\mathbf{F} = \mathbf{U}^T\mathbf{U} = \mathbf{U}^2 \quad \text{and} \quad (2.14)$$

$$\mathbf{b} = \mathbf{F}\mathbf{F}^T = \mathbf{V}\mathbf{V}^T = \mathbf{V}^2 \quad (2.15)$$

do not account for the rotational part  $\mathbf{R}$  of the deformation gradient. They can be used to compute the length  $ds$  of the line element  $d\mathbf{x}$  in the current configuration from the reference line element  $d\mathbf{X}$  or the rotated line element  $\mathbf{R}d\mathbf{X}$ , respectively

$$ds^2 = d\mathbf{x} \cdot d\mathbf{x} = d\mathbf{X} \cdot [\mathbf{C}d\mathbf{X}] = (\mathbf{R}d\mathbf{X}) \cdot [\mathbf{b}(\mathbf{R}d\mathbf{X})]. \quad (2.16)$$

The dot symbolizes the usual inner product of two vectors, i.e.  $\mathbf{a} \cdot \mathbf{b} = a_i b_i$ . In case of a (local) rigid body motion, the right and left Cauchy-Green tensors equal the second order identity tensor ( $\mathbf{C} = \mathbf{b} = \mathbf{1}$ ). This leads to the definition of the *Green-Lagrange strain tensor*

$$\mathbf{E} = \frac{1}{2}(\mathbf{C} - \mathbf{1}) \quad (2.17)$$

and the *Euler-Almansi strain tensor*

$$\mathbf{e} = \frac{1}{2}(\mathbf{1} - \mathbf{b}^{-1}) \quad (2.18)$$

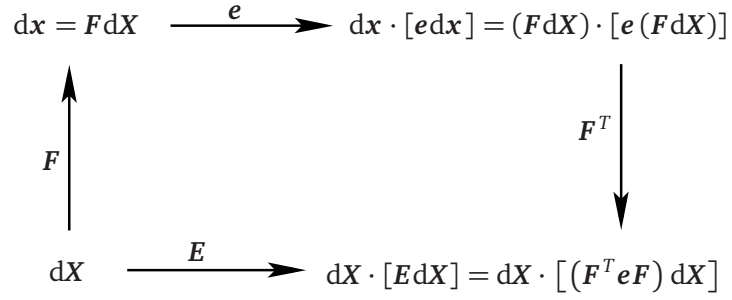


Figure 2.2: Strain tensors in reference and actual configuration.

as strain measures, which vanish in case of a rigid body motion. They describe the stretching  $ds^2 - dS^2$  of line elements in the reference and current configuration, respectively

$$ds^2 - dS^2 = dx \cdot dx - dX \cdot dX = 2dX \cdot [EdX] = 2dx \cdot [edx]. \quad (2.19)$$

The relation

$$E = F^T eF \quad (2.20)$$

between the Green-Lagrange and the Euler-Almansi strain tensors follows immediately from their definitions (Eq. 2.17 and 2.18) or alternatively from Eq. (2.19), see also Fig. 2.2. In terms of the displacement gradient, the Green-Lagrange strain tensor can be expressed as

$$E = \frac{1}{2} (H + H^T + H^T H). \quad (2.21)$$

The material time derivative  $\dot{E}$  of the Green-Lagrange strain tensor is related to the symmetric part

$$d = \frac{1}{2} (l + l^T) \quad (2.22)$$

of the *spatial velocity gradient*  $l$  through the equality

$$\dot{E} = F^T dF. \quad (2.23)$$

The following analogue of Eq. (2.19) holds for the rate  $\frac{d}{dt} (ds^2 - dS^2)$  of the stretching

$$\frac{d}{dt} (ds^2 - dS^2) = 2dX \cdot [\dot{E}dX] = 2dx \cdot [d dx]. \quad (2.24)$$

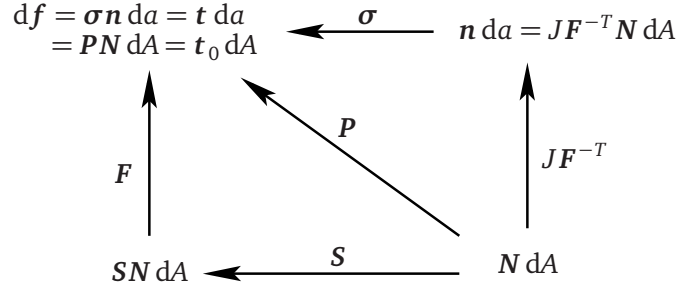


Figure 2.3: Stress tensors in reference and actual configuration.

## 2.3 Stress Measures

The stress resultant force  $d\mathbf{f}$  on an infinitesimal surface  $da$  with normal direction  $\mathbf{n}$  in the current configuration, can be measured with respect to the actual surface element  $da$  or alternatively with respect to the reference surface element  $dA$  in order to define a stress vector. The former defines the *surface traction vector*  $\mathbf{t}$ , the latter defines the *nominal traction vector*  $\mathbf{t}_0$

$$d\mathbf{f} = \mathbf{t} da = \mathbf{t}_0 dA. \quad (2.25)$$

According to the *Cauchy theorem*, there is a second order tensor, the so called *Cauchy stress tensor*  $\boldsymbol{\sigma}$ , which maps a normal vector  $\mathbf{n}$  of the current configuration to the respective surface traction vector through the relation

$$\mathbf{t} = \boldsymbol{\sigma}^T \mathbf{n}.^1 \quad (2.26)$$

The analogue relation for the nominal traction vector reads

$$\mathbf{t}_0 = \mathbf{P} \mathbf{N}, \quad (2.27)$$

where  $\mathbf{P}$  is the *first Piola-Kirchhoff stress tensor* which is a two-point tensor which maps normal vectors  $\mathbf{N}$  from the reference configuration to the respective nominal traction vector  $\mathbf{t}_0$  in the current configuration. Nanson's formula (Eq. 2.8) yields the relation

$$\mathbf{P} = J \mathbf{F}^{-T} \boldsymbol{\sigma} \quad \Leftrightarrow \quad \boldsymbol{\sigma} = \frac{1}{J} \mathbf{F}^T \mathbf{P} \quad (2.28)$$

between  $\boldsymbol{\sigma}$  and  $\mathbf{P}$ , see also Fig. 2.3 for an illustration. The *second Piola-Kirchhoff stress tensor*

$$\mathbf{S} = \mathbf{F}^{-1} \mathbf{P} = J \mathbf{F}^{-1} \boldsymbol{\sigma} \mathbf{F}^{-T} \quad (2.29)$$

is introduced in order to obtain a stress measure which is purely formulated in the reference configuration. From the symmetry of the Cauchy stress tensor  $\boldsymbol{\sigma}$  it can easily be concluded that  $\mathbf{S}$  is symmetric, too.

<sup>1</sup>As the Cauchy stress tensor is symmetric, this formula simplifies to  $\mathbf{t} = \boldsymbol{\sigma} \mathbf{n}$ .

## 2.4 Balance Laws

In the following, balance laws for different physical quantities are formulated. These axiomatic laws postulate that the change of a physical quantity  $\varphi$  integrated over a control volume  $\mathcal{P}_t$  is balanced by the flux  $\mathbf{q}_\varphi$  of  $\varphi$  into the domain and the production  $r_\varphi$  and supply  $s_\varphi$  in the bulk, i.e.

$$\frac{d}{dt} \int_{\mathcal{P}_t} \varphi \, dv = \int_{\partial \mathcal{P}_t} \mathbf{q}_\varphi \cdot \mathbf{n} \, da + \int_{\mathcal{P}_t} (r_\varphi + s_\varphi) \, dv. \quad (2.30)$$

Assuming continuity of matter and smoothness of the field quantities, an application of *Reynold's transport theorem*

$$\frac{d}{dt} \int_{\mathcal{P}_t} \varphi \, dv = \int_{\mathcal{P}_t} \frac{\partial \varphi}{\partial t} \, dv + \int_{\partial \mathcal{P}_t} \varphi \mathbf{v} \cdot \mathbf{n} \, da \quad (2.31)$$

and the *Gauss' divergence theorem* in the format

$$\int_{\partial \mathcal{P}_t} \varphi \mathbf{v} \cdot \mathbf{n} \, da = \int_{\mathcal{P}_t} \operatorname{div} (\varphi \mathbf{v}) \, dv \quad (2.32)$$

yields the local formulation

$$\dot{\varphi} + \varphi \operatorname{div} \mathbf{v} = \operatorname{div} \mathbf{q}_\varphi + r_\varphi + s_\varphi. \quad (2.33)$$

The divergence of a vector field  $\mathbf{a}$  with respect to the actual configuration is defined by

$$\operatorname{div} \mathbf{a} = \frac{\partial a_i}{\partial x_i} = a_{i>i}, \quad (2.34)$$

where the notation  $(\cdot)_{,i}$  is introduced to abbreviate the partial derivative with respect to  $x_i$ .

### 2.4.1 Conservation of Mass

With the *mass density*  $\rho$ , the global and local formulations of the conservation of mass in a closed system with  $\mathbf{q}_\varphi = \mathbf{0}$  and  $r_\varphi = s_\varphi = 0$  read

$$\frac{d}{dt} \int_{\mathcal{P}_t} \rho \, dv = 0 \quad \text{and} \quad \dot{\rho} + \rho \operatorname{div} \mathbf{v} = 0. \quad (2.35)$$

A transformation to the reference configuration with the help of Eq. (2.9) yields

$$0 = \frac{d}{dt} \int_{\mathcal{P}_0} \underbrace{\rho J}_{=\rho_0} \, dV = \int_{\mathcal{P}_0} \dot{\rho}_0 \, dV \quad \Rightarrow \quad \dot{\rho}_0 = 0 \quad (2.36)$$

for the mass density  $\rho_0$  with respect to the reference configuration.

## 2.4.2 Conservation of Linear and Angular Momentum

With the volume density of linear momentum  $\rho \mathbf{v}$ , surface tractions  $\mathbf{t}$  and volume forces  $\mathbf{f}$ , the global form of the conservation of linear momentum reads

$$\frac{d}{dt} \int_{\mathcal{P}_t} \rho \mathbf{v} \, dv = \int_{\partial \mathcal{P}_t} \mathbf{t} \, da + \int_{\mathcal{P}_t} \mathbf{f} \, dv. \quad (2.37)$$

With help of the Cauchy theorem (Eq. 2.26) and the continuity equation (Eq. 2.35) this yields the local format

$$\rho \mathbf{a} = \operatorname{div} \boldsymbol{\sigma}^T + \mathbf{f} \quad \Leftrightarrow \quad \rho a_i = \sigma_{ji,j} + f_i, \quad (2.38)$$

where the index notation is introduced in order to avoid confusion about the definition of the divergence of the second order tensor  $\boldsymbol{\sigma}^T$ . The global balance law for the angular momentum is given by

$$\frac{d}{dt} \int_{\mathcal{P}_t} \mathbf{x} \times \rho \mathbf{v} \, dv = \int_{\partial \mathcal{P}_t} \mathbf{x} \times \mathbf{t} \, da + \int_{\mathcal{P}_t} \mathbf{x} \times \mathbf{f} \, dv, \quad (2.39)$$

where the symbol  $\times$  denotes the cross product. Again using the Cauchy theorem (Eq. 2.26) and the continuity equation (Eq. 2.35) plus the local form of the balance of linear momentum (Eq. 2.38), the local form simplifies to

$$\boldsymbol{\sigma} = \boldsymbol{\sigma}^T \quad \Leftrightarrow \quad \sigma_{ij} = \sigma_{ji}. \quad (2.40)$$

Thus, the balance law (Eq. 2.38) may be rewritten in the more common format

$$\rho \mathbf{a} = \operatorname{div} \boldsymbol{\sigma} + \mathbf{f} \quad \Leftrightarrow \quad \rho a_i = \sigma_{ij,j} + f_i. \quad (2.41)$$

In the static case, the inertia terms  $\rho \mathbf{a}$  are neglected and thus, the left hand sides of Eqs. (2.41) become zero

$$\mathbf{0} = \operatorname{div} \boldsymbol{\sigma} + \mathbf{f} \quad \Leftrightarrow \quad 0 = \sigma_{ij,j} + f_i. \quad (2.42)$$

With  $\mathbf{f}_0 = J\mathbf{f}$ , and the nominal traction  $\mathbf{t}_0$  and density  $\rho_0$  as defined in Eqs. (2.25) and (2.36), respectively, the global balance of linear momentum formulated in the reference configuration reads

$$\frac{d}{dt} \int_{\mathcal{P}_0} \rho_0 \mathbf{v} \, dV = \int_{\partial \mathcal{P}_0} \mathbf{t}_0 \, dA + \int_{\mathcal{P}_0} \mathbf{f}_0 \, dV. \quad (2.43)$$

With the definition of the first Piola-Kirchhoff stress tensor (Eq. 2.27) and the continuity equation in the reference configuration (Eq. 2.36), the local form becomes

$$\rho_0 \mathbf{a} = \text{Div} \mathbf{P} + \mathbf{f}_0. \quad (2.44)$$

### 2.4.3 Conservation of Energy

The first law of thermodynamics is equivalent to the conservation of energy in a control volume  $\mathcal{P}_t$ . It states that the rate of the stored internal and kinetic energy

$$\frac{d}{dt}(E(\mathcal{P}_t) + K(\mathcal{P}_t)) = \frac{d}{dt} \int_{\mathcal{P}_t} \rho \left( \mathcal{U}^* + \frac{|\mathbf{v}|^2}{2} \right) dv = \int_{\mathcal{P}_t} \rho (\dot{\mathcal{U}}^* + \mathbf{v} \cdot \mathbf{a}) dv, \quad (2.45)$$

where  $\mathcal{U}^*$  is the *specific internal energy* per unit mass, is equal to the sum of to the *rate of work of external forces*  $\mathcal{W}(\mathcal{P}_t)$  and the *heat supply*  $\mathcal{Q}(\mathcal{P}_t)$ , i.e.

$$\frac{d}{dt}(E(\mathcal{P}_t) + K(\mathcal{P}_t)) = \mathcal{W}(\mathcal{P}_t) + \mathcal{Q}(\mathcal{P}_t). \quad (2.46)$$

If only mechanical forces are considered, the rate at which external forces perform work on a control volume  $\mathcal{P}_t$  is

$$\mathcal{W}(\mathcal{P}_t) = \int_{\partial \mathcal{P}_t} \mathbf{t} \cdot \mathbf{v} da + \int_{\mathcal{P}_t} \mathbf{f} \cdot \mathbf{v} dv. \quad (2.47)$$

With the *heat flux*  $\mathbf{q}^\theta$  (pointing outwards of  $\mathcal{P}_t$ ) and the *specific heat supply* per unit mass  $s_\theta^*$ , the total heat supply is

$$\mathcal{Q}(\mathcal{P}_t) = \int_{\mathcal{P}_t} \rho s_\theta^* dv - \int_{\partial \mathcal{P}_t} \mathbf{q}^\theta \cdot \mathbf{n} da. \quad (2.48)$$

Using the definition of the symmetric part of the spatial velocity gradient  $\mathbf{d}$  (Eq. 2.22), Gauss' divergence theorem (Eq. 2.32) and the balance of linear momentum (Eq. 2.41), the local form of the energy balance (Eq. 2.46) becomes

$$\rho \dot{\mathcal{U}}^* = \rho s_\theta^* + \boldsymbol{\sigma} : \mathbf{d} - \text{div} \mathbf{q}^\theta. \quad (2.49)$$

Here, the double-dot symbolizes the inner product of two second order tensors, i.e.  $\boldsymbol{\sigma} : \mathbf{d} = \sigma_{ij} d_{ij}$ .

### 2.4.4 Entropy

The *entropy*  $\mathcal{S}$  of a system is assumed to satisfy the global balance law

$$\frac{d}{dt} \int_{\mathcal{D}_t} \rho \mathcal{S}^* dv = \int_{\partial \mathcal{D}_t} -\frac{\mathbf{q}^\theta}{\theta} \cdot \mathbf{n} da + \int_{\mathcal{D}_t} r_{\mathcal{S}} + \rho \frac{s_\theta^*}{\theta} dv, \quad (2.50)$$

where  $\mathcal{S}^*$  is the *entropy density* per unit mass and  $r_{\mathcal{S}}$  is the *production of entropy* in the bulk. The entropy flux and supply are assumed to be the heat flux and supply, respectively, normalized by the *absolute temperature*  $\theta > 0$ . The second law of thermodynamics states that production of entropy must be non-negative, i.e.

$$r_{\mathcal{S}} \geq 0. \quad (2.51)$$

Thus, the local formulation of Eq. (2.50) yields the *Clausius-Duhem inequality*

$$\rho \dot{\mathcal{S}}^* + \operatorname{div} \left( \frac{\mathbf{q}^\theta}{\theta} \right) - \frac{\rho s_\theta^*}{\theta} = r_{\mathcal{S}} \geq 0. \quad (2.52)$$

Multiplied by the absolute temperature  $\theta$  and integrated over the control volume  $\mathcal{D}_t$ , the Clausius-Duhem inequality (Eq. 2.52) takes the global form

$$\int_{\mathcal{D}_t} \rho \theta \dot{\mathcal{S}}^* dv + \int_{\partial \mathcal{D}_t} \mathbf{q}^\theta \cdot \mathbf{n} da - \int_{\mathcal{D}_t} \frac{1}{\theta} \nabla \theta \cdot \mathbf{q}^\theta dv \geq \int_{\mathcal{D}_t} \rho s_\theta^* dv. \quad (2.53)$$

Here, the notation  $\nabla \theta$  is used for the temperature gradient  $\operatorname{grad} \theta$ . In combination with the energy balance (Eq. 2.46) and the definition of the heat supply (Eq. 2.48), this yields

$$\int_{\mathcal{D}_t} [\rho (\dot{\mathcal{U}}^* - \theta \dot{\mathcal{S}}^*) + \rho \mathbf{v} \cdot \mathbf{a}] dv \leq \mathcal{W}(\mathcal{D}_t) - \int_{\mathcal{D}_t} \frac{1}{\theta} \nabla \theta \cdot \mathbf{q}^\theta dv, \quad (2.54)$$

where it is useful to introduce the *Helmholtz free energy* per unit mass

$$\psi^* = \mathcal{U}^* - \theta \mathcal{S}^* \quad \Rightarrow \quad \dot{\psi}^* = \dot{\mathcal{U}}^* - \theta \dot{\mathcal{S}}^* - \dot{\theta} \mathcal{S}^* \quad (2.55)$$

in order to obtain the format

$$\mathcal{W}(\mathcal{D}_t) - \int_{\mathcal{D}_t} \left[ \rho \mathbf{v} \cdot \mathbf{a} - \rho (\dot{\psi}^* + \dot{\theta} \mathcal{S}^*) - \frac{1}{\theta} \nabla \theta \cdot \mathbf{q}^\theta \right] dv \geq 0. \quad (2.56)$$

With the definition of the work of the external forces (Eq. 2.47) and the balance law (Eq. 2.41), this yields the *dissipation inequality*

$$\mathcal{D} = \int_{\mathcal{D}_t} \left[ \boldsymbol{\sigma} : \mathbf{d} - \rho (\dot{\psi}^* + \dot{\theta} \mathcal{S}^*) - \frac{1}{\theta} \nabla \theta \cdot \mathbf{q}^\theta \right] dv \geq 0. \quad (2.57)$$

This inequality must hold independently for the conductive (thermal) part

$$\mathcal{D}_{\text{con}} = - \int_{\mathcal{D}_t} \frac{1}{\theta} \nabla \theta \cdot \mathbf{q}^\theta \, dv \geq 0 \quad (2.58)$$

and the local (intrinsic) part

$$\mathcal{D}_{\text{loc}} = \int_{\mathcal{D}_t} [\boldsymbol{\sigma} : \mathbf{d} - \rho (\dot{\psi}^* + \dot{\theta} \mathcal{S}^*)] \, dv \geq 0. \quad (2.59)$$

The inequality in Eq. (2.58) is commonly referred to as the *heat conduction inequality* and is satisfied e.g. if the heat flux  $\mathbf{q}^\theta$  and the temperature gradient  $\nabla \theta$  are related through the *Fourier law*

$$\mathbf{q}^\theta = -\boldsymbol{\kappa} \nabla \theta \quad (2.60)$$

with a positive semi-definite *heat conduction tensor*  $\boldsymbol{\kappa}$ . Formulated in the reference configuration, the *Clausius-Planck inequality* (Eq. 2.59) for the local dissipation reads

$$\mathcal{D}_{\text{loc}} = \int_{\mathcal{D}_0} [\mathbf{P} : \dot{\mathbf{F}} - \rho_0 (\dot{\psi}^* + \dot{\theta} \mathcal{S}^*)] \, dV \geq 0, \quad (2.61)$$

where the first term  $\mathbf{P} : \dot{\mathbf{F}}$  may be substituted by the equivalent expression  $\mathbf{S} : \dot{\mathbf{E}}$ . In this format, the Clausius-Planck inequality is often used to derive restrictions on the constitutive relations following the reasoning of Coleman and Noll [1963] and Coleman and Gurtin [1967]. Under the assumption that the Helmholtz free energy per unit volume  $\psi = \rho_0 \psi^*$  is a function of the deformation gradient  $\mathbf{F}$  and the absolute temperature  $\theta$

$$\psi = \tilde{\psi}(\mathbf{F}, \theta), \quad (2.62)$$

the local form of the material Clausius-Planck inequality (Eq. 2.61) becomes

$$\left( \mathbf{P} - \frac{\partial \tilde{\psi}}{\partial \mathbf{F}} \right) : \dot{\mathbf{F}} + \left( \mathcal{S} - \frac{\partial \tilde{\psi}}{\partial \theta} \right) \dot{\theta} \geq 0, \quad (2.63)$$

where  $\mathcal{S} = \rho_0 \mathcal{S}^*$  is the entropy per unit volume. This implies the constitutive relations

$$\mathbf{P} = \frac{\partial \tilde{\psi}}{\partial \mathbf{F}} \quad \Leftrightarrow \quad \mathbf{S} = \frac{\partial \tilde{\psi}}{\partial \mathbf{E}} = 2 \frac{\partial \tilde{\psi}}{\partial \mathbf{C}} \quad \text{and} \quad (2.64)$$

$$\mathcal{S} = \frac{\partial \tilde{\psi}}{\partial \theta}. \quad (2.65)$$



## 2.5 Linear Theory

### 2.5.1 Small Deformations

If the material undergoes only small deformations, i.e.

$$|H_{ij}| = \left| \frac{\partial u_i}{\partial X_j} \right| \ll 1 \quad \forall i, j, \quad (2.66)$$

a geometrically linear theory is sufficient to describe the kinematics. In this case, it is no longer necessary to distinguish between differentiations with respect to  $\mathbf{x}$  and  $\mathbf{X}$

$$\frac{\partial}{\partial \mathbf{x}}(\cdot) \approx \frac{\partial}{\partial \mathbf{X}}(\cdot) \quad \Rightarrow \quad \text{grad}(\cdot) \approx \text{Grad}(\cdot), \quad \text{div}(\cdot) \approx \text{Div}(\cdot). \quad (2.67)$$

The notation with lower case letters will be used for the differential operators in the following. Furthermore, as

$$J = \det \mathbf{F} \approx 1, \quad (2.68)$$

it is no longer necessary to distinguish between volume elements and densities in the actual and reference configuration

$$dv \approx dV, \quad \rho_0 \approx \rho. \quad (2.69)$$

Since higher order terms of  $\mathbf{H}$  may be neglected in a small strain setting, the introduced strain tensors  $\mathbf{E}$  and  $\mathbf{e}$  both coincide with the *linearized* or *infinitesimal strain tensor*

$$\boldsymbol{\varepsilon} = \frac{1}{2} \left( \text{grad} \mathbf{u} + (\text{grad} \mathbf{u})^T \right). \quad (2.70)$$

If additionally small deformation rates are assumed, an analogue relation holds for the strain rates

$$\dot{\mathbf{E}} \approx \mathbf{d} \approx \dot{\boldsymbol{\varepsilon}}. \quad (2.71)$$

The trace of the linearized strain tensor equals the relative volume change of an infinitesimal volume element  $dV$

$$\varepsilon_V = \text{tr} \boldsymbol{\varepsilon} = \varepsilon_{kk} = \frac{\Delta dV}{dV}. \quad (2.72)$$

Consequently,  $\varepsilon_V$  is referred to as the *volumetric strain*. With the definition

$$\boldsymbol{\varepsilon}^{\text{dev}} = \boldsymbol{\varepsilon} - \frac{\varepsilon_V}{n} \mathbf{1} \quad (2.73)$$

of the *deviatoric strain tensor* in an  $n$ -dimensional setting, the linearized strain tensor can be split additively into

$$\boldsymbol{\varepsilon} = \frac{\varepsilon_V}{n} \mathbf{1} + \boldsymbol{\varepsilon}^{\text{dev}}, \quad (2.74)$$

where the first term accounts only for the volume change, while the deviatoric strain  $\boldsymbol{\varepsilon}^{\text{dev}}$  describes a pure distortion at constant volume.

### 2.5.2 Linear Elasticity

In a small strain regime, the introduced stress measures,  $\boldsymbol{\sigma}$ ,  $\mathbf{P}$  and  $\mathbf{S}$  do not need to be distinguished. The stress tensor is usually called  $\boldsymbol{\sigma}$ . The global balance of linear momentum for a control volume  $\mathcal{D}^2$  and the local counterpart read

$$\int_{\mathcal{D}} \rho \mathbf{a} \, dV = \int_{\partial \mathcal{D}} \mathbf{t} \, dA + \int_{\mathcal{D}} \mathbf{f} \, dV \quad (2.75)$$

and

$$\rho \mathbf{a} = \text{div } \boldsymbol{\sigma} + \mathbf{f}. \quad (2.76)$$

The Clausius-Planck inequality (Eq. 2.59) becomes

$$\mathcal{D}_{\text{loc}} = \int_{\mathcal{D}} [\boldsymbol{\sigma} : \dot{\boldsymbol{\varepsilon}} - \dot{\psi} + \mathcal{S} \dot{\theta}] \, dV, \quad (2.77)$$

which yields the constitutive relations

$$\boldsymbol{\sigma} = \frac{\partial \psi}{\partial \boldsymbol{\varepsilon}} \quad \text{and} \quad \mathcal{S} = \frac{\partial \psi}{\partial \theta}. \quad (2.78)$$

Under isothermal conditions ( $\dot{\theta} = 0$ ), the definition

$$\psi = \frac{1}{2} \boldsymbol{\varepsilon} : [\mathbb{C} \boldsymbol{\varepsilon}] \quad \Leftrightarrow \quad \psi = \frac{1}{2} \varepsilon_{ij} \mathbb{C}_{ijkl} \varepsilon_{kl} \quad (2.79)$$

of the free energy density as a quadratic function of the linearized strain tensor yields the linear elastic constitutive law

$$\boldsymbol{\sigma} = \mathbb{C} \boldsymbol{\varepsilon} \quad \Leftrightarrow \quad \sigma_{ij} = \mathbb{C}_{ijkl} \varepsilon_{kl}, \quad (2.80)$$

which is a tensor representation of *Hooke's law* of elasticity. The fourth order tensor  $\mathbb{C} = \mathbb{C}_{ijkl}$  is called the *stiffness* or *elasticity tensor*. Due to the symmetry of the stress and strain tensor and the constitutive relation in Eq. (2.80), the tensor components  $\mathbb{C}_{ijkl}$  possess the symmetries

$$\mathbb{C}_{ijkl} = \mathbb{C}_{jikl} = \mathbb{C}_{ijlk} = \mathbb{C}_{klij}. \quad (2.81)$$

For an isotropic material, which shows the same behavior in all directions, the stiffness tensor  $\mathbb{C}$  solely depends on the two independent *Lamé constants*  $\lambda$  and  $\mu$

$$\mathbb{C}_{ijkl} = \lambda \delta_{ij} \delta_{kl} + \mu (\delta_{ik} \delta_{jl} + \delta_{il} \delta_{jk}). \quad (2.82)$$

---

<sup>2</sup>No subscript 0 or  $t$  is used because the reference and actual configurations coincide.

The relations between the Lamé constants and *Young's modulus*  $E$ , *Poisson's ratio*  $\nu$  and the *shear modulus*  $G$  are

$$\lambda = \frac{\nu E}{(1 + \nu)(1 - 2\nu)} \quad \text{and} \quad \mu = G = \frac{E}{2(1 + \nu)}. \quad (2.83)$$

With the split of the linearized strain tensor according to Eq. (2.74), the material law may be decomposed into a hydrostatic (volumetric) and a deviatoric part

$$\boldsymbol{\sigma} = K_n \varepsilon_V \mathbf{1} + 2\mu \boldsymbol{\varepsilon}^{\text{dev}}, \quad (2.84)$$

where

$$K_n = \lambda + \frac{2\mu}{n} \quad (2.85)$$

denotes the  $n$ -dimensional *bulk modulus*.



# 3 Linear Elastic Fracture Mechanics

This chapter gives a short introduction to the basic theories of linear elastic fracture mechanics. The outline follows comprehensive textbooks on fracture mechanics, such as e.g. Gross and Seelig [2010].

## 3.1 General Remarks

This chapter is concerned with a continuum approach to brittle fracture. The description of the physicochemical details of failure, like the breaking of atomic bonds during fracture, goes beyond the scope of this theory. Also the influence of micro cracks, pores and inclusions on the meso scale, or point defects like vacancies or dislocations in the crystal lattice of polycrystalline material on the micro scale, is not explicitly taken into account. Instead, the material is treated as a continuum, and fracture is predicted on the basis of an analysis of the macroscopic quantities stress, strain and energy. From this macroscopic point of view, a crack is a cut in the body at the scale of the structure. In a more mathematical description, cracks are regarded as geometric discontinuities. Generally, the dimension of a crack is considered to be one dimension lower than the geometrical dimension of the surrounding material. Thus, in two-dimensional media, a crack is a line (discontinuity) and the end point is called the *crack tip*. In three-dimensional media, a crack forms a (discontinuity) surface ending at the *crack front*. The opposite boundaries of a crack are called *crack faces* or *crack flanks*. They form the *crack surface*, which plays an important role in the energetically motivated fracture criterion by Griffith [1921], which will be introduced in section 3.4 of this chapter. In most applications, the crack faces are considered to be traction free.

The loading of a crack can be split into three independent components, according to Fig. 3.1. *Mode I* is a symmetric crack opening orthogonal to the local fracture surface. It is the most important case for practical applications. In *mode II*, the crack surfaces slide relatively to each other in the plane of the crack and perpendicular to the crack front, causing shear stresses in the respective direction. In the tearing *mode III*, the crack surfaces also separate in the plane of the crack, but parallel to the crack front. This split of the crack loading into different opening modes is exploited in the fracture criterion which goes back to Irwin [1957] and will be outlined in section 3.3 of this chapter. In this concept, the criticality of a crack is

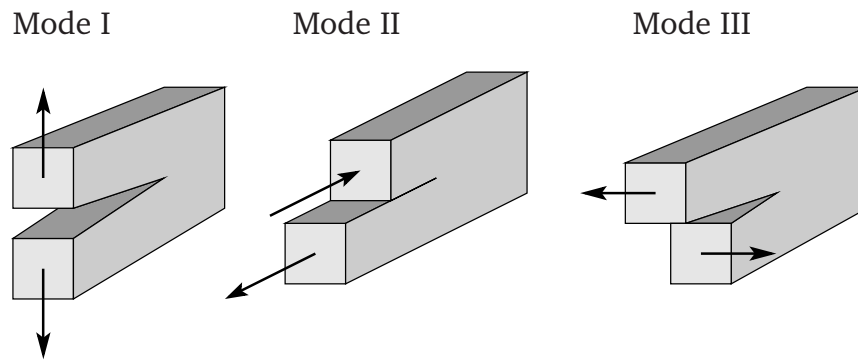


Figure 3.1: Crack opening modes.

evaluated via so called stress intensity factors, which are computed separately for each opening mode.

## 3.2 Model Assumptions in LEFM

As mentioned before, the complex processes of bond breaking in front of the crack front or crack tip, respectively, are not explicitly described by continuum approaches to fracture. Therefore, the so called *process zone*, in which these events take place, must be negligibly small compared to all macroscopic dimensions of the investigated structure, including the crack, if the whole cracked body shall be adequately described by a continuum theory. This assumption holds true for many brittle materials and is also a typical feature of metals.

As already alluded to by its name, linearity is a further assumption in *linear elastic fracture mechanics* (LEFM), i.e. the material is assumed to be linear elastic in the entire region right up to the point of fracture. However, the linear elastic analysis of the crack tip fields yields solutions with stress and strain singularities at the crack tip. This, at first sight, contradicts the assumptions that legitimate the usage of linear elastic theory. In reality, however, the material will deform inelastically in the so called *yielding zone* around the crack tip, so that no infinite stresses or strains do occur. Thus, linear theory is applicable, if this yielding zone is limited to a very small area around the crack, so that outside of this zone, the linear elastic solution is a good approximation of the actual stress and strain states. This is often referred to as the *small scale yielding* (SSY) assumption, which holds true for many brittle but not for ductile materials.

## 3.3 Stress Intensity Factors and the $K$ -Concept

In a two dimensional setting, the linear elastic problem of a stationary straight crack under mechanical loading can be solved analytically by means of the method of

### 3.3 Stress Intensity Factors and the K-Concept

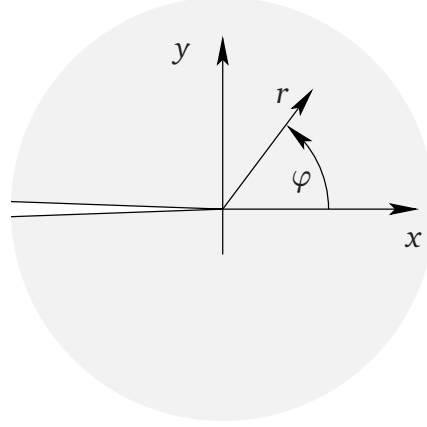


Figure 3.2: Cartesian and polar coordinates at the crack tip.

complex variables. Within a certain area around the crack tip, which is assumed to be significantly larger than the process and yielding zones, the stress fields of this solution are dominated by the singular expressions

$$\begin{Bmatrix} \sigma_x \\ \sigma_y \\ \tau_{xy} \end{Bmatrix} = \frac{K_I}{\sqrt{2\pi r}} \cos(\varphi/2) \begin{Bmatrix} 1 - \sin(\varphi/2) \sin(3\varphi/2) \\ 1 + \sin(\varphi/2) \sin(3\varphi/2) \\ \sin(\varphi/2) \cos(3\varphi/2) \end{Bmatrix}, \quad (3.1)$$

$$\begin{Bmatrix} \sigma_x \\ \sigma_y \\ \tau_{xy} \end{Bmatrix} = \frac{K_{II}}{\sqrt{2\pi r}} \begin{Bmatrix} -\sin(\varphi/2) [2 + \cos(\varphi/2) \cos(3\varphi/2)] \\ \sin(\varphi/2) \cos(\varphi/2) \cos(3\varphi/2) \\ \cos(\varphi/2) [1 - \sin(\varphi/2) \sin(3\varphi/2)] \end{Bmatrix}, \quad (3.2)$$

$$\begin{Bmatrix} \tau_{xz} \\ \tau_{yz} \end{Bmatrix} = \frac{K_{III}}{\sqrt{2\pi r}} \begin{Bmatrix} -\sin(\varphi/2) \\ \cos(\varphi/2) \end{Bmatrix} \quad (3.3)$$

with the polar coordinates  $r$  and  $\varphi$  according to Fig. 3.2. Equations (3.1), (3.2) and (3.3) refer to the crack opening modes I, II and III, respectively. The so called *stress intensity factors*  $K_I$ ,  $K_{II}$  and  $K_{III}$  are constants, which depend on the geometry of the sample, the crack length and the loading. As the magnitude of the crack tip singularity is fully controlled by the stress intensity factors, they can be used to formulate a fracture criterion as introduced by Irwin [1957], where a crack is assumed to propagate if the stress intensity factors reach a material specific critical value. For the pure mode I loading case, the criterion simply reads

$$K_I = K_{Ic} \quad (3.4)$$

with the *fracture toughness*  $K_{Ic}$  of the material. Analogous criteria can be formulated for the pure mode II and mode III loading cases, respectively. The mixed mode case,

requires a more general formulation of the type

$$f(K_I, K_{II}, K_{III}) = 0. \quad (3.5)$$

### 3.4 The Griffith Criterion

In Griffith's energetic approach to fracture, the energy balance (Eq. 2.46) is supplemented by an extra term, in order to account for the energy which is needed for the fracture process. This *fracture surface energy*  $\Gamma$  is assumed to be proportional to the size of the area  $A$  of the crack

$$\Gamma = \mathcal{G}_c A. \quad (3.6)$$

The material constant  $\mathcal{G}_c$  is called *crack resistance* or, alluding to its dimension, *crack resistance force*. The rate of the fracture surface energy enters the left hand side of the energy balance (Eq. 2.46), so that it becomes

$$\dot{E} + \dot{K} + \dot{\Gamma} = \dot{\mathcal{W}} + \dot{\mathcal{Q}}. \quad (3.7)$$

In the special case of quasi static fracture, where cracks proceed comparatively slowly, the contribution of the kinetic energy  $K$  can be neglected. Additionally it is assumed that there is no heat supply or heat flux, i.e.  $\mathcal{Q} = 0$ . Thus, the energy balance (Eq. 3.7) simplifies to

$$\dot{E} + \dot{\Gamma} = \dot{\mathcal{W}}. \quad (3.8)$$

In the purely elastic case, the internal energy  $E$  has the form of an inner potential  $E = \Pi_{\text{int}}$ . If additionally the external forces are conservative and possess the potential  $\Pi_{\text{ext}}$  with  $\dot{\mathcal{W}} = -\frac{d\Pi_{\text{ext}}}{dt}$ , the energy balance may be rewritten in the format

$$\frac{d\Pi}{dt} + \frac{d\Gamma}{dt} = 0 \quad (3.9)$$

with the total potential  $\Pi = \Pi_{\text{int}} + \Pi_{\text{ext}}$ . With respect to an infinitesimal extension  $dA$  of the crack area along an a priori prescribed crack path, Eq. (3.9) is formally equivalent to

$$\left( \frac{d\Pi}{dA} + \frac{d\Gamma}{dA} \right) \frac{dA}{dt} = 0. \quad (3.10)$$

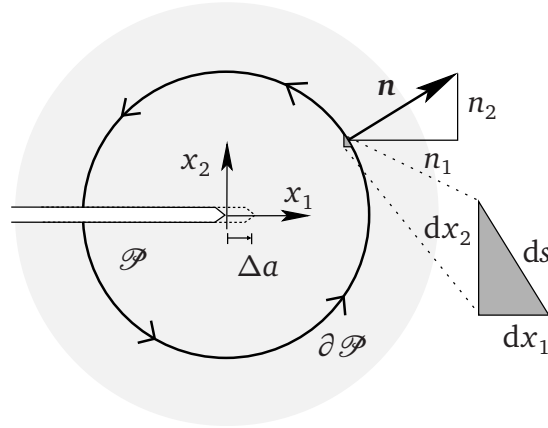
With the *energy release rate* defined as the release of potential energy upon an infinitesimal crack extension

$$\mathcal{G} = -\frac{d\Pi}{dA} \quad (3.11)$$

and the relation  $\frac{d\Gamma}{dA} = \mathcal{G}_c$  following from the definition of the fracture surface energy (Eq. 3.6), Eq. (3.10) simplifies to

$$(\mathcal{G}_c - \mathcal{G}) \dot{A} = 0. \quad (3.12)$$




 Figure 3.3: Definition of the  $\mathcal{J}$ -integral at a crack tip.

Originally, Griffith exploited this energy relation only to derive the condition

$$\mathcal{G} = \mathcal{G}_c \quad (3.13)$$

for the initiation of crack propagation. However, adding the natural postulation of irreversibility, also the subsequent evolution of the crack area is dictated by the energy relation (Eq. 3.12). The evolution law for the crack area  $A$  can be recast into the three-pronged format of the Kuhn-Tucker complementary conditions

- $\dot{A} \geq 0$  (irreversibility),
- $\mathcal{G} - \mathcal{G}_c \leq 0$  (Griffith's criterion),
- $\dot{A} (\mathcal{G} - \mathcal{G}_c) = 0$  (conservation of energy),

see e.g. Chambolle et al. [2009].

For straight growing cracks, there is an equivalence between the  $K$ -concept and the energy release rate in linear elastic fracture mechanics, as it can be shown that

$$\mathcal{G} = \frac{K_I^2 + K_{II}^2}{E'} + \frac{K_{III}^2}{2G}. \quad (3.14)$$

Under plane strain assumptions and in the 3d case, the constant  $E'$  is given by  $E' = E/(1 - \nu)$ , while  $E' = E$  applies for the plane stress case. Thus, the energy release rate  $\mathcal{G}$  can be computed via the stress intensity factors  $K_I$ ,  $K_{II}$  and  $K_{III}$ , which are listed in various handbooks of stress intensity factors for many different loading situations and geometries.

A different approach to the computation of the energy release rate in a 2d setting, is the evaluation of the so called  $\mathcal{J}$ -integral, which was introduced independently by Rice [1968a] and Cherepanov [1967]. Applied to a straight crack in elastic media

### 3 Linear Elastic Fracture Mechanics

as depicted in Fig. 3.3, it is defined as

$$\mathcal{J} = \int_{\partial \mathcal{D}} \psi dx_2 - t_i \frac{\partial u_i}{\partial x_1} ds, \quad (3.15)$$

where  $\partial \mathcal{D}$  is a contour around the crack tip with the arc length parametrization  $s$ . Using the relation  $dx_2 = n_1 ds$  and the Cauchy theorem (Eq. 2.26), it can alternatively be expressed as

$$\mathcal{J} = \int_{\partial \mathcal{D}} (\psi \delta_{j1} - \sigma_{ij} u_{i,1}) n_j ds, \quad (3.16)$$

where  $\mathbf{n} = (n_1, n_2)^T$  is the outward unit normal vector to the area  $\mathcal{D}$ , see Fig. 3.3. Given that the crack faces are free of traction, the material is homogeneous and that there are no volume forces, it can be shown (see Rice [1968b]) that the  $\mathcal{J}$ -integral equals the energy release with respect to an infinitesimal crack extension  $\Delta a$  in the direction of  $x_1$ , i.e.

$$\mathcal{J} = \lim_{\Delta a \rightarrow 0} -\frac{\Delta \Pi}{\Delta a} = -\frac{d\Pi}{da} = \mathcal{G}. \quad (3.17)$$

Thus, the  $\mathcal{J}$ -integral can be applied as a fracture parameter. Furthermore, the  $\mathcal{J}$ -integral is path independent under the above mentioned circumstances, see Rice [1968a]. This property is especially useful for the numerical evaluation of the  $\mathcal{J}$ -integral. It allows to choose a contour  $\partial \mathcal{D}$ , which is sufficiently far away from the crack tip, in order to avoid the numerical difficulties connected with the crack tip singularities.

If the crack is curved or the crack faces are loaded, path independence does not hold. Thus, in this more general setting, the  $\mathcal{J}$ -integral is only an appropriate fracture parameter, if the integration contour is shrunk directly to the crack tip.

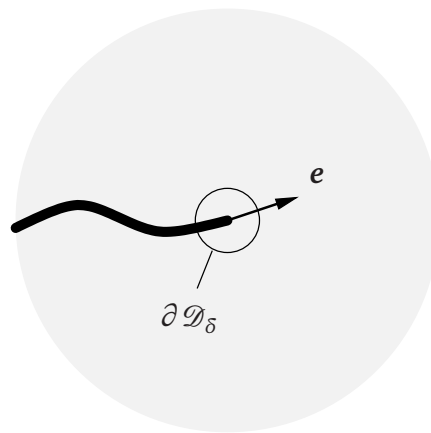


Figure 3.4: Generalization of the  $\mathcal{J}$ -integral for curved cracks.

The appropriate definition

$$\mathcal{J} = e_k \lim_{\delta \rightarrow 0} \int_{\partial \mathcal{D}_\delta} (\psi \delta_{kj} - \sigma_{ij} u_{i,k}) n_j ds = e_k \oint_{\text{tip}} (\psi \delta_{kj} - \sigma_{ij} u_{i,k}) n_j ds \quad (3.18)$$

of the  $\mathcal{J}$ -integral can be found in Gurtin [1979]. Here,  $e_k$  are the components of the tangent vector to the crack at the crack tip, and  $\partial \mathcal{D}_\delta$  is a circle contour of radius  $\delta$  centered at the crack tip<sup>1</sup>, see Fig. 3.4. The notation  $\oint_{\text{tip}}$  for the limit of the contour integral around the crack tip is adopted from Gurtin and Podio-Guidugli [1996]. A proof of the relation (3.17) for the  $\mathcal{J}$ -integral as defined in Eq. (3.18) is given in Gurtin [1979].

### 3.5 Configurational Forces in LEFM

The notion of *configurational* or, as they are also called, *material forces* in continuum mechanics, that are

... introduced to give a picturesque description of energy changes, and must not be confused with the ordinary surface and body forces acting on the material,

goes back to Eshelby [1951]. By now, the concept of configurational forces has become a well established method to evaluate defects in a material. This is on the one hand due to fact, that it provides a unified and elegant framework for the analysis of various kinds of material imperfections. On the other hand, the concept may be generalized to a wide range of different constitutive material behaviors, including finite elasticity theory, plasticity or coupled field theories for piezoelectric or ferroelectric materials. With respect to linear elastic fracture mechanics, the configurational forces are especially of interest due to their close connection to the  $\mathcal{J}$ -integral and the energy release rate, respectively, see e.g. references Steinmann [2000] and Steinmann et al. [2001].

Besides Eshelby's original approach, there are several alternative derivations of the configurational force balance to be found in the literature. For an extensive overview on the subject, the reader is referred to the textbooks of Kienzler and Herrmann [2000], Gurtin [2000], Maugin [1993, 2010] and Müller [2005]. The derivation of the configurational force balance in the context of linear elastic fracture mechanics, which will be outlined in this section, follows the original approach by Eshelby. Starting point is the computation of the gradient of the energy density  $\psi$ , which is considered as a function of the linearized strain tensor  $\boldsymbol{\varepsilon}$ , the location  $\boldsymbol{x}^{\text{tip}}$  of the crack tip and the position  $\boldsymbol{x}$  in order to account for possible inhomogeneities

<sup>1</sup>A circle is chosen for convenience only.  $\partial \mathcal{D}_\delta$  could as well be another family of contours shrinking to the crack tip as  $\delta \rightarrow 0$ .

### 3 Linear Elastic Fracture Mechanics

in the material, i.e.  $\psi = \hat{\psi}(\boldsymbol{\varepsilon}, \mathbf{x}^{\text{tip}}, \mathbf{x})$ . In index notation, a formal chain rule differentiation yields

$$\psi_{,k} = \frac{\partial \hat{\psi}}{\partial \varepsilon_{ij}} \varepsilon_{ij,k} + \frac{\partial \hat{\psi}}{\partial x_i^{\text{tip}}} (x_i^{\text{tip}})_{,k} + \frac{\partial \hat{\psi}}{\partial x_k} \Big|_{\text{expl.}} . \quad (3.19)$$

Following the notation introduced by Eshelby, the partial derivative with respect to  $x_k$  is supplemented by the label ‘‘expl.’’ in order to carefully distinguish from the total differential  $d/dx_k$ . With the equality

$$\frac{\partial \hat{\psi}}{\partial \varepsilon_{ij}} \varepsilon_{ij,k} = \sigma_{ij} \varepsilon_{ij,k} = (\sigma_{ij} u_{i,k})_{,j} - \sigma_{ij,j} u_{i,k} , \quad (3.20)$$

exploiting the symmetry of the Cauchy stress tensor  $\boldsymbol{\sigma}$  and the compatibility of the linearized strain tensor  $\boldsymbol{\varepsilon}$  with the displacements  $\mathbf{u}$ , Eq. (3.19) yields

$$\psi_{,k} = (\sigma_{ij} u_{i,k})_{,j} - \sigma_{ij,j} u_{i,k} + \frac{\partial \hat{\psi}}{\partial x_i^{\text{tip}}} (x_i^{\text{tip}})_{,k} + \frac{\partial \hat{\psi}}{\partial x_k} \Big|_{\text{expl.}} . \quad (3.21)$$

Using the local balance law (Eq. 2.42) for the Cauchy stress tensor  $\sigma_{ij}$ , Eq. (3.21) can be rearranged to

$$\left( \psi \delta_{kj} - \sigma_{ij} u_{i,k} \right)_{,j} - f_i u_{i,k} - \frac{\partial \hat{\psi}}{\partial x_i^{\text{tip}}} (x_i^{\text{tip}})_{,k} - \frac{\partial \hat{\psi}}{\partial x_k} \Big|_{\text{expl.}} = 0 . \quad (3.22)$$

The bracketed term forms a second order tensor which is commonly called the *Eshelby tensor*, or more precisely, in order to avoid confusions with the Eshelby tensor in inclusion problems, the *Eshelby stress tensor*

$$\Sigma_{kj} = \psi \delta_{kj} - \sigma_{ij} u_{i,k} . \quad (3.23)$$

Other appellations of  $\Sigma_{kj}$  are *energy-momentum tensor* or *Maxwell tensor of elasticity*. The remaining terms in Eq. (3.22) are cast together to the *configurational material volume force*

$$g_k = -f_i u_{i,k} - \frac{\partial \hat{\psi}}{\partial x_i^{\text{tip}}} (x_i^{\text{tip}})_{,k} - \frac{\partial \hat{\psi}}{\partial x_k} \Big|_{\text{expl.}} = g_k^{\text{vol}} + g_k^{\text{tip}} + g_k^{\text{inh}} . \quad (3.24)$$

The first contribution  $g_k^{\text{vol}}$  to the configurational volume force  $g_k$  appears only in the presence of physical volume forces  $f_i$ . The last term  $g_k^{\text{inh}}$  appears, where  $\psi$  explicitly depends on the position  $\mathbf{x}$ . This is the case for inhomogeneous materials, with a gradually changing stiffness  $\mathbb{C} = \mathbb{C}(\mathbf{x})$ . A special role is played by the term  $g_k^{\text{tip}}$ , which is a volume force that is concentrated at the crack tip. Effectively, it represents

the configurational point force  $G_k^{\text{tip}}$  acting on the crack tip, i.e.

$$G_k^{\text{tip}} = \int_{\mathcal{D}} g_k^{\text{tip}} dV = \int_{\mathcal{D}} -\frac{\partial \hat{\psi}}{\partial x_i^{\text{tip}}} (x_i^{\text{tip}})_{,k} dV \quad (3.25)$$

for any control volume  $\mathcal{D}$  containing the crack tip but no further singular points of  $\psi$ . On the other hand

$$\int_{\mathcal{D}} g_k^{\text{tip}} dV = 0 \quad (3.26)$$

if the volume  $\mathcal{D}$  does not comprise the crack tip.

With the definitions of the Eshelby stress tensor and the configurational volume force (Eqs. 3.23 and 3.24), Eq. (3.22) can be summarized to the *configurational or material force balance*

$$\Sigma_{k,j} + g_k = 0, \quad (3.27)$$

which has the same structure as the physical force balance (Eq. 2.42). In symbolic notation, Eqs. (3.23), (3.24) and (3.27) read

$$\Sigma = \psi \mathbf{1} - (\text{grad } \mathbf{u})^T \boldsymbol{\sigma}, \quad (3.28)$$

$$\mathbf{g} = -(\text{grad } \mathbf{u})^T \mathbf{f} - (\text{grad } \mathbf{x}^{\text{tip}})^T \frac{\partial \hat{\psi}}{\partial \mathbf{x}^{\text{tip}}} - \frac{\partial \hat{\psi}}{\partial \mathbf{x}} \Big|_{\text{expl.}} \quad (3.29)$$

and

$$\text{div } \Sigma + \mathbf{g} = \mathbf{0}. \quad (3.30)$$

The configurational crack tip force  $\mathbf{G}^{\text{tip}}$  may be computed from the configurational force balance (Eq. 3.30) as

$$\mathbf{G}^{\text{tip}} = \int_{\text{tip}} (-\text{div } \Sigma - \mathbf{g}^{\text{vol}} - \mathbf{g}^{\text{inh}}) dV = \int_{\text{tip}} -\text{div } \Sigma dV, \quad (3.31)$$

with the notation  $\int_{\text{tip}} (\cdot) dV$  for the crack tip limit integral  $\lim_{\delta \rightarrow 0} \int_{\mathcal{D}_\delta} (\cdot) dV$ . The last equality holds upon the assumption that the configurational volume force contributions  $\mathbf{g}^{\text{vol}}$  and  $\mathbf{g}^{\text{inh}}$  are continuous at the crack tip. The scalar product of  $\mathbf{G}^{\text{tip}}$  with the crack tip tangential vector  $\mathbf{e}$  (see Fig. 3.4) coincides with the generalized  $\mathcal{J}$ -integral according to Eq. (3.18) modulo a change of sign, i.e.

$$\mathbf{G}^{\text{tip}} \cdot \mathbf{e} = -\mathcal{J}. \quad (3.32)$$

Given the same premises for path independence as in the previous section, i.e. no volume forces, no material inhomogeneities (other than the crack) and traction free surfaces, the configurational volume force contributions  $\mathbf{g}^{\text{vol}}$  and  $\mathbf{g}^{\text{inh}}$  vanish everywhere in the body and the tip integral may be replaced by an integral over a

larger domain  $\mathcal{P}$  containing the crack tip

$$\mathbf{G}^{\text{tip}} = - \int_{\mathcal{P}} \text{div } \boldsymbol{\Sigma} \, dV = - \int_{\partial \mathcal{P}} \boldsymbol{\Sigma} \mathbf{n} \, ds. \quad (3.33)$$

The latter equality holds by virtue of the divergence theorem. The applicability of the divergence theorem might seem disputable in the presence of the crack tip singularity. However, as the singularity is taken into account by the concentrated configurational volume force  $\mathbf{g}^{\text{tip}}$ , the application can be justified in this more general context.

### 3.6 A Variational Formulation of Brittle Fracture

Griffith's energetic fracture criterion as outlined in section 3.4 has become one of the pillars of modern fracture mechanics and can be found in virtually any textbook on the subject. However, this theory reaches its limits when it comes to the prediction of the crack path, the nucleation of new cracks, or the formation of complicated patterns through kinking and branching of cracks. Also Griffith's theory only considers stable crack propagation, where  $\mathcal{G} = \mathcal{G}_c$  and the crack grows continuously with time. If the energy release rate  $\mathcal{G}$  exceeds the threshold value  $\mathcal{G}_c$ , the crack propagation behavior is considered to be unstable, and no further information about the crack evolution is available.

Over the years, several remedies have been proposed in order to overcome these limitations. Concerning the prediction of the crack path under mixed mode loading, a broad variety of deflection criteria is to be found in the literature. These theories include for example the maximal hoop stress criterion according to Erdogan and Sih [1963], which postulates crack propagation in the direction of maximum circumferential stress, the maximum energy release rate criterion according to Wu [1978], or the principle of local symmetry according to Goldstein and Salganik [1974], only to name a few. A discussion of the different approaches within the context of an energetically motivated fracture criterion can be found in Chambolle et al. [2010]. Different criteria for crack nucleation are examined in Li and Zhang [2006]. Among different two parameter models, the authors favor the fracture criterion introduced by Leguillon [2002] because of its self-consistency. This criterion bases on the combination of an incremental version of Griffith's energetic fracture criterion and a strength criterion. Thus, besides the cracking resistance  $\mathcal{G}_c$  the formulation requires a critical stress value  $\sigma_c$  as an additional fracture parameter. A crack will grow or a new crack will nucleate only if this is indicated by both criteria simultaneously. As a consequence of the crack tip singularity, the strength criterion is always satisfied at a crack tip, and the formulation coincides with Griffith's differential formulation in this limit case. At weaker singularities which appear e.g. at notches, the two fracture parameters in conjunction with the sample geometry and loading yield the characteristic length of the nucleating crack.

Instead of equipping the classical Griffith criterion with this whole toolbox of additional criteria in order to cure its weaknesses, a variational reformulation of the model is proposed in Francfort and Marigo [1998]. This reformulation establishes a unified framework for all kinds of possible crack evolutions. It basically relies only on the principle of global minimality of the total energy, which is the sum of the strain energy, the surface or crack energy and the potential energy of external forces.

To set the stage, the  $n$ -dimensional elastic body  $\mathcal{B}$  under consideration is specified as a bounded connected open domain of  $\mathbb{R}^n$  ( $1 \leq n \leq 3$ ) with a smooth boundary  $\partial \mathcal{B}$ . The set of possible crack configurations is of special importance for the variational formulation. In contrast to classical fracture mechanics, where typically only infinitesimal variations of preexisting cracks are considered, the set of possible crack configurations in the variational formulation is made up by the set of all closed subdomains of  $\bar{\mathcal{B}} = \mathcal{B} \cup \partial \mathcal{B}$  whose dimension is not greater than  $n - 1$ . Besides this dimensional restriction, there is no further assumption on the shape of the possible cracks. As cracks may enter the boundary, this setting allows for debonding scenarios. Assuming that there is no crack healing, a crack set  $\mathcal{C}(t)$  at time  $t$  must contain all its predecessors, i.e.

$$\mathcal{C}(s) \subset \mathcal{C}(t) \quad \text{for all } s < t. \quad (3.34)$$

This models the irreversibility of the fracture process. As a consequent generalization of Griffith's theory, the surface energy  $\Gamma$  of a crack set  $\mathcal{C} \subset \bar{\mathcal{B}}$  is assumed to be proportional to the area occupied by the crack, i.e.

$$\Gamma(\mathcal{C}) = \mathcal{G}_c \mathcal{H}^{n-1}(\mathcal{C}), \quad (3.35)$$

where  $\mathcal{H}^{n-1}$  denotes the  $n - 1$ -dimensional Hausdorff measure, which amounts to the usual surface measure for sufficiently smooth hypersurfaces.

Away from the cracks, a small strain setting with linear elastic material behavior is assumed. Consequently, the elastic energy of a crack-displacement pair  $(\mathcal{C}, \mathbf{u})$  is given by

$$E^e(\mathcal{C}, \mathbf{u}) = \int_{\mathcal{B} \setminus \mathcal{C}} \frac{1}{2} \boldsymbol{\varepsilon}(\mathbf{u}) : \mathbb{C} \boldsymbol{\varepsilon}(\mathbf{u}) \, dV. \quad (3.36)$$

Therein the displacement field  $\mathbf{u}$  is subject to displacement boundary conditions  $\mathbf{u}^*$  where the sample has not debonded, i.e.

$$\mathbf{u}(\mathbf{x}, t) = \mathbf{u}^*(\mathbf{x}, t) \quad \text{on} \quad \partial_u \mathcal{B} \setminus \mathcal{C}(t). \quad (3.37)$$

The basic idea behind the variational formulation is, that at any time  $t$ , among all cracks  $\mathcal{C}$  obeying the irreversibility constraint (Eq. 3.34) and all displacement fields  $\mathbf{u}$  that are kinematically admissible in the sense of Eq. (3.37), the



pair  $(\mathcal{C}(t), \mathbf{u}(\mathbf{x}, t))$  is a global minimizer of the total energy

$$E(\mathcal{C}, \mathbf{u}) = E^e(\mathcal{C}, \mathbf{u}) + \Gamma(\mathcal{C}). \quad (3.38)$$

The postulate of global minimality is very close in spirit to the classical Griffith criterion from section 3.4, which may be interpreted as a first order necessary condition for local minimality of the total energy (see Francfort and Marigo [2005]). In this context, “local” means that only small variations of preexisting cracks are considered in Griffith’s criterion. In other words, cracks are assumed to grow progressively by incremental crack extensions per time increment. In contrast, the variational formulation allows also for brutal crack growth, which adds way more flexibility to the model. By brutal crack growth, the authors understand the occurrence of jump discontinuities in the evolution of the surface measure of the crack set at a time  $t$ , i.e.

$$\lim_{s \searrow t} \mathcal{H}^{n-1}(\mathcal{C}(s)) > \mathcal{H}^{n-1}(\mathcal{C}(t)). \quad (3.39)$$

Of course, such events of brutal growth challenge the limits of a quasi static model and are to be treated with caution, because dynamic effects should be considered whenever the velocity of a mode I crack approaches the Rayleigh wave speed. The paradox occurrence of infinitely fast growing cracks is due to the purely quasi static character of the variational formulation.

As for the prediction of the crack path, the postulate of global minimality is a very selective criterion, which requires no supplementary theories in order to determine the crack path. Thus, the entire crack evolution in the variational formulation, including kinking or branching of preexisting cracks, the nucleation of new cracks, as well as brutal failure of a structure, is solely triggered through the postulate of global minimality of the total energy (Eq. 3.38) and the irreversibility condition (Eq. 3.34).

This generality of the approach, regardless specific loading situations and structural conditions, is extensively highlighted by the authors as one of the main merits of the variational formulation. However, there are some mechanical implications of the model, which need to be commented. First and foremost, dealing with minimizers always raises the question of their existence. For the case of linearly increasing displacement loadings (Eq. 3.37), the existence of quasi static evolutions  $(\mathcal{C}(t), \mathbf{u}(\mathbf{x}, t))$  formed by global minimizers of the total energy (Eq. 3.38) is examined in some mathematically inclined publications. Some results for the antiplane shear case are reported in Maso and Toader [2002] and Francfort and Larsen [2003] under more or less restrictive assumptions regarding the connectedness of possible crack sets. The same restrictions apply for the results for the case of planar elasticity reported in Chambolle [2003].

A further result of the aforementioned publications is, that although the surface energy (Eq. 3.35) and the bulk energy (Eq. 3.36) may suffer jump discontinuities, the total energy (Eq. 3.38) is absolutely continuous in time.

The fact, that global minimizers of the total energy (Eq. 3.38) cannot exist in the



presence of traction loads  $\mathbf{t}$  or volume forces  $\mathbf{f}$  has already been alluded to by the authors of the variational formulation themselves, see e.g. references Francfort and Marigo [1998], Francfort and Marigo [2005], Francfort [2006] or Bourdin et al. [2008]. Thus, in a linearized setting, the variational formulation can only handle displacement loadings. As from a physical point of view, the pertinence of global minimizers is questionable anyway, a criterion based on local minimality seems an appropriate remedy for the inability of handling volume forces and traction loadings. However, the choice of an adequate measure of locality is a rather open question. Furthermore, this ansatz tends to reintroduce the problem of crack nucleation, because in the absence of cracks, the elastic solution is always a local minimizer of the total energy, see e.g. the one dimensional analysis in Charlotte et al. [2000]. If Griffith's surface energy (Eq. 3.35) is replaced by a cohesive surface energy as introduced by Barenblatt [1962], the model is faced with the same difficulties concerning the existence of global minimizers in the presence of traction loads and volume forces. However, with a cohesive surface energy, the elastic solution ceases to be a local minimum of the total energy at a certain load level and thus, a criterion based on a local minimization allows for crack nucleation. Therefore, the combination of a local minimality criterion together with a cohesive surface energy is suggested in Francfort and Marigo [2005] and Francfort [2006] as a cure for the inability of the variational formulation to handle volume forces and traction loads in the framework of linear elasticity.

The variational formulation can easily be extended to the case of finite elasticity. Therefore, the elastic energy (Eq. 3.36) is modified to

$$E^e(\mathcal{C}, \mathbf{u}) = \int_{\mathcal{B}_t \setminus \mathcal{C}} W(\mathbf{H}) \, d\mathbf{v} \quad (3.40)$$

with an appropriate energy density  $W$ , which is a function of the displacement gradient  $\mathbf{H}$ . For time varying displacement loads and notably also for a certain class of volume forces and traction loads, the existence of a quasi static evolution  $(\mathcal{C}(t), \mathbf{u}(\mathbf{x}, t))$  of global minimizers is shown in Maso et al. [2005].

Even though the variational formulation in the linear elastic setting purely relies on energy minimization, the evolution of cracks is crucially influenced by the nature of the stress field of the corresponding elastic solution on  $\mathcal{B} \setminus \mathcal{C}$ . Stress singularities, which occur e.g. at a crack tip, or at reentrant corners of a structure, are of special interest in this context. Assuming that there is no further singular point in the neighborhood of such a critical point  $\mathbf{x}_0 \in \mathcal{B} \setminus \mathcal{C}$ , the displacement field  $\mathbf{u}$  and the stress field  $\boldsymbol{\sigma}$  of the elastic solution in a planar setting, expressed in polar coordinates  $(r, \varphi)$  with their origin at  $\mathbf{x}_0$ , expand to the format

$$\mathbf{u}(r, \varphi) = \mathbf{u}(0, 0) + r^\alpha \mathbf{w}_\alpha(\varphi) + \dots, \quad (3.41)$$

$$\boldsymbol{\sigma}(r, \varphi) = r^{\alpha-1} \mathbf{s}_\alpha(\varphi) + \dots, \quad (3.42)$$

### 3 Linear Elastic Fracture Mechanics

where  $\alpha$  with  $0 < \alpha < 1$  is the dominating exponent if  $r \rightarrow 0$ . The lower bound for the exponent  $\alpha$  ensures the finiteness of the bulk energy, while the upper bound yields the singular character of the stress field, provided that  $\mathbf{w}_\alpha \neq \mathbf{0}$ . Regular points  $\mathbf{x}_0$  (without stress singularities) can be considered by embedding the case  $\alpha = 1$ . Assuming that a crack can only extend from the point  $\mathbf{x}_0$ , Francfort and Marigo [1998] adopt the asymptotic expansion

$$E^e \left( \mathcal{C}_0 \cup \mathcal{C}_l, \mathbf{u} \right) = E^e \left( \mathcal{C}_0, \mathbf{u} \right) - Kl^{2\alpha} + o \left( l^{2\alpha} \right) \quad (3.43)$$

of the bulk energy from Leguillon [1989] in order to study the impact of the exponent  $\alpha$  on the crack evolution in the variational formulation. Therein,  $\mathcal{C}_0$  denotes a (possibly empty) initial crack set, and  $\mathcal{C}_l$  a small add-crack of length  $l$  starting at  $\mathbf{x}_0$ . For a monotonously increasing displacement load, their study yields the following conclusions:

- If the stress field at  $\mathbf{x}_0$  exhibits a strong singularity ( $\alpha < 1/2$ ), progressive crack growth will start as soon as load is applied to the sample. However, this case is of rather academic nature, since these singularities typically occur only at isolated points of a structure. As soon as a crack grows, the singularity becomes weaker.
- If the stress field at  $\mathbf{x}_0$  exhibits a  $\sqrt{r}$ -singularity ( $\alpha = 1/2$ ), which typically appears at the tip of a crack in homogeneous material, progressive crack growth starts at a non-zero, finite critical load level  $\mathbf{u}_{\text{crit.}}^*$ . In this case, the variational formulation coincides with classical Griffith theory for straight growing cracks.
- If the stress field at  $\mathbf{x}_0$  exhibits a weak singularity ( $\alpha > 1/2$ ), then an initial crack of finite length appears brutally at a non-zero, finite load level  $\mathbf{u}_{\text{crit.}}^*$ .
- If the stress field at  $\mathbf{x}_0$  is regular ( $\alpha = 1$ ), either the material behavior is linear elastic and the material remains undamaged, or a crack of finite length forms brutally at a non-zero, finite load level  $\mathbf{u}_{\text{crit.}}^*$  as in the previous case.

Thus, progressive crack growth requires at least a  $\sqrt{r}$ -singularity. At weaker singularities or regular points an infinitesimal crack extension consumes too much surface energy and does not release enough elastic energy to be energetically favorable. Therefore, the onset of new cracks at these points is always brutal. These results have been established in Francfort and Marigo [1998] under some restrictions on the crack path. A more general prove for a larger class of possible crack sets can be found in Chambolle et al. [2008]. The fact that, from an energetic point of view, cracks must nucleate with a finite length is also a basic ingredient of fracture criteria, which fall under the generic term *finite fracture mechanics*, see e.g. Leguillon [2002].

# 4 A Phase Field Model for Fracture

## 4.1 Approximation of the Variational Formulation of Brittle Fracture

A direct numerical implementation of the variational formulation of brittle fracture as introduced in section 3.6 is faced with significant technical problems. This is mainly due to the fact that the total energy is to be minimized with respect to any kinematically admissible (possibly discontinuous) displacement field without any prior knowledge of the crack path, i.e. the location of the discontinuity sets of the displacement field. However, most numerical approaches to the discretization of discontinuous displacement fields, such as the extended finite element method (XFEM) or other techniques based on nodal enrichment, rely to a certain extent on an a priori knowledge of the crack path.

In an effort to make the variational formulation amenable to a numerical implementation, a regularized version of the variational formulation is proposed in Bourdin et al. [2000] and further elaborated in Bourdin [2007a] and Bourdin et al. [2008]. Instead of dealing with free discontinuity sets of the displacement field  $\mathbf{u}(\mathbf{x}, t)$ , a secondary field variable  $s(\mathbf{x}, t)$  is introduced to indicate cracks. This additional scalar field  $s$  interpolates continuously between broken ( $s = 0$ ) and undamaged ( $s = 1$ ) material. The main advantage of this two field ansatz is, that the representation of cracks is no longer mesh or geometry based. This allows a straightforward implementation into a standard finite element framework. Furthermore, the ansatz allows to address different scenarios like crack propagation, kinking, branching or initiation in a unified way, just like the underlying variational formulation.

The core of the regularization is an approximation of the total energy (Eq. 3.38) of a fractured body. In a linear elastic setting, it reads

$$E(\boldsymbol{\varepsilon}(\mathbf{u}), s) = \int_{\mathcal{B}} \left[ \frac{1}{2}(s^2 + \eta)\boldsymbol{\varepsilon}(\mathbf{u}) : [\mathbf{C}\boldsymbol{\varepsilon}(\mathbf{u})] + \mathcal{G}_c \left( \frac{(1-s)^2}{4\epsilon} + \epsilon|\nabla s|^2 \right) \right] dV, \quad (4.1)$$

where  $\nabla s = \text{grad} s$  is the spatial gradient of the crack field  $s$ . Such an energy functional has firstly been introduced in Ambrosio and Tortorelli [1990] as an

approximation for the Mumford-Shah functional in the field of image segmentation. An application of this approximation technique to the variational formulation of brittle fracture can be found in Giacomini [2005]. In addition to the new crack field  $s$ , two new parameters appear in this expression for the total energy. The small dimensionless parameter  $0 < \eta \ll 1$  is introduced mainly to avoid numerical difficulties, where the material is broken ( $s = 0$ ). The parameter  $\epsilon$ , appearing twice in the surface related part of the energy expression, has the dimension of a length and controls the width of the transition zone between broken and undamaged material. A simultaneous minimization of the total energy (Eq. 4.1) with respect to admissible displacement fields  $\mathbf{u}$  and crack fields  $s$  under given boundary constraints and loading conditions yields the crack evolution in the regularized formulation. Being based on global minimization of the total energy, the regularized model suffers the same problems of handling traction loads and volume forces as the underlying variational formulation.

It can be shown that the regularized formulation approximates the variational formulation of brittle fracture in the sense of  $\Gamma$ -convergence. Roughly speaking, this means that in the limit case of  $\epsilon \rightarrow 0$ , minimizers  $(\mathbf{u}, s)$  of the regularized energy (Eq. 4.1) converge to minimizers  $(\mathcal{C}, \mathbf{u})$  of the total energy of the variational formulation (Eq. 3.38). By convergence of the crack field  $s$  to the crack set  $\mathcal{C}$ , it is meant that the zero set of  $s$  converges to the crack set  $\mathcal{C}$ .

The antiplane shear case with constant stiffness and cracking resistance is very close to the original problem from image segmentation, and the proof of  $\Gamma$ -convergence is a direct adaption of the results of Ambrosio and Tortorelli [1990], see Bourdin [1998]. For the more general case of linearized elasticity, a proof of  $\Gamma$ -convergence can be found in Chambolle [2004]. For further insight into the subject of  $\Gamma$ -convergence, the reader is referred to textbooks like Maso [1993], Braides [2002] or Braides [2006].

The energy density

$$\psi(\boldsymbol{\varepsilon}, s) = \underbrace{\frac{1}{2}(s^2 + \eta) \boldsymbol{\varepsilon} : [\mathbb{C}\boldsymbol{\varepsilon}]}_{=\psi^e(\boldsymbol{\varepsilon}, s)} + \underbrace{\mathcal{G}_c \left( \frac{(1-s)^2}{4\epsilon} + \epsilon |\nabla s|^2 \right)}_{=\psi^s(s)} \quad (4.2)$$

of the regularized formulation of brittle fracture, resembles the energy density functional of a phase field model. In this context, the crack field  $s$  is considered as an order parameter, which distinguishes between different phases of the material. In the elastic part  $\psi^e$  of the energy density, the degradation of stiffness in the broken phase is modeled by the factor  $(s^2 + \eta)$ . Accordingly, the stress strain relation (Eq. 2.80) modifies to

$$\boldsymbol{\sigma} = \frac{\partial \psi}{\partial \boldsymbol{\varepsilon}} = \frac{\partial \psi^e}{\partial \boldsymbol{\varepsilon}} = (s^2 + \eta) \mathbb{C}\boldsymbol{\varepsilon}. \quad (4.3)$$

#### 4.1 Approximation of the Variational Formulation of Brittle Fracture

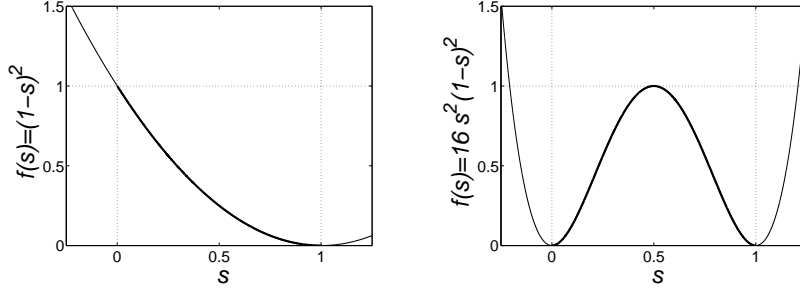


Figure 4.1: Quadratic potential function  $f(s) = (1 - s)^2$  (left) and double well potential  $f(s) = 16s^2(1 - s)^2$  (right).

The gradient term in the surface part  $\psi^s$  of the energy density acts as a regularization and prevents the formation of too many phase interfaces, i.e. crack faces in the context of fracture. Instead of the quadratic term  $(1 - s)^2$  in the surface energy, most phase field fracture models, e.g. Aranson et al. [2000], Karma et al. [2001], Eastgate et al. [2002], Karma and Lobkovsky [2004], Corson et al. [2009], employ a phase field typical double well potential of the type

$$f(s) = 16s^2(1 - s)^2 \quad (4.4)$$

with minima  $f(s) = 0$  at  $s = 0$  and  $s = 1$  and a local maximum at  $s = 0.5$ . Plots of the quadratic potential and the double well potential are displayed in Fig. 4.1. With the local maximum acting as an energy barrier between the broken and undamaged phase, the double well potential (Eq. 4.4) naturally models the irreversibility of fracture processes, at least to a certain extent. In contrast, if the quadratic potential is used, the crack field  $s$  needs to be subjected to additional irreversibility constraints in order to prevent crack healing, because there is no energy barrier between the broken and undamaged states. This issue will be discussed in section 4.2.2. Despite the problems concerning irreversibility, in Bourdin et al. [2011a] the authors strongly advocate the quadratic potential. Their rejection of the double well potential in the context of fracture mechanics is based on two reasons. First, there is no mathematical proof available, that the surface energy  $E^s = \int \psi^s dV$  of a regularized model with a double well potential converges to the surface energy (Eq. 3.35) of the variational formulation. Second, if a double well potential is used, the broken phase ( $s = 0$ ) does not consume more energy than the undamaged phase ( $s = 1$ ). As a result, the crack field tends to evolve away from the cracks, i.e. the phase field cracks tend to grow “fat”. However, as this is a rather slow process compared to the velocity of crack propagation, the effect is negligible for sufficiently fast growing cracks, and the models using a double well potential still render reasonable crack patterns.

From another perspective, the energy density functional (Eq. 4.2) resembles a certain class of gradient damage models with a damage variable  $d$ , a characteristic

length  $\ell$  and an energy density of the format

$$\psi = \frac{1}{2} \boldsymbol{\varepsilon} : [\mathbb{C}(d)\boldsymbol{\varepsilon}] + \mathcal{G}_c \left( \frac{f(d)}{\ell} + \ell |\nabla d|^2 \right). \quad (4.5)$$

In a recent publication Bourdin et al. [2011a], however, the authors disapprove the interpretation of the regularized formulation as a gradient damage model. From their point of view, the regularization parameter  $\epsilon$  is an auxiliary numerical quantity without any physical meaning, which may not be confused with the physically motivated characteristic length  $\ell$  of a damage gradient model. Furthermore, they argue that there is a whole class of energy functionals similar to Eq. (4.2), which exhibit the same asymptotic behavior for  $\epsilon \rightarrow 0$ , and therefore the authors regard the resemblance of Eq. (4.2) to a damage model of the type (Eq. 4.5) as “purely coincidental”.

In contrast to the variational formulation of brittle fracture, the numerical implementation of the regularized model can be done with a standard finite element discretization, where in addition to the displacements  $\mathbf{u}$ , the crack field  $s$  is treated as an extra nodal degree of freedom. For the case of a structured triangulation, some convergence issues are discussed in Negri [2007]. Since the total energy (Eq. 4.1) is separately convex with respect to each of its arguments, an alternate minimizations algorithm is proposed in Bourdin et al. [2008] in order to find a minimizers of the discretized total energy in the finite element formulation. Thus, in each time step, the total energy is minimized alternately with respect to the nodal displacements  $\mathbf{u}$  and the nodal crack field values  $s$  while the respective other argument is held constant. In Bourdin [2007a] it is shown that, if cracks propagate smoothly under linear increasing loadings, the alternate minimizations algorithm converges to the global minimizer of the discrete total energy for sufficiently small load steps. However, if cracks propagate brutally, the alternate minimizations algorithm frequently leads to local minimizers or saddle points of the total energy instead of the global minimum. As a consequence, in these situations the alternate minimizations algorithm yields crack evolutions where the total energy suffers jump discontinuities and is not increasing continuously with the loading. In order to avoid such crack evolutions which are spurious from the standpoint of the variational formulation, a so called backtracking algorithm is introduced in Bourdin [2007a]. In each step, the backtracking algorithm compares the total energy of the solution found by the alternate minimizations procedure to all previously computed total energies. If the total energy is found to drop below a previously computed value, the backtracking algorithm reinitializes the simulation at the load value with the respective energy but with the crack field found in the current iteration. In doing so, solutions obtained from the alternate minimizations algorithm which are obviously no global minimizers can be identified and excluded from the crack evolution. Although this does not guarantee, that the newly computed crack evolution actually represents a series of global minimizers, the total energy now grows monotonously with the load and is continuous in time, as required in the variational formulation. More details



on the backtracking algorithm can be found in the references Bourdin [2007a] and Bourdin et al. [2008]. The impact of the backtracking algorithm on crack evolutions is discussed exemplary in the context of crack nucleation in section 7.1.

## 4.2 Evolution Equation

Bourdin's regularization of the variational formulation of brittle fracture already resembles a phase field model, where the crack field  $s$  functions as the phase field order parameter. The missing evolution law for the order parameter can be formulated adopting the techniques proposed in Fried and Gurtin [1993, 1994] and Gurtin [1996]. In these publications, the Coleman-Noll procedure [Coleman and Noll, 1963] to derive thermodynamically consistent material laws, is generalized for material models, where the free energy depends not only on an internal variable but also on the gradient of an internal variable.

### 4.2.1 Thermodynamical Background

The theory presented in Fried and Gurtin [1993, 1994] and Gurtin [1996] is based on the following two assumptions for a *micro force system*, characterized by a *micro stress vector*  $\xi$  together with scalar *internal* and *external micro forces*  $\pi$  and  $\gamma$ , which are distributed over the volume.

- The micro force is the thermodynamical conjugate to the rate  $\dot{s}$  of the order parameter. Thus, the rate at which the micro forces, *external* to a control volume  $\mathcal{P}_t$ , perform work is

$$\dot{\mathcal{W}}_{\text{mic}}(\mathcal{P}_t) = \int_{\partial\mathcal{P}_t} \dot{s}\xi \cdot \mathbf{n} \, da + \int_{\mathcal{P}_t} \dot{s}\gamma \, dv. \quad (4.6)$$

The work of the *internal* micro force  $\pi$  does not enter this *external* working.

- The micro force system is consistent with the *global micro force balance*

$$\int_{\partial\mathcal{P}_t} \xi \cdot \mathbf{n} \, da + \int_{\mathcal{P}_t} (\pi + \gamma) \, dv = 0 \quad (4.7)$$

for each control volume  $\mathcal{P}_t$ , or equivalently the *local micro force balance*

$$\text{div } \xi + \pi + \gamma = 0. \quad (4.8)$$

This formulation of a balance law implies that micro-structural inertia is neglected.

#### 4 A Phase Field Model for Fracture

Adding the work performed by mechanical forces (Eq. 2.47) to the work of the micro forces (Eq. 4.6), the total rate of work of external forces becomes

$$\mathcal{W}(\mathcal{P}_t) = \int_{\partial\mathcal{P}_t} [\boldsymbol{\sigma}\mathbf{n} \cdot \mathbf{v} + s\xi \cdot \mathbf{n}] \, da + \int_{\mathcal{P}_t} [\mathbf{f} \cdot \mathbf{v} + s\dot{\gamma}] \, dv. \quad (4.9)$$

Thus, the micro forces enter the dissipation inequality according to Eq. (2.56). With the balance laws for the mechanical forces and for the micro forces (Eqs. 2.41 and 4.8), the Clausius-Planck inequality (Eq. 2.59) modifies to

$$\mathcal{D}_{\text{loc}} = \int_{\mathcal{P}_t} [\boldsymbol{\sigma} : \mathbf{d} + \xi \cdot \nabla s - \pi\dot{s} - \rho(\dot{\psi}^* + \dot{\theta}\mathcal{S}^*)] \, dv \geq 0. \quad (4.10)$$

Under the small strain assumption ( $\mathbf{d} \approx \dot{\boldsymbol{\varepsilon}}$ ,  $\rho\dot{\psi}^* \approx \dot{\psi}$ ) and isothermal conditions ( $\dot{\theta} = 0$ ), this inequality simplifies to

$$\int_{\mathcal{P}} [\boldsymbol{\sigma} : \dot{\boldsymbol{\varepsilon}} + \xi \cdot \nabla s - \pi\dot{s} - \dot{\psi}] \, dV \geq 0. \quad (4.11)$$

The regularized energy density (Eq. 4.2) of a cracked body is a function of the linearized strain tensor  $\boldsymbol{\varepsilon}$ , the crack field  $s$  and its gradient  $\nabla s$ , i.e.

$$\psi = \tilde{\psi}(\boldsymbol{\varepsilon}, s, \nabla s) \quad \Rightarrow \quad \dot{\psi} = \frac{\partial \tilde{\psi}}{\partial \boldsymbol{\varepsilon}} : \dot{\boldsymbol{\varepsilon}} + \frac{\partial \tilde{\psi}}{\partial s} \cdot \dot{s} + \frac{\partial \tilde{\psi}}{\partial \nabla s} \nabla \dot{s}. \quad (4.12)$$

Thus, the simplified inequality (Eq. 4.11) becomes

$$\int_{\mathcal{P}} \left[ \left( \boldsymbol{\sigma} - \frac{\partial \tilde{\psi}}{\partial \boldsymbol{\varepsilon}} \right) : \dot{\boldsymbol{\varepsilon}} + \left( \xi - \frac{\partial \tilde{\psi}}{\partial \nabla s} \right) \cdot \nabla \dot{s} - \left( \pi + \frac{\partial \tilde{\psi}}{\partial s} \right) \dot{s} \right] \, dV \geq 0 \quad (4.13)$$

With the generic assumption that the strain rate  $\dot{\boldsymbol{\varepsilon}}$  can have arbitrarily prescribed values and is independent of the rate of the order parameter, Eq. (4.13) immediately yields the constitutive relation

$$\boldsymbol{\sigma} = \frac{\partial \tilde{\psi}}{\partial \boldsymbol{\varepsilon}} = (s^2 + \eta)\mathbb{C}\boldsymbol{\varepsilon} \quad (4.14)$$

for the mechanical stress  $\boldsymbol{\sigma}$ . With the divergence theorem, the remaining inequality (Eq. 4.13) transforms to

$$\int_{\mathcal{P}} \left[ -\text{div} \left( \xi - \frac{\partial \tilde{\psi}}{\partial \nabla s} \right) \dot{s} - \left( \pi + \frac{\partial \tilde{\psi}}{\partial s} \right) \dot{s} \right] \, dV + \int_{\partial\mathcal{P}} \dot{s} \left( \xi - \frac{\partial \tilde{\psi}}{\partial \nabla s} \right) \cdot \mathbf{n} \, dA \geq 0 \quad (4.15)$$

$\Leftrightarrow$

$$\int_{\mathcal{P}} - \left[ \frac{\partial \tilde{\psi}}{\partial s} - \text{div} \left( \frac{\partial \tilde{\psi}}{\partial \nabla s} \right) + \underbrace{\text{div} \xi + \pi}_{=-\gamma} \right] \dot{s} \, dV + \int_{\partial\mathcal{P}} \dot{s} \left( \xi - \frac{\partial \tilde{\psi}}{\partial \nabla s} \right) \cdot \mathbf{n} \, dA \geq 0 \quad (4.16)$$



If this inequality is to be satisfied for any arbitrary rate  $\dot{s}$ , the boundary part yields the constitutive relation

$$\xi = \frac{\partial \tilde{\psi}}{\partial \nabla s} = 2\mathcal{G}_c \epsilon \nabla s \quad (4.17)$$

for the micro stress  $\xi$ . In the absence of external micro forces ( $\gamma = 0$ ), the local formulation of the remaining dissipation inequality is

$$-\frac{\delta \tilde{\psi}}{\delta s} \dot{s} \geq 0, \quad (4.18)$$

where

$$\frac{\delta \tilde{\psi}}{\delta s} = \frac{\partial \tilde{\psi}}{\partial s} - \operatorname{div} \left( \frac{\partial \tilde{\psi}}{\partial \nabla s} \right) \quad (4.19)$$

is the *variational derivative* of  $\tilde{\psi}$  with respect to the crack field  $s$ . It is shown in Gurtin [1996], that the most general form of an evolution equation for  $s$ , which is consistent with Eq. (4.18), is

$$\dot{s} = -\tilde{M} \frac{\delta \tilde{\psi}}{\delta s} = -\tilde{M} \left( s \boldsymbol{\epsilon} : [\mathbf{C} \boldsymbol{\epsilon}] - \mathcal{G}_c \left( 2\epsilon \Delta s + \frac{1-s}{2\epsilon} \right) \right), \quad (4.20)$$

where  $\Delta$  denotes the Laplace operator. The *kinetic coefficient* or *mobility parameter*  $\tilde{M}$  is a scalar, non-negative function  $\tilde{M} = \tilde{M}(\boldsymbol{\epsilon}, s, \nabla s, \dot{s}) \geq 0$ . The most simple assumption,  $\tilde{M} = M = \text{const.}$ , leads to the standard Ginzburg-Landau evolution equation. As far as possible, this ansatz is used for the present phase field fracture model. However, some modifications have to be made in order to take the irreversible character of cracking into account. This will be discussed in section 4.2.2. The limit case  $M \rightarrow \infty$  approximates the quasi static limit case, where  $\frac{\delta \tilde{\psi}}{\delta s} = 0$ . For finite values of  $M$ , the model can be regarded as a viscous approximation of the quasi static case with viscosity  $\frac{1}{M}$ . With the evolution equation (Eq. 4.20), the local dissipation of energy in a control volume  $\mathcal{P}$  becomes

$$\mathcal{D}_{\text{loc}} = \int_{\mathcal{P}} \frac{\dot{s}^2}{\tilde{M}} dV = \int_{\mathcal{P}} \tilde{M} \left( \frac{\delta \tilde{\psi}}{\delta s} \right)^2 dV \geq 0. \quad (4.21)$$

In the quasi static case, there is no local dissipation upon stable crack growth. Very low values of the mobility constant however introduce a large amount of artificial local dissipation to the model. In the underlying energetic fracture model, there is no local dissipation and the entire energy brought into the body, is either stored as elastic energy in the bulk or transformed into surface energy of the cracks. Thus, in the phase field formulation, the mobility parameter should always be chosen sufficiently large, so that the amount of dissipated energy remains small compared to the regularized expressions for the elastic and the surface energy.

## 4.2.2 Irreversibility of Cracking

The thermodynamical derivation of the evolution equation for the crack field  $s$  allows the kinetic coefficient  $\tilde{M}$  to be a non-negative function of the strain tensor  $\boldsymbol{\varepsilon}$ , the crack field  $s$ , its gradient  $\nabla s$  and the time derivative  $\dot{s}$ , i.e.

$$\tilde{M} = \tilde{M}(\boldsymbol{\varepsilon}, s, \nabla s, \dot{s}) \geq 0. \quad (4.22)$$

In the classical Ginzburg-Landau equation  $\tilde{M}$  is simply a positive constant  $M$ . However, this yields a reversible formulation, where the phase field order parameter is free to develop purely according to the loading conditions. In the present context of a phase field fracture model, this would mean that cracks would heal upon unloading. However, on the macroscopic level, which is the scope of the present work, crack growth is an irreversible process, and hence an irreversibility criterion has to be established. Two alternative formulations, which are both thermodynamically consistent and lead to irreversible crack evolutions, are presented and discussed in the following.

### Damage Like Formulation

If the crack field  $s$  is regarded as a damage variable, as for example in Miehe et al. [2010b], the time derivative  $\dot{s}$  should be non-positive ( $\dot{s} \leq 0$ ) in any loading case. This can be enforced by

$$\tilde{M}(\boldsymbol{\varepsilon}, s, \nabla s) = \begin{cases} M & \text{if } \frac{\delta \psi}{\delta s}(\boldsymbol{\varepsilon}, s, \nabla s) \geq 0, \\ 0 & \text{else} \end{cases}, \quad (4.23)$$

where  $M$  is a positive constant. With help of the positive ramp function

$$\langle x \rangle_+ := \frac{|x| + x}{2} \quad (4.24)$$

the evolution equation can be rewritten as

$$\dot{s} = -M \cdot \left\langle \frac{\delta \psi}{\delta s} \right\rangle_+ = -M \cdot \left\langle \frac{\partial \psi^e}{\partial s} + \frac{\delta \psi^s}{\delta s} \right\rangle_+ \quad (4.25)$$

$$= -M \left\langle s \boldsymbol{\varepsilon} : [\mathbf{C} \boldsymbol{\varepsilon}] - \mathcal{G}_c \left( 2\epsilon \Delta s + \frac{1-s}{2\epsilon} \right) \right\rangle_+. \quad (4.26)$$

### Dirichlet Boundary Conditions

The second alternative is more close to Bourdin's formulation in Bourdin et al. [2000], where homogeneous Dirichlet boundary conditions are imposed on the

crack field  $s$ , where a crack has been detected

$$s(\mathbf{x}, t > t_x^*) = 0 \quad \text{if} \quad s(\mathbf{x}, t_x^*) = 0. \quad (4.27)$$

In terms of the constitutive function for the kinetic coefficient, this can be formulated as

$$\tilde{M}(s) = \begin{cases} M & \text{if } s > 0 \\ 0 & \text{else} \end{cases}. \quad (4.28)$$

Note, that opposed to the first alternative, this formulation permits  $\dot{s} > 0$ , i.e. the crack field may recover as long as  $s > 0$ .

### Remark

The specific choice of the irreversibility criterion does not only affect the evolution of the crack field  $s$  but also has some implications on the evolution of the surface energy  $E^s$ .

$$\begin{aligned} \dot{E}^s + \mathcal{D}_{\text{loc}} &= \int_{\mathcal{D}} \dot{\psi}^s \, dV + \mathcal{D}_{\text{loc}} = \int_{\mathcal{D}} \left[ \frac{\delta \psi^s}{\delta s} \dot{s} + \frac{\dot{s}^2}{M} \right] \, dV \\ &= \int_{\mathcal{D}} \left( \frac{\delta \psi^s}{\delta s} + \frac{\dot{s}}{M} \right) \dot{s} \, dV = \int_{\mathcal{D}} \left( -\frac{\partial \psi^e}{\partial s} \right) \dot{s} \, dV \end{aligned} \quad (4.29)$$

As  $\frac{\partial \psi^e}{\partial s} = \mathbf{s}\boldsymbol{\varepsilon} : [\mathbb{C}\boldsymbol{\varepsilon}] \geq 0$ , this implies for the damage like formulation, where  $\dot{s} \leq 0$ , that

$$\dot{E}^s + \mathcal{D}_{\text{loc}} \geq 0. \quad (4.30)$$

For a quasi static solution with  $\dot{s} = 0$ , the dissipation  $\mathcal{D}_{\text{loc}}$  vanishes and the statement can be tightened to  $\dot{E}^s \geq 0$ . For the second proposed alternative these relations do not hold in general. Upon unloading the surface energy  $E^s$  can decrease to a certain extend as the crack field can recover where the material is not fully broken yet. In Miehe et al. [2010a] the sum  $\dot{E}^s + \mathcal{D}_{\text{loc}}$  is considered as the *crack dissipation* which should be non-negative in at any time. From this point of view, only the damage like formulation is admissible. However, according to the derivation in section 4.2.1, where the surface energy is regarded as a portion of the free energy functional, both approaches yield thermodynamically consistent formulations as  $\tilde{M}(\boldsymbol{\varepsilon}, s, \nabla s, \dot{s}) \geq 0$  and hence  $\mathcal{D}_{\text{loc}} \geq 0$  hold.

The impact of the choice of the irreversibility criterion will be further analyzed and discussed in section 5.4, where numerical results obtained with the different strategies are compared to each other.

### 4.3 Dimensional Analysis

The numerical values presented in the sequel will refer to non-dimensional variables obtained by a dimensional analysis of the model equations

$$\mathbf{0} = \operatorname{div} \boldsymbol{\sigma} + \mathbf{f} \quad \text{with} \quad \boldsymbol{\sigma} \mathbf{n}|_{\partial_t \Omega} = \mathbf{t}^*, \quad (4.31)$$

$$\boldsymbol{\sigma} = (s^2 + \eta) \mathbb{C} \boldsymbol{\varepsilon} \quad \text{with} \quad \boldsymbol{\varepsilon} = \frac{1}{2} (\operatorname{grad} \mathbf{u} + \operatorname{grad} \mathbf{u}^T) \quad \text{and} \quad \mathbf{u}|_{\partial_u \Omega} = \mathbf{u}^*, \quad (4.32)$$

$$\dot{s} = -M \left[ s \boldsymbol{\varepsilon} : [\mathbb{C} \boldsymbol{\varepsilon}] - \mathcal{G}_c \left( 2\epsilon \Delta s + \frac{1-s}{2\epsilon} \right) \right]. \quad (4.33)$$

In order to obtain a dimensionless set of equations, the space variable  $\mathbf{x}$  as well as the regularization length  $\epsilon$  are scaled by the macroscopic dimension  $L$  of the considered body, according to

$$\bar{\mathbf{x}} = \frac{\mathbf{x}}{L} \quad \text{and} \quad \bar{\epsilon} = \frac{\epsilon}{L}, \quad (4.34)$$

where the bar denotes the non-dimensional quantities. The stiffness tensor  $\mathbb{C}$  of an isotropic material is scaled with twice the Lamé coefficient  $\mu$ , so that

$$\bar{\mathbb{C}} = \frac{\mathbb{C}}{2\mu}. \quad (4.35)$$

This scaling is motivated by the 1d case ( $\nu = 0$ ), where Young's modulus  $E = 2\mu$  is factored out by this scaling ( $\bar{E} = 1$ ). For the 2d and 3d case, the scaled stiffness tensor  $\bar{\mathbb{C}}$  does only depend on the ratio of the Lamé constants, or equivalently on the Poisson ratio  $\nu$ , because

$$\frac{\lambda}{2\mu} = \frac{\nu}{1-2\nu} \in \left[ -\frac{1}{3}, \infty \right) \quad \text{as} \quad -1 \leq \nu \leq \frac{1}{2}. \quad (4.36)$$

An analysis of the evolution equation (Eq. 4.33) motivates the scaling of the displacements  $\mathbf{u}$  by

$$\mathbf{u} = \sqrt{\frac{\mathcal{G}_c L}{2\mu}} \bar{\mathbf{u}}. \quad (4.37)$$

The scaled strain tensor

$$\bar{\boldsymbol{\varepsilon}} = \frac{1}{2} \left( \operatorname{grad} \bar{\mathbf{u}} + \operatorname{grad} \bar{\mathbf{u}}^T \right), \quad (4.38)$$

where  $\operatorname{grad}$  denotes the gradient with respect to the non-dimensional coordinate  $\bar{\mathbf{x}}$ , thus relates to the actual strain tensor  $\boldsymbol{\varepsilon}$  as

$$\boldsymbol{\varepsilon} = \sqrt{\frac{\mathcal{G}_c}{2\mu L}} \bar{\boldsymbol{\varepsilon}}. \quad (4.39)$$

For the non-dimensional energy density functional  $\bar{\psi}$  and the dimensional counterpart  $\psi$  it follows that

$$\psi = \frac{\mathcal{G}_c}{L} \bar{\psi} \quad \text{with} \quad \bar{\psi} = \frac{1}{2}(s^2 + \eta) \bar{\boldsymbol{\varepsilon}} : [\bar{\mathbb{C}} \bar{\boldsymbol{\varepsilon}}] + \left( \frac{(1-s)^2}{4\bar{\varepsilon}} + \bar{\varepsilon} |\bar{\nabla} s|^2 \right), \quad (4.40)$$

where  $\bar{\nabla} s$  is the gradient of  $s$  with respect to  $\bar{\mathbf{x}}$ . The scaling for the Cauchy stress tensor  $\boldsymbol{\sigma}$  and the traction  $\mathbf{t}^*$

$$\boldsymbol{\sigma} = \sqrt{\frac{2\mu\mathcal{G}_c}{L}} \bar{\boldsymbol{\sigma}} \quad \text{and} \quad \mathbf{t}^* = \sqrt{\frac{2\mu\mathcal{G}_c}{L}} \bar{\mathbf{t}}^* \quad (4.41)$$

follows immediately from Eq. (4.32), taking into account the scalings of the stiffness tensor (Eq. 4.35) and the strain (Eq. 4.39). Volume forces  $\mathbf{f}$  accordingly scale by

$$\mathbf{f} = \sqrt{\frac{2\mu\mathcal{G}_c}{L^3}} \bar{\mathbf{f}}. \quad (4.42)$$

When linear increasing loads are applied, the dimensionless time

$$\bar{t} = \frac{t}{T} \quad (4.43)$$

with respect to a given time scale  $T$  is often referred to as the *load factor*. For the crack field velocity  $\dot{s}$ , this scaling implies

$$\dot{s} = \frac{\partial s}{\partial t} = \frac{\partial \bar{t}}{\partial t} \cdot \frac{\partial s}{\partial \bar{t}} = \frac{1}{T} \bar{\dot{s}} \quad \text{with} \quad \bar{\dot{s}} := \frac{\partial s}{\partial \bar{t}}. \quad (4.44)$$

A similar consideration yields the relation

$$\mathbf{v} = \frac{L}{T} \bar{\mathbf{v}} \quad (4.45)$$

between the velocities

$$\mathbf{v} = \frac{\partial \mathbf{x}}{\partial t} \quad \text{and} \quad \bar{\mathbf{v}} = \frac{\partial \bar{\mathbf{x}}}{\partial \bar{t}} \quad (4.46)$$

in the dimensional and non-dimensional regime, respectively.

With the bar denoting differential operators with respect to  $\bar{\mathbf{x}}$ , the set of equations (Eqs. 4.31-4.33) can be recast in the non-dimensional format

$$\mathbf{0} = \bar{\text{div}} \bar{\boldsymbol{\sigma}} + \bar{\mathbf{f}} \quad \text{with} \quad \bar{\boldsymbol{\sigma}} \mathbf{n}|_{\partial_i \bar{\Omega}} = \bar{\mathbf{t}}^*, \quad (4.47)$$

$$\bar{\boldsymbol{\sigma}} = (s^2 + \eta) \bar{\mathbb{C}} \bar{\boldsymbol{\varepsilon}} \quad \text{with} \quad \bar{\boldsymbol{\varepsilon}} = \frac{1}{2}(\text{grad} \bar{\mathbf{u}} + \text{grad} \bar{\mathbf{u}}^T) \quad \text{and} \quad \bar{\mathbf{u}}|_{\partial_u \bar{\Omega}} = \bar{\mathbf{u}}^*, \quad (4.48)$$

$$\bar{\dot{s}} = -\bar{M} \left[ s \bar{\boldsymbol{\varepsilon}} : [\bar{\mathbb{C}} \bar{\boldsymbol{\varepsilon}}] - \left( 2\bar{\varepsilon} \bar{\Delta} s + \frac{1-s}{2\bar{\varepsilon}} \right) \right], \quad (4.49)$$

where

$$\bar{M} = M \cdot \frac{\mathcal{G}_c T}{L} \quad (4.50)$$

is the scaled kinetic coefficient. Thus, the non-dimensional set of equations (Eqs. 4.47-4.49) is controlled by merely three parameters: the dimensionless regularization parameter  $\bar{\epsilon}$ , the dimensionless stiffness tensor  $\bar{\mathbb{C}}$  (which only depends on the Poisson ratio  $\nu$ ) and the scaled kinetic coefficient  $\bar{M}$ . In the quasi static limit, the stationary solution becomes independent of  $\bar{M}$  and thus, the only relevant material parameters are  $\bar{\epsilon}$  and  $\nu$ .

## 4.4 Analytical Solutions of the 1d Quasi Static Problem

Some properties of the 1d model are analyzed in this section. Exemplary, a homogeneous bar of length  $2L$  under a given displacement load  $u(\pm L) = \pm u_0$ , as depicted in Fig. 4.2, is investigated. The analysis is restricted to the quasi static case  $M \rightarrow \infty$ , and no distributed normal forces are considered. With the scaling introduced in section 4.3, where the factor  $2\mu$  is replaced by the Young's modulus  $E$ , the dimensionless set of equations (Eqs. 4.47-4.49) reduces to:

$$0 = \bar{\sigma}', \quad (4.51)$$

$$\bar{\sigma} = (s^2 + \eta)\bar{\epsilon} \quad \text{with} \quad \bar{\epsilon} = \bar{u}' \quad \text{and} \quad \bar{u}(\pm 1) = \pm \bar{u}_0, \quad (4.52)$$

$$0 = s\bar{\epsilon}^2 - \left( 2\bar{\epsilon}s'' + \frac{1-s}{2\bar{\epsilon}} \right) \quad \text{with} \quad s'(\pm 1) = 0, \quad (4.53)$$

where  $(\cdot)'$  denotes the derivative with respect to  $\bar{x} = \frac{x}{L}$ .

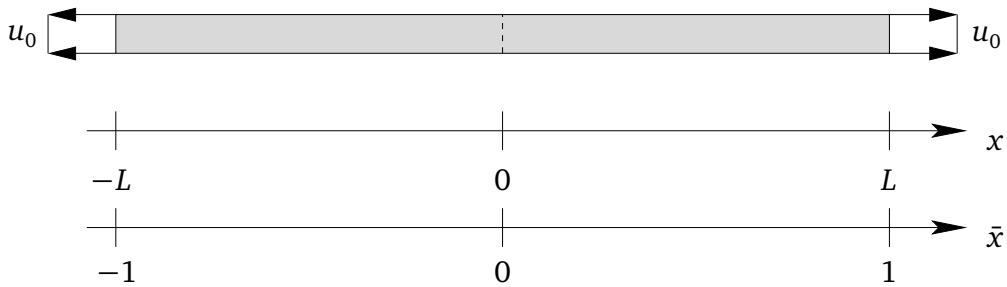


Figure 4.2: 1d problem.

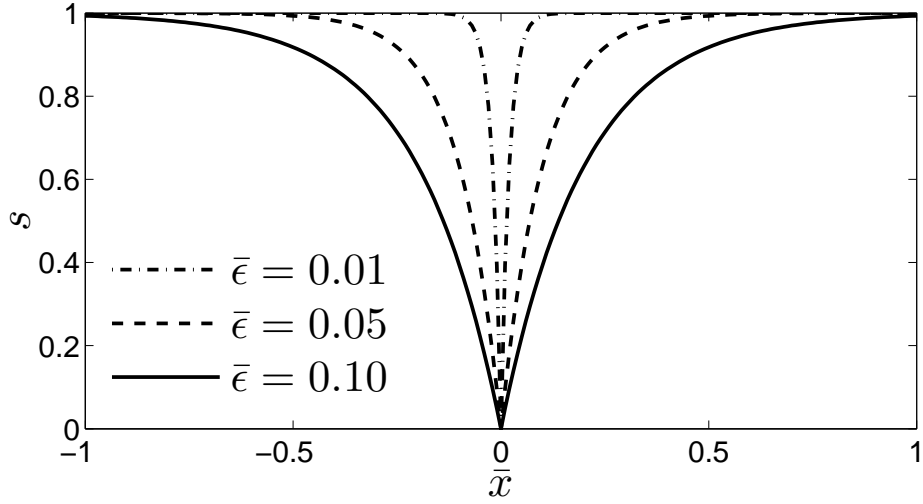


Figure 4.3: Analytical solution of the stationary evolution equation in 1d.

#### 4.4.1 The Unloaded Crack

In a first step, no mechanical loads are applied and as  $\bar{\sigma} = 0$  and  $\bar{\varepsilon} = 0$  the problem reduces to finding a solution of

$$2\bar{\varepsilon}s'' + \frac{1-s}{2\bar{\varepsilon}} = 0 \quad (4.54)$$

with  $s'(\pm 1) = 0$  and  $s(\bar{x}_0) = 0$  if  $x_0$  is part of the crack set  $\mathcal{C}$ . The piecewise defined, exact analytic solution of Eq. (4.54) on the interval  $[-1, 1]$  with a crack at  $\bar{x}_0 = 0$ , i.e.  $s(0) = 0$  is given by the expression

$$s^\pm(\bar{x}) = 1 - \cosh\left(\frac{\bar{x}}{2\bar{\varepsilon}}\right) \pm \coth\left(\frac{1}{2\bar{\varepsilon}}\right) \sinh\left(\frac{\bar{x}}{2\bar{\varepsilon}}\right), \quad (4.55)$$

where  $+$  applies for positive and  $-$  applies for negative values of  $\bar{x}$ . In the limit  $\bar{\varepsilon} \rightarrow 0$  this yields

$$s(\bar{x}) = 1 - \exp\left(\frac{-|\bar{x}|}{2\bar{\varepsilon}}\right). \quad (4.56)$$

Note, that this solution solely depends on the regularization length  $\bar{\varepsilon}$ . Figure 4.3 shows a plot of the crack field (Eq. 4.56) for different values of  $\bar{\varepsilon}$ . Large values of  $\bar{\varepsilon}$  smoothen the crack field, whereas the limit  $\bar{\varepsilon} \rightarrow 0$  yields a discontinuous function which is 0 at  $\bar{x} = 0$  and 1 elsewhere. Inserting the crack field  $s(\bar{x})$  into the dimensionless expression for the surface energy yields

$$\bar{E}^s = \int_{-1}^1 \bar{\psi}^s d\bar{x} = \int_{-1}^1 \left[ \frac{(1-s)^2}{4\bar{\varepsilon}} + \bar{\varepsilon}(s')^2 \right] d\bar{x} = \left[ 1 - \exp\left(\frac{-1}{\bar{\varepsilon}}\right) \right] \rightarrow 1 \quad (4.57)$$

for  $\bar{\varepsilon} \rightarrow 0$ , which is equivalent to  $E^s \rightarrow \mathcal{G}_c$  in the dimensional regime.

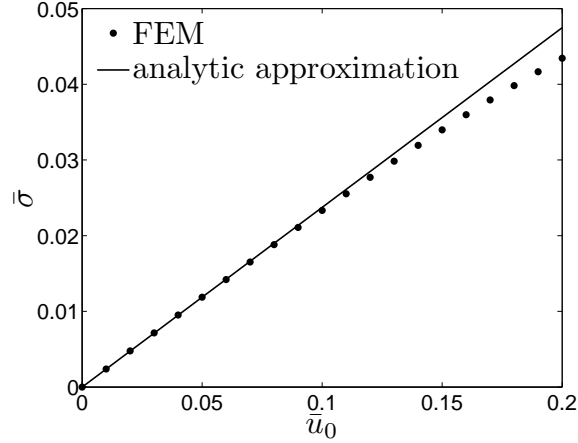


Figure 4.4: Residual stress of the cracked solution.

From another point of view, Eq. (4.56) can also be regarded as the solution of the variational problem:

$$s = \arg \left\{ \inf_{\tilde{s} \in W} \bar{E}^s(\tilde{s}) \right\} = \arg \left\{ \inf_{\tilde{s} \in W} \int_{-1}^{+1} \bar{\psi}(\tilde{s}, \tilde{s}') d\bar{x} \right\} \quad (4.58)$$

with  $W = \{\tilde{s} | \tilde{s}(0) = 0, \tilde{s}'(\pm 1) = 0\}$ . As the evolution equation (Eq. 4.54) was obtained as the variational derivative of  $\bar{\psi}^s$  with respect to  $s$ , it is equivalent to the Euler-Lagrange equation

$$\frac{\partial \bar{\psi}^s}{\partial s} - \left( \frac{\partial \bar{\psi}^s}{\partial s'} \right)' = 0 \quad (4.59)$$

of the variational problem (Eq. 4.58), see Bourdin et al. [2008], Miehe et al. [2010b].

#### 4.4.2 Tensile Loading

Under tensile loading, the solution of the coupled problem (Eqs. 4.51-4.53) yields qualitatively two possibilities: A cracked solution, with a crack field very similar to the unloaded case of the previous section 4.4.1, or an uncracked solution with a homogeneous crack field. These two possibilities are discussed in the following paragraphs. The analysis is restricted to the case  $\bar{\epsilon} \ll 1$ .

##### Approximation of the Cracked Solution

As the crack field does not significantly change upon loading, the solution of the unloaded case (Eq. 4.56) can be used to construct an approximation of the solution of Eqs. (4.51)-(4.53) with a center crack ( $s(0) = 0$ ) as follows. Exploiting the symmetry of the problem, only the positive  $\bar{x}$ -axis is considered. The kinematic relation



#### 4.4 Analytical Solutions of the 1d Quasi Static Problem

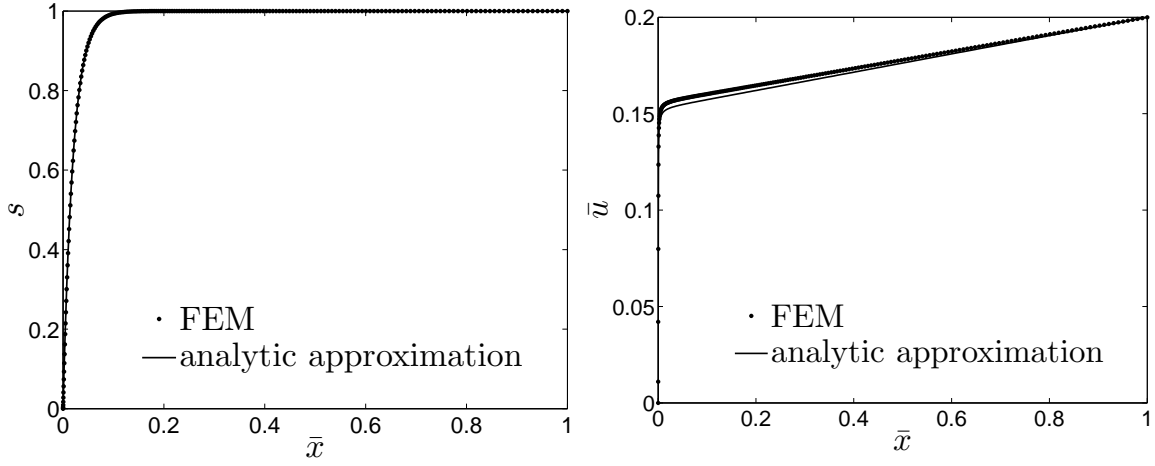


Figure 4.5: Crack field  $s$  (left), and displacement field  $\bar{u}$  (right) of the cracked solution at  $\bar{u}_0 = 0.2$ .

$\bar{\varepsilon} = \bar{u}'$ , together with the boundary condition  $\bar{u}(1) = \bar{u}_0$  and the symmetry constraint  $\bar{u}(0) = 0$  yields

$$\int_0^1 \bar{\varepsilon} d\bar{x} = \bar{u}_0. \quad (4.60)$$

The strain  $\bar{\varepsilon}$  can be eliminated from this expression using the material law (Eq. 4.52). Equation (4.51) immediately implies the stress  $\bar{\sigma}$  to be constant. Thus, the stress  $\bar{\sigma}$  can be separated from the integrand

$$\bar{u}_0 = \bar{\sigma} \int_0^1 \frac{1}{s(\bar{x})^2 + \eta} d\bar{x}. \quad (4.61)$$

Taking Eq. (4.56) as an approximation of the solution of  $s$ , the integral

$$I(\bar{\varepsilon}, \eta) := \int_0^1 \frac{1}{s(\bar{x})^2 + \eta} d\bar{x} \quad (4.62)$$

can be computed with help of the antiderivative

$$\begin{aligned} F(\bar{x}) &= \int \frac{1}{s(\bar{x})^2 + \eta} d\bar{x} = \int \frac{1}{1 + \eta - 2 \exp\left(-\frac{\bar{x}}{2\bar{\varepsilon}}\right) + \exp\left(-\frac{\bar{x}}{\bar{\varepsilon}}\right)} d\bar{x} \\ &= \frac{\bar{\varepsilon}}{1 + \eta} \left[ \ln \left( (1 + \eta) \exp\left(\frac{\bar{x}}{\bar{\varepsilon}}\right) - 2 \exp\left(\frac{\bar{x}}{2\bar{\varepsilon}}\right) + 1 \right) \right. \\ &\quad \left. + \frac{2}{\sqrt{\eta}} \arctan \left( \frac{(1 + \eta) \exp\left(\frac{\bar{x}}{2\bar{\varepsilon}}\right) - 1}{\sqrt{\eta}} \right) \right]. \end{aligned} \quad (4.63)$$

The finiteness of the integral  $I(\bar{\varepsilon}, \eta) = F(1) - F(0)$  crucially depends on the presence

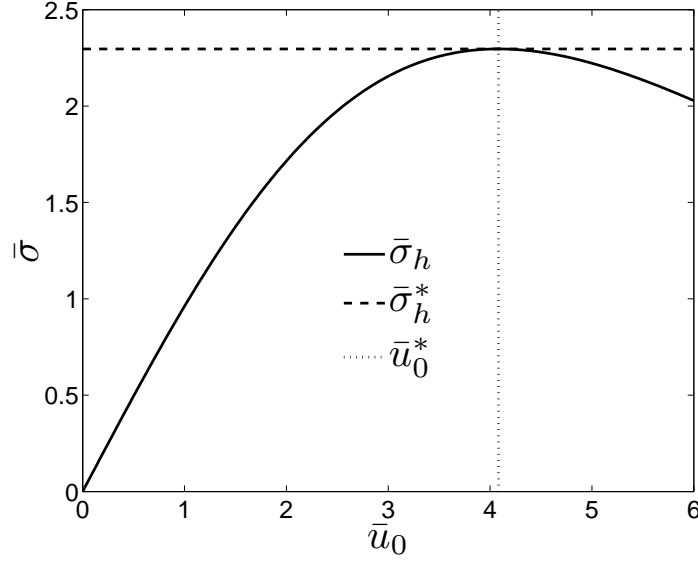


Figure 4.6: Stress response of the homogeneous solution.

of the artificial residual stiffness  $\eta > 0$ . The constant residual stress in the broken bar is given by

$$\bar{\sigma} = \frac{\bar{u}_0}{I(\bar{\epsilon}, \eta)}. \quad (4.64)$$

Figure 4.4 shows a comparison of this stress to results from a 1d FE simulation of the problem. In this example, the regularization length is  $\bar{\epsilon} = 0.01$  and the parameter for the residual stiffness is  $\eta = 0.0001$ . For small loadings, the results are in very good agreement. However, for loadings higher than  $\bar{u}_0 = 0.2$ , the crack in the FE simulation spreads out and occupies more than one single node, and the results are no longer comparable. Again using the material law and the kinematic relation (Eq. 4.52) an approximation of the displacement field of the cracked bar can be computed

$$\bar{u}(\bar{x}) = \int_0^{\bar{x}} \bar{\epsilon} d\bar{\tilde{x}} = \frac{\bar{u}_0}{I(\bar{\epsilon}, \eta)} \int_0^{\bar{x}} \frac{1}{s(\bar{\tilde{x}})^2 + \eta} d\bar{\tilde{x}}. \quad (4.65)$$

Figure 4.5 compares the approximated crack field (Eq. 4.56) and the approximated displacement field (Eq. 4.65) to the results of the FE simulation at a load value of  $\bar{u}_0 = 0.2$ . Also here the results are in very good agreement.

### Homogeneous Solution

The set of equations (Eqs. 4.51-4.53) always has a spatially homogeneous solution with  $s_h(\bar{x}) = \text{const}$ . In this case, Eq. (4.53) immediately yields

$$s_h = \frac{1}{1 + 2\bar{\epsilon}\bar{\epsilon}^2}. \quad (4.66)$$

#### 4.4 Analytical Solutions of the 1d Quasi Static Problem

As  $\bar{s}$  and  $\bar{\sigma}$  are constant, Eq. (4.52) implies that  $\bar{\epsilon}$  must be constant, too. Together with the boundary conditions, this implies  $\bar{\epsilon} = \bar{u}_0$ . Thus, for a given displacement load  $\bar{u}_0$ , the value of the homogeneous crack field is

$$s_h = \frac{1}{1 + 2\bar{\epsilon}\bar{u}_0^2} \quad (4.67)$$

and the according stress is

$$\bar{\sigma}_h = \frac{\bar{u}_0}{(1 + 2\bar{\epsilon}\bar{u}_0^2)^2} + \eta\bar{u}_0 \approx \frac{\bar{u}_0}{(1 + 2\bar{\epsilon}\bar{u}_0^2)^2} \quad \text{for } \eta \rightarrow 0. \quad (4.68)$$

Neglecting  $\eta$ , the stress (Eq. 4.68) is maximal for

$$\bar{u}_0^* = \frac{1}{\sqrt{6\bar{\epsilon}}}. \quad (4.69)$$

The maximum value of the stress is

$$\bar{\sigma}_h^* = \frac{3}{16} \sqrt{\frac{3}{2\bar{\epsilon}}}. \quad (4.70)$$

Figure 4.6 shows a plot of the stress response of the homogeneous solution for  $\bar{\epsilon} = 0.01$ . Interestingly, the value of the homogeneous crack field  $s_h$  at the maximal stress load

$$s_h^* = \frac{3}{4}, \quad (4.71)$$

is independent of the regularization parameter  $\bar{\epsilon}$ . In the next paragraph, it will be shown that the displacement load  $\bar{u}_0^*$  does not only yield the maximal stress response, but is also crucial for the stability of the homogeneous solution.

Again neglecting contributions of the artificial residual stiffness  $\eta$ , the total energy associated with the homogeneous solution is

$$\bar{E} = \int_{-1}^1 \bar{\psi} \, d\bar{x} = \frac{\bar{u}_0^2}{1 + 2\bar{\epsilon}\bar{u}_0^2}. \quad (4.72)$$

For  $\bar{u}_0 = \bar{u}_0^*$ , the total energy takes the value  $\bar{E}^* = \frac{1}{8\bar{\epsilon}}$ .

#### Bifurcation – Critical Stress

If the total energies of the cracked and the homogeneous solutions are compared to each other, the cracked solution becomes energetically favorable at some point. However, in simulations starting from an undamaged bar ( $s \equiv 1$ ), bifurcation from the homogeneous solution to the cracked solution is observed much later. Bourdin shows in Bourdin [2007a], that there is a critical load, at which the homogeneous

solution becomes unstable, yet he does not give a sharp estimate for this critical load.

In order to analyze the stability of the homogeneous solution a family of symmetric test functions  $s_\alpha(\bar{x}) = s_\alpha(-\bar{x})$  with  $s'_\alpha(\pm 1) = s'_\alpha(0) = 0$  and  $s_0(\bar{x}) = s_h(\bar{x})$  is introduced. The restriction  $s'_\alpha(0) = 0$  is placed on the symmetric test functions in order to ensure their differentiability at  $\bar{x} = 0$ . Similar to the construction of the approximation of the cracked solution, the according displacement field  $\bar{u}_\alpha$  with  $\bar{u}_\alpha(\pm 1) = \pm \bar{u}_0$  and  $\bar{u}_0(\bar{x}) = \bar{u}_h(\bar{x})$  can be derived. The kinematic relation and the material law (Eq. 4.52) yield

$$\bar{u}_0 = \int_0^1 \bar{\epsilon}_\alpha d\bar{x} = \int_0^1 \frac{\bar{\sigma}_\alpha}{s_\alpha^2 + \eta} d\bar{x} = \bar{\sigma}_\alpha \int_0^1 \frac{1}{s_\alpha^2 + \eta} d\bar{x}. \quad (4.73)$$

With

$$I_\alpha = \int_0^1 \frac{1}{s_\alpha^2 + \eta} d\bar{x}, \quad (4.74)$$

the constant stress is

$$\bar{\sigma}_\alpha = \frac{\bar{u}_0}{I_\alpha} \quad (4.75)$$

and the according strain equals

$$\bar{\epsilon}_\alpha = \bar{u}'_\alpha = \frac{\bar{u}_0}{(s_\alpha^2 + \eta)I_\alpha}. \quad (4.76)$$

The elastic energy of the disturbed solution on the interval  $[0, 1]$  is

$$\bar{E}^e(s_\alpha) = \int_0^1 \bar{\psi}_\alpha^e d\bar{x} = \int_0^1 \frac{1}{2} \bar{\sigma}_\alpha \bar{u}'_\alpha d\bar{x} = \frac{1}{2} \frac{\bar{u}_0^2}{I_\alpha^2} \int_0^1 \frac{1}{s_\alpha^2 + \eta} d\bar{x} = \frac{\bar{u}_0^2}{2I_\alpha}. \quad (4.77)$$

Adding the surface energy yields the total energy

$$\bar{E}(s_\alpha) = \int_0^1 [\bar{\psi}_\alpha^e + \bar{\psi}_\alpha^s] d\bar{x} = \frac{\bar{u}_0^2}{2I_\alpha} + \int_0^1 \left[ \frac{(1-s_\alpha)^2}{4\bar{\epsilon}} + \bar{\epsilon}(s'_\alpha)^2 \right] d\bar{x}. \quad (4.78)$$

**The first variation** With partial derivatives with respect to  $\alpha$  denoted by  $\partial_\alpha$ , the first variation of the energy (Eq. 4.78) is

$$\begin{aligned} \delta \bar{E}(s_h) &= \frac{d}{d\alpha} \left\{ \frac{\bar{u}_0^2}{2I_\alpha} + \int_0^1 \left[ \frac{(1-s_\alpha)^2}{4\bar{\epsilon}} + \bar{\epsilon}(s'_\alpha)^2 \right] d\bar{x} \right\}_{\alpha=0} \\ &= \left\{ -\frac{\bar{u}_0^2}{2I_\alpha^2} \int_0^1 -\frac{2s_\alpha}{(s_\alpha^2 + \eta)^2} \partial_\alpha s_\alpha d\bar{x} + \int_0^1 \left[ -\frac{1-s_\alpha}{2\bar{\epsilon}} \partial_\alpha s_\alpha + 2\bar{\epsilon} s'_\alpha \partial_\alpha s'_\alpha \right] d\bar{x} \right\}_{\alpha=0}. \end{aligned} \quad (4.79)$$

The first term can be simplified, using the equality

$$I_{\alpha=0} = \frac{1}{s_h^2 + \eta}. \quad (4.80)$$

Partial integration of the last term, taking into account the boundary and symmetry constraints  $s'_\alpha(1) = s'_\alpha(0) = 0$  gives

$$\begin{aligned} \delta \bar{E}(s_h) &= \int_0^1 \left[ \bar{u}_0^2 s_h - \left( \frac{1-s_h}{2\bar{\epsilon}} + 2\bar{\epsilon} s_h'' \right) \right] \partial_\alpha s_\alpha \, d\bar{x} \\ &= \int_0^1 \left[ \frac{\bar{u}_0^2}{1+2\bar{\epsilon}\bar{u}_0^2} - \frac{1}{2\bar{\epsilon}} \left( 1 - \frac{1}{1+2\bar{\epsilon}\bar{u}_0^2} \right) \right] \partial_\alpha s_\alpha \, d\bar{x} = 0, \end{aligned} \quad (4.81)$$

wherein, by a slight abuse of notation,  $\partial_\alpha s_\alpha|_{\alpha=0}$  is replaced by  $\partial_\alpha s_\alpha$  in order to obtain a more compact notation. As the first variation of the homogeneous solution is zero, this solution is always a local extremum or a saddle point of the total energy functional.

**The second variation** The stability of the homogeneous solution depends upon the second variation  $\delta^2 \bar{E}(s_h)$  of the energy functional. As long as  $\delta^2 \bar{E}(s_h) > 0$ , the homogeneous solution is a local minimum and is stable with respect to small perturbations. The second variation of the elastic part of the energy is

$$\begin{aligned} \delta^2 \bar{E}^e(s_h) &= \frac{\bar{u}_0^2}{2} \frac{d^2}{d\alpha^2} \left( \frac{1}{I_\alpha} \right)_{\alpha=0} \\ &= \frac{\bar{u}_0^2}{2} \frac{d}{d\alpha} \left[ \frac{\partial}{\partial I} \left( \frac{1}{I_\alpha} \right) \cdot \frac{d}{d\alpha} I_\alpha \right]_{\alpha=0} \\ &= \frac{\bar{u}_0^2}{2} \left[ \frac{\partial^2}{\partial I^2} \left( \frac{1}{I_\alpha} \right) \cdot \left( \frac{d}{d\alpha} I_\alpha \right)^2 + \frac{\partial}{\partial I} \left( \frac{1}{I_\alpha} \right) \cdot \frac{d^2}{d\alpha^2} I_\alpha \right]_{\alpha=0} \end{aligned} \quad (4.82)$$

For reasons of clarity and comprehensibility the different terms are evaluated one by one. The identity in Eq. (4.80) is used to simplify the following two expressions

$$\frac{\partial}{\partial I} \left( \frac{1}{I_\alpha} \right)_{\alpha=0} = \left( -\frac{1}{I_\alpha^2} \right)_{\alpha=0} = -(s_h^2 + \eta)^2, \quad (4.83)$$

$$\frac{\partial^2}{\partial I^2} \left( \frac{1}{I_\alpha} \right)_{\alpha=0} = \left( \frac{2}{I_\alpha^3} \right)_{\alpha=0} = 2(s_h^2 + \eta)^3. \quad (4.84)$$

Chain rule differentiation of the integral expression  $I_\alpha$  yields

$$\begin{aligned}
 \frac{d}{d\alpha}(I_\alpha)_{\alpha=0} &= \int_0^1 \left[ \frac{\partial}{\partial s_\alpha} \left( \frac{1}{s_\alpha^2 + \eta} \right) \partial_\alpha s_\alpha \right]_{\alpha=0} d\bar{x} \\
 &= \int_0^1 \left[ -\frac{2s_\alpha}{(s_\alpha^2 + \eta)^2} \partial_\alpha s_\alpha \right]_{\alpha=0} d\bar{x} \\
 &= -\frac{2s_h}{(s_h^2 + \eta)^2} \int_0^1 \partial_\alpha s_\alpha d\bar{x}
 \end{aligned} \tag{4.85}$$

and thus

$$\left( \frac{d}{d\alpha}(I_\alpha)_{\alpha=0} \right)^2 = \frac{4s_h^2}{(s_h^2 + \eta)^4} \left( \int_0^1 \partial_\alpha s_\alpha d\bar{x} \right)^2. \tag{4.86}$$

The second derivative of the integral  $I_\alpha$  with respect to  $\alpha$  is computed starting from Eq. (4.85)

$$\begin{aligned}
 \frac{d^2}{d\alpha^2}(I_\alpha)_{\alpha=0} &= \int_0^1 \frac{d}{d\alpha} \left[ -\frac{2s_\alpha}{(s_\alpha^2 + \eta)^2} \partial_\alpha s_\alpha \right]_{\alpha=0} d\bar{x} \\
 &= \int_0^1 \left[ \frac{\partial}{\partial s_\alpha} \left( -\frac{2s_\alpha}{(s_\alpha^2 + \eta)^2} \right) (\partial_\alpha s_\alpha)^2 + \left( -\frac{2s_\alpha}{(s_\alpha^2 + \eta)^2} \right) \partial_{\alpha\alpha} s_\alpha \right]_{\alpha=0} d\bar{x} \\
 &= \frac{6s_h^2 - 2\eta}{(s_h^2 + \eta)^3} \int_0^1 (\partial_\alpha s_\alpha)^2 d\bar{x} - \frac{2s_h}{(s_h^2 + \eta)^2} \int_0^1 \partial_{\alpha\alpha} s_\alpha d\bar{x}.
 \end{aligned} \tag{4.87}$$

Altogether, the second variation of the elastic part of the energy functional is

$$\begin{aligned}
 \delta^2 \bar{E}^e(s_h) &= \frac{4\bar{u}_0^2 s_h^2}{s_h^2 + \eta} \left( \int_0^1 \partial_\alpha s_\alpha d\bar{x} \right)^2 - \frac{3s_h^2 - 2\eta}{s_h^2 + \eta} \bar{u}_0^2 \int_0^1 (\partial_\alpha s_\alpha)^2 d\bar{x} \\
 &\quad + \bar{u}_0^2 s_h \int_0^1 \partial_{\alpha\alpha} s_\alpha d\bar{x}
 \end{aligned} \tag{4.88}$$

For algebraic simplicity, the contribution of  $\eta$  is neglected and the expression simplifies to

$$\delta^2 \bar{E}^e(s_h) = 4\bar{u}_0^2 \left( \int_0^1 \partial_\alpha s_\alpha d\bar{x} \right)^2 - 3\bar{u}_0^2 \int_0^1 (\partial_\alpha s_\alpha)^2 d\bar{x} + \bar{u}_0^2 s_h \int_0^1 \partial_{\alpha\alpha} s_\alpha d\bar{x}. \tag{4.89}$$

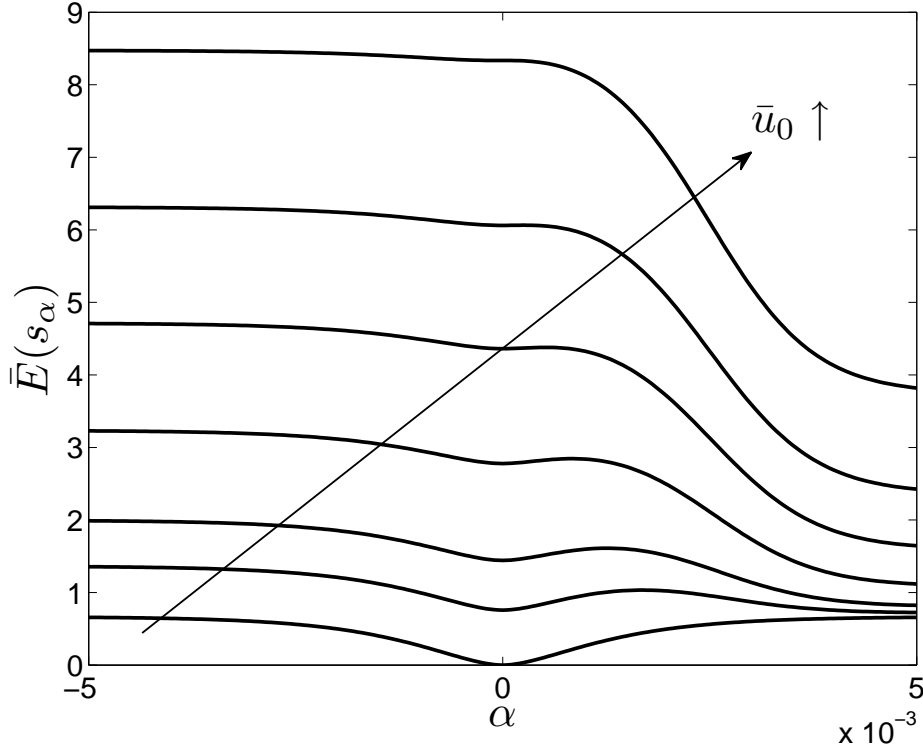


Figure 4.7: Total energy of the disturbed crack field at different load levels.

The second variation of the surface energy is

$$\begin{aligned}
 \delta^2 \bar{E}(s_h) &= \int_0^1 \frac{d^2}{d\alpha^2} (\bar{\psi}^s(s_\alpha, s'_\alpha))_{\alpha=0} d\bar{x} \\
 &= \int_0^1 \left[ \partial_{ss} \bar{\psi}^s (\partial_\alpha s_\alpha)^2 + 2 \partial_{s's} \bar{\psi}^s \partial_\alpha s_\alpha \partial_\alpha s'_\alpha + \partial_{s's'} \bar{\psi}^s (\partial_\alpha s'_\alpha)^2 \right. \\
 &\quad \left. + \partial_s \bar{\psi}^s \partial_{\alpha\alpha} s_\alpha + \partial_{s'} \bar{\psi}^s \partial_{\alpha\alpha} s'_\alpha \right]_{\alpha=0} d\bar{x} \\
 &= \frac{1}{2\bar{\epsilon}} \int_0^1 (\partial_\alpha s_\alpha)^2 d\bar{x} + 2\bar{\epsilon} \int_0^1 (\partial_\alpha s'_\alpha)^2 d\bar{x} \\
 &\quad - \int_0^1 \left[ \frac{1-s_h}{2\bar{\epsilon}} + 2\bar{\epsilon} s''_h \right] \partial_{\alpha\alpha} s_\alpha d\bar{x} \tag{4.90}
 \end{aligned}$$

In the summation of the elastic and the surface part, the terms with  $\partial_{\alpha\alpha} s_\alpha$  cancel out, as the first variation of the energy of the homogeneous solution vanishes. Thus, the second variation of the energy of the homogeneous solution is

$$\delta^2 \bar{E}(s_h) = 4\bar{u}_0^2 \left( \int_0^1 \partial_\alpha s_\alpha d\bar{x} \right)^2 + \left( \frac{1}{2\bar{\epsilon}} - 3\bar{u}_0^2 \right) \int_0^1 (\partial_\alpha s_\alpha)^2 d\bar{x} + 2\bar{\epsilon} \int_0^1 (\partial_\alpha s'_\alpha)^2 d\bar{x}. \tag{4.91}$$

Clearly, this second variation can only become negative if

$$\frac{1}{2\bar{\epsilon}} - 3\bar{u}_0^2 < 0 \quad (4.92)$$

which is equivalent to

$$\bar{u}_0 > \frac{1}{\sqrt{6\bar{\epsilon}}} = \bar{u}_0^*. \quad (4.93)$$

Thus, the load with the maximal stress response represents a lower bound for the stability load of the homogeneous solution. A further analysis of the stability of homogeneous solutions of different gradient damage formulations, is carried out in Benallal and Marigo [2007] and, for a broader class of gradient damage models, in Amor et al. [2008] and Pham et al. [2011a]. More details on the underlying derivations can be found in Pham et al. [2011b]. Concerning the specific phase field model under consideration, the main conclusion from these publications is, that for small values of  $\bar{\epsilon}$ , the actual stability load lies slightly above the lower bound  $\bar{u}_0^*$ . Only for rather large  $\bar{\epsilon}$ , the actual stability load is significantly larger than  $\bar{u}_0^*$ . However, regarding the outcomes from section 4.4.1, the case of large values  $\bar{\epsilon}$ , is of minor interest.

Figure 4.7 visualizes the changing energy landscape under increasing loading. The different lines represent the total energy  $\bar{E}(s_\alpha)$  associated with the disturbed crack field

$$s_\alpha = s_h \left[ 1 - f(\alpha) \operatorname{sech} \left( \frac{\bar{x}}{2\bar{\epsilon}} \right) \right] \quad (4.94)$$

with  $\epsilon = 0.01$  and

$$f(\alpha) = \operatorname{sign}(\alpha) (1 - \exp(-1000|\bar{x}|)) \quad (4.95)$$

for different load levels  $\bar{u}_0$ . The lowest curve refers to the unloaded state. At this stage, there is only one minimum of  $\bar{E}(s_\alpha)$ , which is located at  $\alpha = 0$ , i.e.  $s_\alpha = s_h$ . With the load increasing, the global minimum shifts to the right end of the plot, where  $f(\alpha) \approx 1$ , i.e. the cracked state. The local minimum at  $\alpha = 0$  becomes more and more unstable, until it becomes a saddle point.

### Numerical assessment

The analytical results for the stability of the homogeneous solution are compared to results from a finite element simulation of the problem. An excerpt of the presented results can be found in Kuhn and Müller [2012]. In the simulation, the bar is discretized with 400 standard linear elements. The residual stiffness is  $\eta = 10^{-5}$  and the mobility constant is set to  $\bar{M} = 50$ . The simulation starts from the undamaged state, where  $s \equiv 1$ . In order to promote the bifurcation of the homogeneous solution, the cracking resistance of the two elements sharing a node at  $\bar{x} = 0$  is reduced by 0.01%. Figure 4.8 illustrates the evolution of the crack field. As long as the displacement load  $\bar{u}_0$  stays below the critical value  $\bar{u}_0^* \approx 4.0825$



#### 4.4 Analytical Solutions of the 1d Quasi Static Problem

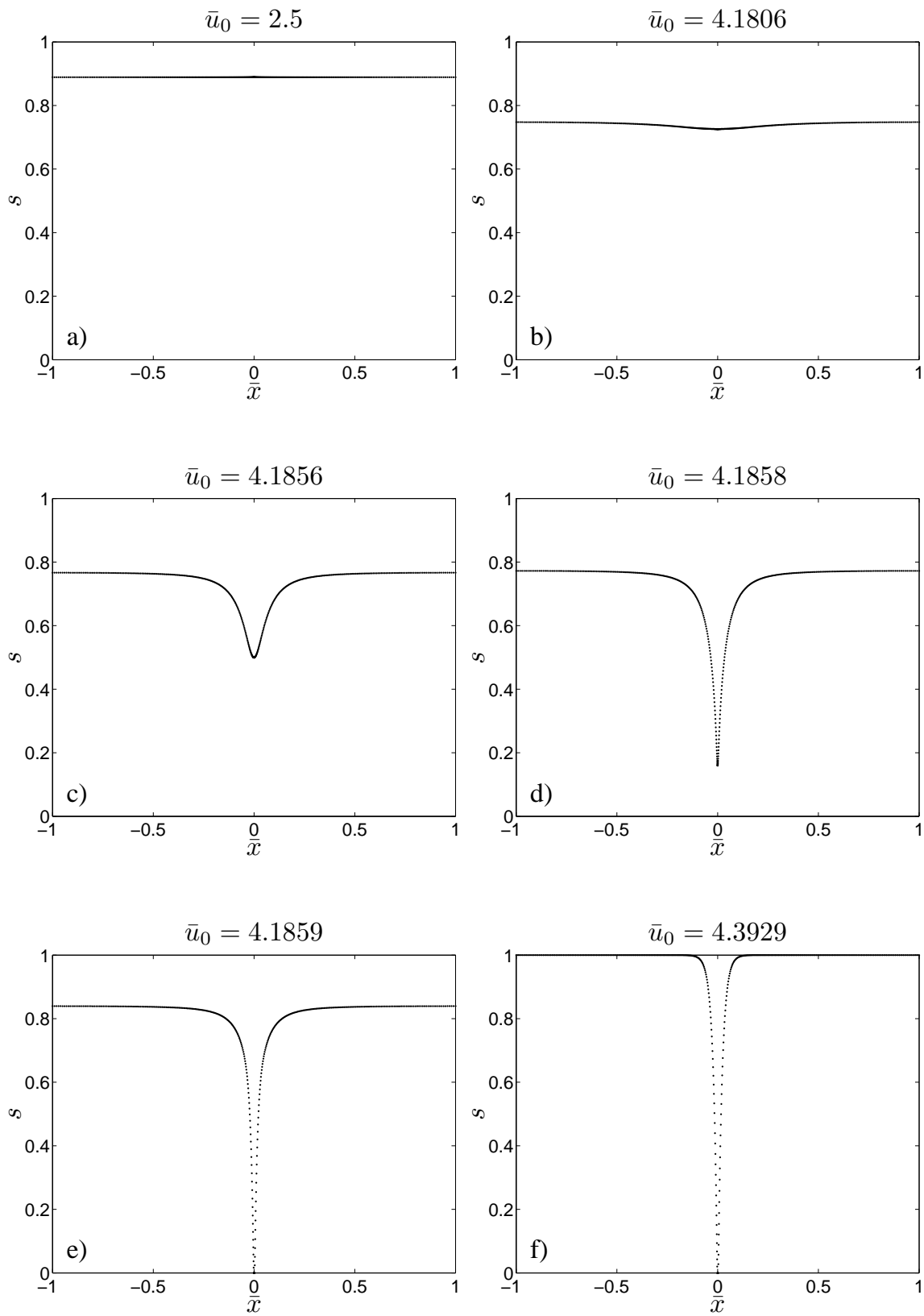


Figure 4.8: Crack field during the bifurcation of the homogeneous solution.

#### 4 A Phase Field Model for Fracture

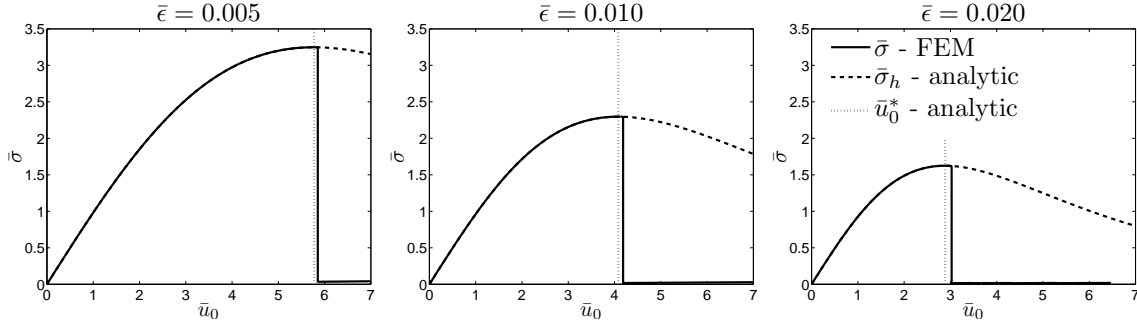


Figure 4.9: Stress response for different regularization parameters  $\bar{\epsilon}$ .

for a regularization length of  $\bar{\epsilon} = 0.01$ , the solution is homogeneous (Fig. 4.8a). As the value of the mobility constant is chosen fairly high, the solution can be considered as stationary at this stage. Bifurcation towards the cracked state starts at about  $\bar{u}_0 \approx 4.18$  (Fig. 4.8b), when  $s \approx s_h^* = 0.75$ . The homogeneous solution is not stable any more, and the crack field rapidly develops towards the cracked solution (Fig. 4.8c, d). At this stage, the solution can no longer be considered as stationary. After a crack has formed, i.e.  $s = 0$  at  $\bar{x} = 0$  (Fig. 4.8e), the crack field at the outer regions recovers up to  $s \approx 1$  (Fig. 4.8f). This is due to the fact that the crack field is not regarded as a damage variable, and irreversibility constraints only apply for  $s = 0$  in this simulation.

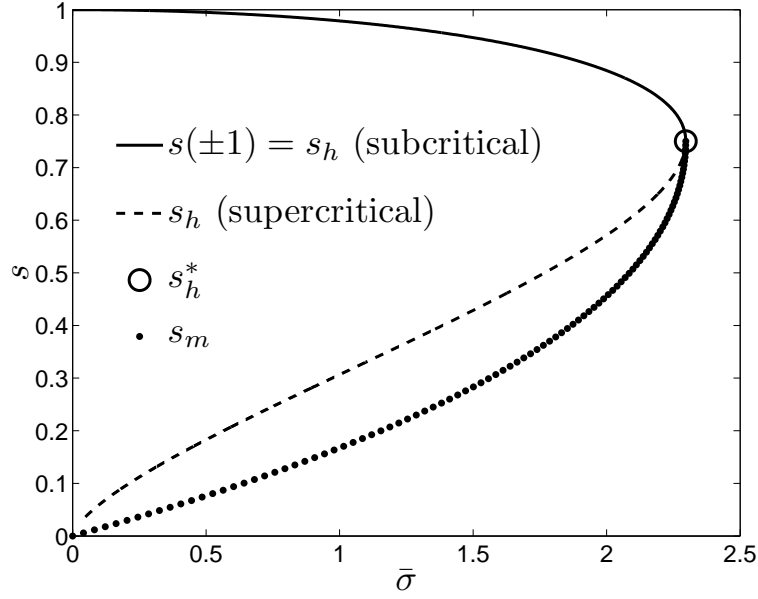
In Fig. 4.9, the stress response of the numeric solution (solid line) is compared to the analytical homogeneous stress response (Eq. 4.68) (dashed line) for three different values of the regularization parameter  $\bar{\epsilon}$ . In all three cases the curves are in perfect agreement until the numerical solution bifurcates towards the cracked state, which can clearly be seen as a sudden drop of the numerical stress response. The lower bound for the stability load of the homogeneous solution  $\bar{u}_0^*$  is marked by the dotted line. In all three cases, the bifurcation of the numerical solution away from the homogeneous towards the cracked solution happens just slightly above this value. However, these numerical results are sensitive to the choice of the mobility constant  $\bar{M}$ , as small values of  $M$  delay the bifurcation.

#### Non-Homogeneous Solution

An analytical approach to the intermediate solution stages plotted in Fig. 4.8 is outlined in Hakim and Karma [2009] and Borden et al. [2012]. The model equations (Eqs. 4.52 and 4.53) combine to the non-linear differential equation

$$\frac{2\bar{\epsilon}\bar{\sigma}^2s}{(s^2 + \eta)^2} + s - 4\bar{\epsilon}^2s'' - 1 = 0. \quad (4.96)$$

For  $\bar{\epsilon} \ll 1$ , the differential equation is supplemented by the far field boundary conditions  $s'(\pm 1) = 0$  and  $s(\pm 1) = s_h(\bar{\sigma})$ , so that the homogeneous solution of


 Figure 4.10: Extremal values  $s_h$  and  $s_m$  of the crack field versus  $\bar{\sigma}$  for  $\bar{\epsilon} = 0.01$ .

section 4.4.2 is also a solution of the present problem. The relation between  $s_h$  and  $\bar{\sigma}$ , needed to compute the value of the homogeneous solution  $s_h(\bar{\sigma})$  at a given stress  $\bar{\sigma} \leq \bar{\sigma}_h^*$ , is implicitly given by Eqs. (4.67) and (4.68) from section 4.4.2, see also the solid line in Fig. 4.10.

Assuming a differentiable, symmetric solution with a minimum value  $s_m$  at  $\bar{x} = 0$ , implies that  $s'(0) = 0$ . With  $\bar{\sigma} = \text{const.}$ , integration of Eq. (4.96) with respect to  $s$  over the domain  $[s_m, s(\bar{x})]$  yields

$$\left[ -\frac{\bar{\epsilon}\bar{\sigma}^2}{s^2 + \eta} + \frac{s^2}{2} - 2\bar{\epsilon}^2(s')^2 - s \right]_{s_m}^{s(\bar{x})} = 0, \quad (4.97)$$

where the identities

$$\frac{d}{ds} \left[ (s^2 + \eta)^{-1} \right] = -\frac{2s}{(s^2 + \eta)^2} \quad \text{and} \quad (4.98)$$

$$\frac{d}{ds} \left[ \left( \frac{ds}{d\bar{x}} \right)^2 \right] = \frac{d}{ds} \left( \frac{ds}{d\bar{x}} \right) \cdot 2 \left( \frac{ds}{d\bar{x}} \right) = 2 \frac{d}{d\bar{x}} \left( \frac{ds}{d\bar{x}} \right) = 2 \frac{d^2 s}{d\bar{x}^2} \quad (4.99)$$

have been used to compute the integral. With the symmetry condition  $s(0) = s_m$  and  $s'(0) = 0$  Eq. (4.97) yields

$$\underbrace{2\bar{\epsilon}^2(s')^2}_{V_{\text{kin}}(s')} + \underbrace{\frac{\bar{\epsilon}\bar{\sigma}^2}{s^2 + \eta} - \frac{s^2}{2} + s}_{V_{\text{eff}}(s)} = \underbrace{\frac{\bar{\epsilon}\bar{\sigma}^2}{s_m^2 + \eta} - \frac{s_m^2}{2} + s_m}_{V_{\text{eff}}(s_m)}, \quad (4.100)$$

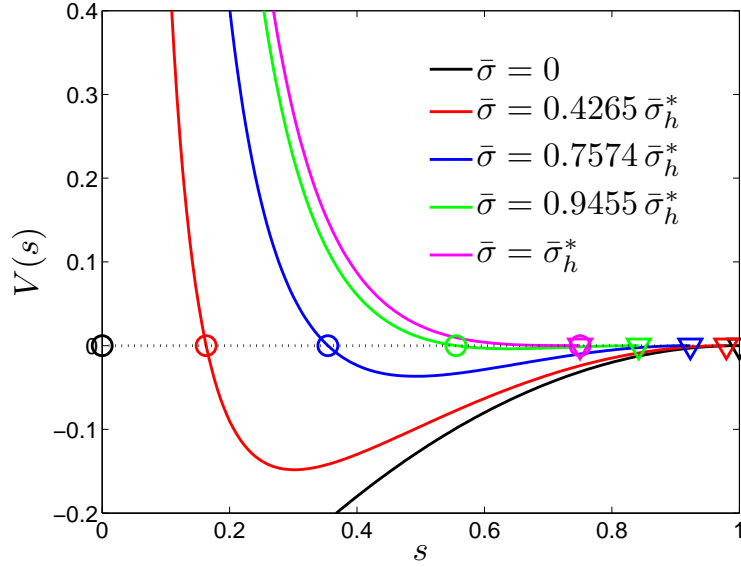


Figure 4.11: Function  $V(s)$  and roots  $s_m$  (circles) and  $s_h$  (triangles) for different values of  $\bar{\sigma}$  and  $\bar{\epsilon} = 0.01$ .

which can be interpreted as a *conservation law*, in which  $V_{\text{eff}}$  plays the role of an effective potential and  $V_{\text{kin}}$  is regarded as the kinetic energy of the phase field variable  $s$ , see Hakim and Karma [2009]. With the far field boundary conditions for  $s$  at  $\bar{x} = 1$ , the conservation law yields the conditional equation

$$\frac{\bar{\epsilon}\bar{\sigma}^2}{s_h^2 + \eta} - \frac{s_h^2}{2} + s_h = \frac{\bar{\epsilon}\bar{\sigma}^2}{s_m^2 + \eta} - \frac{s_m^2}{2} + s_m \quad (4.101)$$

for the minimum value  $s_m$ , i.e.  $s_m$  is a root of the function  $V(s) = V_{\text{eff}}(s) - V_{\text{eff}}(s_h)$  plotted in Fig. 4.11 for different values of  $\bar{\sigma}$  and  $\bar{\epsilon} = 0.01$ . The root referring to  $s = s_h$  is marked by a triangle, and the root referring to  $s = s_m$  is marked by a circle. The extremal cases  $\bar{\sigma} = 0$  (black) and  $\bar{\sigma} = \bar{\sigma}_h^*$  (magenta) require special attention. The case  $\bar{\sigma} = 0$  refers to the cracked state discussed in section 4.4.2. For  $\bar{\sigma} = 0$  and the respective homogeneous crack field value  $s_h(0) = 1$ , the function  $V$  simplifies to  $V(s) = s - \frac{s^2}{2} - \frac{1}{2}$ . Thus, the root defining  $s_m$  vanishes and  $V(s) \leq 0$  in the entire interval  $[0, 1]$ . However, for  $\bar{\sigma} \searrow 0$ , the root  $s_m$  of  $V(s)$  approaches 0. By virtue of these considerations it is legitimate to set  $s_m = 0$  in this case. If  $\bar{\sigma}$  approaches the maximal value  $\bar{\sigma}_h^*$ , the roots defining  $s_h$  and  $s_m$  collapse in a single point  $s_h^*$ . The dots in Fig. 4.10 represent numerically determined values of  $s_m$  at different load levels  $\bar{\sigma}$ . The solid line indicates the corresponding subcritical homogeneous solution or the boundary value  $s(\pm 1)$  of the non-homogeneous solution at supercritical loading, respectively. The circle marks the maximal stress value  $\bar{\sigma}_h^*$  and the corresponding crack field value  $s_h = 0.75$ . The dashed line refers to the unstable homogeneous solution at supercritical loading.

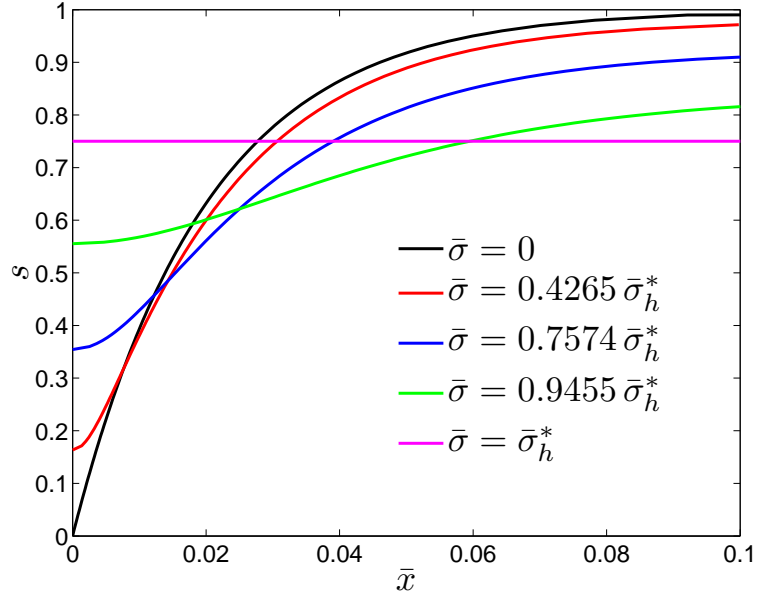


Figure 4.12: Inhomogeneous solution  $s(\bar{x})$  for different values of  $\bar{\sigma}$  and  $\bar{\epsilon} = 0.01$ .

Once the minimum value  $s_m$  has been determined, the conservation law (Eq. 4.100) can be exploited to compute the solution  $s(\bar{x})$  of the differential equation (Eq. 4.96), or rather the inverse  $\bar{x}(s)$  of the solution. Presupposing that the sign of  $s'(\bar{x})$  equals the sign of  $\bar{x}$ , the conservation law yields

$$\frac{ds}{d\bar{x}} = \text{sgn}(\bar{x}) \sqrt{\frac{V_{\text{eff}}(s_m) - V_{\text{eff}}(s)}{2\bar{\epsilon}^2}} \quad (4.102)$$

and thus

$$\bar{x} = \text{sgn}(\bar{x}) \int_{s_m}^{s(\bar{x})} \sqrt{\frac{2\bar{\epsilon}^2}{V_{\text{eff}}(s_m) - V_{\text{eff}}(s)}} ds \quad (4.103)$$

for any  $s(\bar{x}) \in [s_m, s_h]$ . Figure 4.12 shows the results of a numerical evaluation of Eq. (4.103) at the different load levels  $\bar{\sigma}$ . The fully cracked solution (black) is virtually identical with the analytical solution (Eq. 4.56) for the unloaded case, while the limit case  $\bar{\sigma} \nearrow \bar{\sigma}_h^*$  (magenta) yields the homogeneous solution  $s \equiv s_h^* = 0.75$  at the maximal stress load.

### 4.4.3 Conclusion

The above considerations yield a twofold interpretation of the impact of the length scale parameter  $\epsilon$ . In the case of a fractured bar, the regularization character of  $\epsilon$  comes to light. In this case it controls the width of the transition zone between undamaged material ( $s = 1$ ) and cracks ( $s = 0$ ). Additionally, the exact surface energy is obtained in the limit  $\epsilon \rightarrow 0$ .

The stability analysis of the homogeneous solution yields a more mechanically inclined interpretation of  $\epsilon$ . The load with the maximal stress response  $u_0^*$  gives a lower bound for the stability load of the unbroken, homogeneous solution and the actual stability load is only slightly larger than this lower bound, at least for small values of  $\epsilon$ . Thus, it is legitimate to regard the maximal stress response  $\sigma_h^*$  as the strength  $\sigma_c$  of the material. For the dimensionless quantities, it follows by virtue of Eq. (4.70) that through

$$\bar{\sigma}_c = \frac{3}{16} \sqrt{\frac{3}{2\bar{\epsilon}}}, \quad (4.104)$$

the parameter  $\bar{\epsilon}$  is directly related to the strength of the material and may therefore be regarded as a material parameter itself. In the dimensional regime, Eq. (4.104) translates into

$$\sigma_c = \frac{3}{16} \sqrt{\frac{3\mathcal{G}_c E}{2\epsilon}}. \quad (4.105)$$

Thus, the so derived strength is independent of the length  $L$  of the bar under consideration. Nevertheless, slight size effects concerning the stability of homogeneous solutions are present in the material model due to the offset of the actual bifurcation load from the load with the maximal stress response, see Pham et al. [2011a] for a detailed discussion.

## 4.5 Modifications and Extensions

So far, only the basic phase field fracture model, considering fracture of linear elastic material in a small strain setting, has been introduced. Different refinements of the formulation, aiming at a more realistic description and demonstrating the capabilities of the phase field approach concerning the coupling of the fracture problem with additional physical phenomena, are introduced in this section.

### 4.5.1 Compression

The fact that the phase field fracture model introduced in the previous sections, as well as the underlying variational formulation, do not distinguish between compressive and tensile load cases, is often criticized as an unphysical feature of these kind of models. There are different improvements of this aspect proposed in the literature. In Henry and Levine [2004] the evolution equation (Eq. 4.20) is modified in case of a compressive load case in order to avoid unphysical fracture under compression. However, this approach breaks the variational character of the model resulting in a higher effort in numerical simulations. Different approaches which preserve the variational character of the formulation have been proposed in Amor et al. [2009] and Miehe et al. [2010a].

In the so called *unilateral contact* model proposed in Amor et al. [2009], the elastic part of the energy density is split into volumetric and deviatoric contributions. In order to model the different fracture behavior under tension and compression, the degradation function  $(s^2 + \eta)$  does not come into effect in case of a negative volumetric strain. Thus, with the definitions

$$\text{tr}^+(\boldsymbol{\varepsilon}) = \max\{\text{tr}(\boldsymbol{\varepsilon}), 0\} \quad \text{and} \quad \text{tr}^- = \min\{\text{tr}(\boldsymbol{\varepsilon}), 0\}, \quad (4.106)$$

of tensile and compressive volume changes and the deviatoric strain defined according to Eq. (2.73), the elastic part of the energy density (Eq. 4.2) is replaced by

$$\psi^e = \frac{K_n}{2} \text{tr}^-(\boldsymbol{\varepsilon}) + (s^2 + \eta) \left( \frac{K_n}{2} \text{tr}^+(\boldsymbol{\varepsilon})^2 + \mu \boldsymbol{\varepsilon}^{\text{dev}} : \boldsymbol{\varepsilon}^{\text{dev}} \right). \quad (4.107)$$

Consequently, the stress strain relation and the evolution equation, deduced from the energy density functional modify to

$$\boldsymbol{\sigma} = \frac{\partial \psi}{\partial \boldsymbol{\varepsilon}} = K_n \text{tr}^-(\boldsymbol{\varepsilon}) \mathbf{1} + (s^2 + \eta) \left( K_n \text{tr}^+(\boldsymbol{\varepsilon}) \mathbf{1} + 2\mu \boldsymbol{\varepsilon}^{\text{dev}} \right) \quad (4.108)$$

and

$$\dot{s} = -M \frac{\delta \psi}{\delta s} = M \left[ \mathcal{G}_c \varepsilon \Delta s - \left( s \left( K_n \text{tr}^+(\boldsymbol{\varepsilon})^2 + 2\mu \boldsymbol{\varepsilon}^{\text{dev}} : \boldsymbol{\varepsilon}^{\text{dev}} \right) + \frac{\mathcal{G}_c}{2\varepsilon} (s - 1) \right) \right]. \quad (4.109)$$

Note, that compressive volume changes  $\text{tr}^-(\boldsymbol{\varepsilon})$  do not enter the evolution equation. Only the dilatational part of the volumetric strain leads to changes of the crack field, i.e. causes fracture. Additionally, fracture may be induced by shear, which is modeled by the deviatoric contribution.

A similar approach proposed in Miehe et al. [2010a] and adopted by Borden et al. [2012], bases on a spectral decomposition of the infinitesimal strain tensor  $\boldsymbol{\varepsilon}$ . Tensile and compressive contributions to the strain energy are defined by the signs of the principal strains, and the elastic energy is decomposed accordingly.

## 4.5.2 Thermal Fracture

The phase field approach to fracture cannot only be used in the context of linear elasticity. Through an appropriate coupling between the crack field  $s$  and the constitutive relations of the respective material model, it can be applied to a large range of material models in a straightforward way. This is demonstrated exemplary for the coupled thermomechanical problem in this section. An application of the phase field fracture model in the context of ferroelectric material behavior can be found in Xu et al. [2010].

#### 4 A Phase Field Model for Fracture

In order to study thermally induced fracture, non-elastic thermal strains need to be taken into account. For small deformations it is assumed that the overall strain splits additively into an elastic and a thermal component. Therein, the thermal strain  $\boldsymbol{\varepsilon}^\theta$  is defined by the temperature  $\theta$  and the thermal expansion tensor  $\boldsymbol{\alpha}$ , i.e.

$$\boldsymbol{\varepsilon} = \boldsymbol{\varepsilon}^e + \boldsymbol{\varepsilon}^\theta \quad \text{with} \quad \boldsymbol{\varepsilon}^\theta = \theta \boldsymbol{\alpha}. \quad (4.110)$$

Only the elastic part  $\boldsymbol{\varepsilon}^e$  of the strain tensor contributes to the elastic energy density which modifies to

$$\psi^e = \frac{1}{2}(s^2 + \eta)\boldsymbol{\varepsilon}^e : [\mathbb{C}\boldsymbol{\varepsilon}^e] = \frac{1}{2}(s^2 + \eta)(\boldsymbol{\varepsilon} - \boldsymbol{\varepsilon}^\theta) : [\mathbb{C}(\boldsymbol{\varepsilon} - \boldsymbol{\varepsilon}^\theta)]. \quad (4.111)$$

Hence, the thermal strains enter the material law for the Cauchy stress

$$\boldsymbol{\sigma} = \frac{\partial \psi}{\partial \boldsymbol{\varepsilon}} = \frac{1}{2}(s^2 + \eta)\mathbb{C}(\boldsymbol{\varepsilon} - \boldsymbol{\varepsilon}^\theta) \quad (4.112)$$

and the evolution equation for the crack field

$$\dot{s} = -M \frac{\delta \psi}{\delta s} = -M \left( s(\boldsymbol{\varepsilon} - \boldsymbol{\varepsilon}^\theta) : [\mathbb{C}(\boldsymbol{\varepsilon} - \boldsymbol{\varepsilon}^\theta)] - \mathcal{G}_c \left( 2\varepsilon \Delta s + \frac{1-s}{2\varepsilon} \right) \right), \quad (4.113)$$

which are both derived from the energy density. With this adjustment of the phase field model, it is already possible to study crack propagation due to a given temperature distribution, see Bourdin [2007b], Corson et al. [2009], Bourdin et al. or Bourdin et al. [2011b].

However, the phase field approach also permits to study the mutual interference of fracture and thermal effects. Therefore, in addition to the static balance equation (Eq. 2.42) and the modified evolution equation (Eq. 4.113), the *heat equation*

$$-\operatorname{div} \mathbf{q}^\theta = \rho c \dot{\theta} \quad (4.114)$$

needs to be solved. The parameter  $c$  is the *specific heat capacity*. In order to take the impact of the phase field cracks on the heat conduction behavior into account, a modified version of Fourier's law (Eq. 2.60) is proposed in Kuhn and Müller [2009]

$$\mathbf{q}^\theta = - \left( \beta(s^2 + \eta - 1) + 1 \right) \boldsymbol{\kappa} \nabla \theta. \quad (4.115)$$

Here, the parameter  $\beta \in [0, 1]$  defines the influence of the crack field on the thermal conductivity  $\boldsymbol{\kappa}$ . If  $\beta = 0$ , the heat flux is not affected by a crack, i.e. the crack is perfectly conducting. If  $\beta = 1$ , the thermal conductivity degrades in the same way as the stiffness tensor  $\mathbb{C}$  and becomes zero for  $s = 0$ . Consequently, there is no heat flux across a crack, i.e. cracks are isolating.



The elastic potential (Eq. 4.111) can additionally be decomposed into expansive and compressive contributions as explained in the previous section in order to account for different fracture behavior under tension and compression.

### 4.5.3 Finite Deformations

The variational formulation of brittle fracture just as Bourdin's regularization can as well be formulated for finite elasticity. Some preliminary results concerning  $\Gamma$ -convergence and the existence of quasi static evolutions for a large class of hyperelastic, isotropic materials can be found in del Piero et al. [2007]. Exemplary, the modifications of the original phase field model for the case of Neo-Hookean material behavior are briefly outlined in this section. Some results from numerical simulations are reported in Kuhn and Müller [2008]. With the elastic potential of compressive Neo-Hookean material, the regularized elastic energy density becomes

$$\psi^e = (s^2 + \eta) \left[ \frac{\lambda}{4} (J^2 - 1) - \left( \frac{\lambda}{2} + \mu \right) \ln(J) + \frac{\mu}{2} (\text{tr}(\mathbf{C}) - 3) \right], \quad (4.116)$$

where  $J$  is the determinant of the deformation gradient according to Eq. (2.6) and  $\mathbf{C}$  is the right Cauchy-Green tensor as defined in Eq. (2.14). The surface energy density  $\psi^s$  remains unaltered. With the thermodynamical restriction from Eq. (2.64), this yields the constitutive relation

$$\mathbf{S} = 2 \frac{\partial \psi}{\partial \mathbf{C}} = (s^2 + \eta) \left[ \frac{\lambda}{2} (J^2 - 1) \mathbf{C}^{-1} + \mu (\mathbf{1} - \mathbf{C}^{-1}) \right] \quad (4.117)$$

for the second Piola-Kirchhoff stress tensor  $\mathbf{S} = \mathbf{F}^{-1} \mathbf{P}$ . Formulated in the reference configuration, the coupled system of equations of the phase field model consists of the balance equation

$$\mathbf{0} = \text{Div} \mathbf{P} + \mathbf{f}_0 \quad (4.118)$$

for the first Piola-Kirchhoff stress tensor  $\mathbf{P}$  and the modified evolution equation

$$-\frac{\dot{s}}{M} = s \left( \frac{\lambda}{2} (J^2 - 1) - (\lambda + 2\mu) \ln J + \mu (\text{tr}(\mathbf{C}) - 3) \right) - \mathcal{G}_c \left( 2\epsilon \Delta s + \frac{1-s}{2\epsilon} \right) \quad (4.119)$$

for the crack field  $s$ .

## 4 *A Phase Field Model for Fracture*

# 5 Finite Element Implementation

The implementation of the initial boundary value problem formed by Eqs. (4.31)-(4.33) into a finite element scheme is outlined in this chapter. For brevity, this summary focuses on the details, which are directly related to the implementation of the present material model. Further background and extensions of the finite element method can be found in various textbooks as e.g. Zienkiewicz and Taylor [2000], Hughes [2000] and Wriggers [2009]. The present outline of the implementation only covers the 2d case, yet an extension to 3d is straightforward. For the discretization in space, four noded quadrilateral elements with three degrees of freedom per node  $(\mathbf{u}_I, s_I)$  discretize the structure in space. The presence of the transient term  $\dot{s}$  in the evolution equation necessitates the application of a time integration scheme in addition to the spatial discretization with finite elements.

## 5.1 Weak Forms and Spatial Discretization

The starting point for the finite element implementation are the *weak forms* of the mechanical force balance and the evolution equation of the crack field. The weak forms can be obtained by a scalar multiplication of these field equations with the respective virtual test functions  $\delta \mathbf{u}$  and  $\delta s$  and a subsequent integration over the domain  $\Omega$ . Integration by parts, taking into account the respective boundary conditions, leads to the format

$$\int_{\Omega} [-(\nabla \delta \mathbf{u})^T : \boldsymbol{\sigma} + \delta \mathbf{u} \cdot \mathbf{f}] dV + \int_{\partial \Omega_t} \delta \mathbf{u} \cdot \mathbf{t}^* dA = 0 \quad (5.1)$$

and

$$\int_{\Omega} - \left[ \delta s \frac{\dot{s}}{M} + \nabla \delta s \cdot \boldsymbol{\xi} + \delta s \left( s \boldsymbol{\varepsilon} : [\mathbf{C} \boldsymbol{\varepsilon}] - \frac{\mathcal{G}_c}{2\epsilon} (1-s) \right) \right] dV = 0 \quad (5.2)$$

with the micro stress  $\boldsymbol{\xi} = 2\mathcal{G}_c \epsilon \nabla s$ , introduced in section 4.2.1. In the discretization, the displacements  $\mathbf{u}$ , the crack field  $s$ , as well as their virtual counterparts  $\delta \mathbf{u}$  and  $\delta s$  are approximated by scalar *shape functions*  $N_I^u$ ,  $N_I^s$ ,  $N_I^{\delta u}$ , and  $N_I^{\delta s}$ , which interpolate the respective nodal values  $\mathbf{u}_I$ ,  $s_I$ ,  $\delta \mathbf{u}_I$ , and  $\delta s_I$ . The discretized quantities  $\mathbf{u}_h$ ,  $s_h$ ,  $\delta \mathbf{u}_h$ , and  $\delta s_h$ , represented in matrix notation - denoted by an underbar in the following - read

## 5 Finite Element Implementation

$$\underline{\mathbf{u}}_h = \sum_{I=1}^N N_I^u \underline{\mathbf{u}}_I, \quad s_h = \sum_{I=1}^N N_I^s s_I, \quad (5.3)$$

$$\underline{\delta \mathbf{u}}_h = \sum_{I=1}^N N_I^{\delta u} \underline{\delta \mathbf{u}}_I \quad \text{and} \quad \delta s_h = \sum_{I=1}^N N_I^{\delta s} \delta s_I, \quad (5.4)$$

where  $N$  is the total number of nodes used for the discretization. The gradient expressions appearing in Eqs. (5.1)-(5.2) are discretized using the differential operator matrices  $\underline{\mathbf{B}}_I^u$ ,  $\underline{\mathbf{B}}_I^s$ ,  $\underline{\mathbf{B}}_I^{\delta u}$  and  $\underline{\mathbf{B}}_I^{\delta s}$  defined by the derivatives of the shape functions. For the 2d case they read

$$\underline{\mathbf{B}}_I^u = \begin{bmatrix} N_{I,x}^u & 0 \\ 0 & N_{I,y}^u \\ N_{I,y}^u & N_{I,x}^u \end{bmatrix}, \quad \underline{\mathbf{B}}_I^s = \begin{bmatrix} N_{I,x}^s \\ N_{I,y}^s \end{bmatrix}, \quad (5.5)$$

$$\underline{\mathbf{B}}_I^{\delta u} = \begin{bmatrix} N_{I,x}^{\delta u} & 0 \\ 0 & N_{I,y}^{\delta u} \\ N_{I,y}^{\delta u} & N_{I,x}^{\delta u} \end{bmatrix} \quad \text{and} \quad \underline{\mathbf{B}}_I^{\delta s} = \begin{bmatrix} N_{I,x}^{\delta s} \\ N_{I,y}^{\delta s} \end{bmatrix}. \quad (5.6)$$

$N_{I,x}^{(\cdot)}$  and  $N_{I,y}^{(\cdot)}$  denote the partial derivatives of the shape functions with respect to the coordinates  $x$  and  $y$ . With these differential operator matrices at hand, the discretized gradient quantities yield

$$\underline{\boldsymbol{\varepsilon}}_h = \sum_{I=1}^N \underline{\mathbf{B}}_I^u \underline{\mathbf{u}}_I, \quad \nabla s_h = \sum_{I=1}^N \underline{\mathbf{B}}_I^s s_I, \quad (5.7)$$

$$\underline{\delta \boldsymbol{\varepsilon}}_h = \sum_{I=1}^N \underline{\mathbf{B}}_I^{\delta u} \underline{\delta \mathbf{u}}_I, \quad \text{and} \quad \nabla \delta s_h = \sum_{I=1}^N \underline{\mathbf{B}}_I^{\delta s} \delta s_I, \quad (5.8)$$

where the linearized strain tensor  $\boldsymbol{\varepsilon}$  and its virtual counterpart are represented in Voigt-notation, i.e.

$$\underline{\boldsymbol{\varepsilon}} = [\varepsilon_{xx} \quad \varepsilon_{yy} \quad 2\varepsilon_{xy}]^T. \quad (5.9)$$

By virtue of the symmetry of the Cauchy stress  $\boldsymbol{\sigma}$  and the definition of the linearized strain tensor  $\boldsymbol{\varepsilon}$ , the equality

$$(\nabla \delta \mathbf{u})^T : \boldsymbol{\sigma} = \delta \boldsymbol{\varepsilon} : \boldsymbol{\sigma} \quad (5.10)$$

holds. Thus, with the Voigt-notation

$$\underline{\boldsymbol{\sigma}} = [\sigma_{xx} \quad \sigma_{yy} \quad \sigma_{xy}]^T \quad (5.11)$$

for the Cauchy stress tensor  $\boldsymbol{\sigma}$ , the discrete version of Eqs. (5.1)-(5.2) becomes

$$\sum_{I=1}^N (\delta \mathbf{u}_I)^T \left[ \underbrace{\int_{\Omega} \left( -[\mathbf{B}_I^{\delta u}]^T \boldsymbol{\sigma}_h + N_I^{\delta u} \underline{\mathbf{f}}_h \right) dV}_{=R_I^u} + \int_{\partial\Omega_t} N_I^{\delta u} \underline{\mathbf{t}}_h^* dA \right] = 0, \quad (5.12)$$

$$\sum_{I=1}^N \delta s_I \left[ \underbrace{- \int_{\Omega} \left( N_I^{\delta s} \frac{\dot{s}_h}{M} + [\mathbf{B}_I^{\delta s}]^T \underline{\boldsymbol{\xi}}_h + N_I^{\delta s} \left( s_h \underline{\boldsymbol{\epsilon}}_h^T (\mathbb{C} \underline{\boldsymbol{\epsilon}}_h) - \frac{\mathcal{G}_c}{2\epsilon} (1 - s_h) \right) \right) dV}_{=R_I^s} \right] = 0 \quad (5.13)$$

with the Voigt-notation

$$\underline{\mathbb{C}} = \begin{pmatrix} \lambda + 2\mu & \lambda & 0 \\ \lambda & \lambda + 2\mu & 0 \\ 0 & 0 & \mu \end{pmatrix} \quad (5.14)$$

of the isotropic stiffness tensor  $\mathbb{C}$  for the plane strain case expressed through the Lamé constants  $\lambda$  and  $\mu$ . The integrals in Eqs. (5.12)-(5.13) form the *nodal residuals*  $R_I^u$  and  $R_I^s$ . As the support of a finite element shape function  $N_I$  usually only comprises the elements adjacent to the respective node  $I$ , it is convenient to compute the residuals element wise. The contributions of element  $e$  to the residuals of node  $I$  are

$$\begin{aligned} \underline{R}_{I,e}^u &= - \int_{\Omega_e} [\mathbf{B}_I^{\delta u}]^T \boldsymbol{\sigma}_h dV + \int_{\Omega_e} N_I^{\delta u} \underline{\mathbf{f}}_h dV + \int_{\partial\Omega_e \cap \partial\Omega_t} N_I^{\delta u} \underline{\mathbf{t}}_h^* dA \\ &= - \underline{P}_{I,e}^u + \underline{F}_{I,e}^u \end{aligned} \quad (5.15)$$

and

$$\begin{aligned} R_{I,e}^s &= - \int_{\Omega_e} \left[ N_I^{\delta s} \frac{\dot{s}_h}{M} + [\mathbf{B}_I^{\delta s}]^T \underline{\boldsymbol{\xi}}_h + N_I^{\delta s} \left( s_h \underline{\boldsymbol{\epsilon}}_h^T (\mathbb{C} \underline{\boldsymbol{\epsilon}}_h) - \frac{\mathcal{G}_c}{2\epsilon} (1 - s_h) \right) \right] dV, \\ &= - P_{I,e}^s \end{aligned} \quad (5.16)$$

where  $\Omega_e$  is the domain occupied by element  $e$ . The contributions of internal forces to the residuals are denoted by  $\underline{P}_{I,e}^u$  and  $P_{I,e}^s$ . Contributions of external forces (only acting on the mechanical part) are denoted by  $\underline{F}_{I,e}^u$ . In order to obtain a more compact notation, the *mechanical residual*  $\underline{R}_{I,e}^u$  and the *crack field residual*  $R_{I,e}^s$  are assembled to

$$\underline{R}_{I,e} = \left[ \left( \underline{R}_{I,e}^u \right)^T \quad R_{I,e}^s \right]^T. \quad (5.17)$$

For a four noded element  $e$  comprising the nodes  $I, J, K$  and  $L$ , the *element residual*  $\underline{R}_e$  is formed by the contributions of all element nodes

$$\underline{R}_e = \left[ \left( \underline{R}_{I,e} \right)^T \quad \left( \underline{R}_{J,e} \right)^T \quad \left( \underline{R}_{K,e} \right)^T \quad \left( \underline{R}_{L,e} \right)^T \right]^T. \quad (5.18)$$

## 5 Finite Element Implementation

The *global residual*  $\underline{\mathbf{R}}$  is formed by an assembly  $\cup$  of all  $n_e$  elements of the discretization

$$\underline{\mathbf{R}} = \bigcup_{e=1}^{n_e} \underline{\mathbf{R}}_e = \left[ (\underline{\mathbf{R}}_1)^T \quad \dots \quad (\underline{\mathbf{R}}_N)^T \right]^T. \quad (5.19)$$

Herein, the nodal residuals

$$\underline{\mathbf{R}}_I = \sum_{e \in \mathcal{E}_I} \underline{\mathbf{R}}_{I,e} \quad (5.20)$$

are the sum of all element contributions  $\underline{\mathbf{R}}_{I,e}$ , where the element  $e$  is in the set  $\mathcal{E}_I$  of elements adjacent to node  $I$ . With the nodal values of the virtual quantities  $\delta \mathbf{u}$  and  $\delta s$  being assembled in the same fashion as the residuals, i.e.

$$\delta \underline{\mathbf{d}} = \left[ (\delta \underline{\mathbf{d}}_1)^T \quad \dots \quad (\delta \underline{\mathbf{d}}_N)^T \right]^T \quad \text{with} \quad \delta \underline{\mathbf{d}}_I = \left[ (\delta \underline{\mathbf{u}}_I)^T \quad \delta s_I \right]^T \quad (5.21)$$

Eqs. (5.12)-(5.13) may be rewritten in the compact notation

$$(\delta \underline{\mathbf{d}})^T \underline{\mathbf{R}} = 0. \quad (5.22)$$

The generic requirement that Eq. (5.22) must hold for any choice of  $\delta \underline{\mathbf{d}}$  leads to the global system of equations

$$\underline{\mathbf{R}} = \underline{\mathbf{0}} \quad \Leftrightarrow \quad \underline{\mathbf{R}}_I = \underline{\mathbf{0}} \quad \text{for} \quad I = 1, \dots, N. \quad (5.23)$$

## 5.2 Time Discretization and Iterative Solution

With the *global internal and external force vectors*  $\underline{\mathbf{P}}$  and  $\underline{\mathbf{F}}$ , also assembled in the same way as the residuals, the global system of equations may be rewritten in the format

$$\underline{\mathbf{R}} = \underline{\mathbf{F}} - \underline{\mathbf{P}}(\underline{\mathbf{d}}, \dot{\underline{\mathbf{d}}}) = \underline{\mathbf{0}}, \quad (5.24)$$

where  $\underline{\mathbf{d}}$  denotes the *global vector of degrees of freedom*

$$\underline{\mathbf{d}} = \left[ (\underline{\mathbf{d}}_1)^T \quad \dots \quad (\underline{\mathbf{d}}_N)^T \right]^T \quad \text{with} \quad \underline{\mathbf{d}}_I = \left[ \underline{\mathbf{u}}_I^T \quad s_I \right]^T. \quad (5.25)$$

In each time step  $t_n \rightarrow t_{n+1}$ , the non linear system of equations

$$\underline{\mathbf{R}}_{n+1} = \underline{\mathbf{F}}_{n+1} - \underline{\mathbf{P}}(\underline{\mathbf{d}}_{n+1}, \dot{\underline{\mathbf{d}}}_{n+1}) = \underline{\mathbf{0}} \quad (5.26)$$

needs to be solved. In order to obtain a robust implementation, an implicit scheme should be employed for the approximation of the velocities  $\dot{\underline{\mathbf{d}}}_{n+1}$ . Choosing the implicit Euler method, yields

$$\dot{\underline{\mathbf{d}}}_{n+1} = \frac{\underline{\mathbf{d}}_{n+1} - \underline{\mathbf{d}}_n}{\Delta t_n}. \quad (5.27)$$

as approximation for the rate expressions at time  $t_{n+1}$ . The time discretized residual is thus a function of the prescribed external forces  $\underline{F}_{n+1}$ , the known degrees of freedom  $\underline{d}_n$  at time  $t_n$  and the unknown degrees of freedom  $\underline{d}_{n+1}$  at time  $t_{n+1}$ , i.e.

$$\underline{R}_{n+1} = \hat{\underline{R}}(\underline{F}_{n+1}, \underline{d}_n, \underline{d}_{n+1}) = \underline{F}_{n+1} - \hat{\underline{P}}(\underline{d}_n, \underline{d}_{n+1}) = \underline{0}. \quad (5.28)$$

The Newton-Raphson method is used to find the solution  $\underline{d}_{n+1}$  of this system of equations. Initialized with  $\underline{d}_{n+1}^{(0)} = \underline{d}_n$ , the solution is computed iteratively according to the update formula

$$\underline{d}_{n+1}^{(k+1)} = \underline{d}_{n+1}^{(k)} + \Delta \underline{d}_{n+1}^{(k)}, \quad (5.29)$$

where the increment  $\Delta \underline{d}_{n+1}^{(k)}$  is determined from the linearized system of equations

$$\underline{R}_{n+1}^{(k+1)} \approx \underline{R}_{n+1}^{(k)} - \underline{S}_{n+1}^{(k)} \Delta \underline{d}_{n+1}^{(k)} = \underline{0}. \quad (5.30)$$

The superscript  $(k)$  indicates the iteration step. The iteration stops whenever the residual vanishes to a prescribed level of precision. Since the external load vector  $\underline{F}_{n+1}$  is independent of the unknown nodal degrees of freedom  $\underline{d}_{n+1}$ , the system matrix  $\underline{S}$  is the derivative of the internal force vector  $\hat{\underline{P}}$  with respect to  $\underline{d}_{n+1}$ . Thus

$$\underline{S}_{n+1}^{(k)} = \frac{\partial \hat{\underline{P}}}{\partial \underline{d}_{n+1}} (\underline{d}_n, \underline{d}_{n+1}^{(k)}). \quad (5.31)$$

As the approximation of the transient terms with the implicit Euler method yields

$$\underline{S} = \frac{\partial \hat{\underline{P}}}{\partial \underline{d}_{n+1}} = \frac{d\underline{P}}{d\underline{d}_{n+1}} (\underline{d}_{n+1}, \dot{\underline{d}}_{n+1}) = \frac{\partial \underline{P}}{\partial \underline{d}_{n+1}} + \frac{1}{\Delta t_n} \frac{\partial \underline{P}}{\partial \dot{\underline{d}}_{n+1}}, \quad (5.32)$$

the system matrix  $\underline{S}$  can be split into a composition

$$\underline{S} = \underline{K} + \frac{1}{\Delta t_n} \underline{D} \quad (5.33)$$

of the *global stiffness matrix*

$$\underline{K} = \frac{\partial \underline{P}}{\partial \underline{d}_{n+1}} \quad (5.34)$$

and the *global damping matrix*

$$\underline{D} = \frac{\partial \underline{P}}{\partial \dot{\underline{d}}_{n+1}}. \quad (5.35)$$

Just as the residuals, the stiffness and damping matrices are computed at element level and then assembled to the global system matrix. The different contributions to the element stiffness and damping matrices are obtained by derivation of the internal forces  $\underline{P}_{I,e}^u$  and  $P_{I,e}^s$  with respect to  $\underline{u}_J, s_J$  and  $\dot{\underline{u}}_J, \dot{s}_J$ , respectively. This yields

## 5 Finite Element Implementation

the submatrices

$$\underline{\mathbf{K}}_{IJ,e} = \begin{bmatrix} \underline{\mathbf{K}}_{IJ,e}^{uu} & \underline{\mathbf{K}}_{IJ,e}^{us} \\ \underline{\mathbf{K}}_{IJ,e}^{su} & \underline{\mathbf{K}}_{IJ,e}^{ss} \end{bmatrix} \quad (5.36)$$

with

$$\underline{\mathbf{K}}_{IJ,e}^{uu} = \frac{\partial \underline{\mathbf{P}}_{IJ,e}^u}{\partial \underline{\mathbf{u}}_J} = \int_{\Omega_e} [\underline{\mathbf{B}}_I^{\delta u}]^T (s^2 + \eta) \underline{\mathbf{C}} \underline{\mathbf{B}}_J^u dV, \quad (5.37)$$

$$\underline{\mathbf{K}}_{IJ,e}^{us} = \frac{\partial \underline{\mathbf{P}}_{IJ,e}^u}{\partial s_J} = \int_{\Omega_e} [\underline{\mathbf{B}}_I^{\delta u}]^T 2s \underline{\mathbf{C}} \underline{\boldsymbol{\varepsilon}}_h N_J^s dV, \quad (5.38)$$

$$\underline{\mathbf{K}}_{IJ,e}^{su} = \frac{\partial P_{IJ,e}^s}{\partial \underline{\mathbf{u}}_J} = \int_{\Omega_e} N_I^{\delta s} 2s (\underline{\mathbf{C}} \underline{\boldsymbol{\varepsilon}}_h)^T \underline{\mathbf{B}}_J^u dV \quad \text{and} \quad (5.39)$$

$$\underline{\mathbf{K}}_{IJ,e}^{ss} = \frac{\partial P_{IJ,e}^s}{\partial s_J} = \int_{\Omega_e} \left[ [\underline{\mathbf{B}}_I^{\delta s}]^T 2\mathcal{G}_c \epsilon \underline{\mathbf{B}}_J^s + N_I^{\delta s} \left( \underline{\boldsymbol{\varepsilon}}_h^T \underline{\mathbf{C}} \underline{\boldsymbol{\varepsilon}} + \frac{\mathcal{G}_c}{2\epsilon} \right) N_J^s \right] dV, \quad (5.40)$$

which form the *element stiffness matrix*  $\underline{\mathbf{K}}_e$ . Since  $\underline{\mathbf{P}}_{I,e}^u$  and  $P_{I,e}^s$  do not depend on  $\underline{\mathbf{u}}_J$  the submatrices of the *element damping matrix*  $\underline{\mathbf{D}}_e$  simplify to

$$\underline{\mathbf{D}}_{IJ,e} = \begin{bmatrix} \underline{\mathbf{0}} & \underline{\mathbf{0}} \\ \underline{\mathbf{0}} & D_{IJ,e}^{ss} \end{bmatrix} \quad (5.41)$$

with

$$D_{IJ,e}^{ss} = \int_{\Omega_e} N_I^{\delta s} \frac{1}{M} N_J^s dV. \quad (5.42)$$

The submatrices of the element system matrix are computed according to Eq. (5.33)

$$\underline{\mathbf{S}}_{IJ,e} = \underline{\mathbf{K}}_{IJ,e} + \frac{1}{\Delta t_n} \underline{\mathbf{D}}_{IJ,e}. \quad (5.43)$$

These submatrices are then assembled to the *element system matrix*  $\underline{\mathbf{S}}_e$ . For a four noded element comprising the nodes  $I, J, K, L$ , this means

$$\underline{\mathbf{S}}_e = \begin{bmatrix} \underline{\mathbf{S}}_{II,e} & \underline{\mathbf{S}}_{IJ,e} & \underline{\mathbf{S}}_{IK,e} & \underline{\mathbf{S}}_{IL,e} \\ \underline{\mathbf{S}}_{JI,e} & \underline{\mathbf{S}}_{JJ,e} & \underline{\mathbf{S}}_{JK,e} & \underline{\mathbf{S}}_{JL,e} \\ \underline{\mathbf{S}}_{KI,e} & \underline{\mathbf{S}}_{KJ,e} & \underline{\mathbf{S}}_{KK,e} & \underline{\mathbf{S}}_{KL,e} \\ \underline{\mathbf{S}}_{LI,e} & \underline{\mathbf{S}}_{LJ,e} & \underline{\mathbf{S}}_{LK,e} & \underline{\mathbf{S}}_{LL,e} \end{bmatrix}. \quad (5.44)$$

An assembly over all elements yields the global system matrix  $\underline{\mathbf{S}}$ . If, as it is standard in finite element implementations, the same shape functions are chosen for the approximation of the actual values and the virtual quantities, i.e.  $N_I^u = N_I^{\delta u}$  and  $N_I^s = N_I^{\delta s}$ , the assembled system matrix becomes symmetric. This is due to the fact that the field equations are derived from the energy density functional  $\psi$ . In section 5.6, special shape functions are introduced for the discretization of the crack



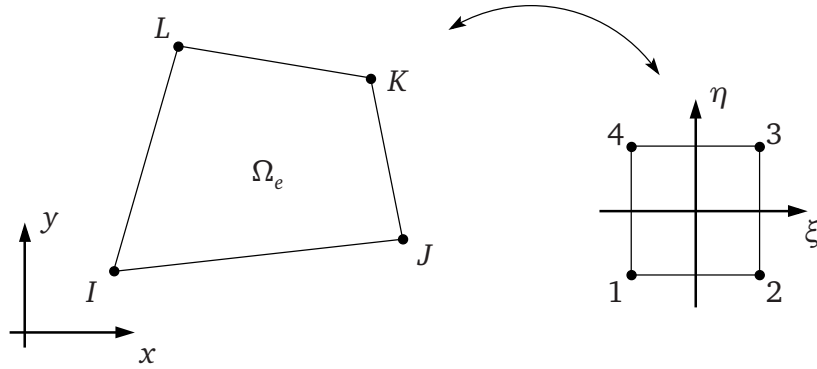


Figure 5.1: Isoparametric representation – quadrilateral element in global (left) and natural coordinates (right).

field  $s$ . In the assessment of these shape functions, also a mixed formulation, where  $N_I^s \neq N_I^{\delta s}$ , is tested. This renders a non-symmetric system matrix.

## 5.3 Isoparametric Representation and Numerical Quadrature

The discretization of arbitrarily shaped structures also requires an approximation of the geometry. The isoparametric concept makes use of the same shape functions for the representation of the element geometry as for the nodal degrees of freedom. Thus, in a 2d setting, it is convenient to define the shape functions element wise as functions of the natural coordinates  $\xi$  and  $\eta$  on the unit square  $[-1, 1] \times [-1, 1]$ . For a four noded quadrilateral element, usually the bilinear Lagrangian shape functions

$$N_i^{\text{lin}}(\xi, \eta) = \frac{1}{4}(1 + \xi_i \xi)(1 + \eta_i \eta), \quad i = 1, \dots, 4 \quad (5.45)$$

are used. Here, the subscript index  $i$  denotes the *local* node number, see Fig. 5.1. Within the element, the global coordinates  $\mathbf{x} = (x, y)$  are thus approximated by the mapping

$$\mathbf{x} = \sum_{i=1}^4 N_i^{\text{lin}}(\xi, \eta) \mathbf{x}_i, \quad (5.46)$$

where  $\mathbf{x}_i$  are the global coordinates of the element nodes. Chain rule differentiation yields the relation between the derivatives with respect to the natural coordinates,  $N_{i,\xi}^{\text{lin}}$  and  $N_{i,\eta}^{\text{lin}}$ , and the derivatives with respect to the global coordinates,  $N_{i,x}^{\text{lin}}$  and  $N_{i,y}^{\text{lin}}$ ,

## 5 Finite Element Implementation

which are needed to form the differential operator matrices in Eqs. (5.5) and (5.6).

$$\begin{aligned} \frac{\partial N_i^{\text{lin}}}{\partial \xi} &= \frac{\partial N_i^{\text{lin}}}{\partial x} \frac{\partial x}{\partial \xi} + \frac{\partial N_i^{\text{lin}}}{\partial y} \frac{\partial y}{\partial \xi} \\ \frac{\partial N_i^{\text{lin}}}{\partial \eta} &= \frac{\partial N_i^{\text{lin}}}{\partial x} \frac{\partial x}{\partial \eta} + \frac{\partial N_i^{\text{lin}}}{\partial y} \frac{\partial y}{\partial \eta} \end{aligned} \Leftrightarrow \begin{bmatrix} N_{i,\xi}^{\text{lin}} \\ N_{i,\eta}^{\text{lin}} \end{bmatrix} = \underbrace{\begin{bmatrix} x_{,\xi} & y_{,\xi} \\ x_{,\eta} & y_{,\eta} \end{bmatrix}}_{=J} \cdot \begin{bmatrix} N_{i,x}^{\text{lin}} \\ N_{i,y}^{\text{lin}} \end{bmatrix} \quad (5.47)$$

With the geometry being approximated according to Eq. (5.46), the *Jacobian matrix*  $J$  yields

$$J = \sum_{i=1}^4 \begin{bmatrix} N_{i,\xi}^{\text{lin}} x_i & N_{i,\xi}^{\text{lin}} y_i \\ N_{i,\eta}^{\text{lin}} x_i & N_{i,\eta}^{\text{lin}} y_i \end{bmatrix}. \quad (5.48)$$

Provided a correct node numbering, the mapping defined through Eq. (5.46) is invertible and preserves the orientation. Thus, the determinant of the Jacobian is positive,  $\det(J) > 0$ .

The integrals, which form the element residuals (Eqs. 5.15-5.16), the contributions to the stiffness matrix (Eqs. 5.37-5.40) and the damping matrix (Eq. 5.42), are evaluated using numerical quadrature formulas. The integration points and weights of these formulas are usually given on the interval  $[-1, 1]$ . Therefore, the integral expressions, which are all of the form

$$\int_{\Omega_e} f(x, y) dV \quad (5.49)$$

need to be transformed to the unit square  $[-1, 1] \times [-1, 1]$  before integration. With the isoparametric representation of the geometry, and the shape functions being defined on the unit square already, this is a very simple task

$$\int_{\Omega_e} f(x, y) dV = \int_{-1}^1 \int_{-1}^1 \tilde{f}(\xi, \eta) \det(J(\xi, \eta)) d\xi d\eta. \quad (5.50)$$

Using a quadrature formula with  $n_{\text{int}}$  integration points  $(\xi_p, \eta_p)$  and weights  $w_p$ , the integral is approximated by the sum

$$\int_{-1}^1 \int_{-1}^1 f(\xi, \eta) \det(J(\xi, \eta)) d\xi d\eta \approx \sum_{p=1}^{n_{\text{int}}} f(\xi_p, \eta_p) \det(J(\xi_p, \eta_p)) w_p. \quad (5.51)$$

The standard practice is the usage of Gaußian integration rules, because they use a minimal number of integration points to achieve a desired level of accuracy. If the linear Lagrangian shape functions (Eq. 5.45) are used, the Gauß quadrature with  $2 \times 2$  integration points gives a sufficiently precise approximation of the integrals. However, the special shape functions for the discretization of the crack field,

which are introduced in section 5.6, require a more precise integration scheme in order to reveal their full potential.

## 5.4 Irreversibility

The different irreversibility constraints proposed in section 4.2.2 are implemented at the element level. Therefore, the element system matrix  $\underline{\mathbf{S}}_e$  and the element residual  $\underline{\mathbf{R}}_e$  are modified if this becomes necessary. This technique is convenient, because it allows to treat both cases very similarly and avoids changing the boundary conditions in the course of the simulation.

### Damage Like Formulation

In case of the damage like formulation, where the constraint  $\dot{s} \leq 0$  enforces the irreversibility of cracking, it is checked after the first iteration step, if for any of the element's nodes  $s_{I,n+1}^{(k)}$  is larger than the value  $s_{I,n}$  of the previous time step. If this is the case, the irreversibility constraint is violated. In order to enforce the constraint numerically, the value  $s_{I,n+1}^{(k+1)}$  of the next iteration step is then *a priori* set to  $s_{I,n}$ . As this prerequisite implies that

$$\dot{s}_{I,n+1}^{(k+1)} = \frac{s_{I,n+1}^{(k+1)} - s_{I,n}}{\Delta t_n} = 0, \quad (5.52)$$

the irreversibility constraint holds in the next iteration step. In order to avoid dealing with changing boundary conditions, the desired result

$$s_{I,n+1}^{(k+1)} = s_{I,n} \quad \Leftrightarrow \quad \Delta s_{I,n+1}^{(k)} = - (s_{I,n+1}^{(k)} - s_{I,n}) \quad (5.53)$$

for the next iteration step, is implicitly attained by the following modifications of the element system matrices  $\underline{\mathbf{S}}_e$  and residuals  $\underline{\mathbf{R}}_e$ , rather than by enforcing it via boundary conditions for the crack field.

- In a first step, the column  $\underline{\mathbf{S}}_e^{[:,s_I]}$  of the system matrix  $\underline{\mathbf{S}}_e$  referring to  $s_I$  is multiplied by the difference  $s_{I,n+1}^{(k)} - s_{I,n}$  of the current iteration value  $s_{I,n+1}^{(k)}$  and the value  $s_{I,n}$  from the previous time step. The result of this multiplication is then added to the residual, i.e.

$$\underline{\mathbf{R}}_e \leftarrow \underline{\mathbf{R}}_e + (s_{I,n+1}^{(k)} - s_{I,n}) \underline{\mathbf{S}}_e^{[:,s_I]}. \quad (5.54)$$

- Next, the residual entry  $\underline{\mathbf{R}}_e^{[s_I]}$  referring to  $s_I$  is overwritten by

$$\underline{\mathbf{R}}_e^{[s_I]} = - (s_{I,n+1}^{(k)} - s_{I,n}). \quad (5.55)$$

## 5 Finite Element Implementation

- As a last step, the row  $\underline{\mathbf{s}}_e^{[s_I, :]}$  and column  $\underline{\mathbf{s}}_e^{[:, s_I]}$  of the system matrix are overwritten with zeros, and the diagonal entry  $\underline{\mathbf{s}}_e^{[s_I, s_I]}$  is set to

$$\underline{\mathbf{s}}_e^{[s_I, s_I]} = 1. \quad (5.56)$$

As a result of these manipulations, the solution  $\Delta \underline{\mathbf{d}}_{I, n+1}^{(k)}$  of the linear system of equations (Eq. 5.30) yields

$$\Delta s_{I, n+1}^{(k)} = - (s_{I, n+1}^{(k)} - s_{I, n}) \quad (5.57)$$

and thus, according to the update formula in Eq. (5.29)

$$s_{I, n+1}^{(k+1)} = s_{I, n+1}^{(k)} + \Delta s_{I, n+1}^{(k)} = s_{I, n}. \quad (5.58)$$

An alternative approach to formulate the irreversibility constraint  $\dot{s} \leq 0$  can be found in Miehe et al. [2010b]. Here, the evolution equation for  $s$  is modified by means of indicator and ramp functions in order to enforce non-positive rates  $\dot{s}$ . Thus, a subsequent modification of the stiffness matrix and residual vector is not necessary.

### Dirichlet Boundary Conditions

In Bourdin's formulation, homogeneous Dirichlet boundary conditions are imposed on the crack field in the further simulation, once a crack has been detected. In the time discretized setting, this yields the constraint

$$s_{I, n+1} = 0 \quad \text{if} \quad s_{I, n} = 0 \quad (5.59)$$

for the nodal crack field values  $s_I$  of the finite element discretization. Thus, in order to meet this requirement, in each iteration step ( $k$ ), the value  $s_{I, n+1}^{(k+1)}$  of the next iteration step is *a priori* set to zero, if  $s_{I, n} = 0$  in the previous time step. As for the damage like formulation, the constraint

$$s_{I, n+1}^{(k+1)} = 0 \quad \Leftrightarrow \quad \Delta s_{I, n+1}^{(k)} = -s_{I, n+1}^{(k)} \quad (5.60)$$

is implicitly attained through modifications of the element system matrices  $\underline{\mathbf{S}}_e$  and residuals  $\underline{\mathbf{R}}_e$ , instead of actually applying boundary conditions on the crack field. The modification steps follow the same scheme as in the damage like formulation.

- In a first step, the column  $\underline{\mathbf{S}}_e^{[:, s_I]}$  of the system matrix  $\underline{\mathbf{S}}_e$  referring to  $s_I$  is multiplied by the current iteration value  $s_{I, n+1}^{(k)}$  and added to the residual, i.e.

$$\underline{\mathbf{R}}_e \leftarrow \underline{\mathbf{R}}_e + s_{I, n+1}^{(k)} \underline{\mathbf{S}}_e^{[:, s_I]}. \quad (5.61)$$

- Next, the residual entry  $\underline{\mathbf{R}}_e^{[s_I]}$  referring to  $s_I$  is overwritten by the current iteration value,

$$\underline{\mathbf{R}}_e^{[s_I]} = -s_{I, n+1}^{(k)}. \quad (5.62)$$

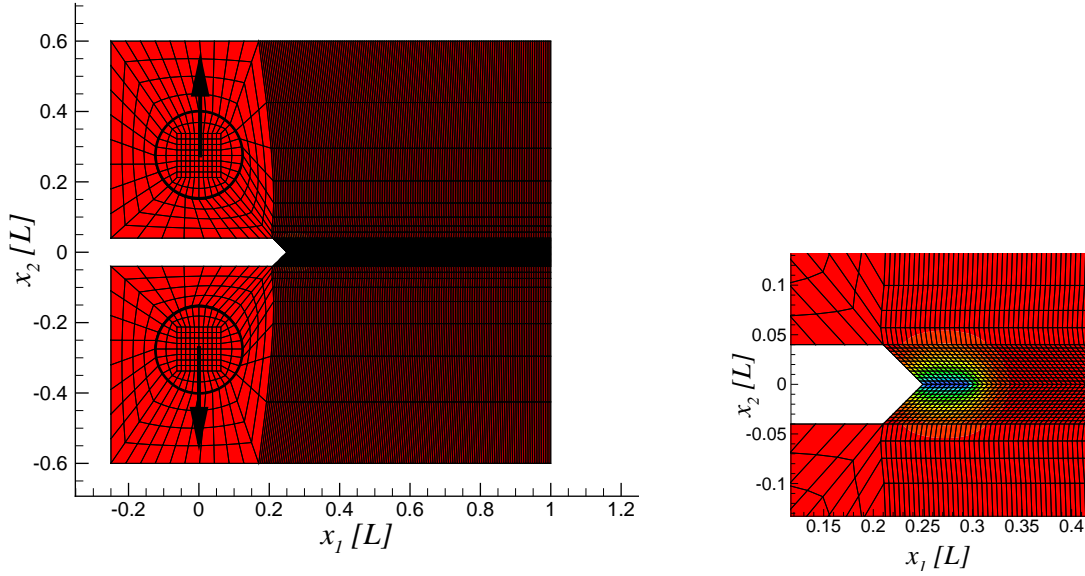


Figure 5.2: Initial contour of  $s$  and FE mesh of the CT specimen. Entire structure (left) and zoom into the notch base region with initial crack (right).

- As a last step, the row  $\underline{\mathbf{s}}_e^{[s_I, :]}$  and column  $\underline{\mathbf{s}}_e^{[:, s_I]}$  of the system matrix are overwritten with zeros, and the diagonal entry  $\underline{\mathbf{s}}_e^{[s_I, s_I]}$  is set to

$$\underline{\mathbf{s}}_e^{[s_I, s_I]} = 1. \quad (5.63)$$

Manipulated in such a manner, the system of equations (Eq. 5.30) yields a solution  $\Delta \underline{\mathbf{d}}_{I, n+1}^{(k)}$  with

$$\Delta s_{I, n+1}^{(k)} = -s_{I, n+1}^{(k)} \quad (5.64)$$

and thus

$$s_{I, n+1}^{(k+1)} = s_{I, n+1}^{(k)} + \Delta s_{I, n+1}^{(k)} = 0 \quad (5.65)$$

according to the update formula in Eq. (5.29).

## 5.5 Examples

### 5.5.1 Simulation of Cyclic Loading of a CT Specimen

The impact of the different approaches of modeling the irreversibility is analyzed in a simulation of a CT specimen under cyclic loading. Figure 5.2 shows the specimen geometry together with a contour plot of the initial crack field  $s$  and the finite element mesh used in the simulations. Along the  $x_1$ -axis, the mesh is refined to an element edge length of about  $h = 0.0045L$  in order to properly resolve the crack

## 5 Finite Element Implementation

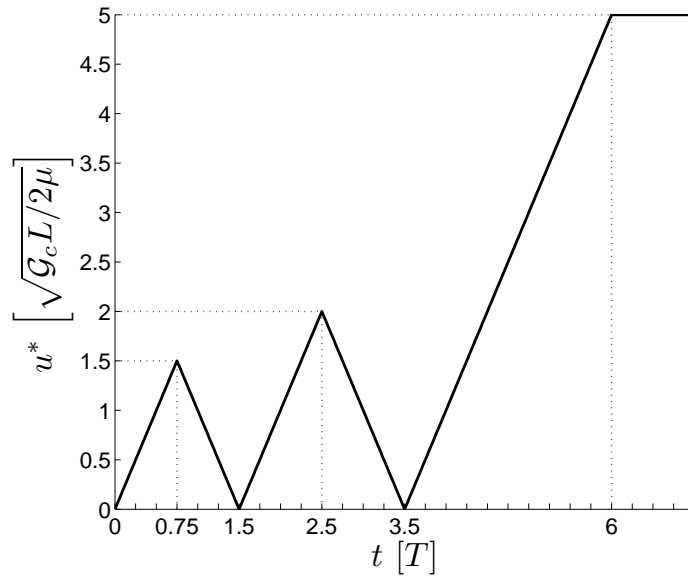


Figure 5.3: Loading history.

field for  $\epsilon = 0.01L$ . The Lamé constants of the specimen are equal ( $\lambda = \mu$ ), the residual stiffness in broken areas is set to  $\eta = 10^{-5}$ . The circular areas around the load application points are modeled as stiff by increasing the stiffness and cracking resistance by a factor of 100. A cyclic increasing displacement load  $u^*(t)$  is applied at the two loading points indicated by the arrows in Fig. 5.2. The magnitude of the loading  $u^*(t)$  is given in Fig. 5.3.

Figures 5.4 and 5.5 show the load displacement curves obtained from simulations in which irreversibility was enforced by means of Dirichlet boundary conditions at the crack set (left) and from simulations of the damage like formulation (right). The red solid lines show the reaction force at the load application points with respect to the displacement load factor  $u^*$ . For the plots of Fig. 5.4, the mobility constant was set to the rather low (compared to the loading velocity) value  $M = 1 \frac{L}{g_c T}$ . For comparison, the simulation was repeated with a higher value  $M = 10 \frac{L}{g_c T}$ , see the plots of Fig. 5.5. For both strategies of enforcing irreversibility, it can be observed that a slightly higher maximum reaction force is attained for the smaller value of the kinetic coefficient  $M$ . This is the typical effect of a viscous overstress, if the transient evolution equation is interpreted as a viscous approximation of the quasi static case, where the reciprocal  $1/M$  plays the role of the viscosity parameter. Additionally, it can be observed in both plots of Fig. 5.4, that the envelope of the load displacement curves is not a smooth function. This artificial effect is due to the delayed response of the crack field to the changing load for small values of the kinetic coefficient and disappears for sufficiently large values of  $M$ , see Fig. 5.5.

While the envelope of the load displacement curves with the respective value of the mobility constant are very similar, there are significant differences during the

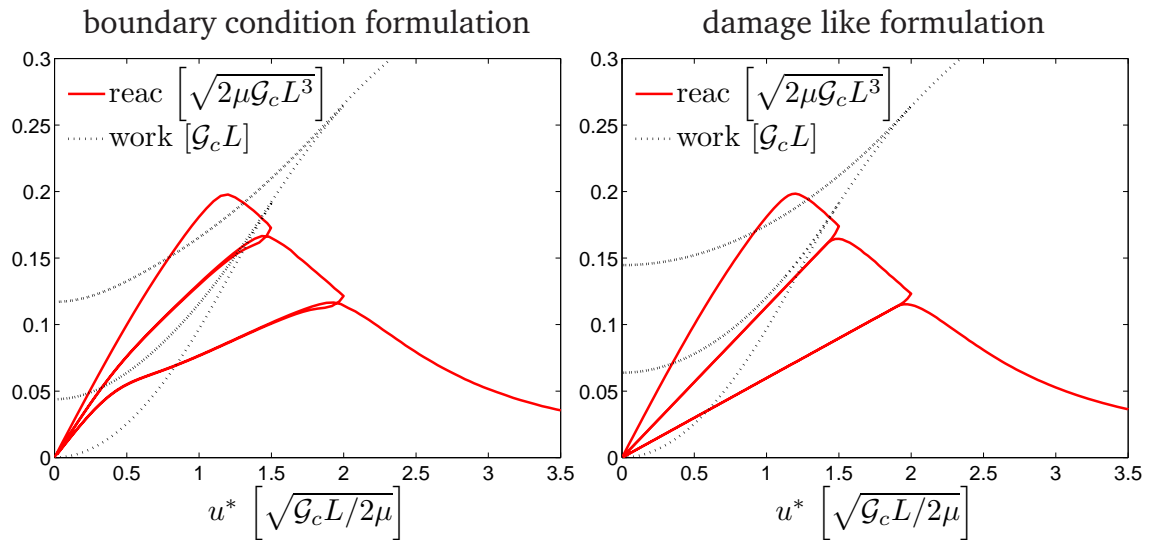


Figure 5.4: Load displacement curves for Dirichlet boundary conditions at the crack set (left) and the damage like formulation (right) with  $M = 1 \frac{L}{q_c T}$ .

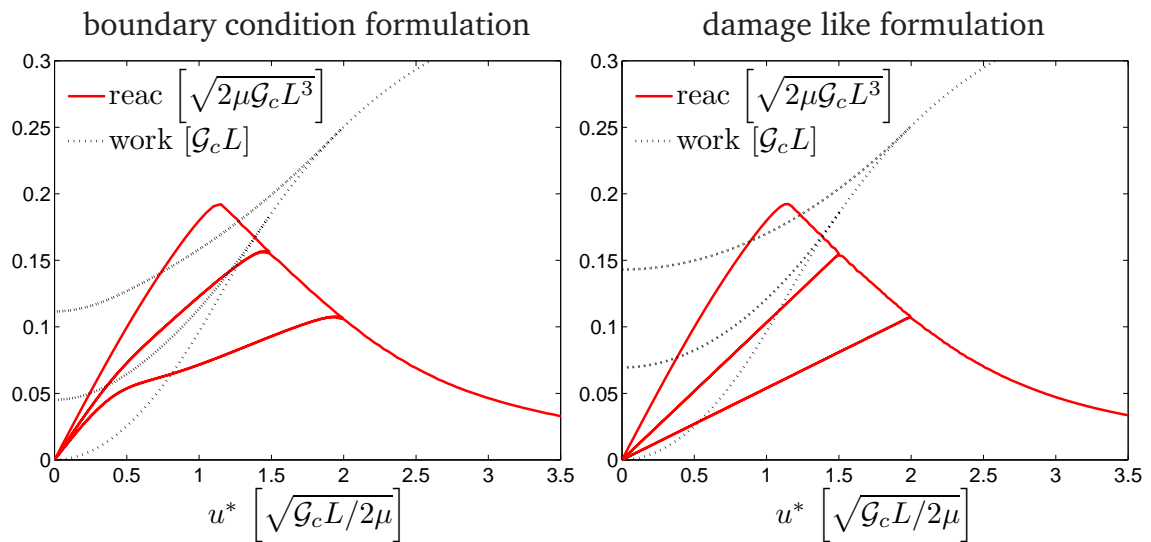


Figure 5.5: Load displacement curves for Dirichlet boundary conditions at the crack set (left) and the damage like formulation (right) with  $M = 10 \frac{L}{q_c T}$ .

## 5 Finite Element Implementation

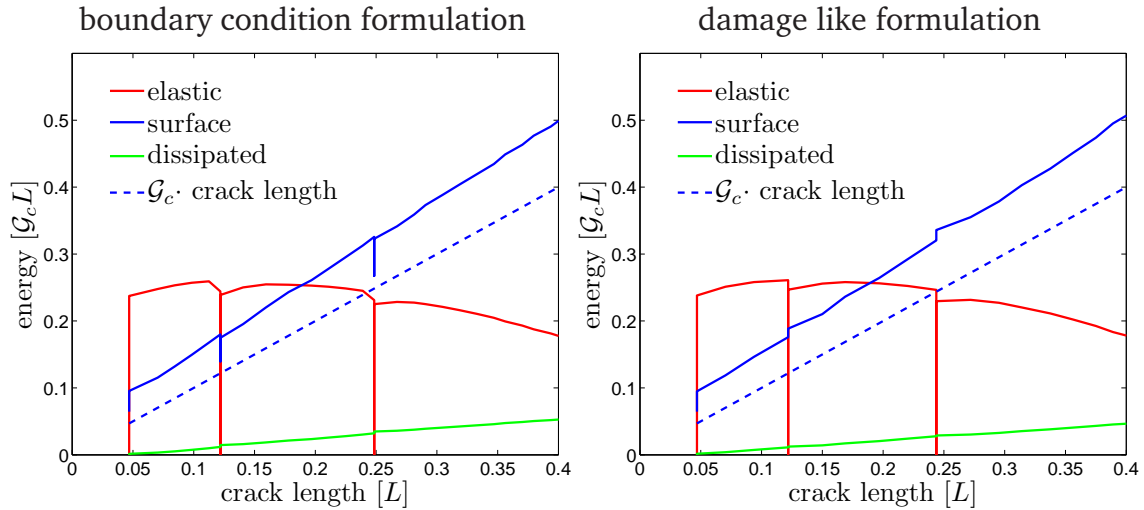


Figure 5.6: Energy evolution with respect to the crack length for Dirichlet boundary conditions at the crack set (left) and the damage like formulation (right) with  $M = 1 \frac{L}{g_c T}$ .

un- and reloading phases. In the damage like formulation, the crack field cannot recover during unloading, because the rate  $\dot{s}$  is forced to be non-positive in the entire structure. Thus, there is no evolution of the crack field during the un- and reloading phases, and the observed material response is linear elastic.

If Dirichlet boundary conditions are imposed on the crack set to model the irreversibility, the material behavior observed in the un- and reloading phases is more complex. Here, the restraints on the crack field evolution only apply at the immediate crack set, where  $s = 0$ . In the crack surrounding zone, where  $0 < s < 1$ , the crack field can recover to a certain extent during unloading. As a result of this crack field evolution, the observed material behavior is nonlinear and the material response is stiffer than in the damage like formulation.

In addition to the load displacement curves, the work performed by the reaction forces (black dotted lines) is plotted in Figs. 5.4 and 5.5. The work corresponds to the area under the load displacement curve and is computed by means of the trapezoidal rule. Resulting from the different material behavior during the unloading process, the amount of work performed after the first and second load cycle (when  $u^* = 0$ ) differs significantly for the two different formulations. At these stages, there is no elastic energy stored in the structure. Thus, except for the small amount of energy being dissipated through the crack field evolution, the work performed after a finished load cycle is equal to the surface energy of the unloaded sample. As to be expected, this energy is higher in the damage like model, where the entire crack field evolution is irreversible, than in the boundary condition formulation, where the crack field can partially recover.

The energy plots in Figs. 5.6 and 5.7 correspond to the load displacement curves of Figs. 5.4 and 5.5, respectively. They show the evolution of the different energy contributions with respect to the crack length. The crack length is obtained as the



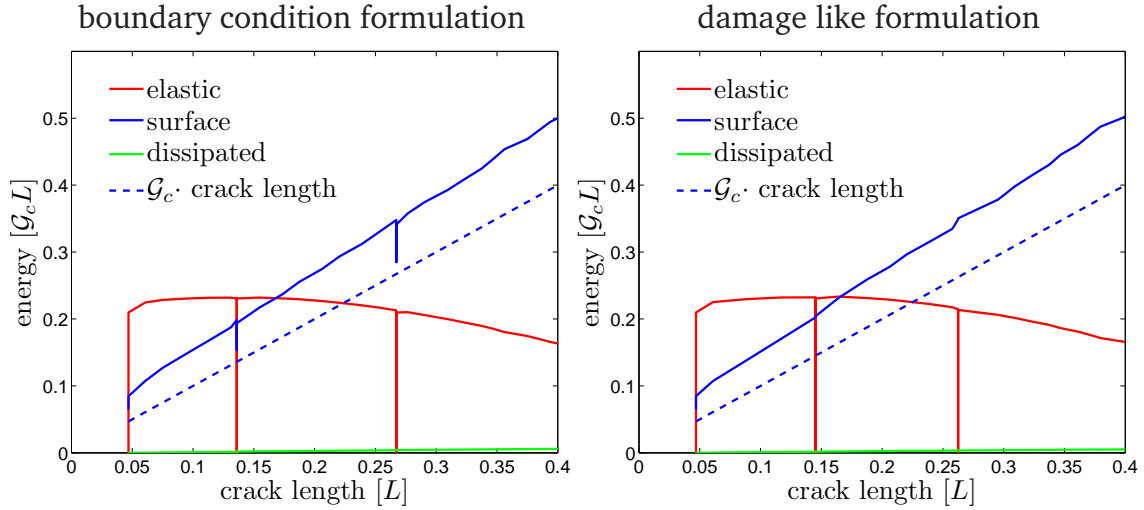


Figure 5.7: Energy evolution with respect to the crack length for Dirichlet boundary conditions at the crack set (left) and the damage like formulation (right) with  $M = 10 \frac{L}{\mathcal{G}_c T}$ .

length of the line along which the crack condition  $s = 0$  holds. At the beginning, only the elastic stored energy (red solid line) grows, while the crack length as well as the other energy contributions remain constant. When the crack starts to propagate, the elastic energy stagnates and the surface energy (blue solid line) grows approximately linearly with the crack length. The impact of the different irreversibility constraints becomes apparent during the unloading phases. For both formulations, the crack length remains constant, and the entire elastic energy is released. However, the evolution of the surface energy differs. As there is no evolution of the crack field during unloading in the damage like formulation, the surface energy remains constant until the crack propagation continues upon reloading. Thus, the surface energy increases monotonously with the crack length. This observation does not hold if irreversibility is enforced through Dirichlet boundary constraints at the crack set. Here, the surface energy decreases to some extent upon unloading. Although this partially reversible character of the surface energy may seem odd at first sight, the soundness of the approach can be reasoned based on the following observation. The minimal surface energy, which is attained in the unloaded state when  $u^* = 0$ , is a good approximation of the theoretical magnitude of the surface energy of an unloaded structure with a crack of the respective length. This theoretical value is obtained by a multiplication of the crack length with the cracking resistance  $\mathcal{G}_c$  and is indicated by the blue dashed lines. This immediate relation between the crack length and the surface energy does not reveal in the damage like formulation.

Thus, both of the proposed irreversibility constraints yield reasonable results. The proper choice of the irreversibility constraint depends on the objectives of the simulation and the interpretation of the crack field  $s$ . If  $s$  is regarded as the damage variable of a gradient damage model, accordingly the corresponding irreversibility

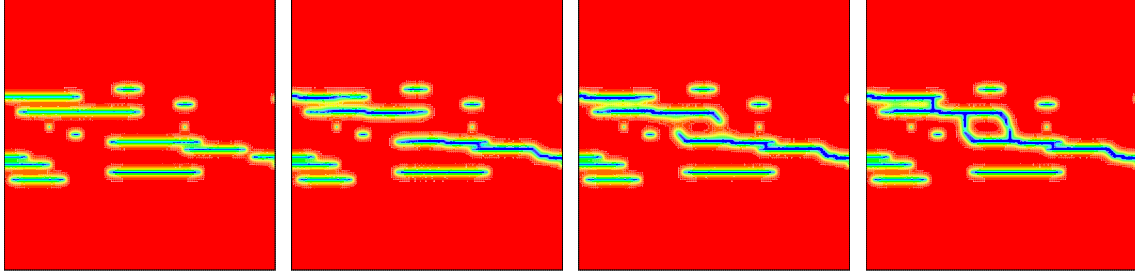


Figure 5.8: Crack interaction of an irregular arrangement of micro-cracks. Unloaded initial configuration and load stages  $\bar{t} = 1.701$ ,  $\bar{t} = 5.034$ ,  $\bar{t} = 12.14$  (from left to right).

constraint should be used. In this work however, the crack field  $s$  is regarded as a purely auxiliary quantity, introduced to indicate cracks, and the surface energy  $E^s$  is understood as an approximation of the surface energy of a sharp crack. In this regard, the modeling of irreversibility through Dirichlet boundary conditions is to be preferred and will be applied in the following.

The impact of the two different values of the kinetic coefficient  $M$  which were used in the simulations can be read off from the dissipated energy (green solid line)

$$E^{\text{dis}} = \int_0^t \mathcal{D}_{\text{loc}} d\bar{t} \quad (5.66)$$

in the plots of Figs. 5.6 and 5.7. Comparably small mobility factors like  $M = 1 \frac{L}{g_{cT}}$  introduce an artificial viscosity into the material model. This results in a considerable amount of energy being dissipated during progressive crack growth, see Fig. 5.6, which biases the competition of elastic vs. surface energy and should therefore be avoided. For  $M = 10 \frac{L}{g_{cT}}$ , the dissipated energy is negligible compared to the magnitudes of the elastic and surface energy contributions, see Fig. 5.7. There is virtually no artificial viscosity and at every load step the numerical solution is very close to the quasi static limit case.

### 5.5.2 Crack Interaction

In order to demonstrate the capabilities and the generality of the phase field method, the interaction and coarsening of an irregular arrangement of micro cracks is studied in this section. Due to the complicated stress fields around the crack tips, a range of different fracture mechanical phenomena can be observed in this example. A similar structure has been analyzed in Spatschek et al. [2006b] using a different phase field fracture model.

For the simulation, a square area of size  $2L \times 2L$  has been discretized by 20736 elements with linear shape functions. The regularization parameter is set to

$\epsilon = 0.01L$  and initial micro cracks of different sizes are modeled by applying homogeneous Dirichlet boundary conditions to the crack field at the respective locations. The left plot of Fig. 5.8 shows the stationary crack field  $s$  before any mechanical load is applied to the sample. Starting from this initial configuration, the structure is strained in perpendicular direction to the orientation of the initial cracks by a linear increasing displacement load of magnitude  $u(\bar{t}) = \sqrt{\frac{g_c L}{2\mu}} \bar{t}$ , where the load factor  $\bar{t} = t/T$  is the dimensionless time with respect to a given time scale  $T$ . In order to obtain a quasi static evolution, the mobility constant is set to a comparatively large value of  $M = 10 \frac{L}{g_c T}$ . For the elastic properties it is assumed that the Lamé constants  $\lambda$  and  $\mu$  are equal, which is equivalent to a Poisson ration of  $\nu = 0.25$ . The artificial residual stiffness in fractured zones is controlled by the constant  $\eta = 10^{-5}$ .

At a load level of  $\bar{t} = 1.701$  (second plot of Fig. 5.8) three fairly close initial cracks on the right hand side of the structure have already merged into one larger crack. From an energetic point of view, the coalescence of adjacent cracks is favorable for two reasons. First, it increases the elastic relaxation of the sample, and second, it minimizes the surface energy. Furthermore, the elastic relaxation reduces the effective crack driving forces on the other surrounding micro cracks, which consequently do not grow. Upon further loading, the two major cracks (the largest initial crack on the upper left and the crack formed by the coalescence of cracks on the lower right) mutually attract each other. Thus, instead of growing straight, the cracks kink and grow towards the other crack. This can be seen in the third plot of Fig. 5.8, showing the crack field at a load level of  $\bar{t} = 5.034$ . The coalescence of the two major cracks is fast-tracked by the formation of two new crack branches, which nucleate at a crack lip of the upper and lower principle crack and then grow towards the crack tip of counter part. The right plot of Fig. 5.8 shows the crack field at  $\bar{t} = 12.14$  just before the primary and the new crack tips meet, which leads to final rupture and the detachment of a fragment from the rest of the structure. Notably, using the phase field approach, the simulation of such difficult topological changes becomes possible without a further refinement of the method. Furthermore, the numerical implementation is very robust through the combination of an implicit time integration scheme and an automatic control of the time step size.

The finally obtained crack pattern is qualitatively in good agreement with the simulation results reported in Spatschek et al. [2006b]. However, as a double well potential is used in this reference, the phase field cracks tend to evolve into thick domains towards the later stages of the simulation. On the contrary, with the crack field potential used in this work, the crack field remains more focused along the individual cracks resulting in a more refined crack pattern.

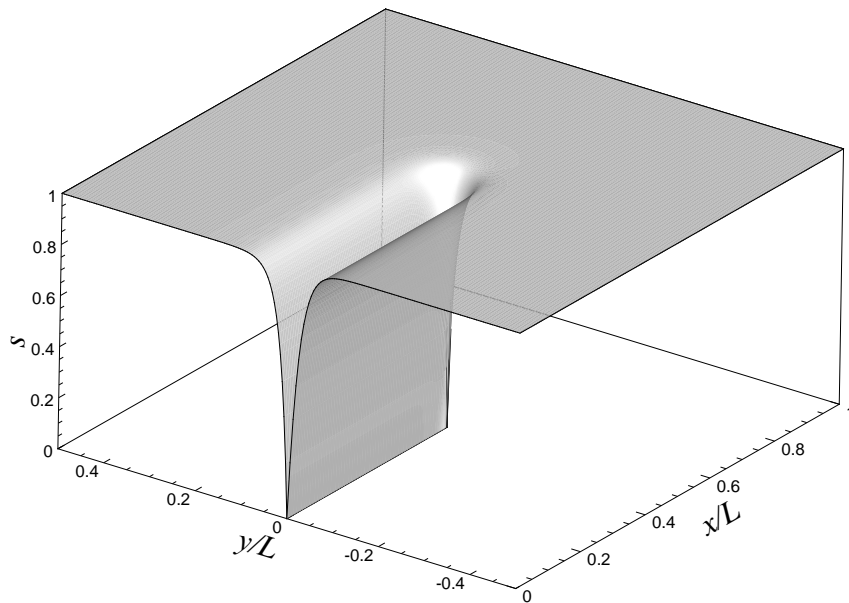


Figure 5.9: 3d representation of the phase field of a crack.

## 5.6 Exponential Shape Functions

As already seen in the analysis of the 1d case in section 4.4, the width of the transition zone, where the crack parameter  $s$  interpolates between 1 and 0 is controlled by the length scale parameter  $\epsilon$ . In order to obtain reasonable results, which do not overestimate the influence of the fractured zone, this length parameter should be chosen sufficiently small with respect to the global dimensions of the considered sample. Amor et al. [2009] propose  $1/100$  of the global geometric dimension of the sample as an appropriate value for the regularization parameter in order to represent macroscopic cracks. However, the finite element implementation of the phase field fracture model is very sensible to the choice of the regularization parameter in conjunction with the mesh size. The size of the elements forming the discretization has to be chosen sufficiently small in order to accurately resolve the steep gradients and high curvatures of the crack field in the transition zones between cracked and uncracked areas. This becomes apparent looking at the 3d representation of the crack field of an unloaded square structure of edge length  $L$  with an initial crack in Fig. 5.9. In this example, the regularization parameter  $\epsilon$  was set to  $0.01L$ . A uniform mesh with  $200 \times 200$  elements of edge length  $h = 0.005L = 0.5\epsilon$  was used for the discretization. The accurate approximation of the crack field is important to capture the surface energy and thus the thresholds and dynamics of crack propagation correctly. Bourdin et al. [2008] show that linear triangular elements of edge length  $h$  overestimate the surface energy by a factor

$$f(h/\epsilon) = 1 + h/4\epsilon, \quad (5.67)$$

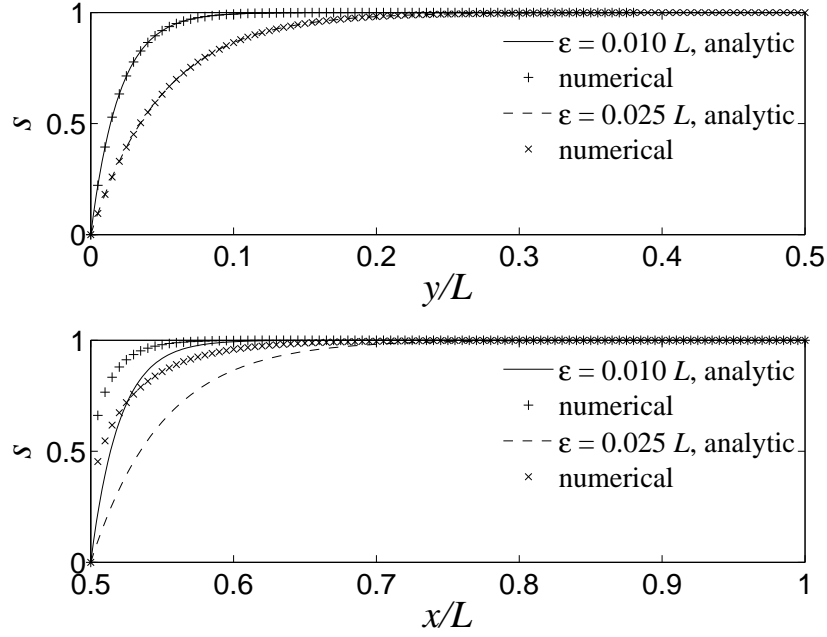


Figure 5.10: Comparison of the computed 2d phase field to the 1d solution (Eq. 4.56) at the specimen edge (top) and at the crack tip (bottom).

and hence different authors [Amor et al., 2009, Miehe et al., 2010b] empirically found  $h \approx \epsilon$  as an upper bound for the element size in a 2d setting. Thus, small values of  $\epsilon$  require a high level of mesh refinement, which is numerically demanding concerning computation time and required memory.

There are several approaches in order to meet the requirements for a sufficiently fine resolution on the one hand and to keep the computation time within bounds on the other hand. Eastgate et al. [2002] make use of Fourier transforms for the solution of the linear terms of their phase field model in order to increase the efficiency of the computations. However, this technique restricts the simulations to problems with periodic boundary conditions. Exploiting the fact that the phase field order parameter varies significantly only near an interface, adaptive remeshing strategies refine the mesh only where it is needed. This approach can be found in Provatas et al. [1998] for a phase field solidification problem or in Bourdin and Chambolle [2000] for an approximation of the Mumford-Shah functional. A material force based  $h$ -type mesh refinement strategy for phase field fracture models can be found in Welschinger et al. [2010], see also Braun [1997], Gross et al. [2003] or Mueller et al. [2004] for the underlying ideas of this technique.

In this section, a different approach introduced in Kuhn and Müller [2010c, 2011a,b] is presented. It takes advantage of the fact that the computed 2d stationary solution of the evolution equation shows the same exponential characteristic as the analytic 1d solution (Eq. 4.56). This is illustrated in Fig. 5.10, where the computed phase field values are compared to the analytic solution (Eq. 4.56)

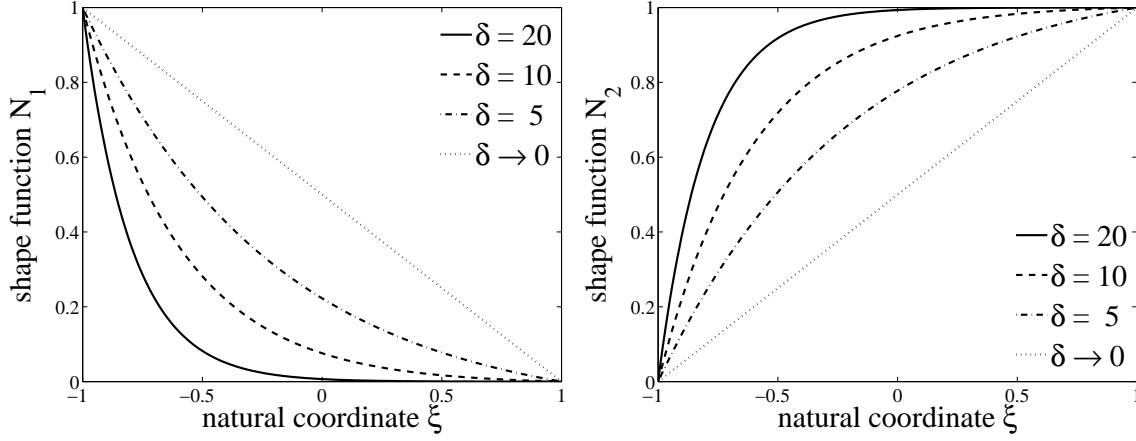


Figure 5.11: 1d exponential shape functions  $\bar{N}_1^{\text{exp}}$  (left) and  $\bar{N}_2^{\text{exp}}$  (right) at different values of  $\delta$ .

at the fractured specimen edge  $\{0\} \times [0, 0.5L]$  far behind the crack tip and in front of the crack tip along the segment  $[0.5L, L] \times \{0\}$  for two different values of  $\epsilon$ . At the specimen edge the analytic solution captures the numerically computed solution values quite perfectly, yet in front of the crack tip, the computed crack field is even steeper than the analytic solution would predict. However, the shape still resembles an exponential function and the impact of  $\epsilon$  on the solution remains the same, i.e. the smaller  $\epsilon$ , the smaller the transition zone between broken ( $s = 0$ ) and undamaged ( $s = 1$ ) material. Hence, particularly along the crack lips but also at the crack tip, special shape functions derived from the 1d solution promise a very accurate approximation of the crack field. This ansatz is inspired by LaZghab et al. [2002], who derived special finite element shape functions for the simulation of extrusion processes from analytical considerations. These simulations are faced with similar difficulties concerning the discretization as shear flow boundary layers, which are characterized by an exponential velocity profile, develop in the bearing channel during such processes.

### 5.6.1 1d Exponential Shape Functions

Adapted to the present phase field fracture model, the exponential shape functions of a two noded 1d element read

$$\begin{aligned} \bar{N}_1^{\text{exp}}(\xi, \delta) &= 1 - \frac{\exp\left(-\frac{\delta(1+\xi)}{4}\right) - 1}{\exp\left(-\frac{\delta}{2}\right) - 1} \quad \text{and} \\ \bar{N}_2^{\text{exp}}(\xi, \delta) &= \frac{\exp\left(-\frac{\delta(1+\xi)}{4}\right) - 1}{\exp\left(-\frac{\delta}{2}\right) - 1}, \end{aligned} \quad (5.68)$$

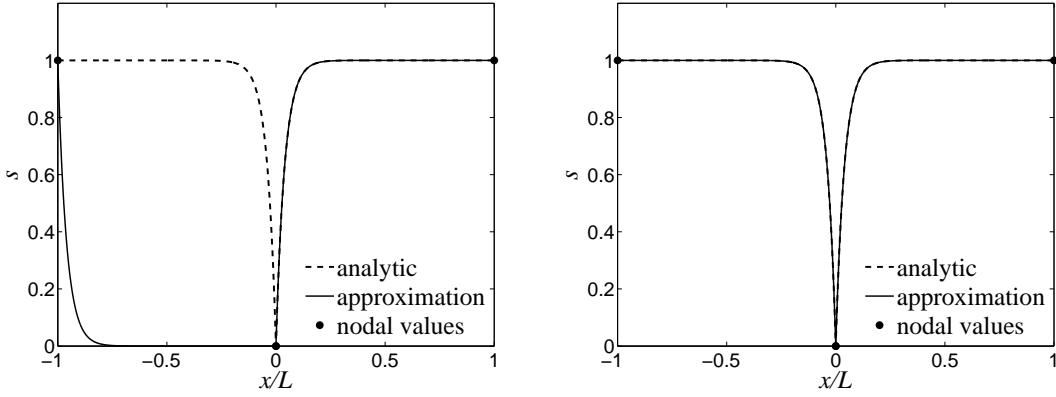


Figure 5.12: Approximation with unswitched shape functions (left), and switched shape functions (right).

where  $\xi$  is the natural coordinate defined on the interval  $[-1, 1]$ . Obviously partition of unity, i.e.  $\bar{N}_1^{\text{exp}}(\xi, \delta) + \bar{N}_2^{\text{exp}}(\xi, \delta) = 1$  holds and  $\bar{N}_i^{\text{exp}}(\xi_j, \delta) = \delta_{ij}$ , where  $\xi_1 = -1$  and  $\xi_2 = +1$  are the local element nodes. Through the ratio  $\delta = h/\epsilon$ , these exponential shape functions depend on the element size  $h$  and the regularization parameter  $\epsilon$ . This makes them adaptive to both, mesh size and regularization length. The impact of the ratio  $\delta$  on the exponential shape functions is illustrated in Fig. 5.11. For large values of  $\delta$ , the exponential character of the new shape functions is clearly visible. In the limit case  $\delta \rightarrow 0$  or equivalently  $h \rightarrow 0$  at fixed  $\epsilon$ , the exponential shape functions converge to the one dimensional linear shape functions

$$\begin{aligned} \lim_{\delta \rightarrow 0} \bar{N}_1^{\text{exp}}(\xi, \delta) &= \frac{1 - \xi}{2} = N_1^{\text{lin}}(\xi) \quad \text{and} \\ \lim_{\delta \rightarrow 0} \bar{N}_2^{\text{exp}}(\xi, \delta) &= \frac{1 + \xi}{2} = N_2^{\text{lin}}(\xi). \end{aligned} \quad (5.69)$$

Figure 5.12 shows an interpolation of the analytic solution (Eq. 4.56) for  $\epsilon = 0.025L$  with two exponential elements of size  $h = L$ . The ratio  $\delta$  is thus  $\delta = 40$ . The approximation is very good, if  $s_1 \leq s_2$  (indices indicate the local node number) holds for the nodal crack field values. However, the exponential shape functions (Eq. 5.68) do not yield a good approximation if  $s_1 > s_2$ , see left plot in Fig. 5.12. This problem arises due to the fact that the exponential shape functions are unsymmetric with respect to  $\xi$ , i.e.  $\bar{N}_1^{\text{exp}}(-\xi) \neq \bar{N}_2^{\text{exp}}(\xi)$ . In order to resolve this deficiency, the orientation of the exponential shape functions needs to be switched according to

$$\begin{aligned} N_1^{\text{exp}}(\xi) &= \begin{cases} \bar{N}_1^{\text{exp}}(\xi, \delta) & \text{if } s_1 \leq s_2 \\ \bar{N}_2^{\text{exp}}(-\xi, \delta) & \text{if } s_1 > s_2 \end{cases} \quad \text{and} \\ N_2^{\text{exp}}(\xi) &= \begin{cases} \bar{N}_2^{\text{exp}}(\xi, \delta) & \text{if } s_1 \leq s_2 \\ \bar{N}_1^{\text{exp}}(-\xi, \delta) & \text{if } s_1 > s_2 \end{cases} \end{aligned} \quad (5.70)$$



## 5 Finite Element Implementation

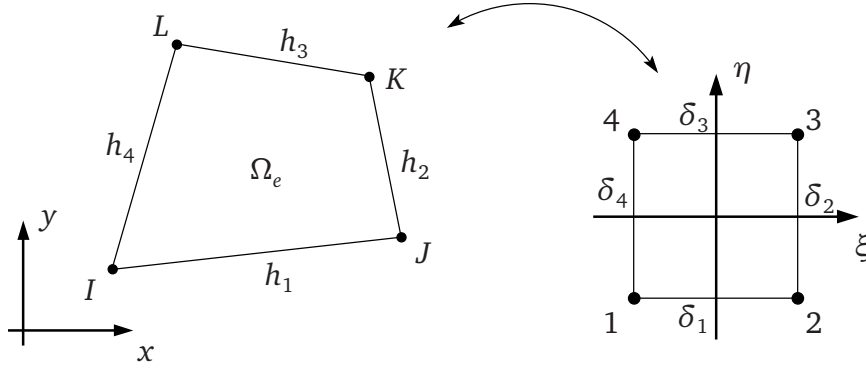


Figure 5.13: Node and edge numbering of the quadrilateral element in global (left) and natural coordinates (right).

in order to adjust to the nodal values of  $s$ . The right plot of Fig. 5.12 shows the improved approximation with the switched shape functions on the left part of the sample. The derivatives, which are required for the approximation of the gradient  $\nabla s$  of the crack field in the finite element discretization, are

$$\frac{\partial N_1^{\text{exp}}}{\partial \xi} = \frac{\delta}{4} \cdot \frac{\exp\left(-\frac{\delta(1+\xi)}{4}\right)}{\exp\left(-\frac{\delta}{2}\right) - 1} \quad \text{and} \quad \frac{\partial N_2^{\text{exp}}}{\partial \xi} = -\frac{\delta}{4} \cdot \frac{\exp\left(-\frac{\delta(1+\xi)}{4}\right)}{\exp\left(-\frac{\delta}{2}\right) - 1} \quad (5.71)$$

where  $+$  applies for  $s_1 \leq s_2$  and  $-$  for  $s_1 > s_2$ . The relation between derivatives with respect to the natural coordinate  $\xi$  and derivatives with respect to the global coordinate  $x$  follows from chain rule differentiation

$$\frac{\partial N_i^{\text{exp}}}{\partial \xi} = \frac{\partial N_i^{\text{exp}}}{\partial x} \cdot \frac{\partial x}{\partial \xi}. \quad (5.72)$$

If the geometry remains approximated by the standard linear shape functions as defined in Eq. (5.69), the last term simplifies to half the size of the element, i.e.

$$\frac{\partial x}{\partial \xi} = \sum_{i=1}^2 \frac{\partial N_i^{\text{lin}}}{\partial \xi} x_i = \frac{x_2 - x_1}{2} = \frac{h}{2}. \quad (5.73)$$

### 5.6.2 Extension to 2d

The velocity field, for which LaZghab et al. [2002] originally constructed the exponential shape functions, is exponential only in one direction. Thus, in order to obtain shape functions for a 2d quadrilateral element, it is sufficient to combine the 1d exponential shape functions with linear 1d shape functions in the second direction. For the present phase field model, this ansatz is only sufficient for the discretization of the crack lips. However, around a crack tip an exponential approximation in both spatial directions is necessary, in order to capture the shape of the crack field. Therefore, the 2d exponential shape functions are derived on the



basis of 1d exponential shape functions for both directions.

The 2d linear shape functions (Eq. 5.45) of each single element node can be obtained by multiplying the 1d linear shape functions belonging to the adjacent edges of the respective node. In a first step, this strategy is adapted to construct 2d exponential shape functions from the 1d shape functions (Eq. 5.70), introduced in the previous section. This yields

$$\begin{aligned}
 \bar{N}_1^{\text{exp}}(\xi, \eta, \delta_k) &= N_1^{\text{exp}}(\xi, \delta_1) \cdot N_1^{\text{exp}}(\eta, \delta_4), \\
 \bar{N}_2^{\text{exp}}(\xi, \eta, \delta_k) &= N_2^{\text{exp}}(\xi, \delta_1) \cdot N_1^{\text{exp}}(\eta, \delta_2), \\
 \bar{N}_3^{\text{exp}}(\xi, \eta, \delta_k) &= N_2^{\text{exp}}(\xi, \delta_3) \cdot N_2^{\text{exp}}(\eta, \delta_2), \\
 \bar{N}_4^{\text{exp}}(\xi, \eta, \delta_k) &= N_1^{\text{exp}}(\xi, \delta_3) \cdot N_2^{\text{exp}}(\eta, \delta_4),
 \end{aligned} \tag{5.74}$$

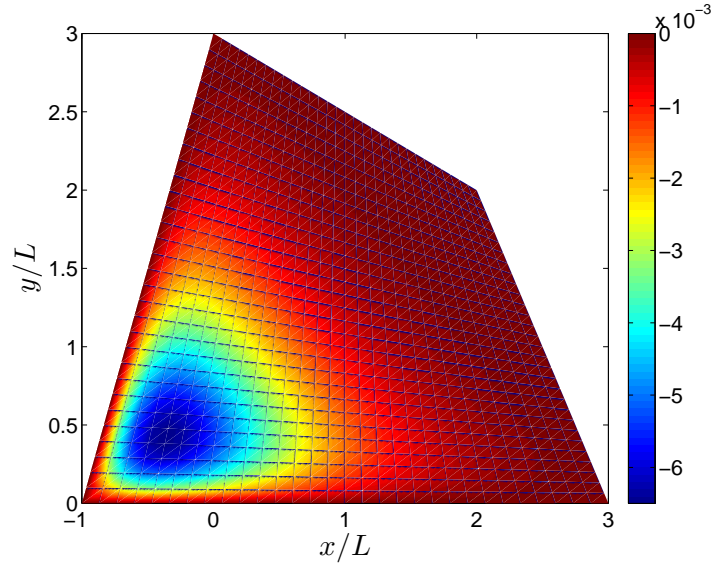
where the element nodes and the element edges are numbered according to the sketch of the element in natural coordinates  $(\xi, \eta)$  in Fig. 5.13. Each shape function depends on the ratio  $\delta_k = \frac{h_k}{\epsilon}$  of both adjacent element edges. By a slight abuse of notation, this is indicated by a  $\delta_k$  in the list of variables of the shape functions  $\bar{N}_i^{\text{exp}}$ . Concerning the orientation issue discussed in the previous section 5.6.1, it must be postulated that in Eq. (5.74) the 1d shape functions of opposite edges must have the same orientation in order to obtain an appropriate approximation behavior of the 2d shape functions. Thus, there are four admissible orientations of the 2d exponential shape functions of a quadrilateral element. The so constructed shape functions possess the Kronecker delta property, i.e.  $\bar{N}_i^{\text{exp}}(\xi_j, \eta_j, \delta_k) = \delta_{ij}$ . The aforementioned orientation issue also affects the continuity of the proposed shape functions, i.e. continuity across element edges only holds, if the orientation of the shared edge of two neighbor elements is the same. This poses further restrictions on the orientation of the elements, but this can usually be handled well, as long as the crack pattern is not too complicated. Another point of concern is the partition of unity. The summation of the four shape functions in Eq. (5.74) gives

$$\sum_{i=1}^4 \bar{N}_i^{\text{exp}}(\xi, \eta, \delta_k) = 1 - \underbrace{\left[ N_1^{\text{exp}}(\xi, \delta_1) - N_1^{\text{exp}}(\xi, \delta_3) \right] \cdot \left[ N_1^{\text{exp}}(\eta, \delta_2) - N_1^{\text{exp}}(\eta, \delta_4) \right]}_{=R(\xi, \eta, \delta_i)}. \tag{5.75}$$

Thus, partition of unity does not hold in any case. Under the constraint that the orientation of the 1d shape functions of opposite edges must be the same, the residual term  $R(\xi, \eta, \delta_k)$  vanishes whenever

$$\delta_1 = \delta_3 \quad \text{or} \quad \delta_2 = \delta_4 \tag{5.76}$$

holds. This is especially true for regular meshes consisting of only square or rectangular elements. However, for arbitrarily shaped elements, the residual term does not vanish and the partition of unity is actually violated. Figure 5.14 exemplary shows a contour plot of the residual term  $R$  of an element with the given geometry


 Figure 5.14: Contour plot of the residual term  $R$  over the global element geometry.

and  $\epsilon = 0.2L$ . The element geometry is approximated by linear shape functions according to Eq. (5.46). One can observe that the residual term is close to zero almost everywhere in the element domain. A peak of approximately  $6.5 \cdot 10^{-3}$  is located near one of the element corners. Since  $R(\xi, \eta, \delta_i)$  vanishes on the entire boundary of the unit square  $[-1, 1] \times [-1, 1]$ , it can be used to modify the shape functions according to

$$N_i^{\text{exp}}(\xi, \eta, \delta_k) = \bar{N}_i^{\text{exp}}(\xi, \eta, \delta_k) + \frac{1}{4}R(\xi, \eta, \delta_k) \quad \text{for } i = 1, \dots, 4. \quad (5.77)$$

in order to satisfy partition of unity, without affecting the continuity and Kronecker delta property of the shape functions. Furthermore one can show that  $\lim_{\delta_i \rightarrow 0} R(\xi, \eta, \delta_i) = 0$ .

The computation of the derivatives  $N_{i,\xi}^{\text{exp}}$  and  $N_{i,\eta}^{\text{exp}}$  of the exponential shape functions with respect to the natural coordinates  $\xi$  and  $\eta$  is straightforward, using the 1d derivatives in Eq. (5.71). The derivatives  $N_{i,x}^{\text{exp}}$  and  $N_{i,y}^{\text{exp}}$  with respect to the global coordinates  $x$  and  $y$  follow from the relation

$$\begin{aligned} \frac{\partial N_i^{\text{exp}}}{\partial \xi} &= \frac{\partial N_i^{\text{exp}}}{\partial x} \frac{\partial x}{\partial \xi} + \frac{\partial N_i^{\text{exp}}}{\partial y} \frac{\partial y}{\partial \xi} \\ \frac{\partial N_i^{\text{exp}}}{\partial \eta} &= \frac{\partial N_i^{\text{exp}}}{\partial x} \frac{\partial x}{\partial \eta} + \frac{\partial N_i^{\text{exp}}}{\partial y} \frac{\partial y}{\partial \eta} \end{aligned} \quad \Leftrightarrow \quad \begin{bmatrix} N_{i,\xi}^{\text{exp}} \\ N_{i,\eta}^{\text{exp}} \end{bmatrix} = \underbrace{\begin{bmatrix} x_{,\xi} & y_{,\xi} \\ x_{,\eta} & y_{,\eta} \end{bmatrix}}_{=J} \cdot \begin{bmatrix} N_{i,x}^{\text{exp}} \\ N_{i,y}^{\text{exp}} \end{bmatrix}. \quad (5.78)$$

As the geometry is approximated with linear shape functions according to Eq. (5.46), the Jacobian matrix  $J$  remains the same as introduced in Eq. (5.48).

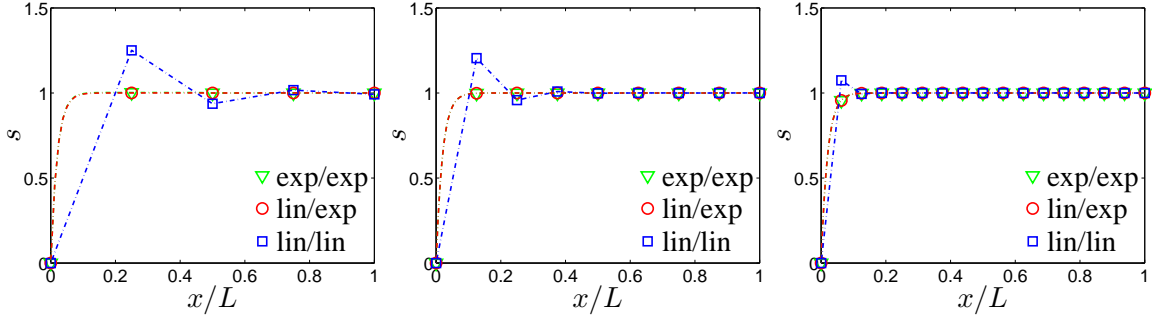


Figure 5.15: Stationary solution of the 1d evolution equation with  $n = 4$  (left),  $n = 8$  (middle) and  $n = 16$  elements (right).

### 5.6.3 Numerical Examples

The performance of the 1d and 2d exponential shape functions is tested in this section. In all simulations, linear shape functions (Eq. 5.45) were used for the approximation of the geometry  $\boldsymbol{x}$  and the actual and virtual mechanical displacements  $\boldsymbol{u}$  and  $\delta\boldsymbol{u}$ , i.e.  $N_i^u = N_i^{\delta u} = N_i^{\text{lin}}$ . For the approximation of the crack field  $s$  and its virtual counterpart  $\delta s$ , three different approximations are compared to each other: The standard approximation with linear shape functions  $N_i^s = N_i^{\delta s} = N_i^{\text{lin}}$  (labeled lin/lin), the approximation with exponential shape functions for  $s$  and  $\delta s$ ,  $N_i^s = N_i^{\delta s} = N_i^{\text{exp}}$  (labeled exp/exp), and a mixed formulation with  $N_i^s = N_i^{\text{exp}}$  but  $N_i^{\delta s} = N_i^{\text{lin}}$  (labeled lin/exp). The two formulations using the same shape functions for the actual and the virtual crack field yield a symmetric system matrix. The mixed formulation results in an unsymmetric system matrix.

#### 1d Stationary Crack Field

As a first test, the stationary crack field of the unloaded bar with crack at  $x = 0$  discussed in section 4.4.1 is computed numerically with the finite element method. The regularization parameter is set to  $\epsilon = 0.01L$ . In order to obtain a sufficiently precise approximation of the integrals, they are evaluated on each element with a 5 point Gauß quadrature rule. As no mechanical loads are applied, the problem reduces to finding a stationary solution to the 1d evolution equation. The superior performance of the exponential shape functions becomes apparent in the plots of the numerical solutions with different numbers of elements in Fig. 5.15. The markers symbolize the computed nodal values, and the dashed dotted lines indicate the interpolation of the crack field within the element with exponential or linear shape functions, respectively. Both versions using exponential shape functions for the approximation of the crack field, yield equally good results almost without any visible error. The linear shape functions fail to properly resolve the transition zone even for the smallest tested element size  $h = L/16$ .

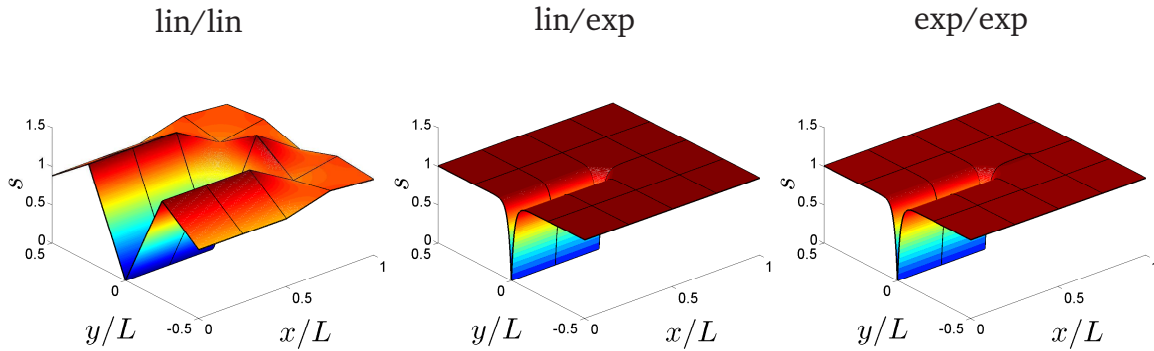


Figure 5.16: Comparison of the crack field for  $\epsilon = 0.01L$  computed with  $4 \times 4$  elements.

### Crack Field and Surface Energy of an Unloaded Crack in 2d

For the first numerical assessment of the 2d exponential shape functions, the different combinations of shape functions for the crack field are now tested on the example introduced at the beginning of this section (see Fig. 5.9). As in the 1d example, no mechanical loads are applied in this test. The problem thus reduces to solving the evolution equation (Eq. 4.33) under the constraint  $s(x, y) = 0$  if  $(x, y) \in [0, L/2] \times \{0\}$  and Neumann boundary conditions  $\nabla s \cdot \mathbf{n} = 0$  on the boundary of the considered area  $[0, L] \times [-L/2, L/2]$ . A regular mesh with square elements is used for the discretization. Thus, the condition in Eq. (5.76) holds and the correction term, needed to ensure partition of unity for arbitrarily shaped elements, is not considered in this simulation. If the exponential shape functions are used, the orientation of the elements must be chosen appropriately with respect to the location of the crack. This requires to use differently oriented elements on the positive and on the negative  $y$ -half-plane. Figure 5.16 shows the crack field for  $\epsilon = 0.01L$  computed with only  $4 \times 4$  elements ( $\delta_i = 25$ ) and  $5 \times 5$  Gauß points per element. With such a coarse mesh, the standard approach using linear shape functions only, fails to give a reasonable solution. However, both computations using the exponential shape functions yield already qualitatively very good results, which are at first sight almost identical. Only directly in front of the crack tip the result from the mixed formulation (lin/exp) is even a bit more accurate.

The plots in Fig. 5.17 show the surface energy  $E^s$  associated with the computed crack field for  $\epsilon = 0.01L$  (left) and  $\epsilon = 0.002L$  (right). Meshes within the range of  $2 \times 2$  to  $400 \times 400$  elements were used for the discretization. Again, the Gauß rule with 5 integration points per direction is used for the numerical integration in each element. The results are compared to the error estimate (Eq. 5.67) for triangular elements with linear shape functions (black dotted line). The performance of the tested linear shape functions is slightly better than it is to be expected from the error estimate. However, especially for discretizations with only few elements both versions using the exponential shape functions perform significantly better. Even if a very coarse mesh is used the surface energy is only slightly underestimated, while

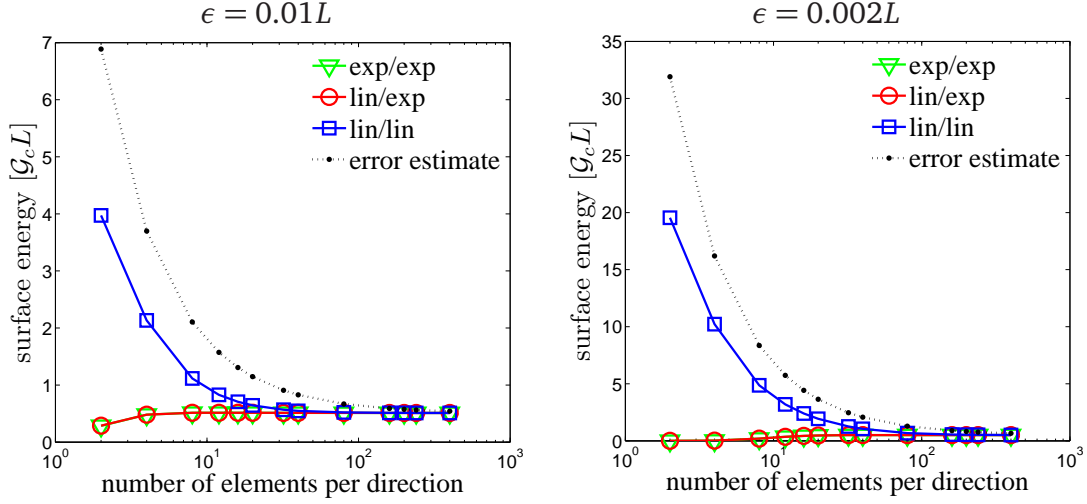


Figure 5.17: Surface energy computed with  $5 \times 5$  Gauß points for  $\epsilon = 0.01L$  (left) and  $\epsilon = 0.002L$  (right).

$\epsilon$	$0.01L$	$0.002L$
$E^s$	$0.51017344300 \mathcal{G}_c L$	$0.50241252899 \mathcal{G}_c L$

Table 5.1: Reference values for the surface energy.

the solution with linear shape functions overestimates it by far. This is even more significant for the smaller value of  $\epsilon$ .

For a further assessment of the exponential shape functions, the relative error of the surface energy is evaluated in Fig. 5.18 for  $\epsilon = 0.01L$  (left) and  $\epsilon = 0.002L$  (right). In order to test the influence of the numerical integration on the performance of the exponential shape functions, the number of Gauß points per direction is varied from 2 (top), to 5 (middle), to 10 (bottom). The reference values for the surface energy of the crack field for  $\epsilon = 0.01L$  and  $\epsilon = 0.002L$  are given in Table 5.1. They are obtained with standard linear shape functions and a non-uniform mesh with square elements of edge length  $h = 7.1429 \cdot 10^{-4}L$  for  $\epsilon = 0.01L$  and  $h = 4.8828 \cdot 10^{-4}L$  for  $\epsilon = 0.002L$  in the vicinity of the crack. Again, the performance of the linear shape functions is slightly better than the error estimate (Eq. 5.67, black dotted line) predicts. The exponential shape functions yield a significantly smaller error than the linear shape functions, yet their full potential only reveals itself if a sufficiently precise quadrature method is employed. Especially if the ratio  $\delta$  of the element size  $h$  and the regularization parameter  $\epsilon$  is large, a higher number of integration points significantly scales down the error in the surface energy computed with exponential shape functions. Thus, a major part of the error is due to the quadrature error. The choice of the quadrature method is therefore crucial for the performance of the exponential shape functions. On the performance of the linear shape functions, the number of Gauß points has practically no impact. Here, the error is actually due to the fact that the shape functions cannot resolve the

## 5 Finite Element Implementation

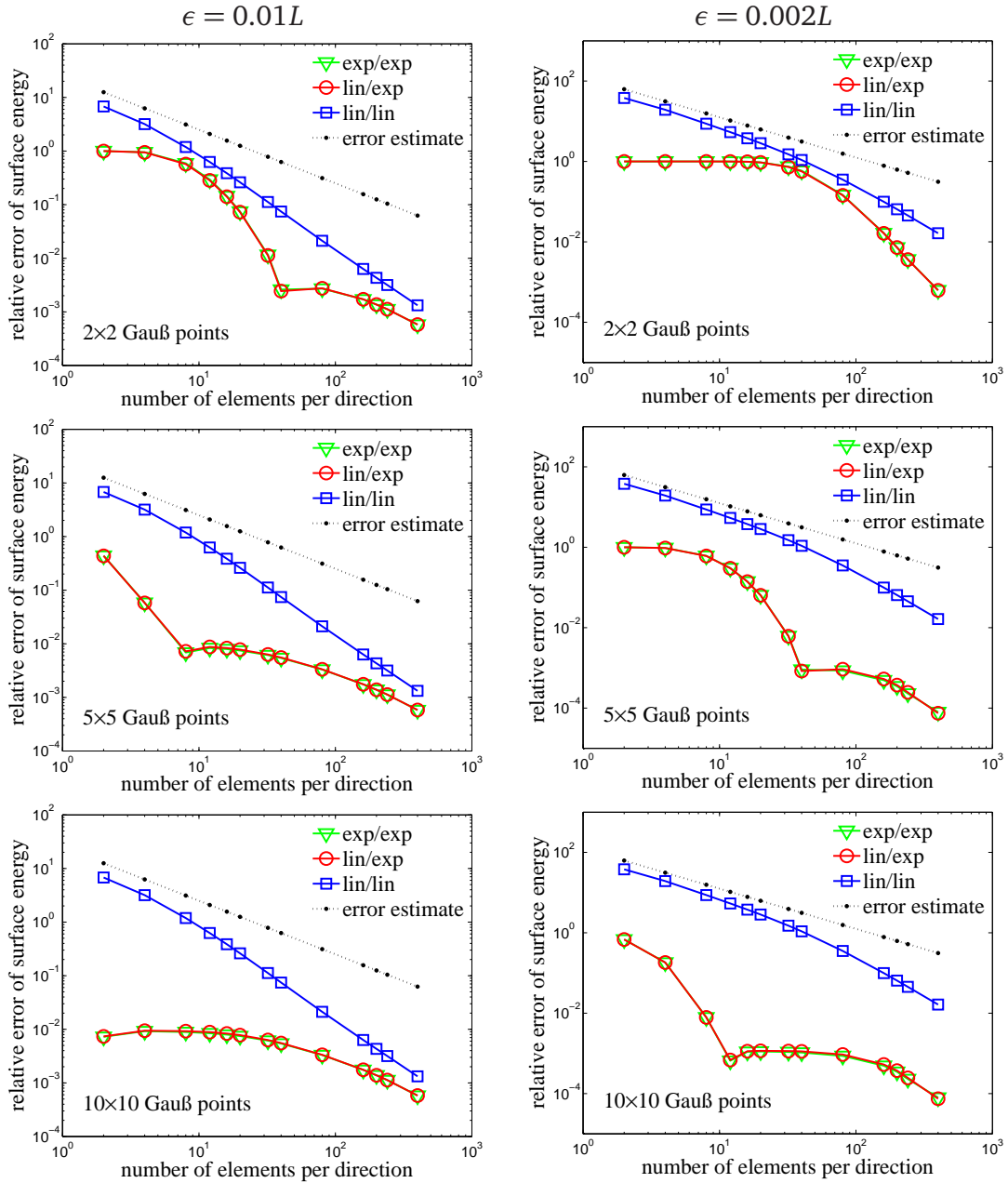


Figure 5.18: Relative error of the surface energy with different numbers of Gauß points (top:  $2 \times 2$ , middle:  $5 \times 5$ , bottom:  $10 \times 10$ ) for  $\epsilon = 0.01L$  (left) and  $\epsilon = 0.002L$  (right).

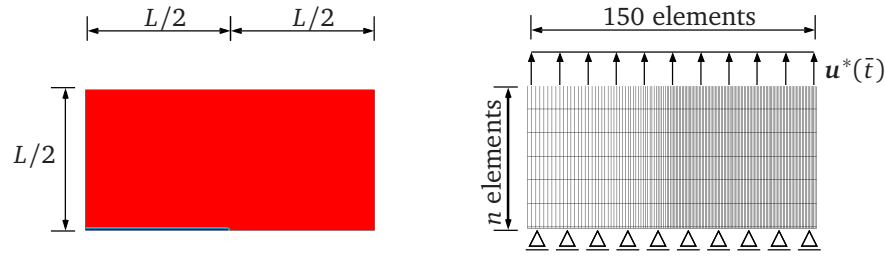


Figure 5.19: Simulation setup of the peel of test: contour plot of initial crack field (left) and finite element mesh (right).

crack field. From the kink in the curves referring to the exponential shape functions, one can derive a rule of thumb for the choice of an adequate number of quadrature points. The number of Gauß points per direction should be greater than  $\sqrt{2\delta}$  in order to take full advantage of the exponential shape functions.

### Peel Off Test

In this simulation the performance of the exponential shape functions is tested under mechanical loading, i.e. the whole set of coupled equations has to be solved. The mixed formulation (lin/exp) yields an unsymmetric system matrix, which is computationally more expensive. As in the previous simulations, the results obtained by the pure exponential formulation (exp/exp) are very similar, the mixed formulation is dismissed in the following. The sample depicted in Fig. 5.19 is loaded by a linearly increasing displacement load  $\mathbf{u}^*(\bar{t}) = \sqrt{\frac{\mathcal{G}_c L}{2\mu}} \bar{t}$ , where  $\bar{t} = t/T$  is a dimensionless load factor. The dimensional analysis of section 4.3 shows that with this scaling of the displacements, the geometric length  $L$  and the cracking resistance  $\mathcal{G}_c$  can be factored out of the equations. The mobility  $M$  is chosen large enough to assume quasi static cracking ( $M = 10^9 \frac{L}{\mathcal{G}_c T}$ ). The solution of the coupled problem thus predominantly depends on the ratio of the Lamé constants  $\lambda/\mu = 1$  and the regularization parameter  $\epsilon = 0.0005L$  in conjunction with  $L$ . The discretization consists of 150 elements in  $x$ -direction and a varying number of  $n$  elements in  $y$ -direction, and the Gauß rule with  $5 \times 5$  quadrature points is used for the numerical integration. Along the presumed crack path along the bottom edge of the sample, one extra layer of thin elements is introduced. This is necessary, because the linear shape functions used for the discretization of the displacement field otherwise cannot properly model the opening of the initial crack. As the crack is located at one edge of the sample, the same orientation can be used for all exponential elements of the discretization. Again, the correction term of the exponential shape functions does not need to be taken into account, because the mesh consists of rectangular elements only.

The two left plots in Fig. 5.20 show the evolution of the elastic energy with respect to the load factor  $\bar{t}$  for different values of  $n$ . The elastic energy increases with



## 5 Finite Element Implementation

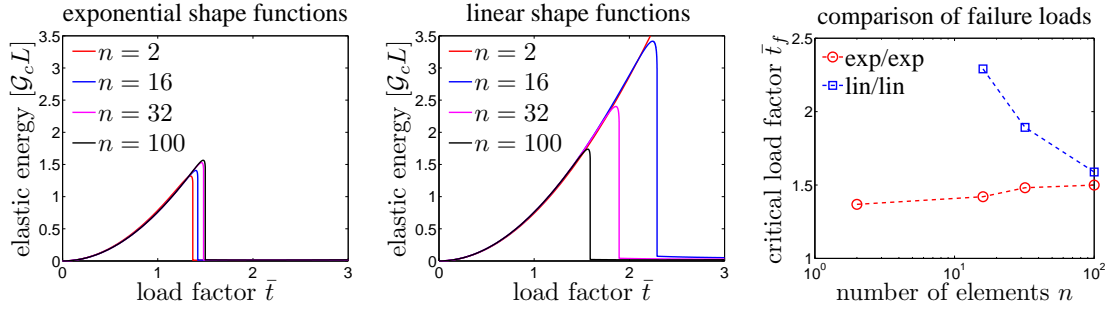


Figure 5.20: Elastic energy obtained with exponential/linear shape functions (left/middle), and comparison of failure loads (right).

the loading until rupture occurs and it drops to zero. Impressively, the simulation with only  $n = 2$  elements in  $y$ -direction already gives a qualitatively good result, when the exponential shape functions are employed. Using the standard linear shape functions, no rupture is observed in the simulation with  $n = 2$  elements up to a load factor of  $t = 3$ , which is about twice the actual critical loading. Also the simulation with  $n = 16$  elements still overestimates the critical loading by far. Only the simulations with more elements produce as accurate results as the simulations with the exponential shape functions. The right plot of Fig. 5.20 compares the computed failure loads. The overestimation of the critical load value of the linear shape functions stems from the overestimation of the surface energy associated with the initial crack, which was observed in the previous section.

### Crack Propagation

In this test, the exponential shape functions are used to simulate crack propagation in the structure depicted in Fig. 5.21. The sample has an initial crack at the notch ground and is loaded by a linearly increasing displacement load  $\mathbf{u}^*(\bar{t}) = \sqrt{\frac{g_c L}{2\mu}} \bar{t}$ . The regularization length is set to  $\epsilon = 0.0007L$ , the ratio of the Lamé constants is  $\lambda/\mu = 1$  and the mobility is set to  $M = 10 \frac{L}{g_c T}$ . Again, the fracture zone is discretized with a fixed number of elements in  $x$ -direction and different degrees of refinement in  $y$ -direction. The numerical integration is performed with  $5 \times 5$  quadrature points in each element. Just as in the previous example, one thin extra row of elements needs to be introduced to allow proper crack opening in  $y$ -direction. In contrast to the previous examples, the mesh is not regular and thus the correction term needs to be taken into account. The orientation of the exponential elements must be chosen differently on the positive and on the negative  $y$ -half-plane in order to get a correct orientation with respect to the crack location.

The right plot in Fig. 5.21 shows the evolution of the elastic energy with respect to a linear increasing displacement load. The solid line curves refer to the exponential shape functions – dashed line curves refer to the linear shape functions. Crack propagation is indicated by a drop of the elastic energy. In contrast to the previous example, where brutal failure occurs, the crack grows rather slowly in this simula-



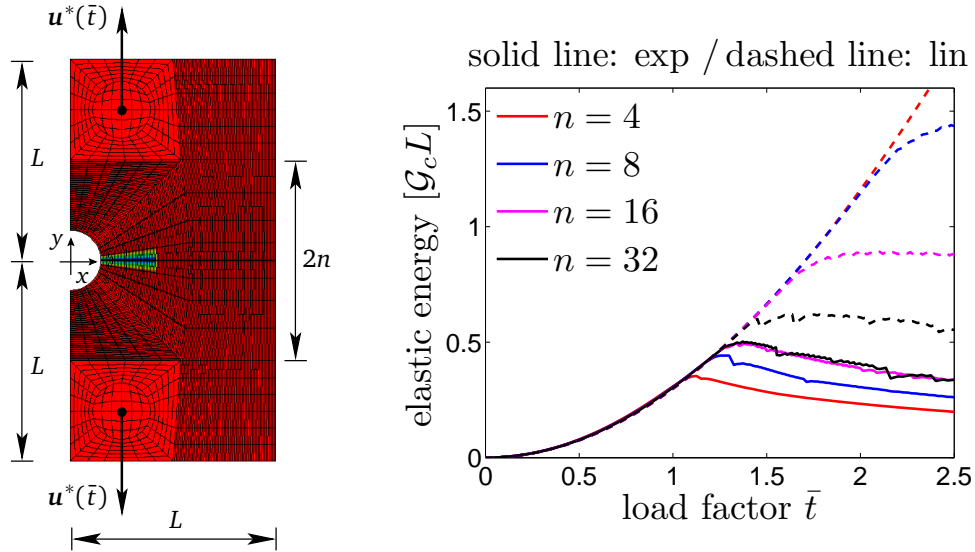


Figure 5.21: Contour plot of initial crack field and finite element mesh (left), elastic energy (right).

tion, i.e. the decrease of the elastic energy is moderate. The simulation affirms the findings from the previous examples. Too few linear elements highly overestimate the surface energy. This leads to a delayed onset of crack propagation. If exponential elements are used, a much lower degree of mesh refinement is necessary to attain the same level of precision as attained with linear elements.

#### 5.6.4 Summary and Outlook

As an alternative to an expensive mesh refinement in cases where the length parameter  $\epsilon$  is very small, special finite element shape functions have been introduced for the 1d and for the 2d setting. These shape functions are derived in such a way that they capture the exponential character of the analytical solution of the 1d stationary evolution equation. As the exponential terms of these shape functions are controlled by the length parameter of the phase field model, they are able to adjust to the shape of the crack field, which depends on this parameter in a similar way. This adaptive property of the exponential shape functions allows computations with virtually arbitrarily small values of the length parameter, which would require an extensive mesh refinement, when standard linear shape functions are used.

The effectiveness of the exponential shape functions has been tested in several numerical simulations. Especially if only the stationary evolution equation is solved, but also if the whole coupled problem of mechanical force balance and the evolution equation is considered, the usage of the exponential shape functions allowed a considerable reduction of the level of refinement without compromise on the accuracy of the results. Additionally, it turned out that the standard linear shape functions generally overestimate the surface energy by far, if the discretization is too coarse, while the exponential shape functions only slightly underestimate the exact

value. As a result of this, more elastic energy is needed to initialize crack growth if linear shape functions are used, i.e. the critical load value is overestimated. The exponential shape functions on the other hand tend to underestimate the failure load, which can be regarded as another advantage seeking for a reliable prediction of the integrity of a structure.

However, when it comes to the simulation of crack nucleation, the exponential shape functions do not yield better results than the standard linear shape functions. This is due to the fact that prior to the formation of a new crack, the crack field does not show its characteristic exponential shape which is adapted by the exponential shape functions. Only if a crack is already present, the usage of exponential shape functions is advantageous.

Two different approaches of incorporating the exponential shape functions in the finite element scheme have been tested. The mixed formulation with exponential shape functions only for the crack field itself and linear shape functions for the test functions seems to yield slightly more accurate results than the purely exponential formulation. Yet the prize to pay is an unsymmetric system matrix, causing a significant increase in computation time and required memory. In this regard, the purely exponential formulation is to be preferred.

If linear shape functions are employed, the quadrature error in the computation of the residuals and the system matrix is not significant. However, it plays an important role concerning the performance of the exponential shape functions. The standard integration scheme using 2 Gauß quadrature points per direction fails to approximate the integrals sufficiently precise if there are large gradients in the crack field and the ratio  $\delta = h/\epsilon$  of element length and regularization length becomes too large. In such cases, a more exact quadrature method with more integration points should be employed, in order to reveal the full potential of the exponential shape functions. However, the evaluation at a higher number of quadrature points increases the computation time and is only necessary where the ratio  $\delta$  is large and high gradients of  $s$  occur. Thus, an automatic choice of a reasonable number of quadrature points in conjunction with  $\delta$  and the magnitude of  $\nabla s$  would be useful.

So far, in simulations with the elements with exponential shape functions, the adequate orientation of the elements with respect to the crack position has to be defined a priori. Thus, the simulations are restricted to simple cases, where the crack path is known in advance. However, the considered phase field model naturally contains the possibility to simulate also complicated crack paths including crack initiations and crack branching. In order to make the exponential shape functions applicable to more general scenarios, the development a stable algorithm that, if necessary, re-defines the orientation of the exponential elements after every time step is essential. The exponential shape functions are especially adequate to approximate the crack field in fractured zones. In undamaged zones, where the crack field is almost constant, the linear shape functions perform equally well. Due to the exponential terms

involved and the necessity of using higher order quadrature rules, the evaluation of the exponential shape functions is computationally more expensive than the evaluation of linear shape functions. Therefore they should only be employed where they are needed, i.e. in the vicinity of cracks. A combination of both raises the problem of constructing blending elements which blend elements with exponential shape functions to those with linear shape functions. The difficulty here is to preserve continuity and partition of unity properties of the shape functions in the blending zones. This problem similarly occurs in XFEM approaches, if enriched elements are to be connected with unenriched ones, see e.g. Chessa et al. [2003].

In the presented ansatz, the focus was laid on improving the shape functions for the crack field. However, also the displacement field features high gradients around the cracks, which also cannot be captured by the linear shape functions if the mesh is too coarse. Thus, further room for improvement lies in enhancing the shape functions used for the approximation of the displacement field. A possible ansatz going in this direction would be the construction of a 9 node element, combining exponential shape functions with 3 nodes per direction, which were also introduced in LaZghab et al. [2002], with quadratic Lagrange shape functions for the displacement field.

Another very recent approach to an improved spatial discretization of phase field fracture models, is an isogeometric discretization based on NURBS and T-splines, which is proposed in Borden et al. [2012]. The smoothness of the isogeometric basis functions is anticipated to have some favorable effects. For example, an improved approximation of the mechanical stresses has been reported in Verhoosel et al. [2011] for a gradient damage model, which is similar to the phase field fracture model at hand.

## 5 *Finite Element Implementation*

# 6 Configurational Forces in the Context of Phase Field Models

The concept of configurational forces, outlined in section 3.5 for linear elastic materials, can be generalized for inelastic material behavior in a straightforward way by taking into account the dependence of the energy density on the additional field variables. For different classes of materials, this can be found e.g. in Maugin [1993], Denzer [2006], Näser et al. [2007]. For a phase field fracture model, similar to the one discussed in the work at hand, a generalized configurational force balance is discussed in Hakim and Karma [2009]. However, a numerical evaluation of the configurational forces is not given in this reference. In this chapter, the concept of configurational forces is generalized to the present phase field formulation. Relations between the generalized configurational forces and the crack evolution in the phase field model are derived and verified in numerical simulations. Preliminary results, restricted to the case of stationary cracks, are reported in Kuhn and Müller [2010a] and Kuhn and Müller [2010b]. First results, including the case of a propagating crack, can be found in Kuhn and Müller [2011c].

Within the scope of a FE analysis, configurational forces are mostly computed to determine the migration of different kinds of defects, see e.g. Kolling et al. [2003], Gross et al. [2003], Goy [2010]. It should be emphasized that they play a slightly different role in the context of a phase field fracture model. Here, the fracture process is entirely determined through the solution of the coupled field equations of the model, and no further criteria for the crack evolution need to be derived. Thus, the computation of configurational forces is actually not necessary in this context. Their benefit may be justified by two reasons. First, it is not very obvious, that the crack evolution in the phase field model is consistent with the energetic considerations of the underlying variational framework described in Francfort and Marigo [1998]. At this point, the concept of configurational forces provides a better understanding of the energetic driving mechanisms behind the evolution of cracks in the phase field model. Second, the configurational forces allow to estimate the criticality of a crack before the onset of crack propagation. Solely from the solution of the phase field problem, one can only observe whether or not a crack does grow under the applied loading.

## 6.1 Generalized Configurational Force Balance

In order to derive a generalization of the configurational force balance (Eq. 3.30), suited for the phase field fracture model, the energy density  $\psi$  is considered as a function of the linearized strain tensor  $\boldsymbol{\varepsilon}$ , the crack field  $s$ , its gradient  $\nabla s$ , the location  $\mathbf{x}^{\text{tip}}$  of the crack and the position  $\mathbf{x}$ . In index notation it reads

$$\psi = \hat{\psi}(\varepsilon_{ij}, s, s_{,j}, x_i^{\text{tip}}, x_i). \quad (6.1)$$

Chain rule differentiation of  $\psi$  yields

$$\psi_{,k} = \frac{\partial \hat{\psi}}{\partial \varepsilon_{ij}} \varepsilon_{ij,k} + \frac{\partial \hat{\psi}}{\partial s} s_{,k} + \frac{\partial \hat{\psi}}{\partial s_{,j}} s_{,jk} + \frac{\partial \hat{\psi}}{\partial x_i^{\text{tip}}} (x_i^{\text{tip}})_{,k} + \frac{\partial \hat{\psi}}{\partial x_k} \Big|_{\text{expl}}. \quad (6.2)$$

Using the identity in Eq. (3.20) and the relation

$$\begin{aligned} \frac{\partial \hat{\psi}}{\partial s} s_{,k} + \frac{\partial \hat{\psi}}{\partial s_{,j}} s_{,jk} &= \frac{\partial \hat{\psi}}{\partial s} s_{,k} + \left( \frac{\partial \hat{\psi}}{\partial s_{,j}} s_{,k} \right)_{,j} - \left( \frac{\partial \hat{\psi}}{\partial s_{,j}} \right)_{,j} s_{,k} \\ &= \left( \frac{\partial \hat{\psi}}{\partial s} - \left( \frac{\partial \hat{\psi}}{\partial s_{,j}} \right)_{,j} \right) s_{,k} + \left( \frac{\partial \hat{\psi}}{\partial s_{,j}} s_{,k} \right)_{,j}, \end{aligned} \quad (6.3)$$

Eq. (6.2) yields

$$\begin{aligned} \psi_{,k} &= (\sigma_{ij} u_{i,k})_{,j} - \sigma_{ij,j} u_{i,k} + \left( \frac{\partial \hat{\psi}}{\partial s} - \left( \frac{\partial \hat{\psi}}{\partial s_{,j}} \right)_{,j} \right) s_{,k} + \left( \frac{\partial \hat{\psi}}{\partial s_{,j}} s_{,k} \right)_{,j} \\ &\quad + \frac{\partial \hat{\psi}}{\partial x_i^{\text{tip}}} (x_i^{\text{tip}})_{,k} + \frac{\partial \hat{\psi}}{\partial x_k} \Big|_{\text{expl}}. \end{aligned} \quad (6.4)$$

Using the local balance law for the physical forces (Eq. 2.42) and the evolution equation for the crack field  $s$  in the format

$$\dot{s} = -M \frac{\delta \hat{\psi}}{\delta s} = -M \left( \frac{\partial \hat{\psi}}{\partial s} - \left( \frac{\partial \hat{\psi}}{\partial s_{,j}} \right)_{,j} \right), \quad (6.5)$$

Eq. (6.4) can be rearranged to

$$\left( \psi \delta_{kj} - \sigma_{ij} u_{i,k} - \frac{\partial \hat{\psi}}{\partial s_{,j}} s_{,k} \right)_{,j} + \frac{\dot{s}}{M} s_{,k} - f_i u_{i,k} - \frac{\partial \hat{\psi}}{\partial x_i^{\text{tip}}} (x_i^{\text{tip}})_{,k} - \frac{\partial \hat{\psi}}{\partial x_k} \Big|_{\text{expl}} = 0, \quad (6.6)$$

which forms a generalization

$$\tilde{\Sigma}_{k,j} + \tilde{g}_k = 0 \quad (6.7)$$

of the classical configurational force balance (Eq. 3.27) for the *generalized Eshelby stress tensor*

$$\tilde{\Sigma}_{kj} = \psi \delta_{kj} - \sigma_{ij} u_{i,k} - \frac{\partial \hat{\psi}}{\partial s_{,j}} s_{,k} \quad (6.8)$$

and the *generalized configurational volume force*

$$\tilde{g}_k = \frac{\dot{s}}{M} s_{,k} - f_i u_{i,k} - \frac{\partial \hat{\psi}}{\partial x_i^{\text{tip}}} (x_i^{\text{tip}})_{,k} - \frac{\partial \hat{\psi}}{\partial x_k} \Big|_{\text{expl.}} \cdot \quad (6.9)$$

In symbolic notation, Eqs. (6.7)-(6.9) read

$$\text{div } \tilde{\Sigma} + \tilde{g} = \mathbf{0}, \quad (6.10)$$

$$\tilde{\Sigma} = \psi \mathbf{1} - (\text{grad } \mathbf{u})^T \boldsymbol{\sigma} - \nabla s \otimes \frac{\partial \hat{\psi}}{\partial \nabla s}, \quad (6.11)$$

where the symbol  $\otimes$  denotes the dyadic product and

$$\tilde{g} = \underbrace{\frac{\dot{s}}{M} \nabla s}_{\tilde{g}^{\text{dis}}} - \underbrace{(\text{grad } \mathbf{u})^T \mathbf{f}}_{=\tilde{g}^{\text{vol}}} - \underbrace{(\text{grad } \mathbf{x}^{\text{tip}})^T \frac{\partial \hat{\psi}}{\partial \mathbf{x}^{\text{tip}}}}_{=\tilde{g}^{\text{tip}}} - \underbrace{\frac{\partial \hat{\psi}}{\partial \mathbf{x}} \Big|_{\text{expl.}}}_{\tilde{g}^{\text{inh}}}. \quad (6.12)$$

Compared to the classical Eshelby tensor and configurational volume forces, new terms arise due to the dependency of the energy density functional  $\psi$  on the phase field parameter  $s$ . Their impact will be discussed in the next section. A similar analysis for the phase field fracture model introduced in Karma et al. [2001] can be found in Hakim and Karma [2009].

## 6.2 Relations to Crack Propagation

In order to find a physical interpretation of the supplementary terms in the configurational force balance, a mode I loading scenario for a straight crack as depicted in Fig. 6.1 is investigated in the following. The crack faces are assumed to be traction free and no volume forces  $\mathbf{f}$  or material inhomogeneities are present. Thus, the configurational volume force contributions  $\tilde{g}^{\text{vol}}$  and  $\tilde{g}^{\text{inh}}$  vanish, and the conditions for path independence of the  $\mathcal{J}$ -integral are given. From the configurational force balance (Eq. 6.10) and the definition of the configurational volume force contributions in Eq. (6.12), it follows that the configurational force acting on the crack tip can be calculated as

$$\tilde{G}^{\text{tip}} = \int_{\mathcal{D}} \tilde{g}^{\text{tip}} dV = \int_{\mathcal{D}} (-\text{div } \tilde{\Sigma} - \tilde{g}^{\text{dis}}) dV = \int_{\mathcal{D}} (-\text{div } \tilde{\Sigma}^e - \text{div } \tilde{\Sigma}^s - \tilde{g}^{\text{dis}}) dV, \quad (6.13)$$

where

$$\tilde{\Sigma}^e = \psi^e \mathbf{1} - (\text{grad } \mathbf{u})^T \boldsymbol{\sigma} \quad (6.14)$$

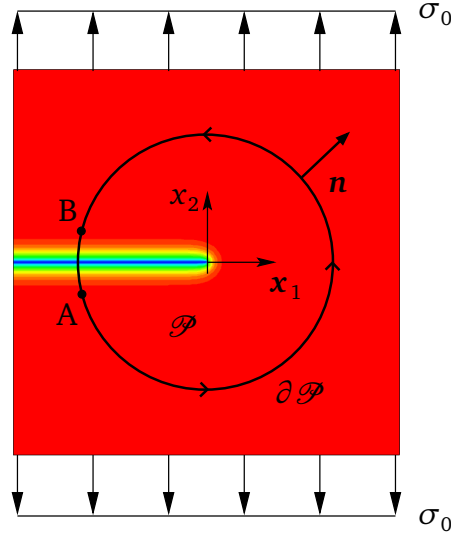


Figure 6.1: Contour of the crack field with integration domain.

is the elastic part of the generalized Eshelby tensor and

$$\tilde{\Sigma}^s = \psi^s \mathbf{1} - \nabla s \otimes \frac{\partial \hat{\psi}}{\partial \nabla s} = \psi^s \mathbf{1} - 2\mathcal{G}_c \epsilon \nabla s \otimes \nabla s \quad (6.15)$$

denotes the surface part. For convenience, a circle centered at the crack tip, is chosen as the integration domain.

### 6.2.1 Elastic Forces and the $\mathcal{J}$ -Integral

For the interpretation of the elastic part

$$\tilde{\mathbf{G}}^e = \int_{\mathcal{P}} -\text{div} \tilde{\Sigma}^e dV \quad (6.16)$$

of the configurational force acting on the crack tip, the divergence theorem is employed to transform the volume integral into a contour integral

$$\tilde{\mathbf{G}}^e = \int_{\partial \mathcal{P}} -\tilde{\Sigma}^e \mathbf{n} ds = - \int_{\partial \mathcal{P}_{A \rightarrow B}} \tilde{\Sigma}^e \mathbf{n} ds - \int_{\partial \mathcal{P}_{B \rightarrow A}} \tilde{\Sigma}^e \mathbf{n} ds. \quad (6.17)$$

As usual, the vector  $\mathbf{n}$  denotes the outer normal vector to the domain  $\mathcal{P}$ . The contour  $\partial \mathcal{P}$  is split into a large circle  $\partial \mathcal{P}_{A \rightarrow B}$  around the crack tip and a segment  $\partial \mathcal{P}_{B \rightarrow A}$  traversing the crack as depicted in Fig. 6.1. The points A and B on the contour  $\partial \mathcal{P}$  are chosen close to each other from a macroscopic point of view, but with a distance larger than the transition zone of the crack field  $s$ . From the presumption of traction free crack faces, together with the observation that the elastic energy vanishes in the fractured zone ( $\psi^e = 0$ ), it can be concluded that  $\tilde{\Sigma}^e \mathbf{n}$  vanishes on the



segment  $\partial \mathcal{P}_{B \rightarrow A}$ . On the contour  $\partial \mathcal{P}_{A \rightarrow B}$ , the crack field is approximately constant and equal to one ( $s \equiv 1$ ) and thus, the elastic part of the generalized Eshelby tensor equals the classical Eshelby tensor as defined in Eq. (3.28), i.e.

$$\tilde{\mathbf{G}}^e = - \int_{\partial \mathcal{P}_{A \rightarrow B}} \tilde{\Sigma}^e \mathbf{n} \, ds = - \int_{\partial \mathcal{P}_{A \rightarrow B}} \Sigma \mathbf{n} \, ds. \quad (6.18)$$

An evaluation of the relation in Eq. (3.32) in the present setting yields that the  $x_2$ -component vanishes and that the  $x_1$ -component is equal to the  $\mathcal{J}$ -integral modulo a change of sign

$$\tilde{G}_1^e = -\mathcal{J}. \quad (6.19)$$

Thus, the elastic contribution to the configurational force  $\tilde{\mathbf{G}}^e$  may be regarded as the negative of the crack extension force.

### 6.2.2 Cohesive Forces

The same consideration as in the previous section for the elastic part is now carried out for the surface contribution to the configurational force

$$\tilde{\mathbf{G}}^s = \int_{\mathcal{D}} -\text{div} \tilde{\Sigma}^s \, dV = \int_{\partial \mathcal{D}} -\tilde{\Sigma}^s \mathbf{n} \, ds = - \int_{\partial \mathcal{P}_{A \rightarrow B}} \tilde{\Sigma}^s \mathbf{n} \, ds - \int_{\partial \mathcal{P}_{B \rightarrow A}} \tilde{\Sigma}^s \mathbf{n} \, ds. \quad (6.20)$$

It can easily be verified that the surface part  $\tilde{\Sigma}^s$  of the generalized Eshelby tensor (Eq. 6.15) vanishes where  $s \equiv 1$ . Thus, there is no contribution to  $\tilde{\mathbf{G}}^s$  on the contour  $\partial \mathcal{P}_{A \rightarrow B}$ . Provided that the segment  $\partial \mathcal{P}_{B \rightarrow A}$  across the crack is sufficiently far away from the crack tip, the crack field is constant in  $x_1$ -direction and has the same shape as the 1d solution (Eq. 4.56) in  $x_2$ -direction

$$s(x_1, x_2) \Big|_{\partial \mathcal{P}_{B \rightarrow A}} = 1 - \exp\left(-\frac{|x_2|}{2\epsilon}\right). \quad (6.21)$$

The surface part  $\tilde{\Sigma}^s$  of the generalized Eshelby tensor (Eq. 6.15), corresponding to this solution is

$$\tilde{\Sigma}^s \Big|_{\partial \mathcal{P}_{B \rightarrow A}} = \begin{pmatrix} \psi^s & 0 \\ 0 & 0 \end{pmatrix} \quad (6.22)$$

with

$$\psi^s = \frac{\mathcal{G}_c}{2\epsilon} \exp\left(\frac{|x_2|}{\epsilon}\right). \quad (6.23)$$

If the circular domain  $\mathcal{D}$  is sufficiently large with respect to the size of the transition zone, the outer normal vector  $\mathbf{n}$  may be regarded as constant,

$$\mathbf{n} = \begin{pmatrix} -1 \\ 0 \end{pmatrix}, \quad (6.24)$$

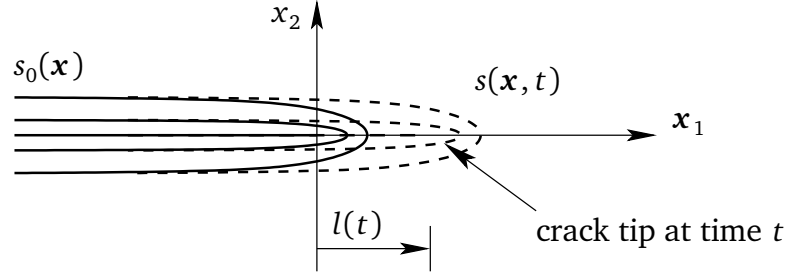


Figure 6.2: Contour lines of  $s$  around the crack – initial state (solid line) and advanced crack (dashed line).

on the crack traversing segment  $\partial \mathcal{P}_{B \rightarrow A}$ . Finally, all the previous considerations yield

$$\tilde{\mathbf{G}}^s = - \int_{\partial \mathcal{P}_{B \rightarrow A}} \tilde{\Sigma}^s \mathbf{n} \, ds = - \int_{\partial \mathcal{P}_{B \rightarrow A}} \begin{pmatrix} -\psi^s \\ 0 \end{pmatrix} ds = \int_{\partial \mathcal{P}_{B \rightarrow A}} \begin{pmatrix} \psi^s \\ 0 \end{pmatrix} ds = \begin{pmatrix} \mathcal{G}_c \\ 0 \end{pmatrix}, \quad (6.25)$$

where the energy integral has been evaluated with the help of Eq. (4.57). As the crack resistance  $\mathcal{G}_c$  is a constant material parameter, it can be expected that this portion of the configurational forces remains constant upon loading in the simulations. Furthermore, it can be observed that the surface force  $\tilde{\mathbf{G}}^s$  acts in the opposite direction of the crack driving elastic force  $\tilde{\mathbf{G}}^e$ . Thus, it can be interpreted as a crack resistance force or, following the interpretation of Hakim and Karma [2009], as a force exerted by cohesive forces in the process zone.

### 6.2.3 Dissipative Forces

The dissipative part of the configurational force is defined as

$$\tilde{\mathbf{G}}^{\text{dis}} = \int_{\mathcal{P}} -\tilde{\mathbf{g}}^{\text{dis}} \, dV = \int_{\mathcal{P}} -\frac{\dot{s}}{M} \nabla s \, dV. \quad (6.26)$$

In order to derive relations to the crack tip velocity and the dissipation  $\mathcal{D}_{\text{loc}}$ , the alteration of the crack field during the fracture process is analyzed. It is assumed, that the crack field maintains its original shape  $s_0$  and is only shifted in  $x_1$ -direction when the crack grows, see Fig. 6.2. Thus, the crack field at time  $t$  can be expressed through the initial crack field function  $s_0(\mathbf{x})$  and the function  $l(t)$  which describes the position of the crack tip at time  $t$

$$s(\mathbf{x}, t) = s_0(x_1 - l(t), x_2). \quad (6.27)$$

Differentiation with respect to  $x_1$  and  $t$ , respectively, yields

$$s_{,1} = \frac{ds}{dx_1} = s_{0,1}(x_1 - l(t), x_2) \quad (6.28)$$

$$\begin{aligned} \text{and} \quad \dot{s} &= \frac{ds}{dt} = \nabla_{s_0}(x_1 - l(t), x_2) \cdot \frac{d}{dt}(x_1 - l(t), x_2) \\ &= -s_{0,1}(x_1 - l(t), x_2) v^{\text{tip}}(t), \end{aligned} \quad (6.29)$$

where  $v^{\text{tip}}(t) = \frac{dl(t)}{dt}$  is the velocity of the crack tip. Equations (6.28)-(6.29) can be summarized to the relation

$$\dot{s}(\mathbf{x}, t) = -v^{\text{tip}}(t) \cdot s_{,1}(\mathbf{x}, t). \quad (6.30)$$

Two conclusions can be drawn on the basis of this relation. First, multiplication of Eq. (6.30) with the ratio  $\frac{\dot{s}}{M}$  and integration over the domain  $\mathcal{D}$  yields

$$\int_{\mathcal{D}} \frac{\dot{s}^2}{M} dV = \int_{\mathcal{D}} -v^{\text{tip}} \frac{\dot{s} s_{,1}}{M} dV = v^{\text{tip}} \int_{\mathcal{D}} -\frac{\dot{s} s_{,1}}{M} dV. \quad (6.31)$$

The left hand side of this equation equals the local dissipation as defined in Eq. (4.21). The integral on the right hand side is the  $x_1$ -component of the dissipative configurational force

$$\mathcal{D}_{\text{loc}} = v^{\text{tip}} \tilde{G}_1^{\text{dis}}. \quad (6.32)$$

Second, multiplication of Eq. (6.30) with the factor  $-\frac{s_{,1}}{M}$  and subsequent integration over  $\mathcal{D}$  yields

$$\int_{\mathcal{D}} -\frac{\dot{s} s_{,1}}{M} dV = \int_{\mathcal{D}} \frac{v^{\text{tip}}}{M} (s_{,1})^2 dV = \frac{v^{\text{tip}}}{M} \int_{\mathcal{D}} (s_{,1})^2 dV \quad (6.33)$$

and hence

$$v^{\text{tip}} = \frac{M \tilde{G}_1^{\text{dis}}}{\beta} \quad \text{with} \quad \beta = \int_{\mathcal{D}} (s_{,1})^2 dV. \quad (6.34)$$

The derived relations (Eq. 6.32 and 6.34) are useful, because they permit to compute the crack tip velocity solely from quantities which are already known from the solution of the phase field problem. Otherwise the position of the crack tip must be tracked in a laborious post-processing procedure in order to determine the velocity of the crack tip.

## 6.2.4 Implementation into FEM

The computation of discrete configurational nodal forces within a finite element program is very similar to the evaluation of physical nodal forces, which is implemented in virtually every finite element code. The procedure outlined here is an adaption of the technique introduced in Mueller et al. [2002] and Gross et al.

[2003] to the present phase field fracture model. In order to be able to verify the physical interpretations of the elastic, surface, and dissipative configurational forces from the previous section in FE simulations, the different nodal force contributions are computed separately.

Starting point of the FE implementation is a weak formulation of the generalized configurational force balance (Eq. 6.10). With vectorial test functions  $\boldsymbol{\eta}$ , vanishing on the boundary of the considered domain  $\Omega$ , the weak formulation reads

$$\int_{\Omega} (\operatorname{div} \tilde{\boldsymbol{\Sigma}} + \tilde{\boldsymbol{g}}) \cdot \boldsymbol{\eta} \, dV = 0, \quad (6.35)$$

and the standard procedure of integration by parts yields

$$\int_{\Omega} (-\tilde{\boldsymbol{\Sigma}} : \operatorname{grad} \boldsymbol{\eta} + \tilde{\boldsymbol{g}} \cdot \boldsymbol{\eta}) \, dV = 0. \quad (6.36)$$

In the following, the matrix notations

$$\underline{\boldsymbol{\eta}} = \begin{bmatrix} \eta_1 \\ \eta_2 \end{bmatrix}, \quad \underline{\tilde{\boldsymbol{g}}} = \begin{bmatrix} \tilde{g}_1 \\ \tilde{g}_2 \end{bmatrix} \quad \text{and} \quad \underline{\tilde{\boldsymbol{\Sigma}}} = \begin{bmatrix} \tilde{\Sigma}_{11} & \tilde{\Sigma}_{12} \\ \tilde{\Sigma}_{21} & \tilde{\Sigma}_{22} \end{bmatrix} \quad (6.37)$$

are used for the test functions, the configurational volume force and the generalized Eshelby tensor in a 2d setting. Within the finite element framework, approximations of the generalized Eshelby tensor

$$\underline{\tilde{\boldsymbol{\Sigma}}}_h = \psi_h \mathbf{1} - \underline{\nabla} \mathbf{u}_h \underline{\boldsymbol{\sigma}}_h - 2\mathcal{G}_c \epsilon \underline{\nabla} s_h \underline{\nabla} s_h^T \quad (6.38)$$

and the dissipative parts of the configurational volume force

$$\underline{\tilde{\boldsymbol{g}}}_h^{\text{dis}} = \frac{\dot{s}_h}{M} \underline{\nabla} s_h \quad (6.39)$$

are obtained from the approximate quantities  $(\cdot)_h$  as introduced in section 5.1. In the absence of physical volume forces and material inhomogeneities, the total configurational volume force is given by

$$\underline{\tilde{\boldsymbol{g}}}_h = \underline{\tilde{\boldsymbol{g}}}_h^{\text{tip}} + \underline{\tilde{\boldsymbol{g}}}_h^{\text{dis}}. \quad (6.40)$$

However, the crack tip contribution  $\underline{\tilde{\boldsymbol{g}}}_h^{\text{tip}}$  cannot be computed directly. With the approximations in Eqs. (6.38)-(6.40) and replacing the test functions  $\boldsymbol{\eta}$  by the interpolation

$$\underline{\boldsymbol{\eta}}_h = \sum_{I=1}^N N_I \underline{\boldsymbol{\eta}}_I \quad (6.41)$$

of the nodal values  $\underline{\eta}_I$  with shape functions  $N_I$ , Eq. (6.36) can be written as

$$\sum_{I=1}^N \underline{\eta}_I^T \left[ \int_{\Omega} \left( -\underline{\tilde{\Sigma}}_h \underline{\mathbf{B}}_I + \underline{\tilde{\mathbf{g}}}_h N_I \right) dV \right] = 0, \quad (6.42)$$

where  $\underline{\mathbf{B}}_I$  is the differential operator

$$\underline{\mathbf{B}}_I = \begin{bmatrix} N_{I,1} \\ N_{I,2} \end{bmatrix}. \quad (6.43)$$

The standard argument, that Eq. (6.42) must hold for any choice of  $\underline{\eta}_I$  leads to the discrete version of the configurational force balance

$$\int_{\Omega} \left( -\underline{\tilde{\Sigma}}_h \underline{\mathbf{B}}_I + \underline{\tilde{\mathbf{g}}}_h N_I \right) dV = \underline{\mathbf{0}} \quad \text{for} \quad I = 1, \dots, N. \quad (6.44)$$

Herein, each single equation defines the discrete configurational force acting on the respective FE node  $I$ . Splitting the generalized Eshelby tensor and the configurational volume force into the different contributions yields the discrete counterpart of Eq. (6.13), which naturally introduces the nodal crack tip, elastic, cohesive and dissipative configurational forces  $\underline{\tilde{\mathbf{G}}}_I^{\text{tip}}$ ,  $\underline{\tilde{\mathbf{G}}}_I^e$ ,  $\underline{\tilde{\mathbf{G}}}_I^s$  and  $\underline{\tilde{\mathbf{G}}}_I^{\text{dis}}$ , respectively

$$\begin{aligned} \int_{\Omega} \underline{\tilde{\mathbf{g}}}_h^{\text{tip}} N_I dV &= \int_{\Omega} \underline{\tilde{\Sigma}}_h^e \underline{\mathbf{B}}_I dV + \int_{\Omega} \underline{\tilde{\Sigma}}_h^s \underline{\mathbf{B}}_I dV + \int_{\Omega} -\underline{\tilde{\mathbf{g}}}_h^{\text{dis}} N_I dV, \\ \Leftrightarrow \underline{\tilde{\mathbf{G}}}_I^{\text{tip}} &= \underline{\tilde{\mathbf{G}}}_I^e + \underline{\tilde{\mathbf{G}}}_I^s + \underline{\tilde{\mathbf{G}}}_I^{\text{dis}}. \end{aligned} \quad (6.45)$$

Thus, the nodal crack tip force  $\underline{\tilde{\mathbf{G}}}_I^{\text{tip}}$  can be computed from the other configurational force contributions. Within the element oriented structure of the FE code, the integrals are usually evaluated element wise and assembled subsequently, i.e.

$$\underline{\tilde{\mathbf{G}}}_I^e = \sum_{e \in \mathcal{E}_I} \underline{\tilde{\mathbf{G}}}_{I,e}^e = \sum_{e \in \mathcal{E}_I} \int_{\Omega_e} \underline{\tilde{\Sigma}}_h^e \underline{\mathbf{B}}_I dV, \quad (6.46)$$

$$\underline{\tilde{\mathbf{G}}}_I^s = \sum_{e \in \mathcal{E}_I} \underline{\tilde{\mathbf{G}}}_{I,e}^s = \sum_{e \in \mathcal{E}_I} \int_{\Omega_e} \underline{\tilde{\Sigma}}_h^s \underline{\mathbf{B}}_I dV, \quad (6.47)$$

$$\underline{\tilde{\mathbf{G}}}_I^{\text{dis}} = \sum_{e \in \mathcal{E}_I} \underline{\tilde{\mathbf{G}}}_{I,e}^{\text{dis}} = \sum_{e \in \mathcal{E}_I} \int_{\Omega_e} -\underline{\tilde{\mathbf{g}}}_h^{\text{dis}} N_I dV, \quad (6.48)$$

where  $\mathcal{E}_I$  is again the set of elements adjacent to node  $I$  as introduced in section 5.1.

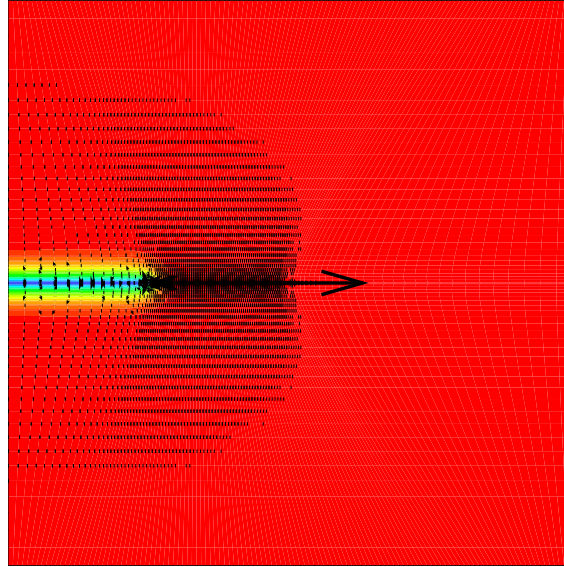


Figure 6.3: Contour plot of the crack field with configurational forces  $\tilde{\mathbf{G}}_I^{\text{tip}}$ , unloaded setting.

## 6.3 Simulations

The analytical findings of section 6.2 are compared to numerical evaluations of the configurational forces in the phase field model in this section. Therefore, a square structure of size  $L \times L$  with an initial edge crack of length  $L/4$  under mode I loading is simulated. The sample is discretized with 7200 quadrilateral elements with linear shape functions. Around the crack tip, the mesh is refined to an element edge length of about  $h = 0.003L$ . Dirichlet boundary conditions are imposed on the crack set in order to model the irreversibility of the fracture process.

### 6.3.1 Unloaded Crack

In this simulation, the length parameter  $\epsilon$  is set to  $0.01L$ , and no mechanical load is applied to the structure. Figure 6.3 shows a contour plot of the stationary crack field together with the configurational forces  $\tilde{\mathbf{G}}_I^{\text{tip}}$  acting on the mesh nodes. The magnitude of the nodal configurational forces is proportional to the length of the arrows in Fig. 6.3. The only significant nodal configurational force appears at the crack tip. The tiny configurational forces, appearing in the transition zone of the crack field, are of minor interest in the present context. They indicate the numerical error introduced by the discretization and could be employed to improve the discretization, see e.g. Mueller et al. [2002], Mueller and Maugin [2002].

In the absence of mechanical loading, an undamaged structure would be energetically favorable compared to the actually given state. Thus, the crack remains stable only through the imposition of the Dirichlet boundary conditions at the crack set. The configurational force, which appears at the crack tip, is caused by this manip-

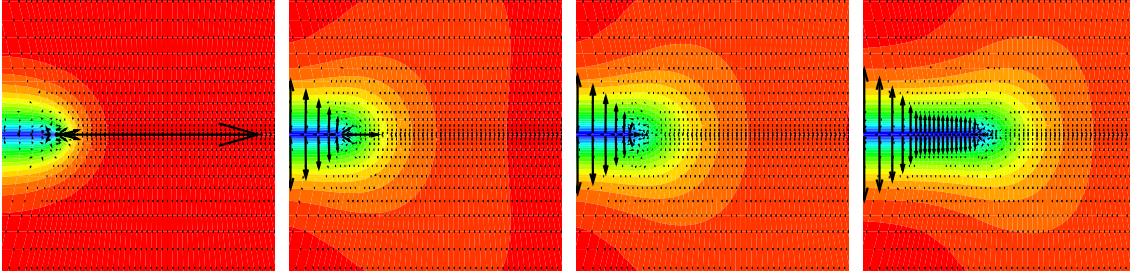


Figure 6.4: Contour plot of the crack field with configurational forces  $\tilde{\mathbf{G}}_I^{\text{tip}}$  at load factors (from left to right)  $\bar{t} = 0$  (unloaded),  $\bar{t} = 0.58$  (subcritical loading),  $\bar{t} = 0.64$  (critical load),  $\bar{t} = 0.675$  (crack propagation).

ulation and can be interpreted as the force which detains the crack from healing. As elastic and dissipative configurational forces are not present for an unloaded stationary crack ( $\tilde{\mathbf{G}}_I^e = \tilde{\mathbf{G}}_I^{\text{dis}} = \mathbf{0}$ ), the crack tip configurational force is purely cohesive at this stage ( $\tilde{\mathbf{G}}_I^{\text{tip}} = \tilde{\mathbf{G}}_I^s$ ). As to be expected from the considerations for the cohesive force in section 6.2.2, the force acts in positive  $x_1$ -direction and has approximately the magnitude  $\mathcal{G}_c$ .

### 6.3.2 Crack Growth under Mode I Loading

A linearly increasing displacement load of magnitude  $u(\bar{t}) = \sqrt{\frac{\mathcal{G}_c L}{2\mu}} \bar{t}$ , acting in positive  $x_2$ -direction on the upper, and in the opposite direction at the lower edge of the sample, is now applied to the structure. The Lamé constants are equal ( $\lambda = \mu$ ), the remaining stiffness  $\eta$  is set to  $10^{-5}$  and the mobility constant has the value  $M = 5 \frac{L}{\mathcal{G}_c T}$ . Figure 6.4 shows the evolution of the crack field  $s$  and the nodal configurational forces  $\tilde{\mathbf{G}}_I^{\text{tip}}$  under the increasing mode I displacement load. Only a zoom into the crack tip region of the structure is shown in these plots. The color scale of the contour plot is the same as in Fig. 6.3, however, the scaling length of the configurational force arrows is different. The first plot shows the initial state, discussed in the previous section. In the second plot, the crack is still stable and does not grow. While the crack tip force in  $x_1$ -direction becomes smaller, configurational forces in  $x_2$ -direction appear at the crack lips. At  $\bar{t} = 0.64$  (third plot), the  $x_1$ -component of the configurational force acting on the crack tip entirely vanishes, i.e. crack driving elastic forces and cohesive forces outbalance each other. This is when the crack becomes unstable and starts to grow. The last plot shows the configurational forces while the crack is growing. The different magnitudes of the arrows at the crack faces stem from differently fine discretizations along the crack. The continuous configurational traction, which they represent, is constant along the crack.

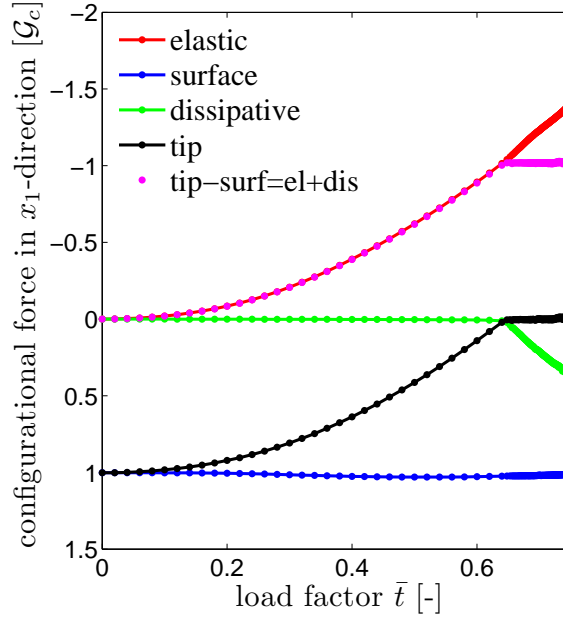


Figure 6.5: Evolution of configurational forces with respect to the load factor.

Under loading, especially in the vicinity of the crack tip the numerical error introduced by the discretization becomes more significant and the discrete configurational forces are distributed in the transition zone of the crack field. Hence, a direct evaluation of the configurational forces at the diffuse crack tip becomes problematic. As the requirements for path independence hold in the given setting, this can be compensated by evaluating the configurational force acting on a domain comprising the crack tip instead of just the single force on the node at the crack tip. The domain should be large enough to cover the whole transition zone of the crack field, but small enough not to intersect with the boundary of the structure. Thus, a circle area of radius  $0.2L$  centered at and moving with the crack tip was chosen for the evaluation of the configurational forces in Fig. 6.5. As the  $x_1$ -component of the configurational force is the decisive factor for the crack evolution under mode I loading, only this component is examined here. The plot shows the evolution of the different configurational forces with respect to the load factor  $\bar{t}$  of the linear increasing displacement load. As according to Eq. (6.19), the  $x_1$ -component of the elastic configurational force may be interpreted as the negative of the crack extension force, the respective axis is reversed in the plot in order to get a more intuitive picture.

As to be expected from Eq. (6.25), the surface part  $\tilde{G}_1^s$  (blue line) remains constant at the value  $\mathcal{G}_c$ . The magnitude of the elastic part  $\tilde{G}_1^e$  (red line) is zero at the beginning and grows with the loading. The onset of cracking is observed at about a load factor of  $\bar{t} = 0.64$ , when the elastic and surface part compensate each other, i.e. when the total configurational force on the crack tip  $\tilde{G}_1^{\text{tip}}$  (black line) vanishes. Before the onset of crack propagation, the dissipative part  $\tilde{G}_1^{\text{dis}}$  (green



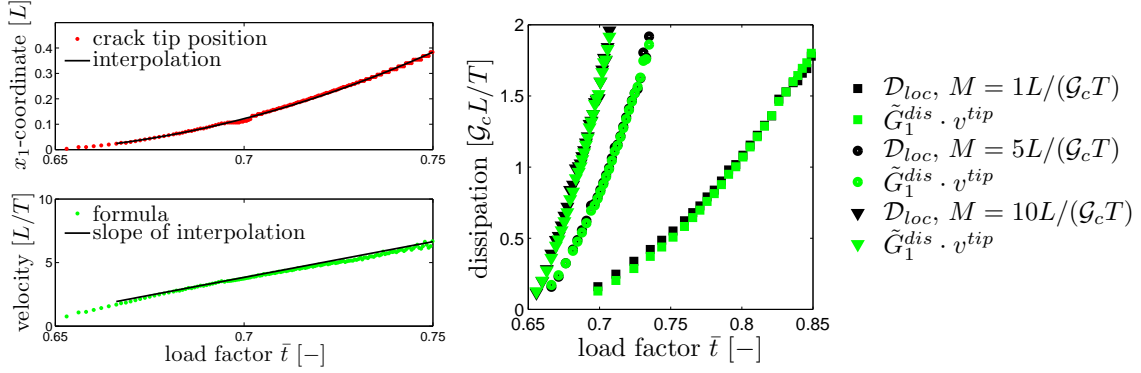


Figure 6.6: Crack tip position and velocity versus load factor (left) and dissipation versus load factor (right).

line) remains zero, but upon cracking it compensates the departure of the elastic part from the Griffith threshold:  $\tilde{G}_1^e + \tilde{G}_1^{\text{dis}} = -\mathcal{G}_c$  (magenta line), so that the total force remains zero.

The relations between the dissipative configurational force, the dissipation and the crack tip velocity elaborated in section 6.2.3 are verified in the plots of Fig. 6.6. In the lower plot on the left, the velocity value obtained by the formula in Eq. (6.34) (green dots) is compared to the crack tip velocity (black solid line) that is actually observed in the simulation. Here, the actual velocity was obtained as the slope of a least square quadratic interpolation of the crack tip position (upper left plot). The very good agreement of both curves is also confirmed in simulations with different values of the kinetic coefficient  $M$  and thus, Eq. (6.34) provides a reliable estimate for the crack speed. In the right plot of Fig. 6.6, the dissipation  $\mathcal{D}_{\text{loc}}$  (black markers) is compared to the value  $v^{\text{tip}} \cdot \tilde{G}_1^{\text{dis}}$  (green markers) in order to verify the relation in Eq. (6.32). Again, the crack tip velocity was obtained from a tracking of the crack tip position and a subsequent least square quadratic interpolation. Three different values of the kinetic coefficient  $M$  have been tested. The curves in the middle refer to a simulation with the same moderate value of the mobility that was used in the previous simulations ( $M = 5 \frac{L}{\mathcal{G}_c T}$ ). The lower curves refer to a very low value of the mobility ( $M = 1 \frac{L}{\mathcal{G}_c T}$ ), and the steeper curves refer to a very high mobility ( $M = 10 \frac{L}{\mathcal{G}_c T}$ ). In all three cases the respective curves are in good agreement.

Figure 6.7 shows plots of the crack speed versus the  $x_1$ -component of the configurational forces. Here, the velocity of the crack tip has been computed according to Eq. (6.34). As to be expected from this formula, the slope of the lines referring to the elastic and dissipative configurational forces is proportional to the mobility parameter  $M$ . These plots underline the driving force character of the elastic configurational force  $\tilde{G}_1^e$ , as well as the threshold character of the cohesive contribution  $\tilde{G}_1^s$ , when compared to the general sketch of thermodynamically admissible relations of the crack tip velocity and the crack driving force in Fig. 6.8.

## 6 Configurational Forces in the Context of Phase Field Models

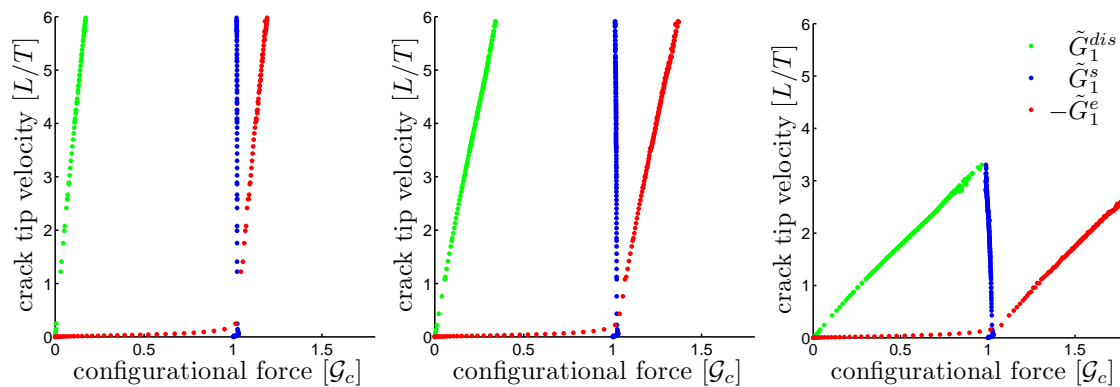


Figure 6.7: Crack tip velocity versus configurational forces for  $M = 10 \frac{L}{g_c T}$  (left),  $M = 5 \frac{L}{g_c T}$  (center) and  $M = 1 \frac{L}{g_c T}$  (right).

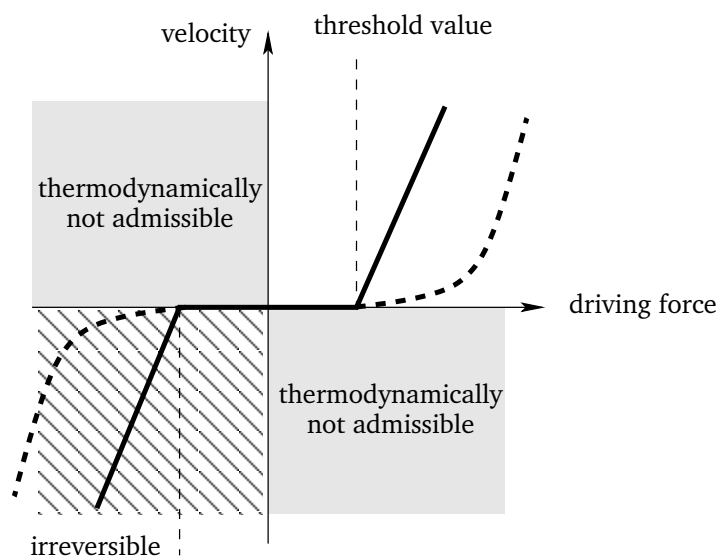


Figure 6.8: Sketch of thermodynamically admissible kinetic relations.

# 7 Crack Nucleation

Fracture models employing the energy release rate as a fracture criterion fail to predict crack growth in the absence of a  $\sqrt{r}$ -stress singularity in the domain under consideration. As these singularities typically appear only at a crack tip, an initial crack is essential in these formulations. In order to investigate the fracture behavior of previously undamaged samples, additional criteria for the formation of an initial crack have to be formulated.

In an effort to establish a fracture criterion, which is on the one hand consistent with Griffith's theory in the presence of cracks and on the other hand allows to predict crack nucleation, Leguillon proposes the concept of Finite Fracture Mechanics (FFM), see e.g. Leguillon [2001, 2002]. This is a two fold formulation which combines a strength criterion with an incremental form of the energy criterion. In the case of weak singularities, which may e.g be found at a V-notch, the model predicts the formation of an initial crack of finite length at some critical load level. This is consistent with the considerations about possible crack evolutions in the variational framework summarized in section 3.6.

A careful study of the crack nucleation behavior of the present phase field fracture model will be given in this section. As regardless of stress singularities, the crack evolution in the phase field model is obtained from a simultaneous solution of the mechanical boundary value problem and the evolution equation of the crack field, the influence of singularities on the crack evolution is not obvious. Thus, one objective of the following section is to check to which extent the crack evolutions obtained from phase field simulations are consistent with the energetic considerations of the variational formulation. A second objective is to gain a better understanding of the driving mechanisms of crack nucleation in the phase field model and to examine similarities to strength criteria as employed in FFM.

## 7.1 Simulation of Crack Nucleation

In order to examine the crack nucleation behavior of the phase field model, simulations of the two specimens depicted in Fig. 7.1 have been performed. The corresponding linear elastic solutions exhibit a stress concentration in case of the circular notch and a weak singularity in case of the V-shaped notch. Thus, in both cases classical Griffith theory fails to predict the onset of cracking. For both specimens, the crack field is set to 1 in the entire domain in order to model the undamaged initial state. The Lamé constants are equal ( $\lambda = \mu$ ) which is equivalent

## 7 Crack Nucleation

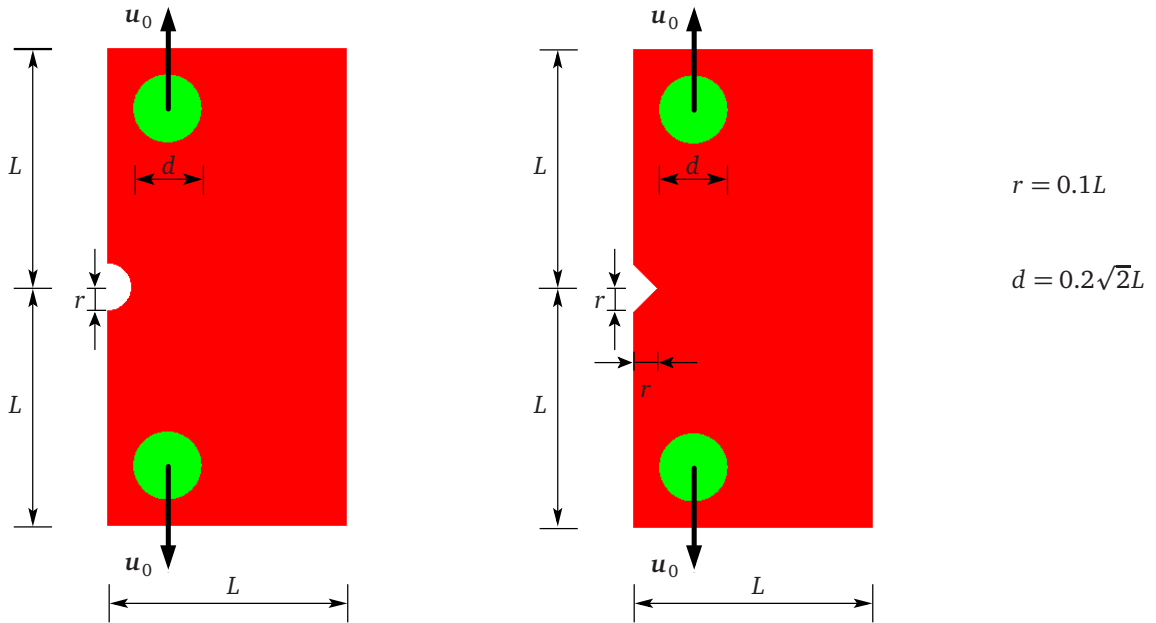


Figure 7.1: Specimen geometries for the crack nucleation simulations: circular notched specimen (left) and V-notched specimen (right).

to a Poisson ratio of  $\nu = 0.25$ . The regularization length is  $\epsilon = 0.01L$ , the artificial residual stiffness in broken areas is set to  $\eta = 10^{-5}$  and the mobility factor is set to  $M = 10 \frac{L}{\varrho_{cT}}$ . The circular areas around the load application points (green) are modeled as stiff by increasing the stiffness and cracking resistance by a factor of 100. A linear increasing displacement load  $u_0$  acting in  $y$ -direction is applied to the samples. The time step size is controlled by an adaptive time step procedure. Irreversibility is modeled by applying homogeneous Dirichlet boundary conditions on the crack field where the material is broken.

In both simulations a crack forms at the notch ground and then grows along the  $x$ -axis. Figure 7.2 shows the position  $x_{ct}$  of the crack tip on the  $x$ -axis with respect to the linearly increasing displacement load (black solid line). Before the onset of fracture, the position is identified with the notch ground located at  $x = 0.1L$ . When the critical load level is reached, an initial crack of finite length forms brutally at a quasi constant load level. As to be expected, due to the presence of a stress singularity at the V-notch, the crack nucleation at the V-notch occurs at a lower load level than at the circular notch. The formation of the initial crack is followed by a phase of stable crack extension, where the crack grows progressively with the loading. A second phase of brutal crack extension is observed when total rupture occurs after the crack tip passes  $x = 0.9L$ . The dotted lines indicate the beginning and ending of the phase of stable crack growth in the respective plot. Remarkably, the transition from brutal to stable crack extension and vice versa is mastered without any technical difficulties. The brutal formation of an initial crack at a stress concentration or weak stress singularity prior to progressive crack extension is in

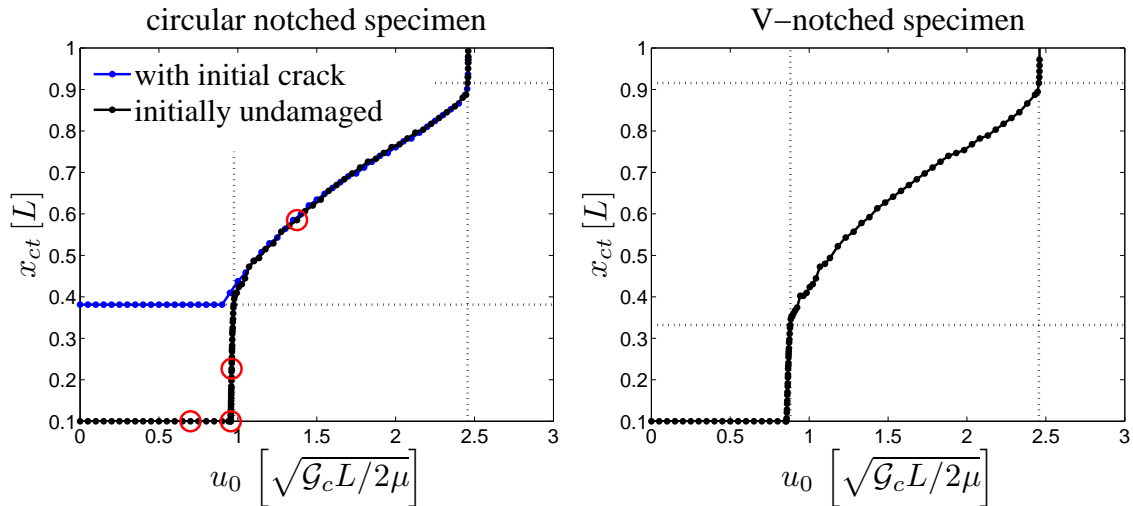


Figure 7.2: Crack tip position vs. load for the circular notched specimen (left) and V-notched specimen (right).

good agreement with possible crack evolutions in the variational formulation of fracture outlined in section 3.6.

For comparison, the simulation of the circular notched specimen is repeated with an initial crack of the same size as the initial crack which forms in the simulation of the initially undamaged sample. Figure 7.3 shows a contour plot of the initial crack field of this second simulation. The crack tip position with respect to the load factor is marked as a blue solid line in the left plot of Fig. 7.2. Slightly before the onset of fracture of the initially undamaged specimen, the initial crack starts to extend progressively. No brutal crack growth is observed here. When the previously undamaged structure enters the phase of stable crack growth (indicated by the dotted line) both crack position curves coincide.

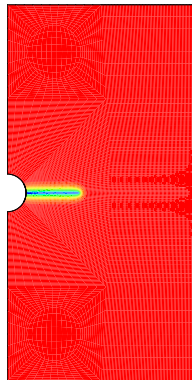


Figure 7.3: Contour plot of the crack field of the circular notched specimen with initial crack.

## 7 Crack Nucleation

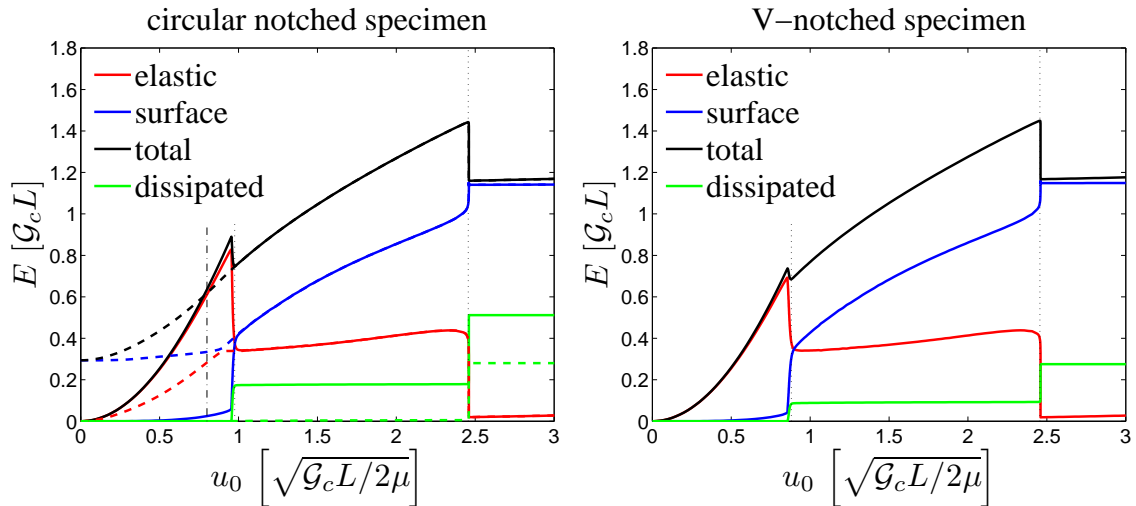


Figure 7.4: Energy contributions for the circular notched specimen (left) and V-notched specimen (right).

The evolution of the different energy contributions during the simulations is shown in the plots of Fig. 7.4. Events of brutal rupture at crack nucleation and total failure are marked by the vertical black dotted lines. These events are characterized by abrupt changes in the different energy contributions. Especially striking is the abrupt increase of the dissipated energy (green solid line), which remains constant during phases of stable crack growth, because the mobility constant is chosen fairly high in order to obtain a quasi static solution. As a result of the sudden dissipation of energy during brutal fracture, the total energy (black solid line), which is the sum of elastic energy (red solid line) and the surface energy (blue solid line), decreases abruptly. The occurrence of brutal fracture with infinitely large crack velocities, which is accompanied by dissipation of energy, is an unphysical artefact of the present phase field formulation. If cracks grow at a considerable speed, inertia effects and kinetic contributions to the energy functional need to be taken into account in order to obtain a physically sound material model.

The dashed lines in the left plot of Fig. 7.4 refer to the simulation of the circular notched specimen with initial crack. As there is no brutal fracture at the onset of crack propagation, there is no dissipation or decrease of total energy observed at this point. A link between the onset of crack extension and the energy evolution can only be seen in the evolutions of the elastic and surface energies. In the subsequent phase of stable crack growth, the elastic and surface energies, and consequently the total energy, coincide with the respective energies of the initially undamaged specimen.

The comparison of the energy evolutions of the initially uncracked sample and the sample with initial crack shows, that the crack evolution obtained by the phase field model differs in some points from the global minimization principle of the

variational formulation of brittle fracture. In order to be consistent with the global minimization principle, the numerical solution would have to be a global minimizer of the total energy at every load level. The obtained solution for the initially undamaged structure, however, does not represent such a global minimizer during the entire simulation. Above a load level of approximately  $u_0 = 0.8\sqrt{\frac{g_c L}{2\mu}}$  (vertical dash-dotted line) until crack nucleation is observed at a load level of approximately  $u_0 = 1\sqrt{\frac{g_c L}{2\mu}}$ , the total energy of the structure with initial crack (black dashed line) is smaller than the total energy of the undamaged sample (black solid line). Thus, from a purely energetic point of view, a crack should already form at a load level of about  $u_0 = 0.8\sqrt{\frac{g_c L}{2\mu}}$ , in order to obtain a global minimizer among all possible crack evolutions. The fact, that the phase field solution of the initially undamaged structure cannot be a global minimizer among all possible crack evolutions, can alternatively be deduced from the decrease of the total energy upon the formation of the initial crack. Such a decrease of the total energy cannot occur, if the obtained evolution has been a global minimizer at all previous time steps, see Francfort and Marigo [1998]. The backtracking algorithm suggested by Bourdin et al. [2008] exploits this fact in order to manipulate the crack field evolution in the regularized model in such a way, that actual global minimizers of the total energy can be recovered.

## 7.2 Strength Estimates

In the simulations of the circular notched specimen with and without initial crack, it has been observed, that the formation of an initial crack happens at a higher load level than it would be expected from purely energetic considerations. Thus, global energy minimization is not the driving principle of crack nucleation in the phase field model. This is consistent with the findings for the 1d case from section 4.4, where the phenomenon of crack nucleation could be linked to a loss of stability of the uncracked homogeneous solution. Furthermore, the length scale parameter  $\epsilon$  was found to have a crucial impact on the stability point of uncracked solutions and can be reinterpreted as a material parameter related to the strength  $\sigma_c$  of the material. The numerical results of the previous section in conjunction with the findings in the 1d case, suggest the assumption that, also in 2d, crack nucleation is triggered by a loss of stability of the uncracked solution. However, analytical solutions of nonhomogeneous 2d problems are not available, and thus, a rigorous mathematical stability analysis cannot be carried out.

On the basis of the derivation of the relation between  $\epsilon$  and  $\sigma_c$  from the maximal stress response of the 1d homogeneous solution, analogous relations can be derived from the two homogeneous 2d problems depicted in Fig. 7.5. For both cases, it fol-

## 7 Crack Nucleation

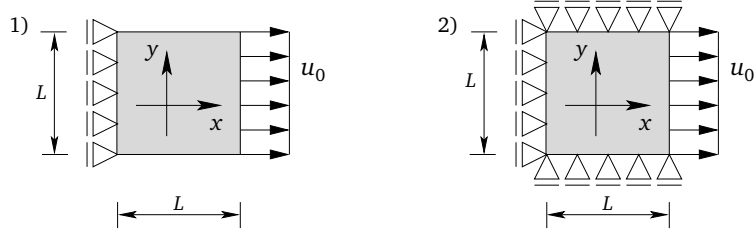


Figure 7.5: Homogeneous 2d problems for the derivation of strength estimates.

lows from the evolution equation Eq. (4.33) for the crack field  $s$ , that the stationary, homogeneous crack field is given by

$$s_h = \frac{\mathcal{G}_c}{2\epsilon\boldsymbol{\varepsilon} : [\mathbf{C}\boldsymbol{\varepsilon}] + \mathcal{G}_c} = \frac{1}{2\bar{\epsilon}\bar{\boldsymbol{\varepsilon}} : [\bar{\mathbf{C}}\bar{\boldsymbol{\varepsilon}}] + 1}, \quad (7.1)$$

where the variables with a bar denote dimensionless quantities as introduced in section 4.3. Due to the different boundary conditions, the elastic contribution  $\bar{\boldsymbol{\varepsilon}} : \bar{\mathbf{C}}\bar{\boldsymbol{\varepsilon}}$  differs slightly, depending on the ratio of the Lamé constants.

$$\bar{\boldsymbol{\varepsilon}} : [\bar{\mathbf{C}}\bar{\boldsymbol{\varepsilon}}] = \kappa_i \bar{u}_0^2 \quad \text{with} \quad \kappa_i = \begin{cases} \frac{2\lambda + 2\mu}{\lambda + 2\mu} = \frac{2\bar{\lambda} + 1}{\bar{\lambda} + 1} & \text{for } i = 1 \\ \frac{\lambda + 2\mu}{2\mu} = \bar{\lambda} + 1 & \text{for } i = 2 \end{cases} \quad (7.2)$$

The index  $i = 1, 2$  refers to the left and right problem depicted in Fig. 7.5. The corresponding homogeneous stress response is

$$\bar{\sigma}_x = (s^2 + \eta)\kappa_i \bar{u}_0 \approx \frac{\kappa_i \bar{u}_0}{(2\bar{\epsilon}\kappa_i \bar{u}_0^2 + 1)^2} \quad \text{for } i = 1, 2 \quad (7.3)$$

$$\bar{\sigma}_y = \begin{cases} 0 & \text{for } i = 1 \\ (s^2 + \eta)\bar{\lambda}\bar{u}_0 \approx \frac{\bar{\lambda}\bar{u}_0}{(2\bar{\epsilon}\kappa_i \bar{u}_0^2 + 1)^2} & \text{for } i = 2, \end{cases} \quad (7.4)$$

where  $\eta \approx 0$  for algebraic simplicity. The maximal stress response in  $x$ -direction

$$\bar{\sigma}_x^* = \frac{3}{16} \sqrt{\frac{3\kappa_i}{2\bar{\epsilon}}} \quad \text{for } i = 1, 2 \quad (7.5)$$

is attained at a load level of

$$\bar{u}_0^* = \frac{1}{\sqrt{6\bar{\epsilon}\kappa_i}} \quad \text{for } i = 1, 2. \quad (7.6)$$



The maximal stress response  $\bar{\sigma}_x^*$  and the respective loading  $\bar{u}_0^*$  exhibit the same asymptotic behavior with respect to  $\bar{\epsilon}$  as in the 1d case. For  $\bar{\epsilon} \rightarrow 0$  both quantities become infinitely large, while for  $\bar{\epsilon} \rightarrow \infty$  they approach the value 0. However, in 2d these quantities additionally depend on the factor  $\kappa_i$ . As in the 1d case, the value of the homogeneous crack field at the maximal stress response is

$$s_h^* = \frac{3}{4}, \quad (7.7)$$

independent of  $\bar{\epsilon}$  and  $\kappa_i$ . Reinterpreting the maximal stress response (Eq. 7.5) as the strength of the material yields the relation

$$\bar{\sigma}_c = \frac{3}{16} \sqrt{\frac{3\kappa_i}{2\bar{\epsilon}}} \quad \text{for } i = 1, 2 \quad (7.8)$$

between the dimensionless strength  $\bar{\sigma}_c$  and the dimensionless length scale  $\bar{\epsilon}$ . The respective relation with dimensional quantities reads

$$\sigma_c = \frac{3}{16} \sqrt{\frac{3\kappa_i \mu \mathcal{G}_c}{\epsilon}} \quad \text{for } i = 1, 2. \quad (7.9)$$

In the following, these strength estimates are compared to the actually computed stress states at crack nucleation in the phase field model. Figure 7.6 shows the stress component  $\bar{\sigma}_y$  (red) and the crack field  $s$  (blue) along the  $x$ -axis of the circular notched specimen at the four load stages marked by the red circles in Fig. 7.2. The vertical black dotted line marks the position of the crack tip after the formation of the initial crack. The horizontal black solid and dash-dotted lines indicate the strength estimates (Eq. 7.8) for the cases  $i = 1$  and  $i = 2$ , respectively. At the load level of  $\bar{u}_0 = 0.7$ , see Fig. 7.6a), no crack nucleation is observed yet and the evaluation of the energy yields the conclusion that the numerical solution is stationary and stable. However, very close to the notch ground located at  $\bar{x} = 0.1$ , the stress component  $\sigma_y$  already exceeds the strength estimates. The value of the crack field at the notch ground is  $s = 0.8066$ , which is higher than the assumed critical value  $s_h^* = 0.75$ . Figure 7.6b) shows the  $y$ -stress and crack field at the beginning of the phase of brutal crack nucleation at the load level  $\bar{u}_0 = 0.955$ . At this stage, the numerical solution becomes unstable and can no longer be considered stationary. The crack field immediately at the notch ground is decreased to  $s = 0.2164$ . Due to the loss of stiffness caused by the decreasing crack field, the stress at the notch ground decreases, too, and a stress peak develops in front of the notch. Figure 7.6c) shows the  $y$ -stress and crack field at  $\bar{u}_0 = 0.9608$ , during the phase of brutal crack extension. The crack field has developed its characteristic exponential shape where the material is not yet broken and is constantly zero in the fractured area. During this phase, the peak stress in  $y$ -direction significantly exceeds the strength estimates. The last plot, Fig. 7.6d), shows the stress component  $\bar{\sigma}_y$  and the crack field at  $\bar{u}_0 = 1.3751$ , during the phase of stable crack extension. The peak stress is

## 7 Crack Nucleation

now in good agreement with the strength estimates. The crack field maintains its shape and is only shifted in  $x$ -direction.

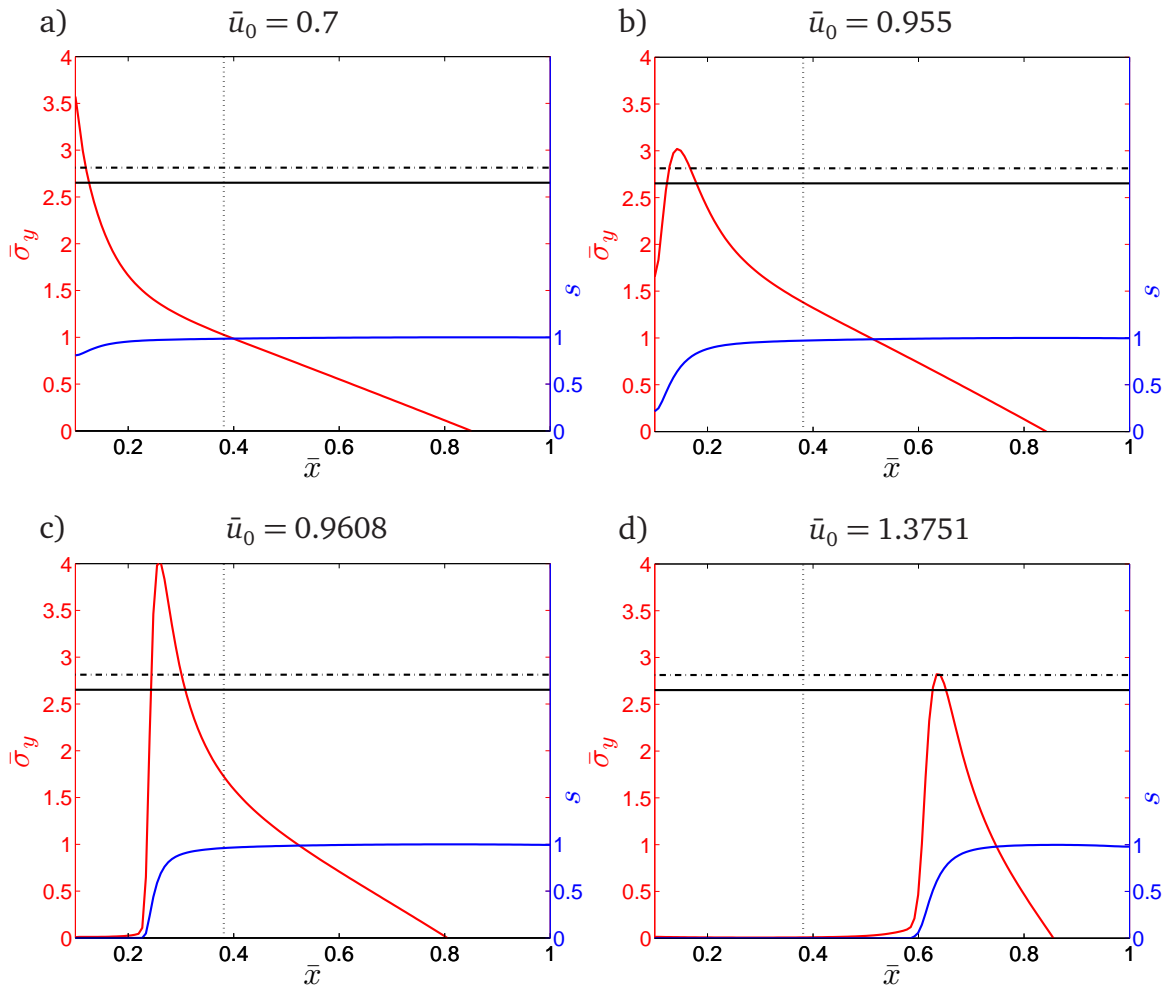


Figure 7.6: Stress in  $y$ -direction (red) and crack field (blue) along the  $x$ -axis at different load levels.

From the evaluation of the stress and crack field states in Fig. 7.6, it can be concluded that for the inhomogeneous stress state in the notched specimen, the exceedance of the assumed strength in a small area does not immediately yield crack nucleation in the phase field model. However, if the stress becomes supercritical in a sufficiently large area, an initial crack forms. Thus, the maximal stress value by itself does not provide an appropriate indicator for crack nucleation. The plots of Fig. 7.7 show the evolution of the average of  $\bar{\sigma}_y$  over a distance of  $10\bar{\epsilon}$  in front of the notch with respect to the load factor  $\bar{u}_0$ . The left and right plot refer to the circular and V-notched specimen, respectively. Again, the horizontal black solid and dash-dotted lines indicate the strength estimates, and the vertical dotted line indicates the load at which the initial crack forms. The size of the averaging domain  $10\bar{\epsilon}$  was chosen such that for both structures, the averaged stress attains its

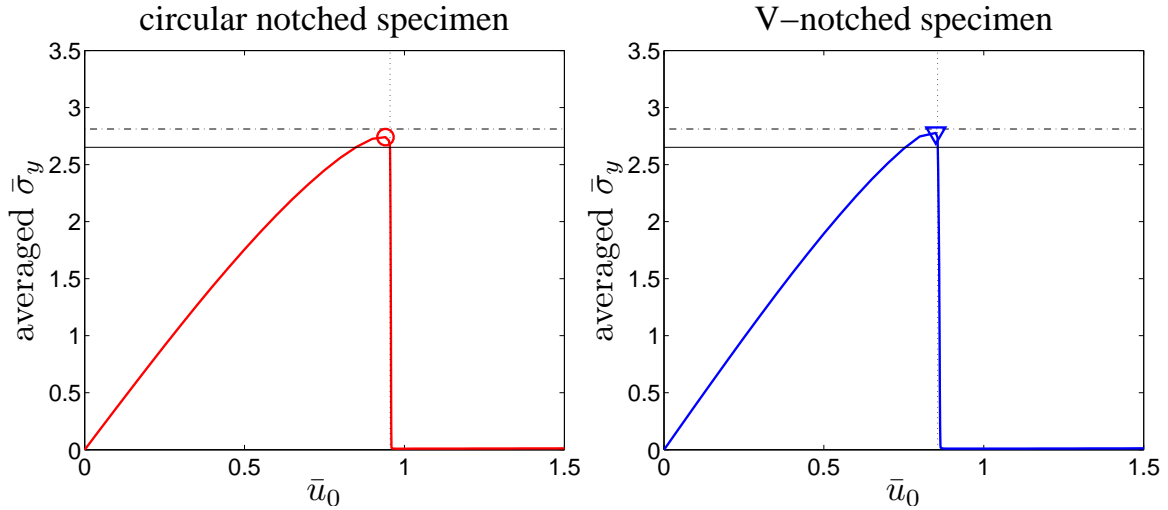


Figure 7.7: Averaged stress at circular notch (left) and V-notch (right) for  $\bar{\epsilon} = 0.01$ .

maximal value (indicated by the marker) just before the onset of fracture, and the maximal value is in good agreement with the estimated strength. If the averaging domain is chosen smaller, the maximal average stress exceeds the stress estimates. For larger averaging domains, the average stress does not reach the stress estimates. The adequacy of the average stress as an indicator for crack nucleation and the suitability of the choice of the averaging domain is confirmed by further simulations with different values of  $\bar{\epsilon}$ . In Fig. 7.8 the maximal average stress values observed in simulations with 5 different values of  $\bar{\epsilon}$  are compared to the estimated strength. For all of the tested values of  $\bar{\epsilon}$ , the maximal average stress is attained just before the onset of fracture and the maximal average stress is in good agreement with the strength estimates. Thus, rather than the maximal stress value at a single point, an average stress computed on a small domain comprising the point of maximal stress, can serve as a reliable indicator for crack nucleation in an inhomogeneous 2d problem.

This result permits to judge the criticality of a computed stress state prior to crack nucleation, which is not possible without the derived strength estimates. Furthermore, together with the previous simulation results, it justifies the conclusion that the phase field model naturally combines a strength criterion for the nucleation of new cracks with an energetically motivated Griffith type evolution law for stable crack growth. As a consequence of this interpretation, the length scale  $\epsilon$  is no longer just an arbitrary regularization length, but a material parameter which can be determined according to Eq. (7.9) from experimentally measurable material data, i.e. from the cracking resistance  $\mathcal{G}_c$ , the strength  $\sigma_c$ , and the elastic Lamé constants  $\lambda$  and  $\mu$  or the Young's modulus  $E$  and the Poisson ratio  $\nu$ , respectively.

## 7 Crack Nucleation

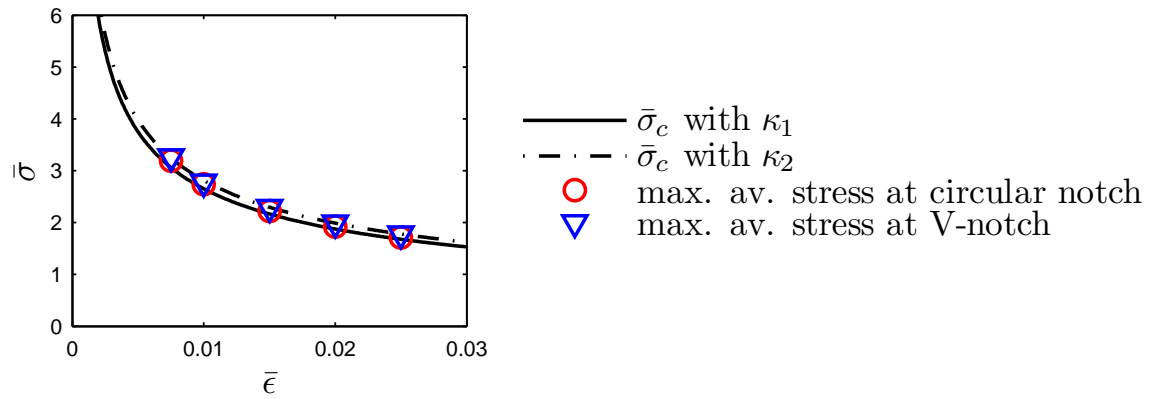


Figure 7.8: Maximal averaged stress compared to strength estimates for different values of  $\bar{\epsilon}$ .

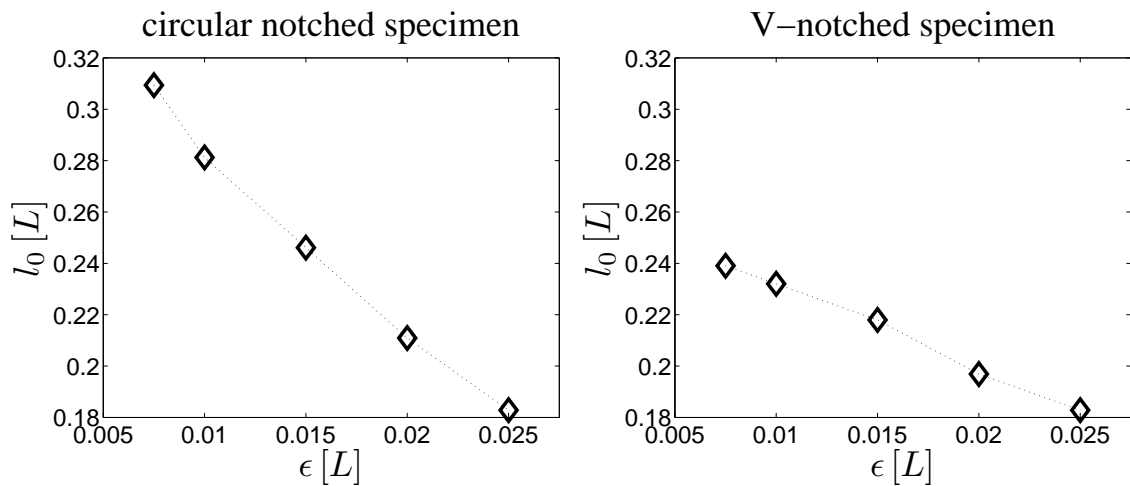


Figure 7.9: Length of initial crack for different values of  $\epsilon$  for the circular notched specimen (left) and V-notched specimen (right).

The length scale parameter  $\epsilon$  does not only determine the strength of the material, but has also an impact on the length of initial cracks which form at stress concentrations. Figure 7.9 shows the lengths of the initial cracks observed in the simulations of the circular and V-notched specimens for different values of  $\epsilon$ . The higher material strength associated with small values of  $\epsilon$  leads to a delay in the onset of fracture. As a result, fracture occurs at a higher load level and there is more elastic energy available to be transformed into surface energy at the moment of crack nucleation. Consequently, longer initial cracks are obtained for smaller values of  $\epsilon$ .

Additionally it is observed that the initial cracks which form at the circular notch are longer than the initial cracks at the V-notch. This is due to the fact that the degree of stress concentration at the circular notch is lower than at the V-notch, where the linear elastic solution exhibits a weak singularity. Therefore, the critical stress state at the V-notch is attained at a lower load level with less elastic stored energy available for the formation of new crack surfaces. This effect is less significant for larger values of  $\epsilon$ , as these high values dampen the impact of stress concentration in both structures.

## 7.3 Tensile Specimen with Different Hole Sizes

From the analysis in Pham et al. [2011a] it can be concluded, that the 1d phase field model is able to reproduce size effects, i.e. that the sample size has an influence on the failure load. In this section it is checked to which extend size effects in 2d can be reproduced by the phase field fracture model. To this end, simulation results are compared to experimental data reported in Li and Zhang [2006]. In the experiments, plates made of polymethyl metacrylate (PMMA) with holes of different sizes were subjected to a linear increasing displacement load  $u_0(t)$ . A sketch of the specimen geometry and the simulation domain is shown in Fig. 7.10. Specimens with hole radii of 0.3, 0.6, 1.0 and 1.5 mm as well as specimens without a hole were used for the experiments.

For the numerical simulation, the simulation domain, shaded in gray in Fig. 7.10, has been discretized with 16120 elements with linear shape functions. Symmetry boundary conditions are applied along the  $y$ -axis. Around the hole, the mesh is refined to an element edge length about  $h = 0.5\epsilon$ , depending on the length parameter  $\epsilon$  used in the respective simulation. In addition to the hole radii used for the experiments, simulations have also been performed for hole radii of 0.1 and 0.2 mm. From the plane strain material data  $E' = 3000 \text{ N/mm}^2$  and  $\nu' = 0.36$  given in Li and Zhang [2006], the Lamé coefficients are obtained as

$$\lambda = \frac{\nu' E'}{1 - \nu'^2} = 1240.8 \frac{\text{N}}{\text{mm}^2} \quad \text{and} \quad \mu = \frac{E'}{2(1 + \nu')} = 1102.9 \frac{\text{N}}{\text{mm}^2}. \quad (7.10)$$

## 7 Crack Nucleation

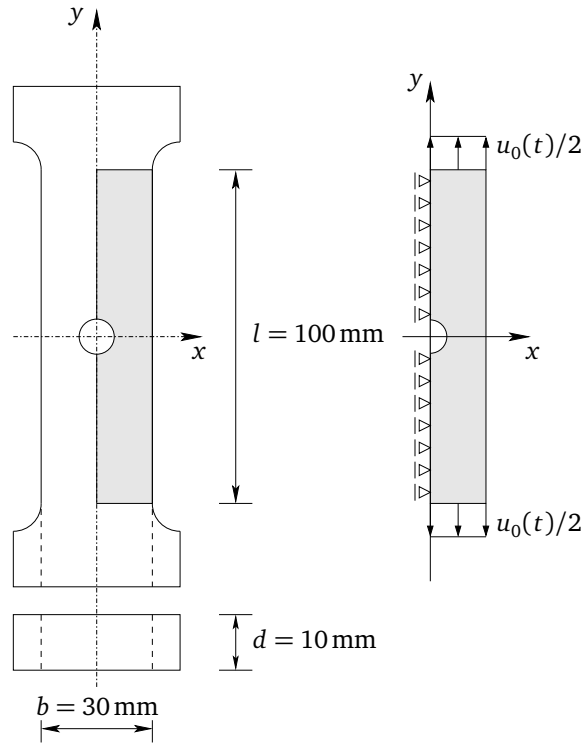


Figure 7.10: Specimen geometry and simulation domain for the size effect experiment.

With the tensile strength  $\sigma_c = 72 \text{ N/mm}^2$  and critical energy release rate  $\mathcal{G}_c = 290 \text{ J/m}^2 = 0.29 \text{ N/mm}$ , also taken from Li and Zhang [2006], and  $\kappa_1$  and  $\kappa_2$  computed according to Eq. (7.2), the relation in Eq. (7.9) yields the two values

$$\epsilon_1 = 0.00885 \text{ mm} \quad \text{and} \quad \epsilon_2 = 0.01017 \text{ mm} \quad (7.11)$$

for the length parameter  $\epsilon$ . The left plot of Fig. 7.11 shows the remote stress  $\sigma_\infty$  with respect to the nominal strain in  $y$ -direction  $\epsilon_0 = u_0(t)/l$  for all simulated hole radii and  $\epsilon = 0.01017 \text{ mm}$ . The remote stress is computed as the average stress in  $y$ -direction along the boundary where the displacement load is applied. Since all of the tested hole radii are comparably small, the global specimen rigidity is not much influenced by the hole and the stress strain curves are close to the linear elastic response of a plate without hole (dotted line) at the beginning of loading. The offset of the simulated stress strain curves from the linear elastic response before fracture indicates that the crack field starts to evolve away from the initially undamaged state  $s \equiv 1$  and is the same for all simulated hole radii. The impact of the hole size only becomes evident through the different failure loads observed in the simulations. For smaller hole radii, fracture occurs at a higher loading.

The right plot of Fig. 7.11 shows the maximal remote stress  $\hat{\sigma}_\infty$ , which is observed just before fracture, for all simulated radii  $r$ . The triangle and square markers refer to maximal stress values obtained in simulations with  $\epsilon = 0.00885 \text{ mm}$  and  $\epsilon = 0.01017 \text{ mm}$ , respectively. As to be expected from Eq. (7.9), higher stress values

### 7.3 Tensile Specimen with Different Hole Sizes

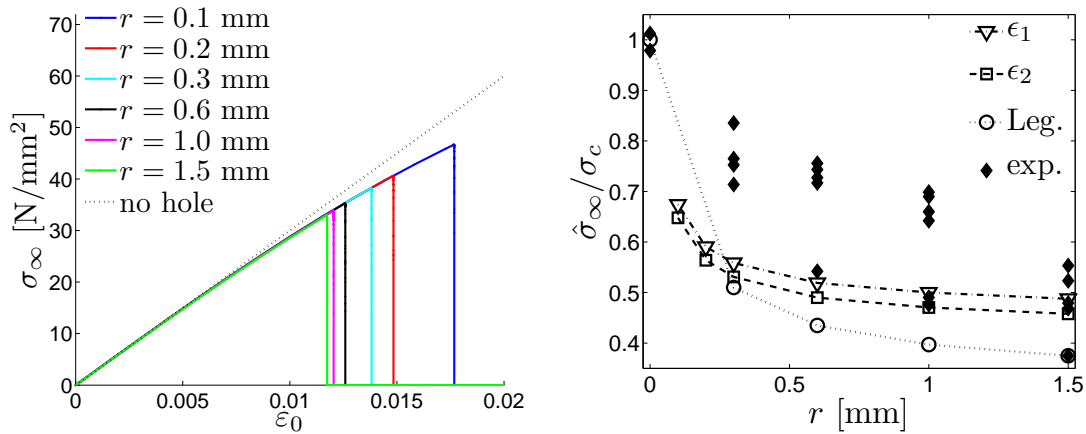


Figure 7.11: Stress strain curves from simulations with  $\epsilon = 0.01017$  mm (left) and comparison of fracture stresses (right).

are obtained in the simulations with the smaller value of  $\epsilon$ . The values are compared to the experimental data reported in Li and Zhang [2006] (black diamonds) and to simulations with Leguillon's criterion (circles) performed by Hebel [2010]. The phase field model, as well as Leguillon's criterion are both capable to model size effects, i.e. the fracture stress decreases with increasing hole radii. However, compared to the experimental data both criteria underestimate the actual effective strength of the material observed in the experiments. This tendency has been observed for several other established two parameter criteria examined in Li and Zhang [2006]. Thus, the authors conclude, that at least a three parameter criterion is necessary in order to properly reproduce size effects concerning crack nucleation at non-singular stress concentrations.

## 7 Crack Nucleation



## 8 Conclusion and Outlook

In this work, a phase field fracture model has been investigated. The core of the considered phase field model is an energy density functional which was introduced by Bourdin et al. [2000] in order to establish a regularization of the variational formulation of brittle fracture by Francfort and Marigo [1998]. This basis has been chosen, because the underlying physical concepts of Griffith's theory are well understood and have proven useful for technical applications. Earlier phase field formulations of brittle fracture typically employ a different type of energy density functional with a double well potential, that naturally separates the broken and undamaged phase. However, for such kind of energy density functionals, no proofs of convergence to a sharp crack formulation with a Griffith type surface energy are available.

The absence of a double well potential in the chosen energy functional, intensifies the problem of modeling the irreversibility of fracture in the phase field model. Two different modeling approaches have been introduced and discussed in this work. From a thermodynamical point of view, both methods can be reasoned to be admissible, i.e. thermodynamically consistent and neither one is to be preferred. Therefore, and because both approaches are connected with different interpretations of the crack field – an auxiliary indicator field vs. a damage variable – the correct choice of the irreversibility constraint remains a delicate question. Within the scope of this work, the interpretation of the crack field as an auxiliary indicator for cracks, is more appropriate. Accordingly, irreversibility constraints in terms of boundary conditions have been chosen in order to recover the correct amount of surface energy upon unloading.

In an effort to highlight the connection between the crack evolution in the phase field model and the energetic crack extension laws of Griffith's theory, the concept of configurational forces has been generalized to the phase field fracture model. The analytically derived relations have been verified in numerical simulations. Therefore, discrete configurational forces have been computed in the finite element code by means of a post processing procedure. The discrete configurational forces have additionally proven to be a valuable tool for the visualization of the energetic driving mechanisms of crack propagation in the simulations. Moreover, they can serve to gain information about the criticality of stationary cracks in the phase field model before the onset of crack propagation is observed.

## 8 Conclusion and Outlook

In Bourdin's regularized version of the variational formulation of brittle fracture, the global minimization of the total energy precludes the handling of soft devices. In contrast, the phase field model, where the crack evolution is instead governed by an evolution equation, is able to consider traction loads and body forces without any further modification. A second major impact of the replacement of global minimization by a Ginzburg-Landau evolution equation comes to light in crack nucleation scenarios. Here, formulations based on global minimization are plagued by spurious size effects, i.e. the fracture load significantly depends on the sample size. In contrast, the size effects observed for the phase field fracture model are in a physically acceptable range. Here, the fracture load essentially depends on the elastic properties of the material in conjunction with its cracking resistance and the phase field length scale. In consequence, this observation means that the parameter  $\epsilon$  is determined by the elasticity constants  $\lambda$  and  $\mu$ , the cracking resistance  $\mathcal{G}_c$  and the strength  $\sigma_c$  of the material and should therefore be regarded as a material parameter itself. From the standpoint of global minimization, however, this interpretation is pointless. In this respect, a local rather than a global minimization principle could render the basis for a consensus. Even the advocators of the variational formulation themselves admit in Bourdin et al. [2000], that local minimizers certainly yield a more realistic crack evolution. However, the notion of locality is a delicate topic in this context and the mathematical implications of such a modification are still object of ongoing research, see e.g. Larsen [2010a] or Larsen [2012].

The numerical implementation of the phase field fracture model into a standard finite element framework has turned out to be very straightforward. Merely the implementation of the irreversibility constraints requires special attention. The proposed techniques implement the irreversibility constraints at element level. This is advantageous because it does not require to change the global boundary conditions in the course of a simulation. The latter would be far more difficult from a technical point of view, because it would require to interfere with the finite element framework on the global level.

In order to increase the efficiency of the simulations, a new discretization technique using so-called exponential shape functions has been developed. Simulations have shown, that the exponential shape functions actually allow for a coarser discretization without compromise on the accuracy of the approximation of the surface energy. Yet, up to now, the application of this technique is restricted to rather simple test scenarios with an a priori known crack path.

Even though an implicit time integration scheme has been employed for the integration of the evolution equation, fracture processes need to be resolved with very small time steps due to the rapidly changing crack field. Therefore, an automatic step size control has been employed for the simulations. This combination of implicit time integration and automatic step size control has rendered a very robust

simulation strategy.

In summary, the phase field model proposed in this work is a very general and flexible instrument for the simulation of fracture processes. From a user's point of view, the application of the phase field code to different examples does not require much expertise on the subject. In this regard, the method is also attractive for the usage in commercial software.

As mentioned before, the extension of the code to a 3d setting is straightforward. Preliminary works in this direction can be found in Keller [2011]. Yet, simulations of 3d structures are very computation intensive so that most simulations require the utilization of parallel computing techniques.

Since events of brutal crack extension are inherent to the phase field model, dynamic effects in the bulk should be considered in future work. Just recently, in Larsen [2010b] and Bourdin et al. [2011a], the underlying regularized variational fracture criterion has been considered in a dynamic setting, and dynamic versions of earlier phase field fracture models do also exist, see e.g. Karma et al. [2001], Spatschek et al. [2006a], Borden et al. [2012] or Hofacker and Miehe [2012]. Thus, an extension of the present phase field model to the dynamic case should be manageable.

## 8 *Conclusion and Outlook*

# Bibliography

- L. Ambrosio and V. M. Tortorelli. Approximation of functional depending on jumps by elliptic functional via  $\gamma$ -convergence. *Commun. Pure Appl. Maths*, 43(8):999–1036, 1990.
- H. Amor, J.-J. Marigo, C. Maurini, and N. K. Pham. Stability analysis and numerical implementation of non-local damage models via a global variational approach. In *WCCM8 - ECCOMAS 2008*, 2008.
- H. Amor, J.-J. Marigo, and C. Maurini. Regularized formulation of the variational brittle fracture with unilateral contact: Numerical experiments. *J. Mech. Phys. Solid.*, 57(8):1209–1229, 2009.
- I. S. Aranson, V. A. Kalatsky, and V. M. Vinokur. Continuum field description of crack propagation. *Phys. Rev. Let.*, 85(1):118–121, 2000.
- I. Babuska and J. M. Melenk. The partition of unity method. *Int. J. Numer. Meth. Eng.*, 40:727–758, 1996.
- G. I. Barenblatt. The mathematical theory of equilibrium cracks in brittle fracture. In H. L. Dryden, T. von Kármán, G. Kuerti, F. H. van den Dungen, and L. Howarth, editors, *Advances in Applied Mechanics*, volume 7 of *Adv. Appl. Mech.*, pages 55–129. Elsevier, 1962.
- A. Benallal and J.-J. Marigo. Bifurcation and stability issues in gradient theories with softening. *Modell. Simul. Mater. Sci. Eng.*, 15(1):283–295, 2007.
- M. J. Borden, C. V. Verhoosel, M. A. Scott, T. J. R. Hughes, and C. M. Landis. A phase-field description of dynamic brittle fracture. *Comput. Meth. Appl. Mech. Eng.*, 217–220:77–95, 2012.
- B. Bourdin. *Une Méthode variationnelle en mécanique de la rupture*. PhD thesis, Université Paris-Nord, 1998.
- B. Bourdin. Numerical implementation of the variational formulation of quasi-static brittle fracture. *Interfaces Free Bound.*, 9:411–430, 2007a.
- B. Bourdin. The variational formulation of brittle fracture: Numerical implementation and extensions. In A. Combescure, R. Borst, and T. Belytschko, editors, *IUTAM Symposium on Discretization Methods for Evolving Discontinuities*, volume 5 of *IUTAM Bookseries*, chapter 22, pages 381–393. Springer Netherlands, 2007b.

## Bibliography

- B. Bourdin and A. Chambolle. Implementation of an adaptive finite-element approximation of the Mumford-Shah functional. *Numer. Mat.*, 85:609–646, 2000.
- B. Bourdin, M. Knepley, and C. Maurini. Secondary thermal cracks in EGS: A variational approach. In *GRC Transactions*.
- B. Bourdin, G. A. Francfort, and J.-J. Marigo. Numerical experiments in revisited brittle fracture. *J. Mech. Phys. Solid.*, 48(4):797–826, 2000.
- B. Bourdin, G. Francfort, and J.-J. Marigo. The variational approach to fracture. *J. Elasticity*, 91(1):5–148, 2008.
- B. Bourdin, C. Larsen, and C. Richardson. A time-discrete model for dynamic fracture based on crack regularization. *Int. J. Fract.*, 168:133–143, 2011a.
- B. Bourdin, C. Maurini, and M. G. Knepley. Numerical simulation of reservoir stimulation - a variational approach. In *Proceedings of the 36th Stanford Geothermal Workshop*, Stanford, CA, 2011b.
- A. Braides.  $\Gamma$ -convergence for beginners, volume 22 of *Oxford Lecture Series in Mathematics and Its Applications*. Oxford University Press, 2002.
- A. Braides. A handbook of  $\gamma$ -convergence. In M. Chipot and P. Quittner, editors, *Stationary Partial Differential Equations*, volume 3 of *Handbook of Differential Equations*, chapter 2, pages 101–213. North-Holland, 2006.
- M. Braun. Configurational forces induced by finite-element discretization. *Proc. Estonian Acad. Sci. Phys. Math.*, 46(1–2):24–31, 1997.
- G. Caginalp and P. Fife. Phase-field methods for interfacial boundaries. *Phys. Rev. B*, 33:7792–7794, 1986.
- A. Chambolle. A density result in two-dimensional linearized elasticity, and applications. *Arch. Rat. Mech. Anal.*, 167:211–233, 2003.
- A. Chambolle. An approximation result for special functions with bounded deformation. *J. Math. Pure Appl.*, 83(7):929–954, 2004.
- A. Chambolle, A. Giacomini, and M. Ponsiglione. Crack initiation in brittle materials. *Arch. Rat. Mech. Anal.*, 188:309–349, 2008.
- A. Chambolle, G. A. Francfort, and J.-J. Marigo. When and how do cracks propagate? *J. Mech. Phys. Solid.*, 57(9):1614–1622, 2009.
- A. Chambolle, G. A. Francfort, and J.-J. Marigo. Revisiting energy release rates in brittle fracture. *J. Nonlinear Sci.*, 20:395–424, 2010.

- M. Charlotte, G. A. Francfort, J.-J. Marigo, and L. Truskinovsky. Revisiting brittle fracture as an energy minimization problem: Comparisons of Griffith and Barenblatt surface energy models. In A. Benallal, editor, *Symposium on continuous damage and fracture*. 2000.
- G. P. Cherepanov. The propagation of cracks in a continuous medium. *J. Appl. Math. Mech.*, 31(3):503–512, 1967.
- J. Chessa, H. Wang, and T. Belytschko. On the construction of blending elements for local partition of unity enriched finite elements. *Int. J. Numer. Meth. Eng.*, 57(7):1015–1038, 2003.
- B. D. Coleman and M. E. Gurtin. Thermodynamics with internal state variables. *J. Chem. Phys.*, 47(2):597–613, 1967.
- B. D. Coleman and W. Noll. The thermodynamics of elastic materials with heat conduction and viscosity. *Arch. Rat. Mech. Anal.*, 13:167–178, 1963.
- J. B. Collins and H. Levine. Diffuse interface model of diffusion-limited crystal growth. *Phys. Rev. B*, 31:6119–6122, 1985.
- F. Corson, M. Adda-Bedia, H. Henry, and E. Katzav. Thermal fracture as a framework for quasi-static crack propagation. *Int. J. Fract.*, 158:1–14, 2009.
- R. de Borst, J. Pamin, R. H. J. Peerlings, and L. Sluys. On gradient-enhanced damage and plasticity models for failure in quasi-brittle and frictional materials. *Comput. Mech.*, 17(1-2):130–141, 1995.
- G. del Piero, G. Lancioni, and R. March. A variational model for fracture mechanics: Numerical experiments. *J. Mech. Phys. Solids*, 55(12):2513–2537, 2007.
- R. Denzer. *Computational Configurational Mechanics*. Phd thesis, Technische Universität Kaiserslautern, 2006.
- L. O. Eastgate, J. P. Sethna, M. Rauscher, T. Cretegnny, C.-S. Chen, and C. R. Myers. Fracture in mode I using a conserved phase-field model. *Phys. Rev. E*, 65(3):036117, 2002.
- B. Echebarria, R. Folch, A. Karma, and M. Plapp. Quantitative phase-field model of alloy solidification. *Phys. Rev. E*, 70:061604, 2004.
- B. Eidel and C. Kuhn. Order reduction in computational inelasticity: Why it happens and how to overcome it - the ode-case of viscoelasticity. *Int. J. Numer. Meth. Eng.*, 87(11):1046–1073, 2011.
- F. Erdogan and G. C. Sih. On the crack extension in plates under plane loading and transverse shear. *J. Basic Engineering*, 85(4):519–525, 1963.

## Bibliography

- J. D. Eshelby. The force on an elastic singularity. *Phil. Trans. Roy. Soc. Lond. A*, 244 (877):87–112, 1951.
- G. A. Francfort. Quasistatic brittle fracture seen as an energy minimization movement. *GAMM-Mitt.*, 29(2):172–191, 2006.
- G. A. Francfort and C. J. Larsen. Existence and convergence for quasi-static evolution in brittle fracture. *Commun. Pure Appl. Maths*, 56:1465–1500, 2003.
- G. A. Francfort and J.-J. Marigo. Revisiting brittle fracture as an energy minimization problem. *J. Mech. Phys. Solid.*, 46(8):1319–1342, 1998.
- G. A. Francfort and J.-J. Marigo. Griffith theory of brittle fracture revisited: Merits and drawbacks. *Latin Amer. J. Solids Struct.*, 2:57–64, 2005.
- E. Fried and M. E. Gurtin. Continuum theory of thermally induced phase transitions based on an order parameter. *Physica D*, 68(3–4):326–343, 1993.
- E. Fried and M. E. Gurtin. Dynamic solid-solid transitions with phase characterized by an order parameter. *Physica D*, 72(4):287–308, 1994.
- A. Giacomini. Ambrosio-tortorelli approximation of quasi-static evolution of brittle fractures. *Calc. Var.*, 22:129–172, 2005.
- V. Ginzburg and L. Landau. On the theory of superconductivity. *Zh. Eksp. Teor. Fiz.*, 20:1064–1082, 1959.
- R. V. Goldstein and R. L. Salganik. Brittle fracture of solids with arbitrary cracks. *Int. J. Fract.*, 10:507–523, 1974.
- O. Goy. *Point defects in piezoelectric materials – continuum mechanical modelling and numerical simulation*. Phd thesis, Technische Universität Kaiserslautern, 2010.
- A. A. Griffith. The phenomena of rupture and flow in solids. *Phil. Trans. Roy. Soc. Lond. A*, 221:163–198, 1921.
- D. Gross and T. Seelig. *Fracture Mechanics: With an Introduction to Micromechanics*. Mechanical Engineering Series. Springer, 2010.
- D. Gross, S. Kolling, R. Mueller, and I. Schmidt. Configurational forces and their application in solid mechanics. *Eur. J. Mech. Solid*, 22(5):669–692, 2003.
- M. E. Gurtin. On the energy release rate in quasi-static elastic crack propagation. *J. Elasticity*, 9:187–195, 1979.
- M. E. Gurtin. *An Introduction to Continuum Mechanics*. Mathematics in Science and Engineering. Academic Press, 1981.
- M. E. Gurtin. Generalized Ginzburg-Landau and Cahn-Hilliard equations based on a microforce balance. *Physica D*, 92(3–4):178–192, 1996.



- M. E. Gurtin. *Configurational forces as basic concepts of continuum physics*. Applied mathematical sciences. Springer, 2000.
- M. E. Gurtin and P. Podio-Guidugli. Configurational forces and the basic laws for crack propagation. *J. Mech. Phys. Solid.*, 44(6):905–927, 1996.
- V. Hakim and A. Karma. Crack path prediction in anisotropic brittle materials. *Phys. Rev. Let.*, 95(23):235501, Dec 2005.
- V. Hakim and A. Karma. Laws of crack motion and phase-field models of fracture. *J. Mech. Phys. Solid.*, 57(2):342–368, 2009.
- J. Hebel. *Modellierung spröder Rissbildung an Spannungskonzentrationen mit der Bruchmechanik finiter Risse*. Phd thesis, Technische Universität Darmstadt, 2010.
- H. Henry and H. Levine. Dynamic instabilities of fracture under biaxial strain using a phase field model. *Phys. Rev. Let.*, 93(10):105504, Sep 2004.
- M. Hofacker and C. Miehe. Continuum phase field modeling of dynamic fracture: Variational principles and staggered FE implementation. *Int. J. Fract.*, pages 1–17, 2012.
- G. A. Holzapfel. *Nonlinear solid mechanics: A continuum approach for engineering*. Wiley, 2000.
- T. J. R. Hughes. *The Finite Element Method: Linear Static and Dynamic Finite Element Analysis*. Dover Publications, Inc., Mineola, New York, 2000.
- G. R. Irwin. Analysis of stresses and strains near the end of a crack traversing a plate. *J. Appl. Mech.*, 24:361–364, 1957.
- L. M. Kachanov. *Introduction to Continuum Damage Mechanics*. Mechanics of Elastic Stability. Springer Netherlands, 1986.
- A. Karma and A. E. Lobkovsky. Unsteady crack motion and branching in a phase-field model of brittle fracture. *Phys. Rev. Let.*, 92(24):245510, 2004.
- A. Karma and W.-J. Rappel. Quantitative phase-field modeling of dendritic growth in two and three dimensions. *Phys. Rev. E*, 57:4323–4349, 1998.
- A. Karma, D. A. Kessler, and H. Levine. Phase-field model of mode III dynamic fracture. *Phys. Rev. Let.*, 87(4):45501, 2001.
- M. Keller. *Implementierung eines Phasenfeldmodells in einen 3D-Finite-Elemente-Methode-Code zur Berechnung von Rissfortschritt in spröden Materialien*. Diploma thesis, Technische Universität Kaiserslautern, 2011.
- R. Kienzler and G. Herrmann. *Mechanics in material space: With applications to defect and fracture mechanics*. Engineering online library. Springer, 2000.

## Bibliography

- R. Kobayashi and J. A. Warren. Modeling the formation and dynamics of polycrystals in 3d. *Physica A*, 356(1):127–132, 2005.
- S. Kolling, R. Müller, and D. Gross. A computational concept for the kinetics of defects in anisotropic materials. *Comp. Mat. Sci.*, 26:87–94, 2003.
- C. Kuhn and B. Eidel. Time integration of inelastic material models exhibits an order reduction for higher-order methods - can this be avoided? *PAMM*, 7(1):2090019–2090020, 2007.
- C. Kuhn and R. Müller. A phase field model for fracture. *PAMM*, 8(1):10223–10224, 2008.
- C. Kuhn and R. Müller. Phase field simulation of thermomechanical fracture. *PAMM*, 9(1):191–192, 2009.
- C. Kuhn and R. Müller. A continuum phase field model for fracture. *Eng. Fract. Mech.*, 77(18):3625–3634, 2010a. Computational Mechanics in Fracture and Damage: A Special Issue in Honor of Prof. Gross.
- C. Kuhn and R. Müller. Configurational forces in a phase field model for fracture. In *18th European Conference on Fracture*. DVM, 2010b.
- C. Kuhn and R. Müller. Exponential finite elements for a phase field fracture model. *PAMM*, 10(1):121–122, 2010c.
- C. Kuhn and R. Müller. A new finite element technique for a phase field model of brittle fracture. *J. Theor. Appl. Mech.*, 49(4):1115–1133, 2011a.
- C. Kuhn and R. Müller. Exponential finite element shape functions for a phase field model of brittle fracture. In E. O nate and D. R. J. Owen, editors, *XI International Conference on Computational Plasticity. Fundamentals and Applications (COMPLAS XI)*, 2011b.
- C. Kuhn and R. Müller. On an energetic interpretation of a phase field model for fracture. *PAMM*, 11(1):159–160, 2011c.
- C. Kuhn and R. Müller. Interpretation of parameters in phase field models for fracture. 2012.
- C. J. Larsen. Epsilon-stable quasi-static brittle fracture evolution. *Commun. Pure Appl. Maths*, 63(5):630–654, 2010a.
- C. J. Larsen. Models for dynamic fracture based on Griffith’s criterion. In K. Hackl, editor, *IUTAM Symposium on Variational Concepts with Applications to the Mechanics of Materials*, volume 21 of *IUTAM Bookseries (closed)*, pages 131–140. Springer Netherlands, 2010b.

- C. J. Larsen. Local minimality and crack prediction in quasi-static Griffith fracture evolution. *Discrete Contin. Dyn. Syst. Series S*, to appear, 2012.
- S. LaZghab, T. Aukrust, and K. Holthe. Adaptive exponential finite elements for the shear boundary layer in the bearing channel during extrusion. *Comput. Meth. Appl. Mech. Eng.*, 191(11-12):1113–1128, 2002.
- D. Leguillon. Calcul du taux de restitution de l'énergie au voisinage d'une singularité. *C. R. Acad. Sci., Série IIB*, 309(10):945–950, 1989.
- D. Leguillon. A criterion for crack nucleation at a notch in homogeneous materials. *C. R. Acad. Sci., Série IIB*, 329(2):97–102, 2001.
- D. Leguillon. Strength or toughness? A criterion for crack onset at a notch. *Eur. J. Mech. Solid*, 21(1):61–72, 2002.
- J. Li and X. B. Zhang. A criterion study for non-singular stress concentrations in brittle or quasi-brittle materials. *Eng. Fract. Mech.*, 73(4):505–523, 2006.
- G. D. Maso. *Introduction to  $\Gamma$ -convergence*. Progress in Nonlinear Differential Equations and Their Applications. Birkhäuser, 1993.
- G. Dal Maso and R. Toader. A model for the quasi-static growth of brittle fractures: Existence and approximation results. *Arch. Rat. Mech. Anal.*, 162:101–135, 2002.
- G. Dal Maso, G. A. Francfort, and R. Toader. Quasistatic crack growth in nonlinear elasticity. *Arch. Rat. Mech. Anal.*, 176:165–225, 2005.
- G. A. Maugin. *Material Inhomogeneities in Elasticity*. Applied mathematics and mathematical computation. Taylor & Francis, 1993.
- G. A. Maugin. *Configurational forces: Thermomechanics, physics, mathematics, and numerics*. CRC series—modern mechanics and mathematics. Taylor and Francis, 2010.
- C. Miehe, M. Hofacker, and F. Welschinger. A phase field model for rate-independent crack propagation: Robust algorithmic implementation based on operator splits. *Comput. Meth. Appl. Mech. Eng.*, 199(45–48):2765–2778, 2010a.
- C. Miehe, F. Welschinger, and M. Hofacker. Thermodynamically consistent phase-field models for fracture: Variational principles and multi-field FE implementations. *Int. J. Numer. Meth. Eng.*, 83(10):1273–1311, 2010b.
- N. Moës, J. Dolbow, and T. Belytschko. A finite element method for crack growth without remeshing. *Int. J. Numer. Meth. Eng.*, 46(1):131–150, 1999.
- R. Mueller and G. A. Maugin. On material forces and finite element discretizations. *Comput. Mech.*, 29(1):52–60, 2002.

## Bibliography

- R. Mueller, S. Kolling, and D. Gross. On configurational forces in the context of the finite element method. *Int. J. Numer. Meth. Eng.*, 53(7):1557–1574, 2002.
- R. Mueller, D. Gross, and G. A. Maugin. Use of material forces in adaptive finite element methods. *Comput. Mech.*, 33(6):421–434, 2004.
- R. Müller. *Configurational forces in defect mechanics and in computational methods*. Habilitation thesis, Technische Universität Darmstadt, Institut für Mechanik, 2005.
- R. Müller, D. Gross, D. Schrade, and B. X. Xu. Phase field simulation of domain structures in ferroelectric materials within the context of configurational forces. *Int. J. Fract.*, 147:173–180, 2007.
- S. Murakami. *Continuum Damage Mechanics*. Solid Mechanics and Its Applications. Springer Science+Business Media, 2012.
- B. Näser, M. Kaliske, and R. Müller. Material forces for inelastic models at large strains: Application to fracture mechanics. *Comput. Mech.*, 40:1005–1013, 2007.
- M. Negri. Convergence analysis for a smeared crack approach in brittle fracture. *Interfaces Free Bound.*, 9:307–330, 2007.
- R. J. Nuismer. An energy release rate criterion for mixed mode fracture. *Int. J. Fract.*, 11:245–250, 1975.
- K. Pham, H. Amor, J.-J. Marigo, and C. Maurini. Gradient damage models and their use to approximate brittle fracture. *Int. J. Damage Mech.*, 20(4):618–652, 2011a.
- K. Pham, J.-J. Marigo, and C. Maurini. The issues of the uniqueness and the stability of the homogeneous response in uniaxial tests with gradient damage models. *J. Mech. Phys. Solid.*, 59(6):1163–1190, 2011b.
- N. Provatas, N. Goldenfeld, and J. Dantzig. Efficient computation of dendritic microstructures using adaptive mesh refinement. *Phys. Rev. Lett.*, 80(15):3308–3311, 1998.
- J. R. Rice. A path independent integral and the approximate analysis of strain concentration by notches and cracks. *J. Appl. Mech.*, 35:379–386, 1968a.
- J. R. Rice. Mathematical analysis in the mechanics of fracture. In H. Liebowitz, editor, *Fracture: An Advanced Treatise*, volume 2, chapter 3, pages 191–311. Academic Press, N.Y., 1968b.
- D. Schrade, R. Mueller, B. X. Xu, and D. Gross. Domain evolution in ferroelectric materials: A continuum phase field model and finite element implementation. *Comput. Meth. Appl. Mech. Eng.*, 196(41–44):4365–4374, 2007.

- R. Spatschek, M. Hartmann, E. Brener, H. Müller-Krumbhaar, and K. Kassner. Phase field modeling of fast crack propagation. *Phys. Rev. Let.*, 96(1):015502, 2006a.
- R. Spatschek, D. Pilipenko, C. Müller-Gugenberger, and E. A. Brener. Phase field modeling of fracture and composite materials. In *CDCM 2006 - Conference on Damage in Composite Materials 2006*, volume 12, pages 1–10. ndt.net, 2006b.
- P. Steinmann. Application of material forces to hyperelastostatic fracture mechanics. I. Continuum mechanical setting. *Int. J. Solid Struct.*, 37(48–50):7371–7391, 2000.
- P. Steinmann, D. Ackermann, and F. J. Barth. Application of material forces to hyperelastostatic fracture mechanics. II. Computational setting. *Int. J. Solid Struct.*, 38(32–33):5509–5526, 2001.
- N. Triantafyllidis and E. C. Aifantis. A gradient approach to localization of deformation. I. Hyperelastic materials. *J. Elasticity*, 16(3):225–237, 1986.
- C. V. Verhoosel, M. A. Scott, T. J. R. Hughes, and R. de Borst. An isogeometric analysis approach to gradient damage models. *Int. J. Numer. Meth. Eng.*, 86(1): 115–134, 2011.
- F. Welschinger, M. Hofacker, and C. Miehe. Configurational–force–based adaptive FE solver for a phase field model of fracture. In *PAMM*, volume 10, pages 689–692, 2010.
- P. Wriggers. *Nonlinear Finite Element Methods*. Springer-Verlag, Berlin, Heidelberg, 2009.
- C. W. Wu. Maximum energy release rate criterion. *J. Elasticity*, 8:2235–2257, 1978.
- B. X. Xu, D. Schrade, D. Gross, and R. Mueller. Fracture simulation of ferroelectrics based on the phase field continuum and a damage variable. *Int. J. Fract.*, 166: 163–172, 2010.
- O. C. Zienkiewicz and R. L. Taylor. *The Finite Element Method*. Butterworth-Heinemann, Oxford, Auckland, Boston, Johannesburg, Melbourne, New Delhi, 5 edition, 2000.

# Curriculum Vitae

Name: Charlotte Kuhn

Geburtsort: Mainz

---

09.1988 – 07.1992 Bürgermeister-Klingler-Schule, Grundschule Mörfelden-Walldorf

08.1992 – 08.1996 Prälat-Diehl-Schule, Gymnasium Groß-Gerau

09.1996 – 07.2001 Mörike-Gymnasium Ludwigsburg

Abschluss: Allgemeine Hochschulreife

10.2001 – 02.2007 Studium der Mathematik  
mit Schwerpunkt Technik und Naturwissenschaften  
an der Technischen Universität Darmstadt

Diplomarbeit:  
*Zeitintegrationsverfahren höherer Ordnung  
für Plastizitätsmodelle mit Fließfläche*

Abschluss: Diplom Mathematikerin

04.2007 – 07.2009 Wissenschaftliche Mitarbeiterin  
am Fachgebiet Festkörpermechanik,  
Fachbereich Bauingenieurwesen und Geodäsie  
der Technischen Universität Darmstadt

seit 08.2009 Wissenschaftliche Mitarbeiterin  
am Lehrstuhl für Technische Mechanik,  
Fachbereich Maschinenbau und Verfahrenstechnik  
der Technischen Universität Kaiserslautern